THE GEOCHEMISTRY OF ORE FLUIDS AND CONTROL OF GOLD MINERALIZATION IN BANDED IRON-FORMATION AT THE KALAHARI GOLDRIDGE DEPOSIT, KRAAIPAN GREENSTONE BELT, SOUTH AFRICA

A thesis submitted in fulfilment of the requirements for the Degree of
DOCTOR OF PHILOSOPHY OF RHODES UNIVERSITY

By

Napoleon Quaye Hammond
BSc (Hons) Ghana, MSc Tokyo

May 2002

PREFACE

This thesis contains results of fundamental work carried out on the D Zone orebody of the Kalahari Goldridge deposit in the Kraaipan Greenstone Belt, South Africa. The thesis consists of seven chapters. The introduction (Chapter 1) provides a review of the various genetic concepts of banded iron-formation and Archaean greenstones as important hosts for gold mineralization. A review of major genetic models of gold in these terranes as well as the objectives for this project is presented. Chapter 2 describes the geological setting of the deposit. The major lithological units on both regional and local scales, and structural features that control the ore shoots are also described.

In chapter 3, the mineralogy and chemistry of gangue and ore minerals in host rocks and their relationship to the mineralization are discussed. The implication of the silicate mineralogy in the BIF to the metamorphic setting of the host rock is inferred. Chapter 4 focuses on geochemical distribution of the elements in each lithology in the orebody. It aimed also to reveals correlation if any, between various elements in the deposit to determine the degree of mobility of the elements in order to delineate alteration trends. Most importantly, correlation between Au and other elements and mass changes accompanying hydrothermal alteration is examined to determine a possible geochemical tool for exploration in the Kraaipan.

The basis for chapter 5 is to characterize the chemistry of the ore fluid responsible for gold mineralization at the Kalahari Goldridge deposit and to define pressure, temperature and composition (P-T-X) paleo-conditions during the mineralization event(s). This has been evaluated based on compositional properties of fluid inclusions derived from microthermometric data along with compositional estimates from laser Raman analyses of the inclusions. These data have been used in conjunction with the composition of alteration mineral assemblages to constrain ambient chemical conditions during mineralization.

In chapter 6, the source of hydrothermal fluid as well as the source of sulphur and carbon in the fluid has been evaluated from the light stable isotopes of C, O, and S of various mineral phases present in the deposit. Chapter 7, the concluding chapter, provides a discussion of a model for the mineralization history at the Kalahari Goldridge deposit. In particular, the sources of the mineralizing fluid and gold, mechanisms of transport and conditions that caused the precipitation of the gold, are discussed. Furthermore, implications for exploring for further deposits both on a local and regional scale are highlighted.

ABSTRACT

The Kalahari Goldridge mine is located within the Archaean Kraaipan Greenstone Belt about 60 km SW of Mafikeng in the Northwestern Province, South Africa. Several gold deposits are located within approximately north-south-striking banded iron-formation (BIF). Current opencast mining operations are focused on the largest of these (D Zone). The orebody is stratabound and hosted primarily in the BIF, which consists of alternating chert and magnetite-chlorite-stilpnomelane-sulphide-carbonate bands ranging from mm to cm scale. The orebody varies in thickness from 15 to 45 m along a strike length of about 1.5 km. The BIF is sandwiched between a sericite-carbonate-chlorite schist at the immediate footwall and carbonaceous meta-pelites in the hanging-wall. Further west in the footwall, the schists are underlain by mafic meta-volcanic amphibolite. Overlying the hanging-wall carbonaceous meta-pelites are schist units and meta-greywackes that become increasingly conglomeratic up the stratigraphy. Stilpnomelane-, chlorite- and minnesotaite-bearing assemblages in the BIFs indicate metamorphic temperatures of 300 - 450°C and pressures of less than 5 kbars. The BIF generally strikes approximately 340° and dips from 60 to 75°E. Brittle-ductile deformation is evidenced by small-scale isoclinal folds, brecciation, extension fractures and boudinaging of cherty BIF units. Fold axial planes are sub-parallel to the foliation orientation with sub-vertical plunges parallel to prominent rodding and mineral lineation in the footwall.

Gold mineralization at the Kalahari Goldridge deposit is associated with two generations of subhorizontal quartz-carbonate veins dips approximately 20 to 40°W. The first generation consists of ladder vein sets (Group IIA) preferentially developed in Fe-rich mesobands, whilst the second generation consists of large

quartz-carbonate veins (Group IIB), which crosscut the entire orebody extending into the footwall and hanging-wall in places. Major structures that control the orebody are related to meso-scale isoclinal folds with fold axes subparallel to mineral elongation lineations, which plunge approximately 067°E. These linear structures form orthogonal orientation with the plane of the mineralized shallow-dipping veins indicating stretching and development of fluid-focusing conduits. A second-order controlling feature corresponds to the intersection of the mineralized veins and foliation planes of host rock, plunging approximately 008°N and trending 341°.

Gold is closely associated with sulphides, mainly pyrite and pyrrhotite and to a lesser extent with bismuth tellurides, and carbonate gangue. The ore fluid responsible for the gold deposition is in the C-O-H system with increased CH_4 contents attributed to localized hydrolysis reaction between interbedded carbonaceous sediment and ore fluid. The fluid is characterized by significant CO_2 contents and low salinities below 7.0 wt % NaCl equivalent (averages of 3.5 and 3.0 wt % NaCl equivalent for the first and second episodes of the mineralization respectively). Calculated values of fO_2, ranging from $10^{-29.98}$ to $10^{-32.96}$ bars, bracket the CO_2-CH_4 and pyrite-pyrrhotite-magnetite buffer boundaries and reveal the reducing nature of the ore fluid at deposition. Calculated total sulphur content in the ore fluid ($m_{\Sigma S}$), ranges from 0.011 to 0.018M and is consistent with the range ($10^{-3.5}$ to 10^{-1}M) reported for sub-amphibolite facies ore fluids. The close association of sulphides with the Au and nature of the fluid also give credence that the Au was carried in solution by the $Au(HS)_2^-$ complex. Extensive epigenetic replacement of magnetite and chlorite in BIF and other meta-pelitic sediments in the deposit by sulphides and carbonates, both on mesoscopic and microscopic scales gives evidence of an interaction by a CO_2- and H_2S-bearing fluid with the Fe-rich host rocks in the deposit. This

facilitated Au precipitation due to changes in the physico-chemical conditions of the ore fluid such as a decrease in the $m_{\Sigma S}$ and pH leading to the destabilization of the reduced sulphur complexes. Local gradients in fO_2 may account for gold precipitation in places within carbonaceous sediments.

The fineness of the gold grains (1000*Au/(Au + Ag) ranges from 823 to 921. This compares favourably with the fineness reported for some Archaean BIF-hosted deposits (851-970). Mass balance transfer calculations indicate that major chemical changes associated with the hydrothermal alteration of BIF include enrichment of Au, Ag, Bi, Te, volatiles (S and CO_2), MgO, Ba, K and Rb but significant depletion of SiO_2 and minor losses of Fe_2O_3. In addition, anomalous enrichment of Sc (average, 1247%) suggests its possible use as an exploration tool in the ferruginous sediments in the Kraaipan greenstone terrane.

Evidence from light stable isotopes and fluid inclusions suggests that the mineralized veins crystallized from a single homogeneous fluid source during the two episodes of mineralization under the similar physicochemical conditions. Deposition occurred at temperatures ranging from 350 to 400°C and fluid pressures ranging from 0.7 to 2.0kbars. Stable isotope constraints indicate the following range for the hydrothermal fluid; $\delta^{18}O_{H_2O}$ = 6.65 to 10.48‰, $\delta^{13}C_{\Sigma C}$ = -6.0 to -8.0 ‰ and $\delta^{34}S_{\Sigma S}$ = + 1.69 to + 4.0‰. These data do not offer conclusive evidence for the source of fluid associated with the mineralization at the Kalahari Goldridge deposit as they overlap the range prescribed for fluid derived from devolatization of deep-seated volcano-sedimentary piles near the brittle-ductile transition in greenstone belts during prograde metamorphism, and magmatic hydrothermal fluids.

ACKNOWLEDGEMENT

I would like to express my sincere appreciation and thanks to Professor John M. Moore for his dedication in supervision throughout the 4 years of this study. I also wish to express my heartfelt appreciation for the several discussions and constructive criticisms, which always served as an encouragement to put in my best. His critical review of the first draft of the thesis improved significantly, numerous grammatical errors. I also express my appreciation to him for providing financial support during the fourth of this study through an FRD research grant.

My thanks also go to Dr. R. Sheets and Prof. R. Jacob who contributed valuably through various discussions. My special appreciation to Professor J. Marsh for assisting with the processing of XRF data. Many thanks to other academic staff members, Dr. M. Roberts, Prof. H. Eales and Dr. E. Ferré who assisted me various ways. I am indebted to Dr. A. Imai of the Geological Institute, University of Tokyo for analyzing sulphides samples for sulphur isotopes. My gratitude also to Prof. T. Miyano of the Institute of Geosciences, University of Tsukuba who through various discussions provided a significant understanding of the chemistry and behaviour of Fe-rich silicates typically stilpnomelane and minnesotaite in banded iron-formation.

My gratitude to J. Hepple and his technical staff (Bennett Bongwana, Chris Pikoli and Wilberforce Hashe) for their contribution towards thin and polished sections preparations and Andre Visagie for assistance with sample preparation for XRF runs. I also appreciate the assistance of Miss S. Bramdeo during microprobe analysis. I wish to say a big thank you to the secretary of Exploration Geology,

Mrs. A. Goddard for her friendly environment and readiness to assist me whenever I call on her.

I wish to thank the management of the Kalahari Goldridge Mine for a 3-year doctoral bursary and also for providing logistic support while on the field. My thanks to the following staff geologists, F. Dabrowski and Dr. D. Grobler who were always helpful during field visits to the mine, and Dr. P. Hilliard of the West Rand Consolidated Mines provided fruitful insight of the structural setting of the deposit. My appreciation to the Society of Economic Geologists Foundation for selecting me as one of the recipients of the 1999 Hugh E. McKinstry student research grants. I also express my appreciation to the FRD for the Mobility Grant award to enable me to cover the cost for using the Laser Raman facility at the University of Witwatersrand.

I wish to thank the 1998 and 1999 groups of MSc Mineral Exploration students who, as part of their structural geology module, assisted me with the collection of structural data. They include, E. Mills, T. Kachigunda, J. Sliep, P. Naidoo, T. Zvinoera, G. Hope, N. Giroux, K. Hoglund and K. Muchenje. Fellow economic geology research students, H. Tsikos, T. Strauss, S. Polteau and M. Skead are greatly thanked for their various contributions during the course of this project.

Finally, I am grateful to my wife Awura Abena Pokuah and two daughters Naa Dedei and Naa Korkoi for their sacrifice and patience during all these years because my role as a husband and father greatly diminished during these years.

DECLARATION

The content of this thesis is the original work of the author except where specific acknowledgement is made to the work of others.

No part of this thesis may be reproduced or published without the written permission of the author.

Date: May, 2002

Signed:

DEDICATION

This thesis is dedicated to my mum Naomi A. Quartey for her selfless effort to provide me with a sound education.

TABLE OF CONTENTS

Appendices

1.1 General

1.1.1: Banded iron-formation

The term banded iron-formation (BIF), described by James (1954), was broadly classified as banded cherty and siliceous sediments containing 15 % or more iron (Fe), and iron-rich bands associated with siliceous and clastic sediments. This has subsequently being defined as a chemically precipitated sedimentary rock displaying alternating microscale (microband) to mesoscale (mesoband) bands of oxide, carbonate and silicate facies with quartz (chert), (Gross, 1980; Gross, 1988), where mesoband is defined as thickness of a few millimetres, and microband, defined as repetition of couplets of Fe-poor and Fe-rich laminae within the mesobands (Trendall, 1973). These are mostly developed in Archaean and Proterozoic terranes (Windley, 1986).

Two classifications of BIF based on the (i) environment of deposition, and (ii) the lithological facies have been accepted widely in literature (Gross and MacLeod, 1980; Gross, 1988). The first classification scheme is subdivided into Algoma- and Superior-type BIFs. The latter has a wide distribution in Proterozoic terranes and is believed to have formed in near-shore continental shelf or shallow basins by low temperature fluids (Laberge, 1973). They are commonly associated with carbonates, typically dolomites, quartzites, black shale and minor amounts of volcanic rocks (Gross, 1988). The Algoma-type BIF is commonly found interlayered in both sedimentary and volcanic successions. They are generally regarded as chemical sediments precipitated from seawater that has been enriched in metals from volcanogenic sources (Gross, 1988).

The lithological facies concept is defined on the basis of the mineralogical, chemical and sedimentation factors. Four main facies have been recognised and these include oxide, silicate, carbonate and sulphide. The formation of these has been attributed changes in environmental conditions related to the pH and Eh stability fields (James, 1954). The various facies of the iron formation have been host to giant gold deposits worldwide (e.g. Homestake mine in Early Proterozoic formation, South Dakota, Caddey et al., 1991; Morro Velho in Brazil, Lobato et al., 2001).

1.1.2: Gold mineralization in Archaean greenstones

The Archaean forms an important metallogenic epoch of the Earth's history hosting a vast amount of the Earth's mineral deposits including gold, copper-zinc, iron (Algoma type), nickel, pegmatites, etc. (Boyle, 1979). Mesothermal lode Au deposits have been documented (Hodgson et al., 1993) to constitute the bulk of these deposits with over 60% of the global gold production derived from Archaean greenstone belts. Furthermore, nearly 80 % of the world's largest gold deposits occur in Archaean greenstone belts (Hodgson et al., 1993). Such deposits have been mined extensively in South Africa, Canada, Australia, Zimbabwe, India and Brazil.

Well known deposits include the mines of the Val'Or and Timmins gold camps in the Abitibi greenstone belt in Canada; the Barberton and Murchison greenstone belts in South Africa; Morro Velho and Raposo mines in Brazil; the Kolar gold deposits in India; the Golden Mile in the Yilgan Province of Western Australia; Vubachikwe and Shamva mines in Zimbabwe (Ho and Groves, 1987; Macdonald, 1986; Foster, 1984). These greenstone terranes are characterised by volcano-sedimentary rocks with ages varying from 3.5 to 2.3 Ga and intruded by a succession of granitoid and gnessic rocks (Windley, 1989). An idealised cross-section of these greenstone belts provided by Anhaeusser and Viljoen (1986) indicate a lowermost sequence consisting of ultramafic to mafic units, an intermediate zone consisting of mafic to felsic units and the topmost units consisting of sediments. The sediments consist primarily of chemical precipitates including cherts, jaspers and BIF.

Lode gold deposits in Archaean greenstone belts have been classified broadly into two main subdivisions, (i) vein-associated deposits in metavolcanics or intrusive rocks and to a lesser extent in sediments (e.g., Kalgoorlie deposits, Eastern Goldfields, Western Australia, Phillips, 1986; Val d'Or gold camps in Abitibi, Burrows and Spooner 1989; and several gold deposits in the Barberton greenstone belt, South Africa, de Ronde et al. 1988) and (ii) stratiform-stratabound deposits in banded iron-formation or Fe-rich cherts (e.g., Mt Morgans deposits in the Eastern Goldfield Province, Western Australia, Vielreicher et al. 1994; Vubachikwe deposit, Zimbabwe, Saager et al., 1987; Kolar deposit, India, Hamilton and Hodson, 1986; Lupin deposit, Canada, Lhotka and Nesbitt, 1989; and Fumani gold deposits in the Sutherland greenstone belt, South Africa, Pretorius et al. 1988). The style of gold mineralization in banded iron-formation has led to the proposition of three genetic models for its deposition. This includes syngenetic, epigenetic and a hybrid of both the epigenetic and syngenetic (multistage) models.

The syngenetic model proposes that sulphides, carbonates, chert and gold were deposited from the hydrothermal fluids on the seafloor during chemical sedimentation (e.g., Vubachikwe, Fripp, 1976; Morro Velho, Ladeira, 1991). In the epigenetic models (Phillips et al., 1984; Groves et al., 1987), it is proposed that, gold was introduced from an external source to the iron-formation during vein-forming hydrothermal activity associated with later deformation or metamorphic event. The model proposes that gold and sulphides were precipitated by interaction between iron-rich host rocks and the hydrothermal fluids carrying gold as sulphide complexes in a replacement reaction causing the destabilization of the gold-sulphide complexes resulting in gold deposition. This conclusion is based on several lines of evidence including i) association of gold with veins in many deposits, ii) structural controls of the mineralization in most deposits, iii) unequivocal replacement of iron oxides and silicates by sulphides, iv) similar ore-element ratios to comfirmed epigenetic gold deposits in mafic and ultramafic rocks (Phillips et al., 1984). In the multi-stage model (e.g. Rye and Rye, 1974; Kerswill and Anglin, 1984; Saager et al., 1987), it is proposed that gold mineralization occurred synchronously with chemical sedimentation of the iron-formation. However, gold was remobilised during subsequent metamorphism and deformation and was redistributed into late structures.

The genetic model ascribed to a particular BIF-hosted gold would have important implication for its exploration therefore, determining factors should identify whether the mineralization is associated with a deformation event with the subsequent introduction of gold to the BIF from external source by hydrothermal activity during deformation or whether the ore shoot was generated by localized redistribution of Au within the iron-formation. For example, for deposits in Archaean greenstones ascribed to epigenesis, exploration would target second or third order structures (e.g. fold hinges, shears, faults, splays) associated with regional structures transecting BIF units, whereas, in syngenetic mineralization, exploration would be targeted along the stratified mineralized zones.

1.2: Objectives

The Archaean Kraaipan greenstone belt, located in the northwestern province of South Africa, has received little geological study in the past. This has largely been attributed to the rare occurrence of outcrops obscured by large thicknesses of Kalahari sand and calcretes. The potential of the belt as an exploration target has also been ignored in the past in favour of the Murchison and Barberton greenstone belts due to a combination of lack of knowledge of the geological setting, geochronology and history of the hydrothermal activity in the region and also lack of known deposits.

Initial exploration activity by Shell Exploration Inc. which was later intensified by the West Rand Consolidated Mines in the Kraaipan region between 1987 and 1990 led to the discovery of gold, and the subsequent development and mining operations of the Kalahari Goldridge mine. This discovery has created a renewed interest in the region as a new gold mining district in South Africa. The discovery also served to emphasize the need for detailed studies for a thorough understanding of the geology and the hydrothermal activity in the greenstone belt in order to realize its mineralization potential. It is on this basis that the current study was undertaken through a collaborative initiative between the Department of Geology, Rhodes University and the management of the Kalahari Goldridge mine.

Four potentially mineable ore bodies, including D Zone, A Zone, Watertank and Windmill constitute the ore reserves at the Kalahari Goldridge deposit. The D Zone (Fig. 1.1), which forms the subject of this study, is the largest of the deposits. Mining operation at an average gold grade of 2.4g/ton in the D Zone, began in 1996.

In order to provide a fundamental knowledge of the hydrothermal activity in the Kraaipan greenstone belt, major emphasis of this investigation has been placed on the geochemical aspects of the deposit, including the mineralogy and fluids associated with the mineralization, to define the sources of the ore components and fluid, as well as the mechanism and physico-chemical conditions which facilitated the deposition of the gold. It is anticipated that the current study would serve as a foundation for future research as well as guide exploration activities in the immediate vicinity of the Kalahari Goldridge deposit and the Kraaipan region as a whole. On a global scale, the study is envisaged to contribute towards the on-going debate on the genetic model of BIF-hosted gold in Archaean terranes.

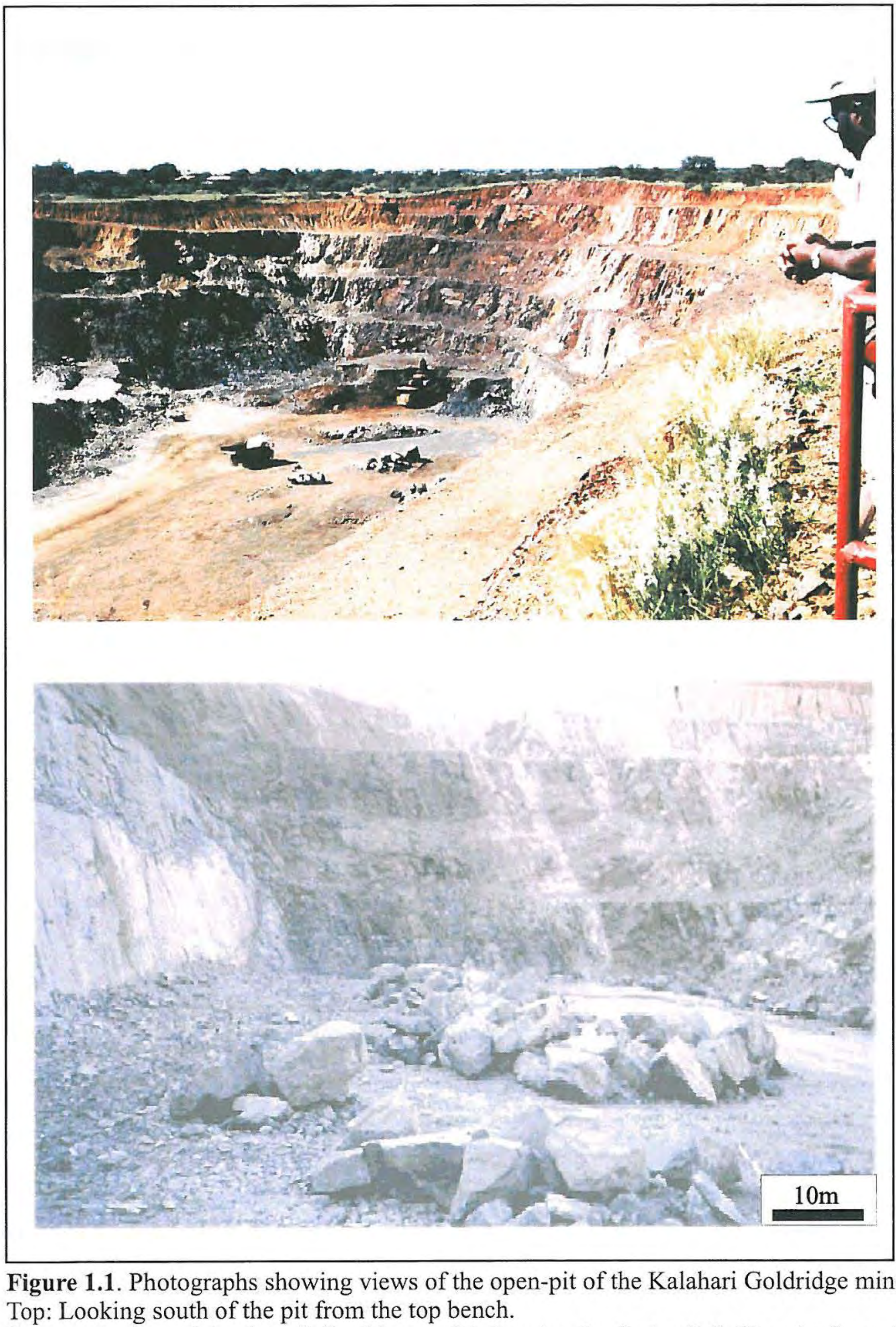

Figure 1.1. Photographs showing views of the open-pit of the Kalahari Goldridge mine.
Top: Looking south of the pit from the top bench.
Bottom: A view of the deposit (looking north) showing the footwall (left) and a face of the orebody (BIF) dipping to the east.

CHAPTER 2: GEOLOGICAL SETTING

2.1: Regional Geological Setting

The Kraaipan greenstone belt is located in the Northwestern Province of South Africa, and forms part of the Kaapvaal Craton (Fig 2.1). Late Archaean Ventersdorp lavas and Tertiary sediments overlie a large portion of the belt, thus creating poor exposures. Earlier work on the greenstone belt was undertaken by Du Toit (1906) who gave the name Kraaipan to a group of banded ferruginous rocks in discontinuous outcrops in the Mafikeng area. Subsequent work in the region was undertaken by Rogers (1908), Van Eeden et al. (1963), Van Zyl (1972) and SACS (1980). Because of the poor exposures, these studies have been unable to establish a clear stratigraphic succession for the greenstone belt.

Recent investigations on the geology of the Kraaipan Greenstone belt (Zimmerman and Anhaeusser, 1991; Jones and Anhaeusser, 1993; Anhaeusser and Walraven, 1999) have been aided by drill-hole intersections by mining companies exploring for extensions of the gold mineralization in the Witwatersrand basin and hydro-geologic operations for groundwater, as well as airborne-geophysical surveys. These studies show that the Kraaipan greenstone belt (Fig. 2.2) stretches discontinuously in an approximately north-south orientation and falls into two domains: northern and southern domains (Anhaeusser and Walraven, 1999). The greenstones in the north consist of three narrow NNW-striking belts extending from the Botswana border in the north to Delareyville in the south, and consist of metamorphosed mafic volcanic rocks interlayered with ferruginous and siliceous sediments.

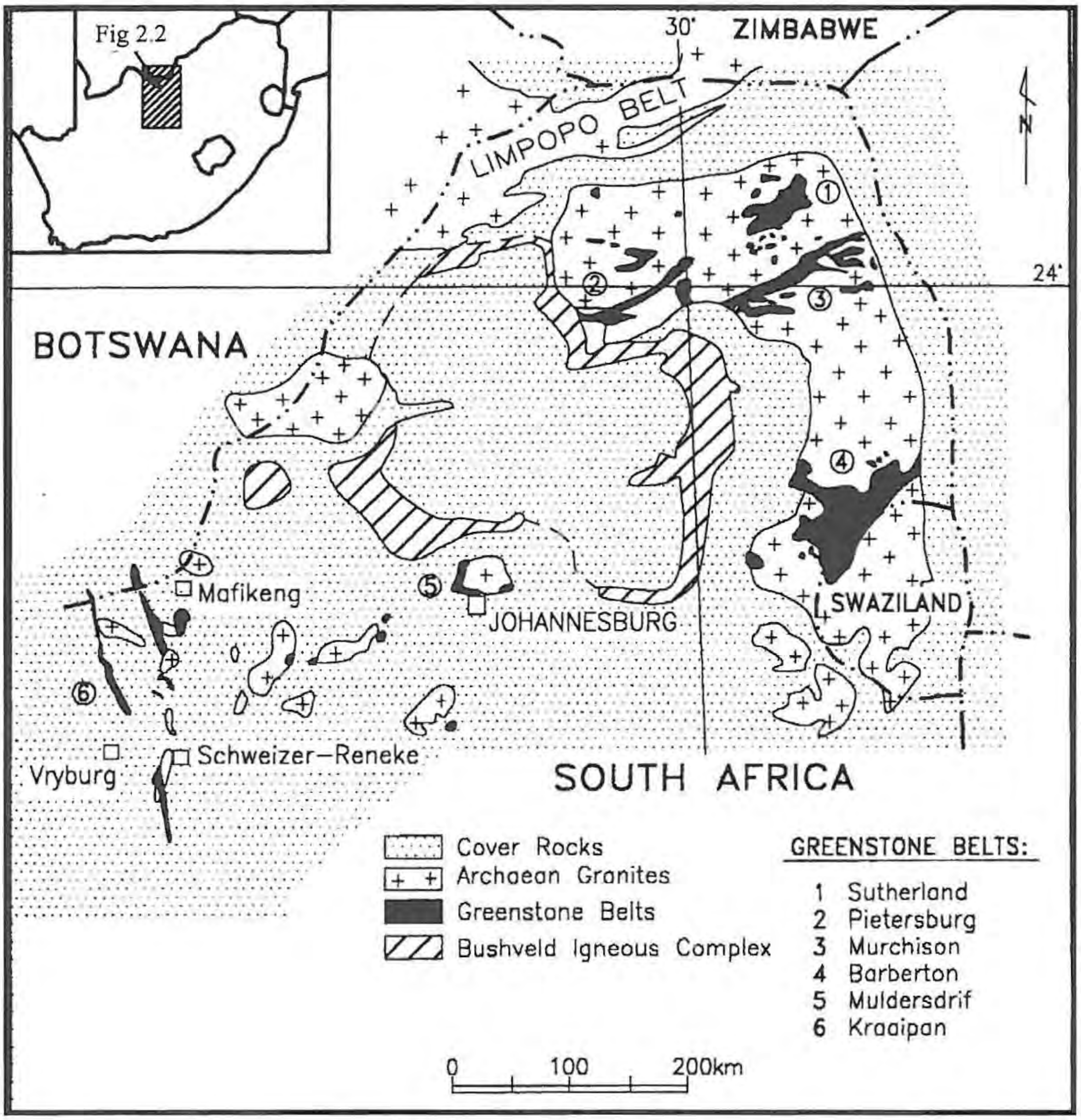

Figure 2.1. Simplified geological map of the Kaapvaal Craton, South Africa, showing the distribution of Archaean basement rocks and of greenstone terranes (modified from Anhaeusser and Walraven, 1999).

The southern sector is characterized by one greenstone sliver and outcrops mainly in the vicinity of Amalia. The volcanic rocks in the greenstones include massive, pillowed basalts, and mafic tuff, which has been subjected to variable degrees of deformation and hydrothermal alteration. Du Toit (1908), Van Eeden et al. (1963), SACS (1980) and Jones and Anhaeusser (1993) have reported minor occurrences of serpentinite and accretionary lapilli. The ferruginous sediments consist mainly of banded iron-formation and ferruginous chert. Pb-Pb isotopic dating of the banded iron-formation indicates a minimum age of 3400 Ma (Anhaeusser and Walraven, 1999). Further work by Poujol et al. (2000) from a U-Pb dating of plutonic xenolith conformably interlayered with the Kraaipan greenstone suggest that the Kraaipan greenstones were older than 3010Ma. The regional metamorphic pattern in the Kraaipan region is poorly documented due the paucity of outcrop occurrence. However, based on amphibole-chlorite-epidote assemblage in some volcanic rocks, Anhaeusser and Walraven (1999) noted that metamorphism may vary from lower greenschist to amphibolite facies grades.

Kraaipan plutonic rocks

The Kraaipan greenstone belt has been intruded by a variety of granitoids. Zimmerman and Anhaeusser (1991) have classified the plutonic rocks into three groups based on the field relationships, petrology, geochemical and geochronological constraints. These include a tonalite-trondhjemitic gneiss-migmatite suite, granodiorite-adamellite suite and the Mosita adamellites. The oldest group consists of a tonalitic, trondhjemitic and migmatitic gneiss suite, with zircon evaporation dates from 3070 to 3162 Ma (Anhaeusser and Walraven 1999), and U-Pb dates of approximately 3010 Ma (Poujol et al., 2000) and forms

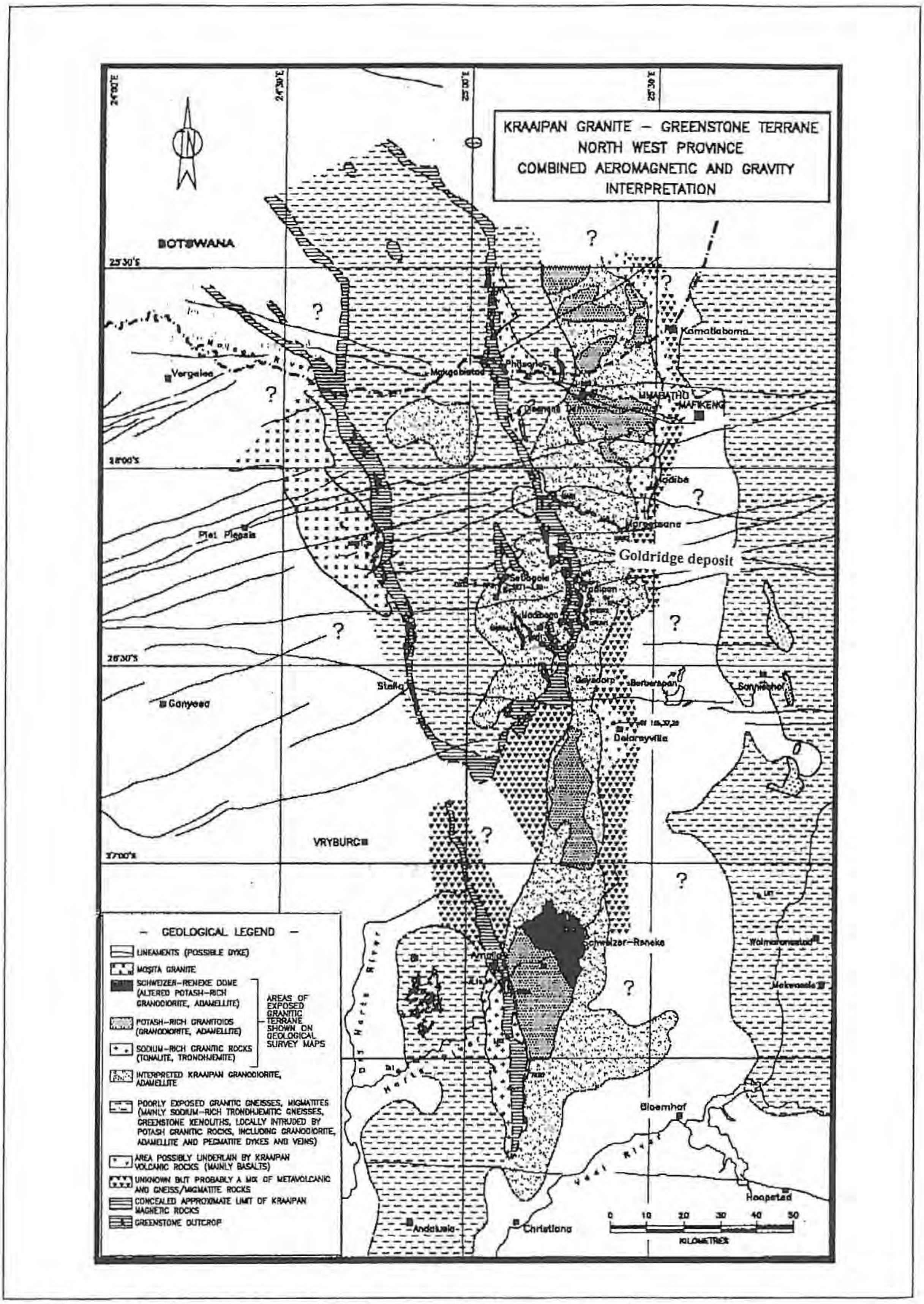

Figure 2.2. Simplified geological map of the Kraaipan granite-greenstone terrane (from Anhaeusser and Walraven, 1999). Map is largely based on suboutcrop interpretation due to limited outcrop occurrence.

the basement to the supracrustal rocks. The rocks show an extensive coverage throughout the Kraaipan terrane. Anhaeusser and Walraven (1999) showed that

Anhaeusser and Walraven (1999) showed that this group of granitoids are Na-rich and have subvertical mineral fabric showing a general orientation subparallel to the trend of the Kraaipan greenstones. Zircon evaporation (Anhaeusser and Walraven, 1999) and U-Pb (Poujol et al., 2000) dates indicate a range from 2846 to 2880 Ma and 2880 to 2930 Ma respectively for the granodiorite-adamellite suite. These rocks exhibit an erratic distribution throughout the entire Kraaipan region.

The Mosita adamellites (U-Pb: 2718 Ma, Burger and Walraven, 1979; zircon evaporation: 2749 Ma, Anhaeusser and Walraven, 1999; U-Pb: 2800Ma, Poujol et al., 2000) form the youngest granitic intrusions in the Kraaipan greenstone terrane. These granitoids are mostly buried beneath the Tertiary Kalahari cover with only sporadic outcrops. Their presence has been discovered mostly through borehole intersections and they occur in the northern sector extending from Kraaipan village and Stella to the Botswana border.

Integrating field with geophysical, petrographic, geochemical and geochronological constraints, Anhaeusser and Walraven (1999) proposed that the Kraaipan volcano-sedimentary greenstone belt and associated granitoids are documented (Anhaeusser and Walraven, 1999; Poujol et al., 2000) to have evolved as a result of episodic accretion onto the western boundary of the Kaapvaal Craton over a time-span of approximately 250 to 450 Ma.

2.2: Local Geology

Due to limited rock exposure at the Kalahari Goldridge deposit, information on the geology has been derived mainly from drill hole intersections and exposures in the open-pit operations and sporadic outcrops outside of the mine area. Figure 2.3 shows a simplified geological map of the open-pit compiled with the aid of MSc Exploration geology students at Rhodes University as part of a structural geology exercise. Figure 2.4 also shows an idealized section from borehole GDP 525 showing the various lithologies occurring at the Kalahari Goldridge deposit.

2.2.1: Lithological units

The Kalahari Goldridge deposit is located about 60 km southwest of Mafikeng in the Kraaipan greenstone belt. Major rock units in the deposit include mafic schist, which forms the footwall of the orebody, a BIF horizon, as the main host of the orebody and a succession of clastic sediments consisting of phyllite, schist and graywacke, which overlie the orebody in the hanging-wall.

Mafic meta-volcanic rocks

This unit forms the footwall of the orebody and consists of rocks of basaltic bulk composition. The rocks are mostly observed in the pit of the mine with sporadic outcrops occurring outside of the mine area. Some of these outcrops have been observed further west of the mine, a distance of about 30km along river channels (Fig. 2.5). The rocks are highly foliated and have experienced some degree of alteration. Actinolite and lesser amounts of epidote, quartz, calcite and plagioclase constitute the main mineral assemblage. The calcite and plagioclase

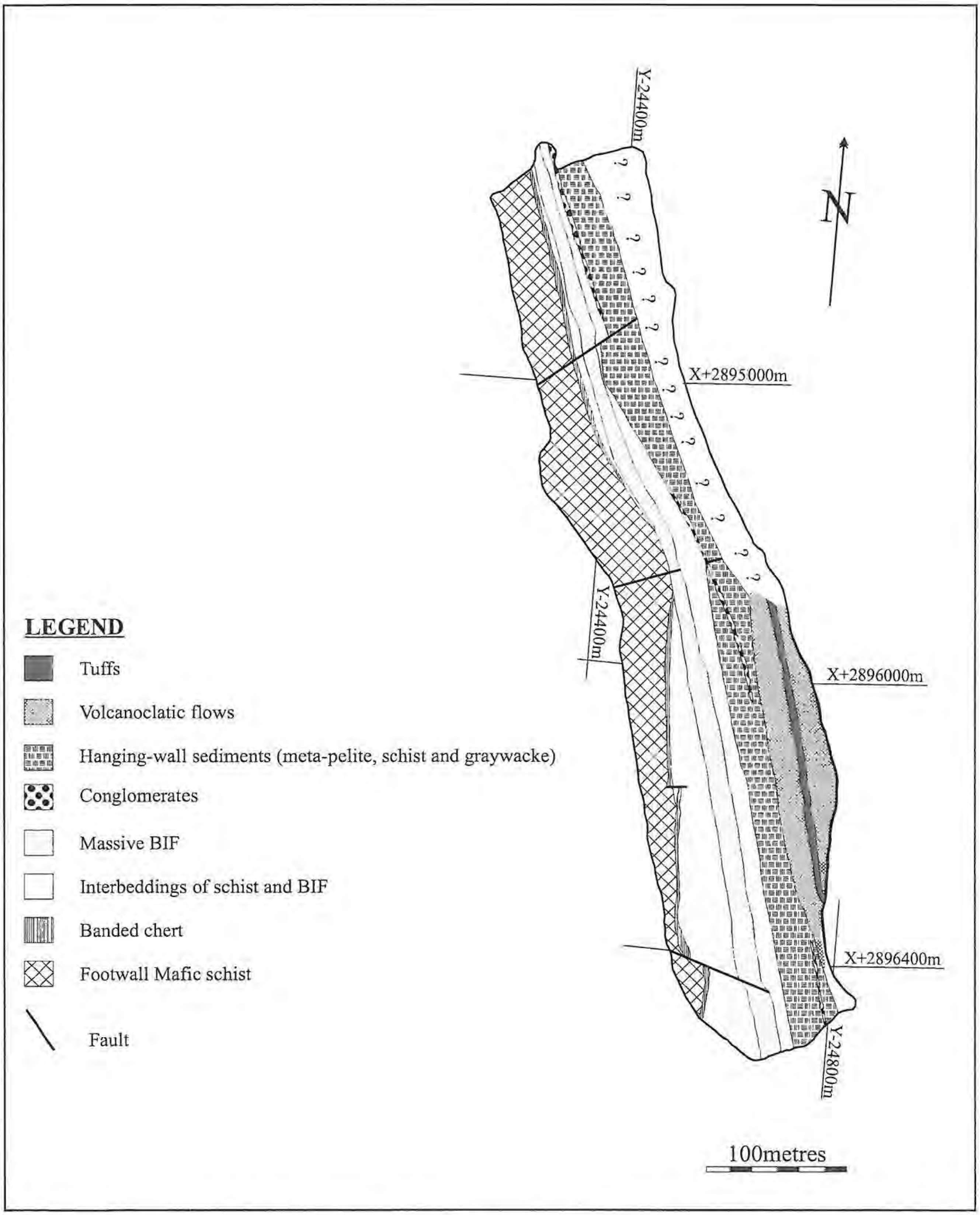

Figure 2.3. Simplified geological map of the D Zone open pit at the Kalahari Goldridge deposit.

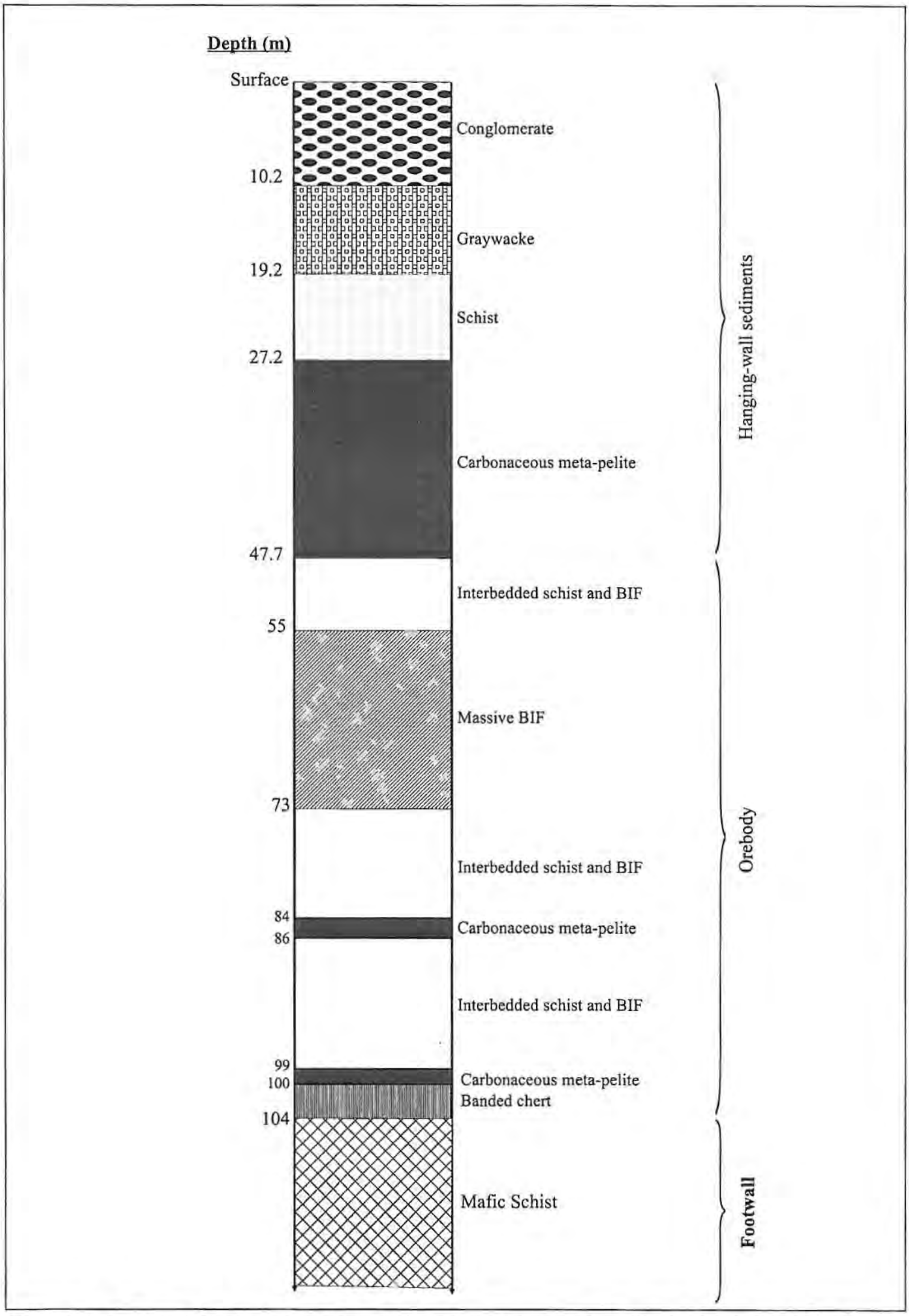

Figure 2.4. Simplified section through borehole intersection GDP 525 (13650N) showing the major lithologies at the Kalahari Goldridge deposit.

in the assemblage appear secondary as they replace epidote and quartz respectively. In places, evidence of the basaltic protolith is characterized by well-preserved pillow structures and amygdales. The immediate footwall unit consists of intensively altered mafic schist, which is evidenced by the bleached appearance and loss of original basaltic texture.

The mineralogy consists essentially of carbonate, sericite and quartz in varying proportions and minor amounts of chlorite. The schists have strong foliations, which parallels the regional trend.

Banded iron formation (BIF)

The BIF, which constitutes the main orebody varies in thickness from about 15 to 45m along a strike length of 1.5km. It forms a massive unit in the central part of deposit but grades into banded ferruginous chert interbedded with chloritic schist at the margins towards the hanging and footwall schist. The BIF consists of alternating chert and magnetite bands ranging from mm to cm scale (mesobands). Petrographic work indicates that the magnetite and chert mesobands may contain microbands of chert and magnetite respectively, which range from 0.1 to 1mm. The mineralogy of the magnetite mesobands consists mainly of magnetite, with minor amounts of stilpnomelane in less altered mesobands in some cases. In more altered samples, phyllosilicates, carbonates and sulphides predominate over magnetite and quartz. Most abundant silicates are chlorites, stilpnomelane and lesser amounts of mica (muscovite and sericite). Chert mesobands range from mm to several cm thick. They are composed of a mosaic of polygonal quartz grains with size reaching up to 0.5mm. Occasionally, subhedral to euhedral magnetite grains are present, but commonly consist of quartz as the primary constituents of these layers. Further description of the mineralogy and the metamorphic implication of the host BIF is provided in Chapter 3. Bulk-rock geochemistry (Chapter 4) characterizes the BIF at Kalahari Goldridge as Algoma type iron-formation. Thin discontinuous carbonaceous- and pyrite-bearing metamorphosed pelites (meta-pelites) ranging between 1 to 2 m in thickness occurs discontinuously between the contacts of the orebody and footwall and also between the orebody and immediate hanging-wall units. The meta-pelites have been subjected to intense deformation as evidenced by the tight to isoclinal folding associated with the unit and have a characteristic black appearance. In thin section, the meta-pelites consist of thin carbonaceous materials anastomosing quartz and carbonate augens (Fig. 2.6).

Interbedded schist

These are metamorphosed pelitic sediments interbedded with ferruginous cherts units within the orebody. The rock consists of two separate units, sandwiched between the centrally located massive BIF and the footwall and hanging-wall. They form thin lenses or beds generally less than 1 m thick of chlorite-rich bands. Centimeter-scale magnetite-rich and cherty bands sometimes alternate with the chlorite-rich bands.

Chlorite, stilpnomelane, muscovite (sericite), carbonate and quartz constitute the main mineralogy associated with the pelites. The modal proportion of these minerals varies considerably in this unit. In less altered samples, chlorite forms the dominant mineral and occurs as dark green in a foliated matrix. Opaque minerals such as magnetite and sulphides (pyrite and pyrrhotite) locally occur in significant proportions and may constitute about 40-50 % modal abundance in some samples. In altered samples, variable amounts of quartz, carbonate and sericite occur with their modal abundance related to the degree of alteration.

Figure 2.5. Amphibolite outcrop in a river channel about 30km west from the Kalahari Goldridge Mine.

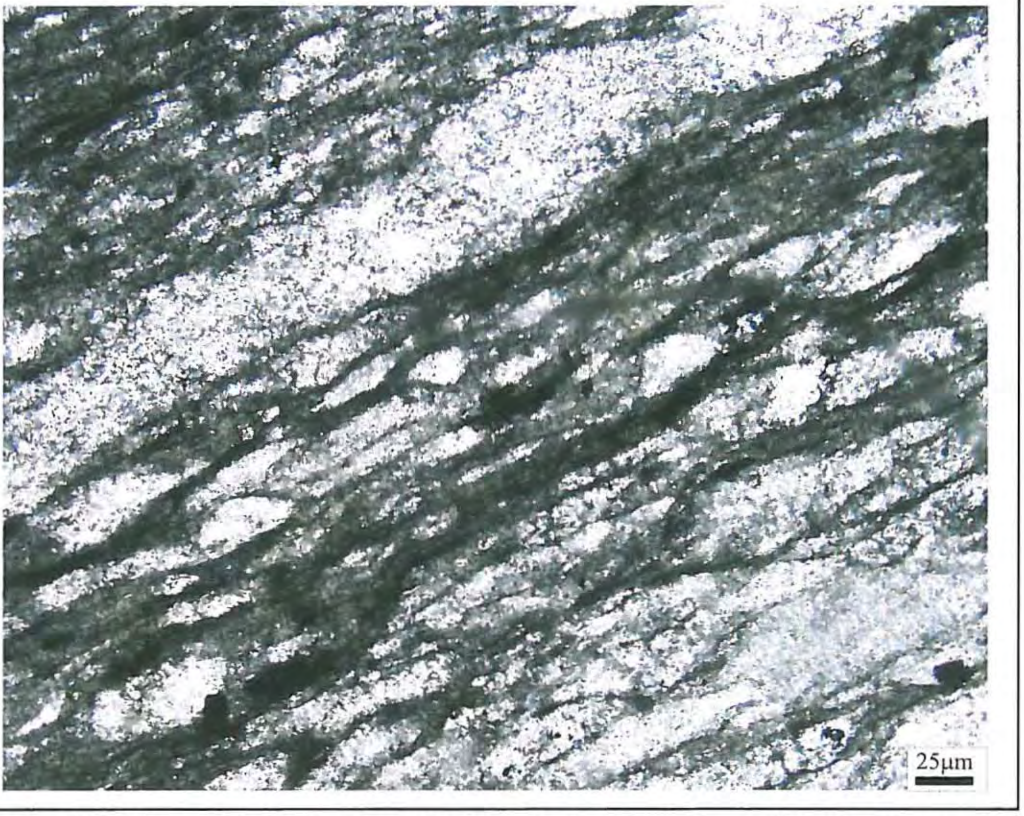

Figure 2.6. Plane polarized photomicrograph showing thin carbonaceous materials anastomosing carbonate augens in meta-pelitic sediments at the Kalahari Goldridge deposit

Hanging-wall sediments

The hanging-wall is a succession of clastic sediments consisting of meta-pelites (phyllites and schist) and greywacke, which consists of graded beds that coarsens up the stratigraphy. In general, the phyllites form the underlying unit while greywackes form the top in the sequence. The phyllites have a characteristic black appearance, which is attributed to presence of carbonaceous materials. Coarse-grained pyrite mineralization is very commonly associated with the phyllites. Chlorite and variable amounts of quartz, sericite and carbonates constitute the main mineralogy in the schist. In hand specimen, large pyrite cubics (1-3mm) are common in the schist. The greywacke consists dominantly of quartz with lesser amounts of chlorites and carbonates.

Within the hanging-wall sediments is a series of fine-grained volcanic and quartz (chert) clasts, with shapes ranging from subrounded to oblates and sizes ranging up to 50cm in diameter. The volcanic clasts are fine-grained and may contain coarse-grained pyrites. The large clasts may be debris flow associated with arc volcanics. Also overlying the graywackes are fine-grained and dark-green tuffaceous layer with thickness of approximately 10m. Series of steeply dipping dolerite dykes ranging up to about 1 meter thick intrude the orebody in places. Crosscutting relationships suggests the dykes postdate the mineralization.

2.2.2: Structure

Structural elements at the Kalahari Goldridge deposit are characterized by steeply dipping primary layering and planar shape fabrics, stretching and intersection lineations, as well as brittle structures. Figure 2.7A illustrates a stereographic projection of various structural elements measured in the deposit. The earliest tectonic fabric developed in the area is bedding-parallel foliation defined by preferred orientation of phyllosilicates and carbonate, which is best observed in the schist and phyllites. The foliation is consistent with the regional trend of the greenstone belt and shows an average orientation of approximately 339°/067°E and may be associated with the regional deformation event (D_1). A localized shear deformation related to later deformation (D_2), is characterized by a narrow mylonite zone, which stretches up to about 5m wide and sandwiched between the immediate footwall and the ore body. At the southern end of the deposit, truncation of portions of the BIF along the shear zone has resulted in the duplication of the orebody. Pyrite and quartz in the mylonite zone have been deformed into ellipsoidal shapes.

The plane of the shear zone hosting the deposit is sub-parallel to the foliation and bedding planes strikes N-S and dips approximately 65°E. Mineral lineations are defined by elongate quartz and sulphide growth in the schistose foliation plane, and strained clasts in the conglomeritic units in the hanging-wall and roddings in BIF's. The mineral lineations trend approximately 108° and have an average plunge of 67°E, which is subparallel to the foliation plane.

Small-scale isoclinal folds are common in the schist and BIF and have axial plane (334°/061°E) subparallel to the foliation planes. Both the plunge of the isoclinal folds axis and the mineral elongation lineation are subparallel to the foliation and fold axial planes. This has been interpreted to be the result of rotation of the fold axes into parallelism with foliation plane during the shearing deformation (Hilliard, 1996). Large open folds stretch along the entire length of the orebody in a north-south direction and plunge steeply to the east with subvertical axial planes.

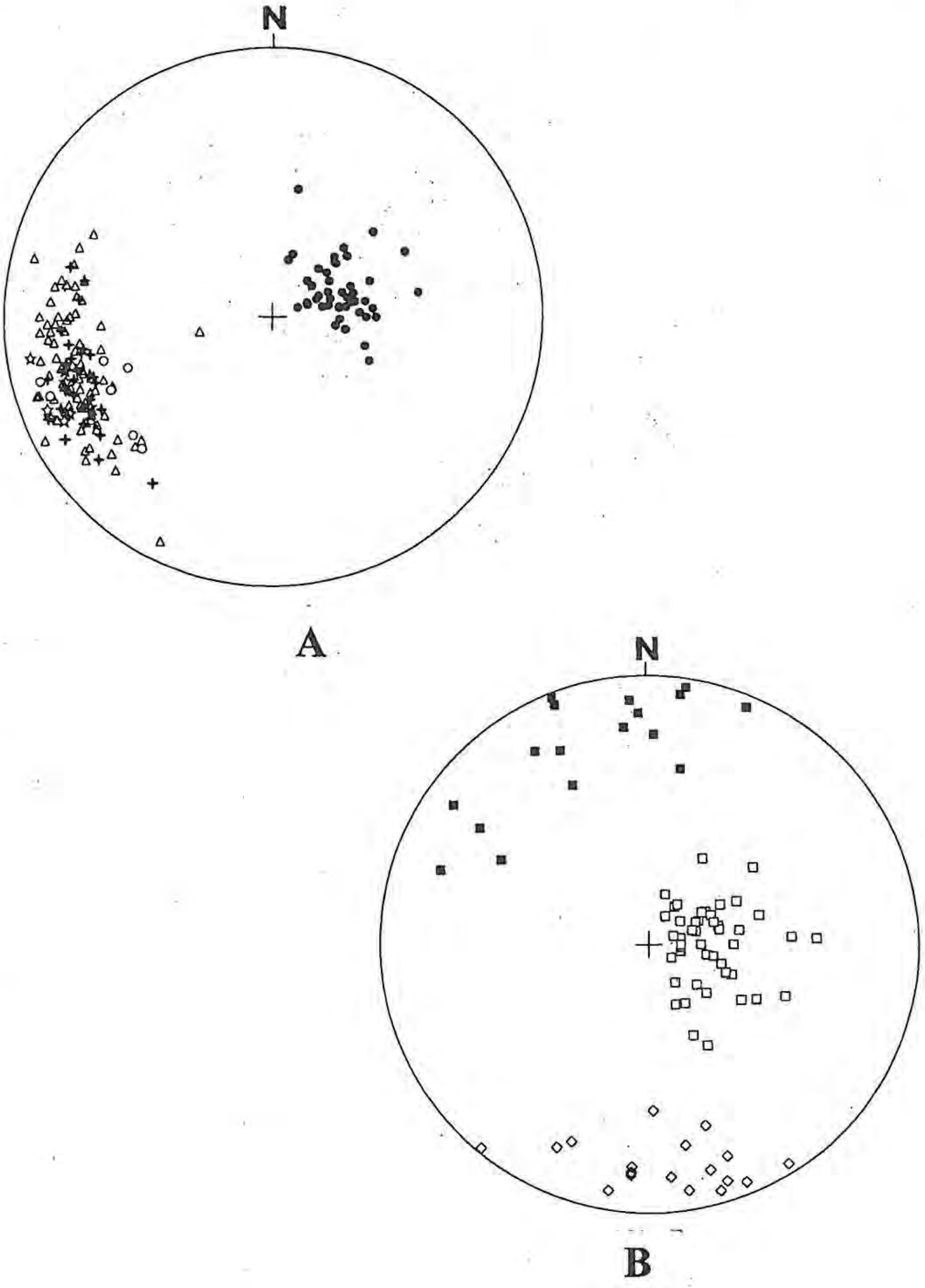

Figure 2.7. Stereographic projection (lower hemisphere) of major structural features and the distribution of quartz-carbonate veins at the Kalahari Goldridge deposit. A. Stereographic projection of poles to bedding plane (crosses), poles to foliation plane (triangles), poles to axial plane of isoclinal fold (circles), poles to shear plane (stars) and mineral lineations (filled circles). B. Stereographic projection of the three groups of quartz-carbonate veins at the Kalahari Goldridge deposit: Group I veins (filled squares), Group II veins (open squares) and Group III veins (diamonds).

Small-scale boudins are developed in some mineralized cherty BIF bands, which hosts the shallow-dipping extension veins. The boudins are defined by the pulling-apart of Fe-rich and siliceous bands. They are characterized by cm scale to rectangular to subrectangular segments separated by extension fractures commonly filled with quartz ± carbonates. The boudins are best and commonly developed in more Fe-rich (magnetite-rich) mesobands than the siliceous mesobands. This observation provides a useful indicator of the relative competence of the magnetite and the siliceous bands. Large-scale boudins are commonly associated with the interbedded chlorite schist where foliated chlorite schist wraps around large BIF blocks forming anastomosing networks of boudins.

At Kalahari Goldridge deposit, the selective and preferential development of extension veins in the magnetite-rich mesobands of the BIF is likely to have been influenced by mineralogical composition and textures coupled with low tensile strength in the BIF bands. The relative competence of the magnetite-rich bands may be influenced by the modal proportion of silica in each band inducing plasticity in the more siliceous bands and also viscosity contrast between layers. This conclusion is based on the observation by Lloyd et al. (1982) that minerals such as quartz enhance plastic deformation during the development of mylonitic microstructure in polymineralic rocks. This is consistent with field observations, which showed that more siliceous magnetite mesobands exhibit limited fracturing and extension veining than more magnetite-rich bands. Further support for this is provided by field observations by Foster and Gilligan (1981) who listed several observations including gross mineralogy and the mineralogy of the individual bands, metamorphic grade, the strain rate and the stress domain, and fluid pressure as potential factors for brittle failure in banded iron-formation. They asserted that magnetite-rich units are more prone to brittle deformation than silicate-rich units. The close association of the small-scale boudins with bedding-perpendicular extension veins at the Kalahari Goldridge deposit also suggests that the deformation was progressive with the initial development of necking followed by through-going extension fractures and vein formation.

2.2.3: Deformational history

The limited geological literature on the Kraaipan greenstone belt, coupled with the lack of outcrops, makes attempts to constrain the tectonic history and the associated mineralization difficult. However, regional aeromagnetic data and local field observations at the Kalahari Goldridge deposit provide some information for interpretation of the deformational history and how it relates to the mineralization. Hilliard (1996) documented an early regional deformational episode D_1, which he concluded to be associated with the mineralization and major structural features at Kalahari Goldridge deposit. A latter event D_2, was also concluded by Hilliard (1996) to have resulted in the flexuring of the deposit but causing minor effects on the geometry of D_1 in the deposit.

In this study, observed structural features in the orebody indicate at least three deformational episodes, D_1 to D_3. The earliest deformational episode, D_1, is synchronous with the low-grade regional metamorphism of the greenstone units in the region. This is characterized by the NNW-SSE-trending penetrative regional schistosity developed subparallel to the primary lithological layering and bedding plane. The mine sequence is inferred to be in a subsidiary shear zone, which runs subparallel to a regional shear zone and attributed to the D_1 deformation event (Hilliard, personal communication).

The D_2 deformational event was largely ductile and accompanied by crustal shortening resulting in the development of the tight isoclinal folding, boudins and shearing within the BIF. The D_2 deformation is likely to have been progressive toward a more brittle deformation characterized by extension fractures in more competent and Fe-rich BIF. The D_2 event is also likely to have orientated the axial plane of the tight to isoclinal folds into parallelism with the foliation plane (Hilliard (1996). Further evidence for crustal thickening during this event is commonly exhibited by the buckling of the earliest-formed Group I (metamorphic) quartz-carbonate veins. These features also suggest that the deformation was due to shortening normal to the NNW-SSE foliation trend. The D_2 event also represent mineralization event and controlled the geometry of lode systems which is characterized by shallow-dipping extention veins. The similar structural orientation of the two episodes of the mineralizing veins may suggest that mineralization was accompanied by a uniform stress regime in a progressive deformation.

D_3 is associated with the flexuring of the major N-S belt and development of the broad open folds with easterly dipping vertical axial planes. A localized shear zone, which truncates the orebody at the southern end, is inferred to be associated with the D_3 event. The consistency of the bedding and foliation planes in the deposit suggests the D_2 and D_3 deformational events did not cause major changes in the geometry associated with the D_1 tectonic event.

2.2.4: Vein systems and geometry

Structural mapping in the open-pit at Kalahari Goldridge allowed for three broad classifications of quartz veins on the basis of structural orientation, mineralogy and crosscutting relationships. These are identified as Groups I, II and III. Chronological relationships between these veins were established based on the crosscutting relationships. The structural orientation of veins is illustrated in a stereographic projection (Fig. 2.7B).

Group I veins are steeply dipping oriented approximately at 064°/74°S. They exhibit a simple mineralogy consisting dominantly of carbonates with variable amounts of quartz. About 90-95 % of vein-filling material consists of carbonate. They are emplaced as lenses extending several centimeters in length and width not extending 5 cm. The vein are buckled and distorted in many places, which is indicative of compressive deformation. Crosscutting relationships suggest that the Group I veins are the earliest generation, and considered to have been emplaced from advecting fluids during regional metamorphism and which is attributed to the D_1 deformational event.

Group II veins are the most dominant of the veins at the Kalahari Goldridge deposit and are inferred to have developed during the D_2 deformational episode The mineralogy of the veins consists of carbonate, quartz, sulphides and phyllosilicates. Gold mineralization is associated mainly with these veins. The orientation of the veins is sub-perpendicular to the foliation of the host rock with an average strike of about 174° and dips ranging from about 10° to 40°W. The adjacent wall rocks to these veins display minimal or no evidence of displacement.

The nature of the Group II veins in regard to the size (length and thickness) and crosscutting relationships allows for a further subdivision of into Group IIA and Group IIB veins. The Group IIA veins are best developed in the BIF, are preferentially and selectively developed in Fe-rich bands, and exhibit regular spacing sub-perpendicular to layering in a ladder array (Fig. 2.8A and B). They may extend beyond the Fe-rich bands in places. The thickness of the veins is variable ranging from a few millimeters to about 2 cm and their lateral extensions generally defined by the width of the Fe-rich band but typically up to 5 cm, reaching up to about 12 cm where they extend beyond the Fe-rich bands. The Group IIB veins (Fig. 2.8B) on the other hand, are massive with thickness ranging up to 20 cm and lateral extensions in excess of 20 meters, which cut through the entire orebody into the hanging-wall and footwall in places. Banding is rare in these veins, suggesting that the veins formed from a single-stage depositional event. Carbonate selvages along the contact between the host BIF and vein commonly characterize the large veins. Sulphide haloes at the contacts measuring up to the several centimeters into the host BIF are commonly seen in places. Field relationships indicate that the Group IIB veins postdate the Group IIA (Fig. 2.8B).

The Group III veins are steeply dipping with average orientation of 266°/74°N. Carbonates and quartz are the main mineralogy. The veins have uniform thickness ranging up to about 10cm, and extending several meters in length. Thin pyrite laminations along the selvedges with the host rock are very characteristic of the Group III veins. Crosscutting relationships between the veins indicate that the Group III veins form the latest sets and show no association with gold mineralization. These veins are likely to be associated with tectonism processes associated with the D_3 deformation episode.

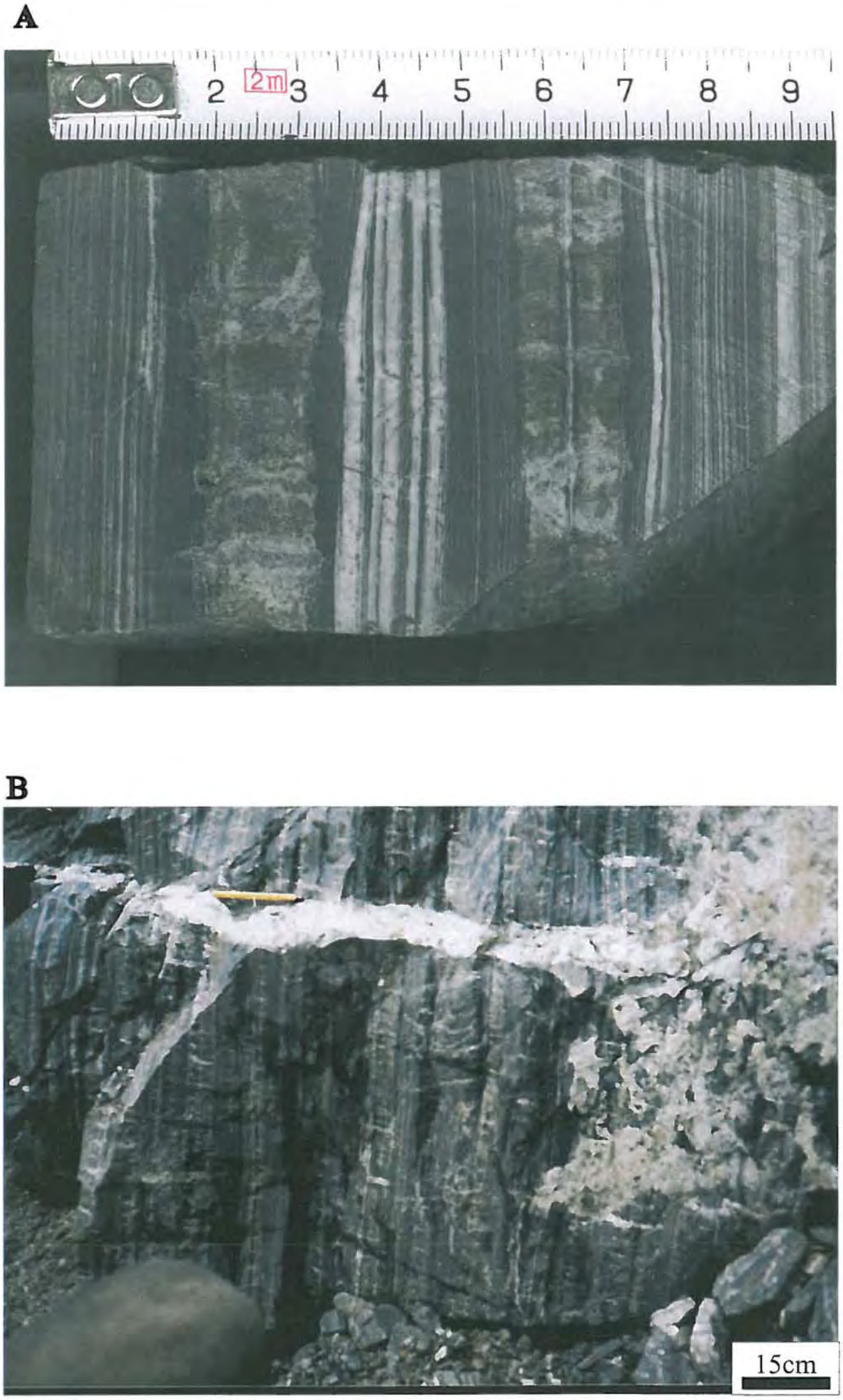

Figure 2.8. Photographs showing the mineralized (Group II) quartz-carbonate veins in banded iron-formation at the Kalahari Goldridge deposit.

A: Group IIA vein preferentially developed in BIF mesobands.

B: Both Group IIA (ladder) veins and Group IIB vein cutting through entire BIF.

2.2.6: Internal structure of mineralizing veins

The internal structure of Group IIB veins consists dominantly of large subhedral-to euhedral interlocking grains of carbonate and quartz with elongated quartz grains (fibres) at the margins in places. The internal structure of the Group IIA veins is dominantly characterized by quartz fibres (Fig. 3.1). The fibres associated with the ladder veins commonly contain slivers of the host rock. The long axes of the fibres are generally parallel to the mineral elongation lineation in the host rock and perpendicular to the vein walls. The long axes of the fibres in the ladder veins are generally straight with sub-perpendicular orientation at high angle to the vein walls and show no evidence of secondary deformation or strain. This is supported by the fact that the vein margins with the bedding planes on opposite sides of show no shear displacement.

Ramsay (1980) referred to this micro-structural feature as anti-axial veining and provided a comprehensive mechanism for its formation. According to Ramsay (1980), these are commonly developed under low-grade metamorphic conditions (e.g., greenschist and sub-greenschist facies) by a cycle of crack-seal process resulting from a build-up of elastic strains in response to rising fluid pressure (P_f), often induced by poor or limited rock permeability leading to fracture. Precipitation of mineral species, diffusion and/or solution mass transfer, leads to the sealing of the fracture and the repeat of the cycle. The opening is commonly associated with trails of wall-rock fragments or fluid inclusions aligned parallel to the wallrock with the central inclusion trails defining the site of the initial fracture.

Studies by some workers (e.g., Ramsay and Huber, 1983) also showed that the fibrous habits in veins might be an original feature produced in response to an active stress field, by crystals growing in crystallographic continuity with adjacent wall-rock minerals. This controls the fibres such that their growth is parallel to the displacement path of their wall-rock boundaries as they move apart.

Cox and Etheridge (1983) and Cox (1987) have argued that free-growing fibre into a fluid-filled micro-crack produces fibres with the long axes at high angle to the growth surface crack-seal increment, irrespective of the sense of displacement across the micro-crack. They concluded that the shape of such fibres would be growth-surface controlled rather than displacement controlled.

2.2.7: Fluid pressure and stress regime

Etheridge (1983), Ridley (1993), and Sibson and Scott (1998), among others, have shown that important factors which determine the development of shear or extension fracture and fluid discharge, leading to mineralization in a particular rock-unit, are the differential stress ($\sigma_1 - \sigma_3$), the rock tensile strength (T) and the magnitude of the fluid pressure (P_f). The difference between the fluid pressure and the stress acting perpendicular to the opening crack (σ_N), which is known as the effective pressure ($P_f - \sigma_N$), is very critical in the development of hydraulic fractures.

In accordance with the criterion for hydraulic fracturing represented by the equation,

$P_f > \sigma_3 + T$,

extension fracture prevails when $(\sigma_1 - \sigma_3) \leq 4T$ while shear failure is characterized by conditions where $(\sigma_1 - \sigma_3) > 6T$ (Etheridge, 1983).

Under these conditions, the development of extension fractures or tension gashes is characterized by relatively low differential stress and high fluid pressures near lithostatic, while shear fracture is induced by high differential stress and high fluid pressures. Strӧngard (1973) also deduced that under conditions where σ_3 is subparallel to lithologic layering, regions of low mean stress would be focused in more competent units. Theoretical considerations by Ridley (1993) also showed that upwelling fluids are highly focused into such low mean-stress zones. Therefore, the extensive shallow-dipping veins associated with the BIF can be attributed to high fluid pressures resulting from intensive focusing of fluid into the more competent units. In addition, the shallow-dipping attitude of the veins is likely to have been controlled by a subvertical minimum principal stress (σ_3). The crack-seal features of Group IIA veins at the Kalahari Goldridge deposit therefore suggest vein growth was accompanied by supralithostatic fluid pressure regimes. In this case, the average rate of sealing kept pace with or exceeded the rate of separation of vein walls (Cox et al., 1995). On the other hand, the Group IIB veins indicate features of single-stage vein growth, in which case the rate of vein-wall separation is faster than the mineral deposition during the period of vein growth (Cox et al., 1995). These features are attributed to the spatial and temporal variation in the effective fluid pressure during hydraulic fracturing. Furthermore, the abundance of the Group II veins associated with the mineralization indicates that high fluid pressures were maintained throughout the gold mineralization stages.

2.2.8: Gold mineralization

The distribution of gold mineralization at the Kalahari Goldridge deposit is largely controlled by lithological variation and structure. Highest concentrations of gold are confined to the central part of the orebody within Fe-rich and more competent BIF that also forms the most sulphidized section of the orebody (Fig 2.9). Centimeter-scale sulphidation haloes are associated with the large shallow-dipping veins (Group IIB) are occur mainly within the BIF. A large proportion of the shallow-dipping ladder veins (Group IIA) are confined to the BIF units, which indicate that high fluid pressure may have played an important role during fluid infiltration and gold mineralization.

The direction of the oreshoots may be predicted based on the relationship between the shallow-dipping veins, mineral lineations and tight to isoclinal folds associated with BIF. The mineral lineations trend approximately subparallel to the foliation plane and orthogonal to the shallow-dipping veins. Two major controlling factors are therefore envisaged to have played active role in the localization of gold mineralization at the Kalahari Goldridge deposit (Fig. 2.10). The primary structural control is inferred to plunge subvertically, subparallel to the fold axes of tight isoclinal folds plunging approximately 080°E and orthogonal to the shallow dipping mineralized veins. A secondary controlling feature is related to the intersection of shallow-dipping extension veins with host rock foliation planes plunging approximately 08°N and trending 341°.

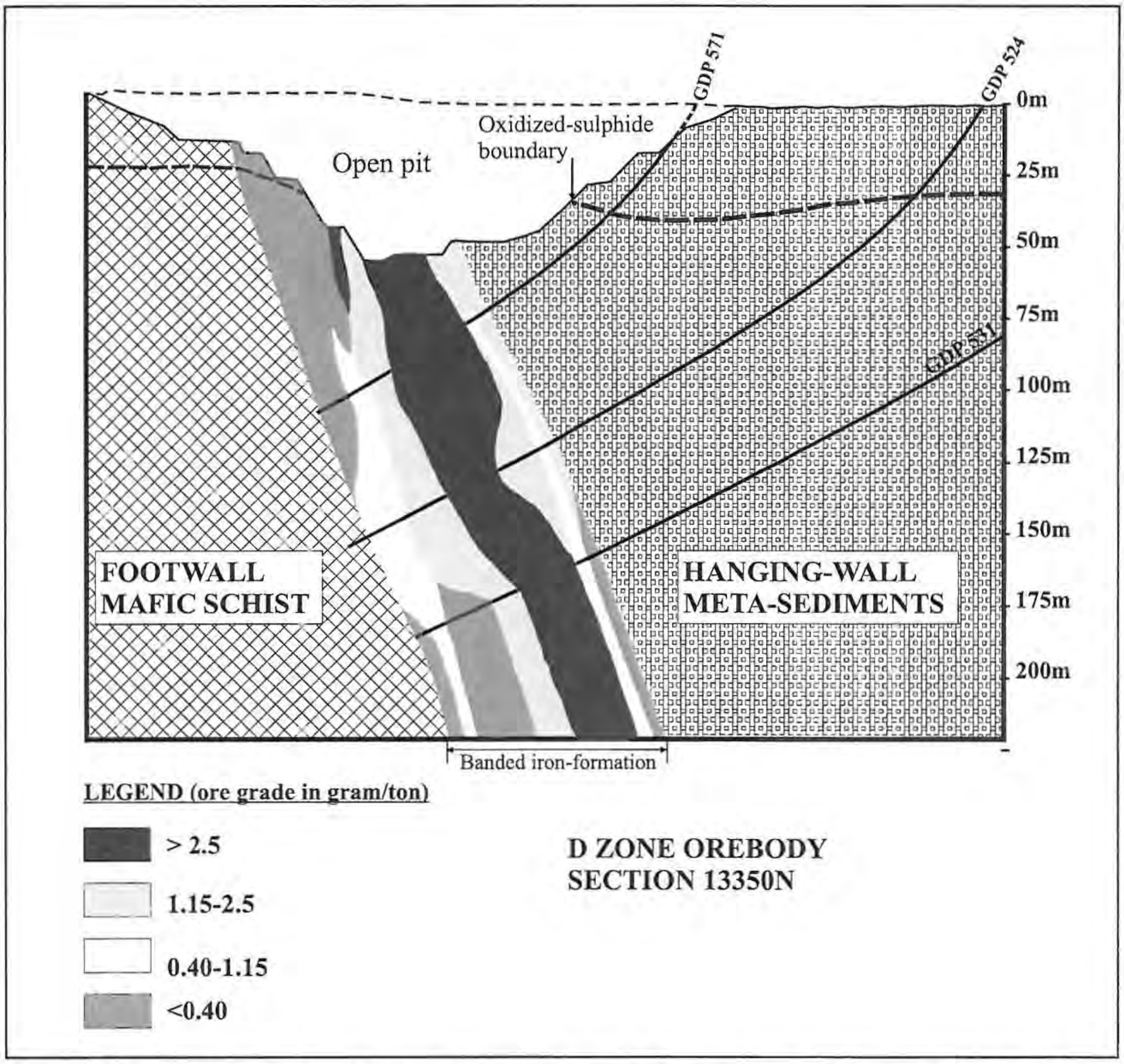

Figure 2.9. Distribution of gold mineralization in the D Zone orebody, Kalahari Goldridge deposit. Highest grade occur in massive BIF located centrally in the orebody (Figure redrawn from Kalahari Goldridge Mine annual report, 1998).

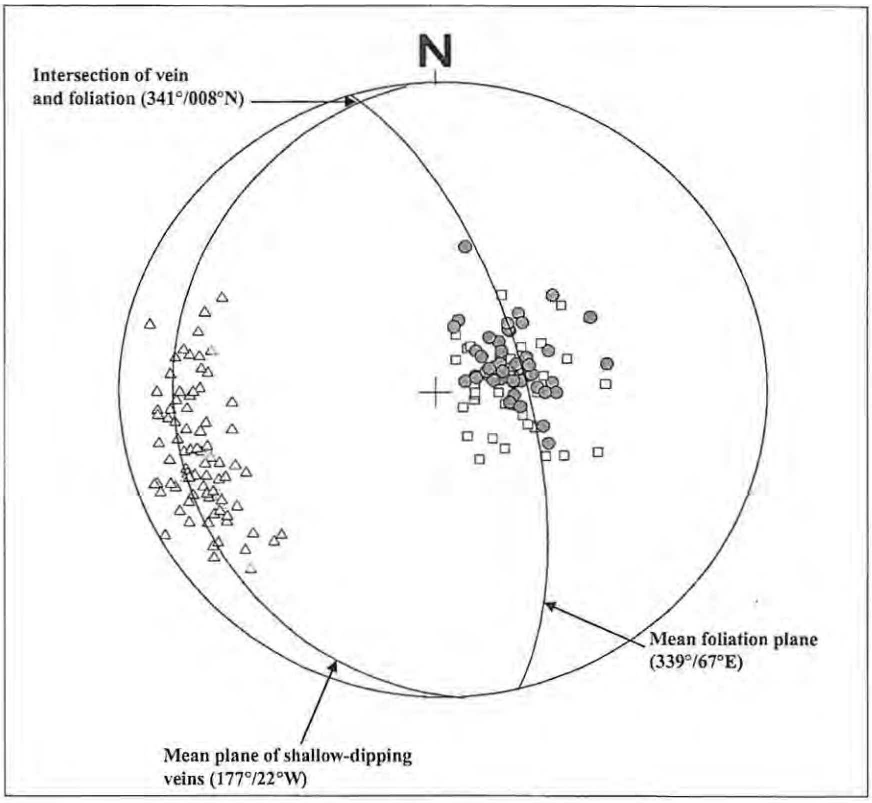

Figure 2.10. Stereographic projection (lower hemisphere), of the majorstructurescontrolling mineralization at the Kalahari Goldridge deposit. The primary control is illustrated by the orthogonal orientation of the mineral elongation lineations (filled circles) to the shallow-dipping (Group II) veins. A secondary predicted control is the intersection of the planes of the foliation and the shallow-dipping veins at approximately 341°/008°N. Legends: triangles = poles to foliation plane, squares = poles to plane of mineralised veins, filled circles = mineral elongation lineations

3.1 Introduction

The identification of major and minor mineral constituents in all lithologies at the Kalahari Goldridge deposit was carried out by standard microscopic studies under reflected and transmitted light on thin and polished sections respectively. The mineral identification was also supplemented by qualitative X-ray diffraction analysis of powdered samples. The textural relationship between gangue and ore minerals was determined by a combination of transmitted and reflected light in polished thin sections. The paragenetic sequence of primary and secondary phases has been facilitated by textural relationships of the constituent assemblages. The chemical composition of the minerals was determined by electron microprobe analysis.

Fifty thin sections, 30 polished thin sections and 70 polished sections from drill cores and pit samples were studied and the mineralogical description of the minerals is given below. The principal minerals identified in the studied samples in the ore body are silicates, including stilpnomelane, minnesotaite, chlorite, quartz and muscovite; carbonates, including siderite, ankerite-dolomite series and calcite; sulphides, such as pyrite, pyrrhotite, chalcopyrite, and native bismuth and bismuth telluride. Other minerals such as epidote, actinolite and plagioclase were also identified in minor amounts in the altered mafic units in the footwall. Recalculation of mineral composition was done on the basis of 11 oxygens for muscovite, stilpnomelane and minnesotaite, 14 oxygens for chlorite and 2 cations for the carbonates. The relative abundances of the minerals are illustrated in Table 3.1.

Table 3.1. Modal abundance of principal minerals identified in ore body at the Kalahari Goldridge deposit.

	HANGING-WALL			ORE BODY				FOOTWALL
	Graywacke	Schist	Shale	BIF	Schist	Group IIA	Group IIB	Mafic schist
Mineral								
Oxides								
magnetite	–	–	–	XXXX	XX	X	X	–
quartz	XXXX	XXX	XXX	XXXX	XXXX	XXXX	XXXX	XXX
Ilmenite	–	X	–	–	XX	–	–	X
Sulphides								
pyrite	X	XX	XX	XXXX	XX	XX	XX	X
pyrrhotite	–	X	X	XXXX	XX			X
chalcopyrite	–	–	–	XX	XX	X	X	–
Carbonate								
siderite	–	–	–	XXXX	–	XX	XX	–
ankerite-dolomite	X	XXX	XXX	XX	XXX	XXX	XXX	XX
calcite	X	XX	X	–	–	–	–	XXX
Silicates								
chlorite	XXX	XXXX	XXX	XXX	XXXX	XX	XX	XXX
stilpnomelane	–	–	–	XXXX	XXX	XX	XX	–
muscovite	XXX	XXX	XXX	X	XXXX	X	X	XXX
minnesotaite	–	–	–	X	X	–	–	–
biotite?	–	–	–	X	–	X	X	–
plagioclase	–	–	–	–	–	–	–	X
epidote	–	–	–	–	–	–	–	X
actinolite	–	–	–	–	–	–	–	X
Bismuth minerals								
native bismuth	–	–	–	X	–	–	–	–
bismuth telluride	–	–	–	X	–	–	–	–
Gold	–	–	–	XX	X	X	X	–

XXXX = Abundant; XXX = Common; XX = less common; X = rare; – = not found. Where abundant > 60 modal %, 20 modal %< Common < 60 modal %, 20 modal % >less common >5 modal % and rare< 5 modal %.

3.2 Silicate Minerals

3.2.1: Quartz

Quartz is the most dominant silicate mineral and occurs in all lithologies in the deposit. Primary quartz occurs in the chert and less altered chert-magnetite mesobands as finely crystalline, mostly 5- to 30 μm-sized, equigranular grains in bands sub-parallel to magnetite microbands. Recrystallization of the fine-grained quartz is characterized by development of coarser grains and quartz veinlets in the cryptocrystalline aggregates. In several bands, the recrytallized grains occur as fibrous aggregates parallel or perpendicular to the boundaries, or in radiating textures. In brecciated and altered samples, quartz is recrystallised to coarser grains in mosaic textures with carbonates and to lesser extent with chlorites. It is the principal vein-filling mineral and forms up to 70 % by volume of the Au-bearing veins. Generally, it occupies the central part of the vein and interstices between other minerals. Quartz in tension gashes displays microstructures, which indicates that the veins were formed by crack-seal mechanisms. In such cases, the quartz exhibits crack-seal fiber growth adjacent to wall rock, with quartz, elongated perpendicular to the boundary of the wall rock (Fig. 3.1). The quartz in the brecciated samples and some veins typically commonly show low to moderate degree of strain as evidenced by undulose extinction in most samples. The grain boundaries between adjacent grains are locally sutured.

Quartz exhibits similar characteristics in the schist units, occurring as isolated, angular to subrounded subhedral grains dispersed in chlorite or sericite matrix. Quartz commonly accompanies sericite as replacement of chlorite in altered schist samples. In pervasively altered schist samples, quartz occurs sporadically and commonly replaced by carbonates (ankerite, ferron dolomite), and is characterized by carbonate pseudomorphs in some samples. Quartz in the greywacke constitutes >85 % modal abundance.

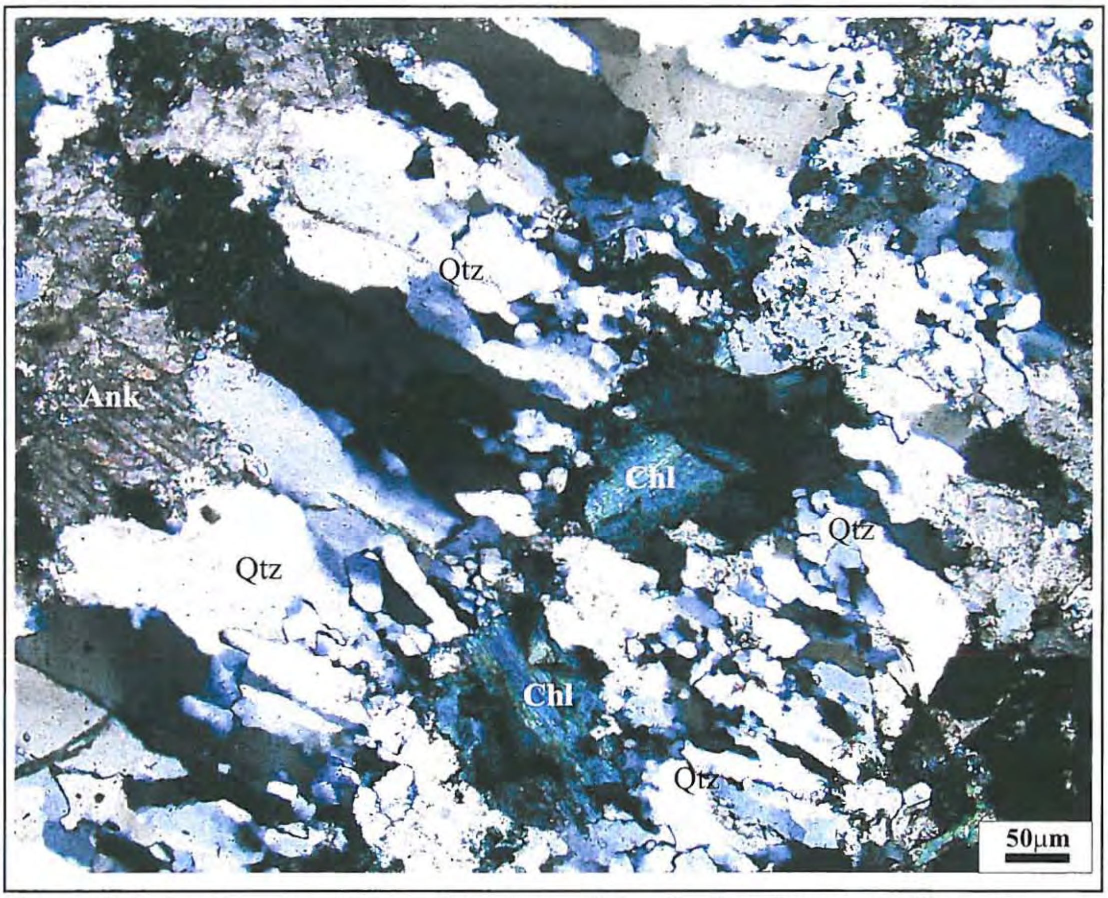

Figure 3.1. Crack-seal vein growth in Group IIA vein showing quartz fibres developed sub-perpendicular to margin of wall rock (BIF). Also shown are growth of chlorite (Chl) in the centre and ankerite (Ank) along the vein margins with host rock. Crossed nicols.

3.2.2: Chlorite

Chlorite occurs in all the lithological units at the Kalahari Goldridge deposit. In the BIF, chlorites have olive green colours and are coarse grained. Chlorite occurs as tabular to equigranular grains intergrown with magnetite and other alteration minerals. Inclusions of chlorites are commonly associated with siderite, magnetite and pyrite. Chlorite is rare in less altered chert-magnetite mesobands. In the pelitic sediments, chlorite typically occurs as fine- to medium-grained schistose or felt-like mass. The colour is variable from deep green in less altered samples to pale blue in highly altered samples. In the orebody schist, chlorite occurs as medium- to coarse-grained equigranular grains in mosaic texture and commonly in bands. The colour of chlorite in the orebody schist appears to depend on the Fe content, varying from deep green in magnetite-absent samples to pale blue in samples containing magnetite disseminations. Chlorite associated with the mineralized quartz veins exhibits pale green pleochroic colours and occurs as sheaves rosettes or felt-like equigranular aggregates, which may be intergrown with carbonate and quartz in a mosaic texture (Figs. 3.1, 3.3A and B).

The composition of the chlorite reflects the host rock composition with Fe-rich varieties associated with the BIF whereas more Mg-rich chlorites occur mostly in the veins and the schist. X-ray diffraction of powdered samples shows a 7Å chlorite as most dominant in the deposit.

Microprobe data of the chlorites showing the average compositions are given in Table 3.4A to 3.4C. Based on the classification of Hey (1954), the chlorites are mainly ripidolite in compositions, with a few samples in the Group IIB veins showing composition characteristic of pycnochlorite (Fig. 3.2).

Table 3.2A. Summary of microprobe analysis of chlorite in interbedded schist at the Kalahari Goldridge deposit.

	Interbedded Schist									
Sample	452/25B		DD17/3B		525/20		NQH/19B		589/19G	
	Mean	std	Mean	std	Mean	std	Mean	std	Mean	std
No.of grains	2		4		4		2		2	
No. of analyses	4		8		7		4		4	
Wt %										
SiO_2	25.79	0.19	23.46	0.36	23.59	0.47	23.90	0.34	23.35	0.04
TiO_2	0.06	0.01	0.07	0.02	0.07	0.01	0.08	0.00	0.06	0.01
Al_2O_3	21.19	0.06	20.92	0.32	21.25	0.95	20.46	0.65	21.24	0.34
FeO	33.03	0.42	32.93	0.58	36.04	1.03	36.29	1.34	36.85	0.42
MnO	0.27	0.01	0.12	0.01	0.11	0.05	0.19	0.00	0.12	0.01
MgO	10.01	0.07	8.17	0.33	8.47	0.36	7.47	0.00	6.58	0.13
CaO	0.09	0.05	0.08	0.03	0.03	0.01	0.05	0.03	0.02	0.02
Na_2O	0.14	0.01	0.03	0.03	0.01	0.02	0.03	0.05	0.05	0.06
K_2O	0.07	0.05	0.02	0.01	0.01	0.01	0.02	0.01	0.04	0.05
Total	90.64		85.82		89.59		88.50		88.31	
Cations per formula unit based on 14 oxygens										
Si	2.73		2.65		2.58		2.66		2.61	
Al (iv)	1.27		1.35		1.42		1.34		1.39	
Tetrahedral total	4.00		4.00		4.00		4.00		4.00	
Al (vi)	1.38		1.43		1.33		1.34		1.41	
Ti	0.01		0.01		0.01		0.01		0.00	
Fe^{2+}	2.93		3.11		3.30		3.38		3.45	
Mn	0.02		0.01		0.01		0.02		0.01	
Mg	1.58		1.38		1.38		1.24		1.10	
Octahedral total	5.91		5.94		6.03		5.98		5.97	
Ca	0.01		0.01		0.00		0.01		0.00	
Na	0.03		0.01		0.00		0.01		0.01	
K	0.01		0.00		0.00		0.00		0.01	
Totals	0.05		0.02		0.01		0.01		0.02	
Temperature °C	346.6	1.0	372.9	3.8	393.6	6.0	369.9	7.4	385.1	0.0
Fe/(Fe+Mg)	0.65		0.69		0.70		0.73		0.76	
Activity of Chl-1	8.9E-02		1.3E-01		1.5E-01		1.7E-01		2.0E-01	
Activity of Chl-2	4.1E-03		2.2E-03		1.9E-03		1.1E-03		6.7E-04	
Activity of Chl-3	1.7E-04		6.8E-05		6.1E-05		3.5E-05		1.6E-05	

Chl-1 = clinochlore, Chl-2 = daphnite and Chl-3 = Al-free chlorite. Activity of chlorite calculated according to the data of Walshe (1986). Temperature is calculated based on the data of Cathelineau (1988).
Formulae for calculating activities are listed in appendix III. std = one standard deviation. *All Fe as FeO

Table 3.2B. Summary of microprobe analysis of chlorite in mineralized BIF at the Kalahari Goldridge deposit.

					Mineralized BIF						
Sample	NQH/10A		525/12A		589/4		524/8		13175 /2C	532/9	
	Mean	std	Mean	std	Mean	std	Mean	std		Mean	std
No.of grains	1		3		2		4		1	2	
No. of analyses	7		8		2		8		1	4	
Wt %											
SiO_2	23.48	0.13	22.86	0.41	22.99	0.86	22.87	0.47	22.13	22.11	0.48
TiO_2	0.05	0.02	0.06	0.01	0.04	0.02	0.04	0.01	0.05	0.08	0.00
Al_2O_3	19.23	0.33	20.44	0.57	19.64	0.05	20.06	0.53	19.61	20.27	0.38
FeO*	39.74	0.12	38.30	0.86	37.94	3.70	41.70	0.38	36.62	40.44	0.46
MnO	0.07	0.05	0.06	0.02	0.11	0.00	0.09	0.02	0.16	0.08	0.01
MgO	4.84	0.11	5.80	0.86	6.62	2.64	4.24	0.39	5.37	4.15	0.76
CaO	0.03	0.01	0.07	0.04	0.05	0.04	0.04	0.03	0.10	0.08	0.06
Na_2O	0.05	0.03	0.06	0.07	0.03	0.02	0.04	0.03	0.24	0.06	0.08
K_2O	0.03	0.02	0.04	0.05	0.04	0.05	0.01	0.01	0.09	0.04	0.06
Total	87.52		87.70		87.46		89.10		84.37	87.31	
Cations per formula unit based on 14 oxygens											
Si	2.70		2.61		2.63		2.61		2.62	2.57	
Al (iv)	1.30		1.39		1.37		1.39		1.38	1.43	
Tetrahedral total	4.00		4.00		4.00		4.00		4.00	4.00	
Al (vi)	1.31		1.35		1.27		1.31		1.36	1.35	
Ti	0.00		0.01		0.00		0.00		0.00	0.01	
Fe^{2+}	3.82		3.65		3.63		3.98		3.63	3.93	
Mn	0.01		0.01		0.01		0.01		0.02	0.01	
Mg	0.83		0.98		1.12		0.72		0.95	0.72	
Octahedral total	5.97		6.00		6.04		6.03		5.96	6.01	
Ca	0.00		0.01		0.01		0.00		0.01	0.01	
Na	0.01		0.01		0.01		0.01		0.06	0.01	
K	0.00		0.01		0.01		0.00		0.01	0.01	
Totals	0.02		0.03		0.02		0.01		0.08	0.03	
Temperature °C	355.9		387.0	1.5	380.6	12.5	385.3	9.4	381.9	398.4	1.4
Fe/(Fe+Mg)	0.82		0.79		0.76		0.85		0.79	0.85	
Activity of Chl-1	3.1E-01		2.6E-01		2.4E-01		3.7E-01		2.6E-01	3.7E-01	
Activity of Chl-2	1.5E-04		4.0E-04		1.1E-03		7.6E-05		3.1E-04	8.5E-05	
Activity of Chl-3	3.3E-06		9.8E-06		4.0E-05		1.4E-06		7.0E-06	1.5E-06	

The average formulae in the host lithologies are given as:

Interbedded schist: $Fe_{3.23}Mg_{1.33}Al_{2.73}Si_{2.65}O_{10}(OH)_8$

BIF: $Fe_{3.77}Mg_{0.89}Al_{2.70}Si_{2.62}O_{10}(OH)_8$

Table 3.2C. Summary of microprobe analyses of chlorite in mineralized veins at the Kalahari Goldridge deposit

	Group IIA veins								Group IIB veins						
Sample	525/12A		13175 /2C	531/184		PH/6		588-10C	532-11A		585-20		587/2C-4		DD17/183
	Mean	std		Mean	std	Mean	std	Mean	Mean	std	Mean	std	Mean	std	
No.of grains	3		1	4		2		1	2		2		3		1
No. of analyses	6		1	8		6		1	5		5		13		1
SiO_2	24.69	0.73	23.41	23.52	0.87	23.71	0.60	25.41	24.37	0.69	25.29	0.49	24.42	1.17	22.05
TiO_2	0.04	0.01	0.05	0.03	0.02	0.05	0.03	0.04	0.07	0.02	0.05	0.01	0.06	0.01	0.07
Al_2O_3	20.44	0.95	20.28	19.42	0.28	19.58	0.44	19.37	19.61	0.30	21.38	0.47	19.28	1.31	20.17
FeO*	33.98	0.82	34.82	36.07	0.69	36.38	0.88	34.88	33.54	1.66	28.97	0.33	32.37	1.08	36.11
MnO	0.08	0.02	0.11	0.04	0.02	0.14	0.04	0.14	0.12	0.00	0.08	0.01	0.17	0.02	0.11
MgO	8.69	0.72	5.72	7.08	0.59	6.66	0.14	6.63	9.58	1.13	12.18	0.78	9.55	0.39	6.27
CaO	0.04	0.03	0.09	0.00	0.01	0.10	0.01	0.00	0.03	0.02	0.05	0.04	0.03	0.02	0.00
Na_2O	0.05	0.02	0.43	0.01	0.01	0.01	0.00	0.04	0.02	0.01	0.03	0.02	0.02	0.01	0.00
K_2O	0.07	0.07	0.15	0.00	0.00	0.00	0.00	0.00	0.01	0.00	0.01	0.00	0.00	0.00	0.00
Total	88.08		85.06	86.19		86.63		86.51	87.37		88.03		85.90		85.69
Cations per formula unit based on 11 oxygens															
Si	2.70		2.71	2.69		2.71		2.86	2.71		2.71		2.74		2.65
Al (iv)	1.30		1.29	1.31		1.29		1.14	1.29		1.29		1.26		1.35
Tetrahedral total	4.00		4.00	4.00		4.00		4.00	4.00		4.00		4.00		4.00
Al (vi)	1.38		1.47	1.32		1.34		1.43	1.28		1.41		1.30		1.39
Ti	0.00		0.00	0.00		0.01		0.00	0.00		0.01		0.00		0.01
Fe^{2+}	3.17		3.37	3.46		3.47		3.28	3.12		2.59		3.04		3.48
Mn	0.01		0.01	0.00		0.01		0.01	0.01		0.00		0.02		0.01
Mg	1.42		0.99	1.21		1.13		1.11	1.59		1.94		1.60		1.08
Octahedral total	5.99		5.84	5.99		5.96		5.85	6.00		5.95		5.96		5.97
Ca	0.01		0.00	0.00		0.01		0.00	0.01		0.00		0.00		0.00
Na	0.01		0.01	0.00		0.00		0.00	0.01		0.01		0.00		0.00
K	0.01		0.00	0.00		0.00		0.00	0.00		0.00		0.00		0.00
Totals	0.03		0.01	0.00		0.01			0.02		0.01		0.01		0.00
Temperature °C	356.9	6.1	354.6	358.4	9.0	354.2	24.0	304.4	354.0	10.0	354.1	10.0	342.2	34.4	373.1
Fe/(Fe+Mg)	0.69		0.77	0.74		0.75		0.75	0.66		0.57		0.66		0.76
Activity of Chl-1	2.4E-03		4.5E-04	9.8E-04		7.3E-04		7.4E-04	3.8E-03		0.01		0.17		0.11
Activity of Chl-2	1.3E-01		2.1E-01	1.9E-01		2.0E-01		1.7E-01	1.1E-01		0.05		0.36		0.38
Activity of Chl-3	8.5E-05		1.1E-05	3.2E-05		2.2E-05		2.4E-05	1.7E-04		0.00		0.01		0.00

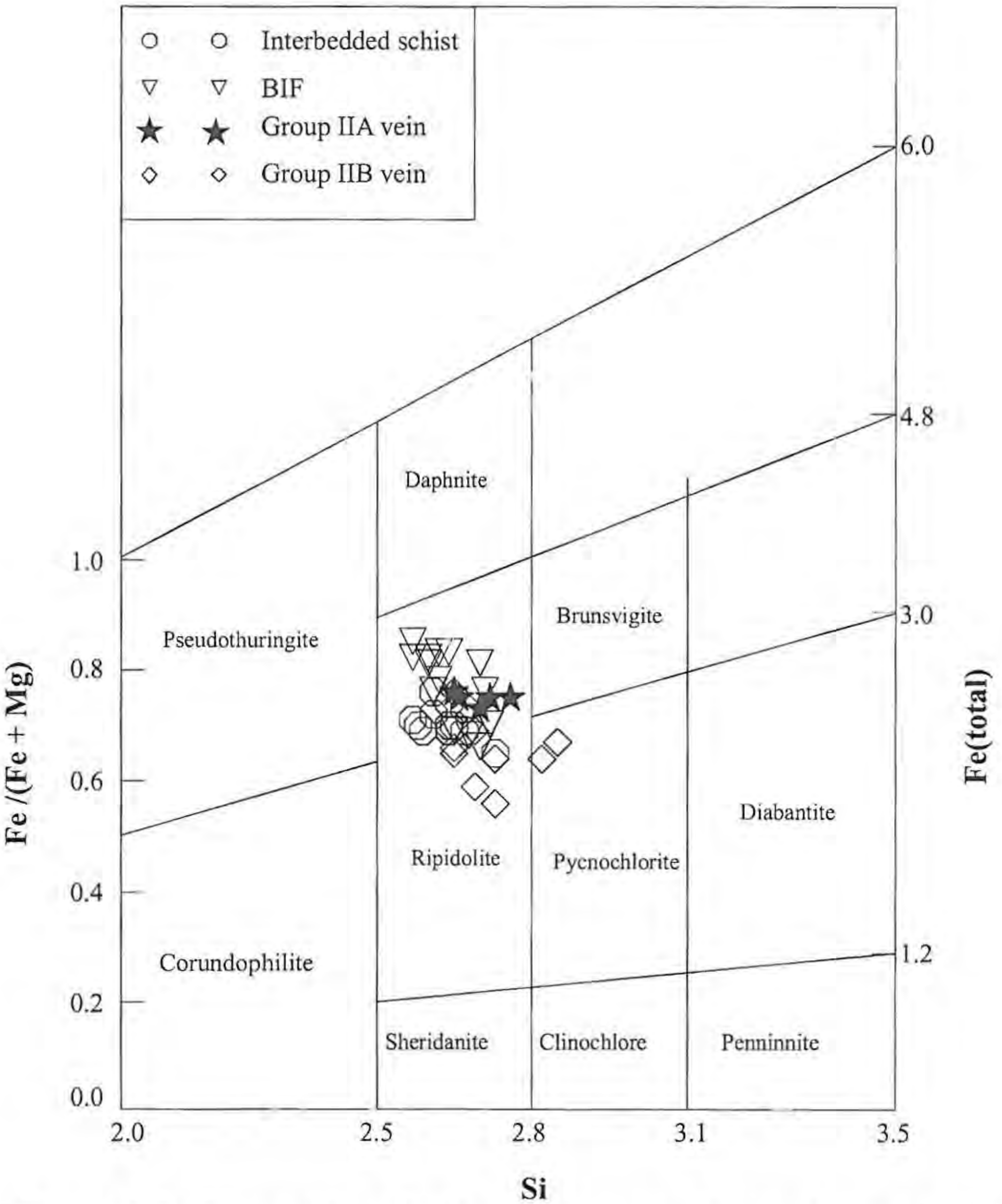

Figure 3.2. Composition of chlorite in various lithologies at the Kalahari Goldridge deposit plotted in the Hey (1954) diagram

Group IIA vein: $Fe_{3.35}Mg_{1.17}Al_{2.66}Si_{2.73}O_{10}(OH)_8$

Group IIB vein: $Fe_{3.06}Mg_{1.55}Al_{2.64}Si_{2.70}O_{10}(OH)_8$.

The average stoichiometry of the chlorites in the veins shows some variation between Fe and Mg, with the chlorites in the Group IIA veins showing increased

Fe contents. This may be attributed to increased pyrrhotite mineralization associated with the host BIF during the Group IIA stages of the mineralization (see section on sulphides). This is further explained by the fact that pyrrhotite accommodates less amounts of Fe therefore, high amounts of pyrrhotite associated with the Group IIA stage of the mineralization suggests high amounts of Fe is the solution would be partitioned into other Fe-accommodating silicates such as chlorite.

3.2.3: Stilpnomelane

Stilpnomelane is one of the dominant Fe-silicates occurring at the Kalahari Goldridge deposit. It occurs mainly in lithologies within the orebody, notably the BIF and schist. Stilpnomelane exhibits a variety of habits, including fibrous aggregates, interlocking acicular grains or lathes, and sheaves and rosettes. Stilpnomelane also shows variety of colours ranging from pale green to brown and reddish-brown (Figs. 3.3 to 3.5). Stilpnomelane in the deposit occurs primarily as a product of hydrothermal alteration.

In the BIF, stilpnomelane has variable abundances in the less altered and altered units. It has minor occurrence in less altered BIF, and occurs as fine- to medium-grained lathes, tabular bundles or sheaves, or closely associated with magnetite microbands in chert-magnetite mesobands. Most stilpnomelane in the less altered BIF mesobands is green with a few brown varieties and is commonly associated with magnetite microbands (Fig 3.3). The magnetite in most of the microbands may be partially altered to pyrite, pyrrhotite and siderite, which give an indication of subtle replacement by the hydrothermal fluid along these bands.

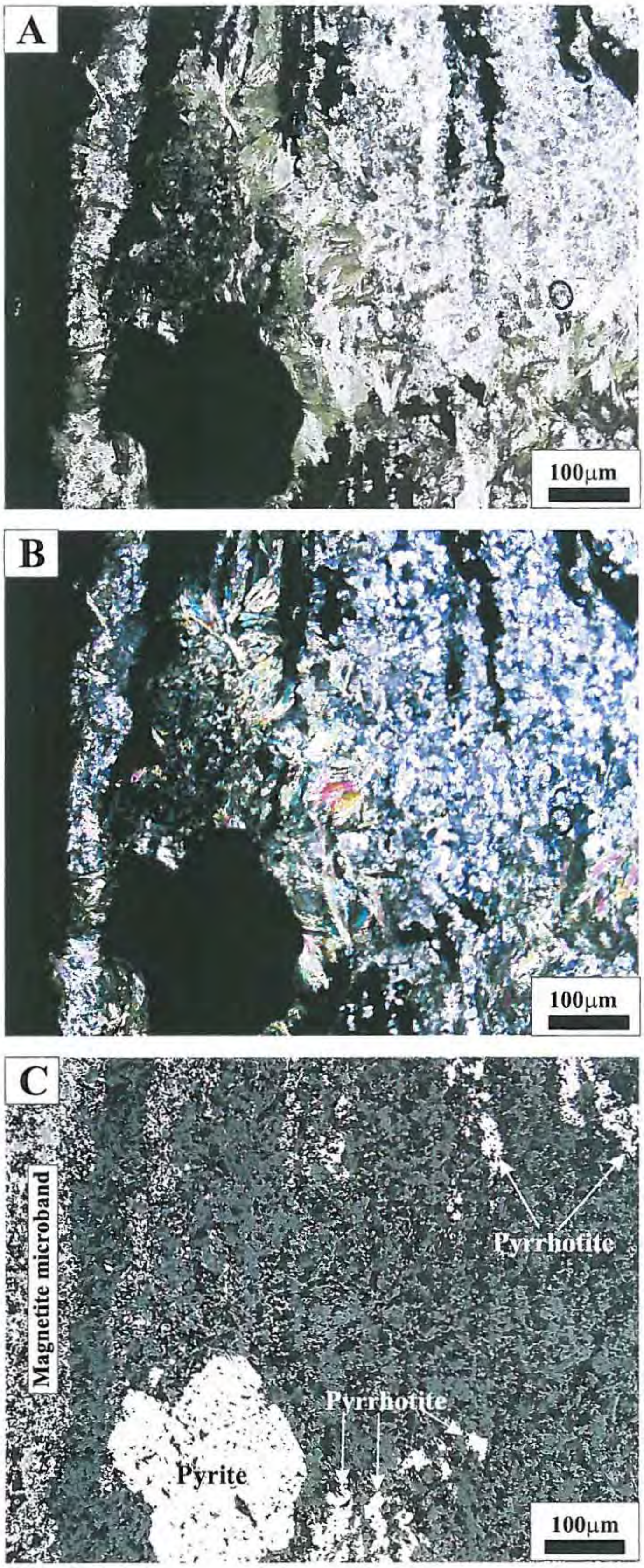

Figure 3.3. Photomicrographs showing development of green stilpnomelane from the reaction of magnetite and quartz in altered BIF microband. **A**. Photograph in plane polarized light. **B** is crossed polarized photograph of **A** whilst **C** is taken in reflected light and shows replacement of magnetite by pyrite and pyrrhotite along with stilpnomelane in the magnetite band.

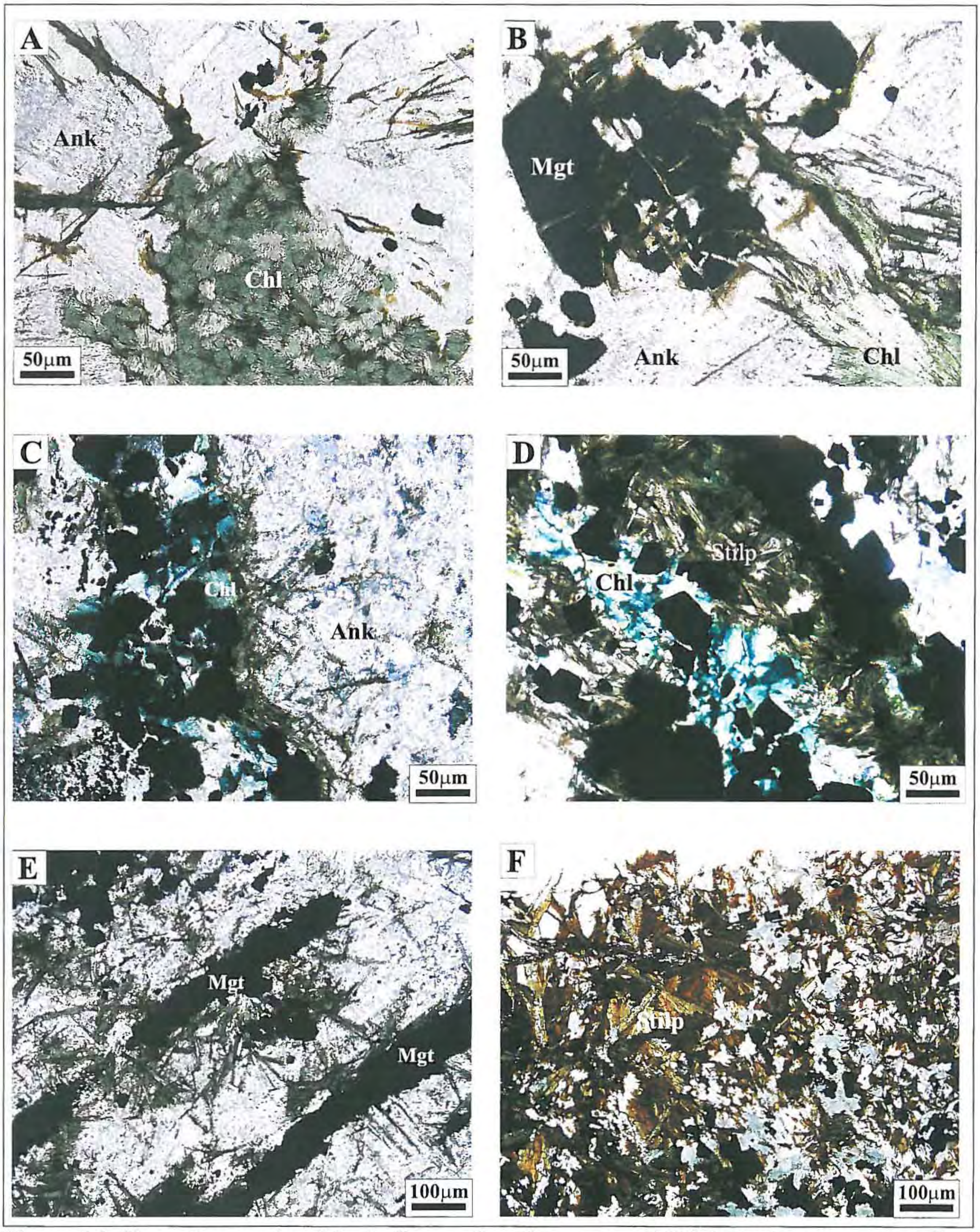

Figure 3.4. Photomicrographs of ferri-stilpnomelane (brown to reddish brown) occurrences at the Kalahari Goldridge deposit. **A** and **B** occur in mineralized quartz veins. Photograph taken in plane polarized light. Stilpnomelane in **C** to **F** occur in altered BIF. Photographs taken in crossed polarized light. Stipnomelane replaces chlorites (green) along grain boundaries in photographs **A** to **E**, whilst it replaces magnetite in **B.**

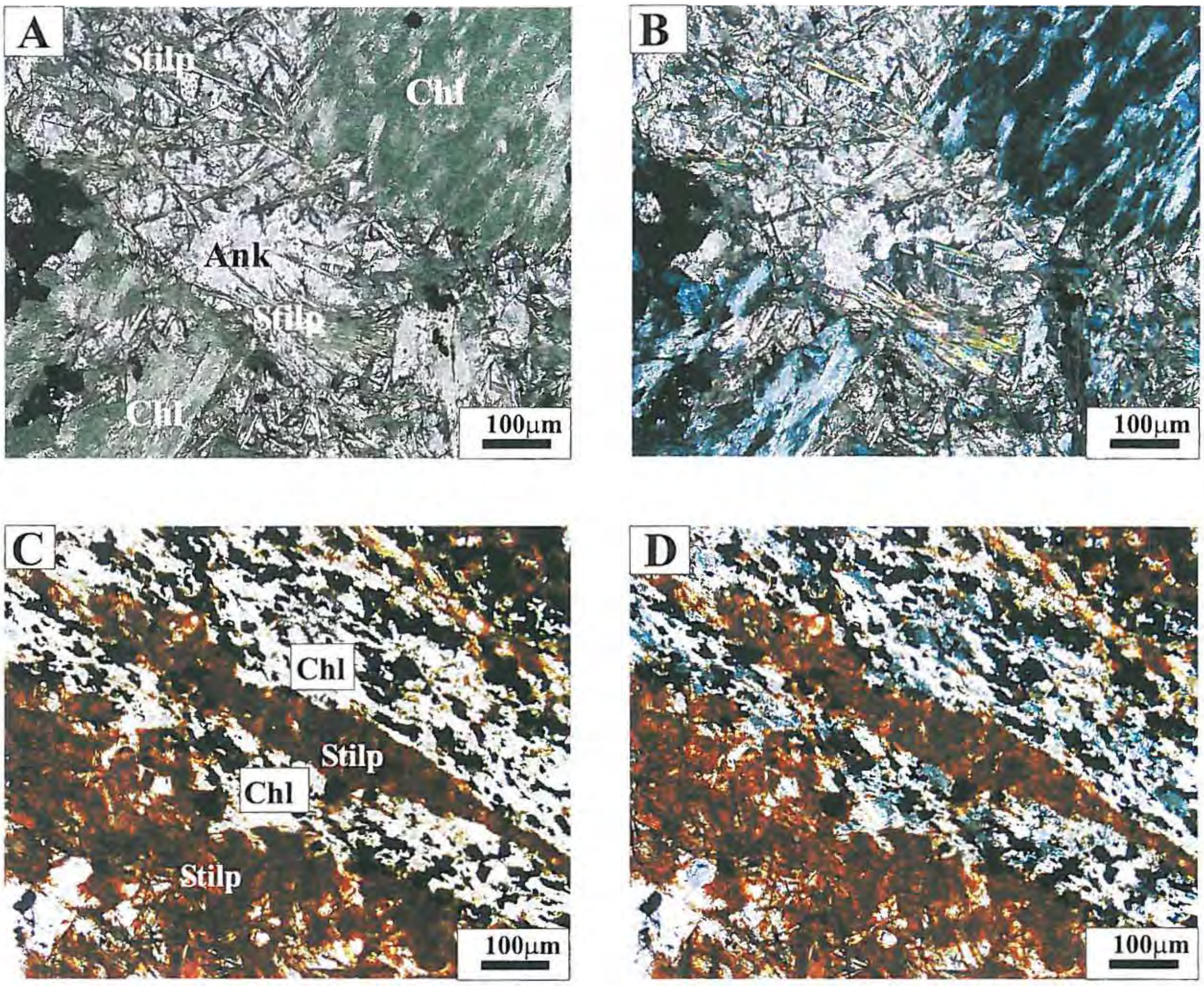

Figure 3.5. Photomicrographs of replacement of chlorite by stilpnomelane of various colours in schist in orebody. Replacement typically occur where there is evidence of fluid infiltration either along foliation plane or crosscutting vein.

A and **B**. Replacement of chlorite band (Chl) by green stilpnomelane (Stilp) and ankerite (Ank). Sample 527/2B. A and B are same photos taken in plane and crossed polarized light respectively.

C and **D**. Reddish-brown stilpnomelane (Stilp) replacing chlorite (Chl) in band. Dispersed opaque grains are magnetite grains which have been partially replaced by pyrite and pyrrhotite. Sample 589/12A. C and D are same photos taken in plane and crossed polarized light respectively.

Stilpnomelane in highly altered chert-magnetite and magnetite mesobands in the BIF are normally well crystallized and coarse-grained acicular aggregates, sheaves and rosettes. The colour of the stilpnomelane varies from green to brown or reddish-brown with the green variety exhibiting high pleochroic colours. The brown variety forms the dominant occurrence as interlocking acicular or lath-like habit and is intimately associated with fine-grained carbonates, where it replaces green stilpnomelane sheaves or chlorites (Fig. 3.4). Sheaves and laths of stilpnomelane also occur in mineralized veins (both Group IIA and Group IIB) primarily as a replacement of chlorite and show mainly brown colours (Fig. 3.4A and 3.4B). Stilpnomelane in the altered chert-magnetite mesobands is commonly intergrown with sulphides, carbonates and chlorites.

In the interbedded schist, stilpnomelane occurs as medium- to coarse-grained sheaves and rosettes or interlocking acicular or lath-like grains, and exhibits similar variety of colours as those in the altered BIF. It commonly develops at the expense of chlorite in areas where fluid infiltration is evidenced by transgressive veins and fractures. In such areas, the stilpnomelane occurs as interlocking laths or fibrous networks along the fluid path (Figs 3.5B and 3.5C). Stilpnomelane in the schist is commonly developed in areas containing disseminations of magnetite.

Evidence based on the several textural relationships between stilpnomelane and coexisting mineral assemblages in altered lithologies at the Kalahari Goldridge deposit suggest that it developed as a product of ore fluid interaction with wall rock, with Fe-rich lithologies playing an important role in the growth of stilpnomelane.

In most iron formations, primary stilpnomelane is green in colour (ferrostilpnomelane) but is highly susceptible to oxidation to the brown variety (ferristilpnomelane). It is worth noting that brown stilpnomelane bears strong similarity with biotite, such that, their positive identification where they coexist can be inhibited. Therefore XRD patterns serves as an important tool to distinguish between brown stilpnomelane and biotite. Eggleton (1972) pointed out that the high susceptibility of the primary green variety of stilpnomelane to oxidation is due to its loose structure, which easily accommodates oxygen in the tetrahedral sites on exposure to weathering. The Fe^{2+} is subsequently oxidized to Fe^{3+} yielding the brown colour. Wet chemical analyses (e.g., Brown, 1971) have also shown that the variable colours seen in stilpnomelane are attributed to variation in the proportion of Fe^{2+}/Fe^{3+} in the mineral with Fe^{2+} being dominant in the green stilpnomelane (ferro-stilpnomelane) and Fe^{3+} in ferri-stilpnomelane.

At the Kalahari Goldridge deposit, the dominance of the brown to reddish-brown varieties of the stilpnomelane suggests that a significant proportion of the Fe in the stilpnomelane occurs in the ferric state. The X-ray powder diffraction patterns of BIF and schist samples in the ore body show a d_{100} spacing range from 11.86 to 12.2Å for stilpnomelane (Appendix V). Miyano (1982) pointed out that pure ferrous stilpnomelane has a d_{100} spacing of 12.1Å, and therefore the slight variation in the peak of stilpnomelane observed at the Kalahari Goldridge deposit may be attributed to intergrowth of stilpnomelane with other silicates and/or due to the co-existence within stilpnomelane of variable oxidation states.

The variation of colours of the stilpnomelane in the deposit does not show any significant correlation with the associated mineral assemblage. In other words, samples containing all colour varieties of stilpnomelane may coexist with pyrrhotite, pyrite or magnetite. This observation suggests that the variable colours exhibited in stilpnomelane may be attributed to weathering possibly by the interaction with surface-derived aqueous fluids.

The chemical composition of the stilpnomelane consists of major elements including K_2O, FeO, MgO, Al_2O_3 and SiO_2 (Tab. 3.3). Other components such as TiO_2, Na_2O, CaO, and MnO have lesser concentrations, usually less than 0.5 wt %. The composition shows a wide range of Al_2O_3 from 4.76 to 9.6 wt %. The total Fe as FeO in the stilpnomelane is variable from 32.13 to 32.5 wt %. The composition of Fe in the stilpnomelane bears no relationship to host rock as occurs with the carbonates and chlorites. The microprobe analyses revealed that some of the brown minerals commonly replacing chlorite have compositions containing higher TiO_2 (1.2-1.48 wt %) and Al_2O_3 (14.40-15.79 wt %), which is characteristic of biotite but lower K_2O contents ranging from 2.22 to 5.31 wt % (Table 3.4). This observation suggests that stilpnomelane was more stable than biotite, and could possibly be attributed to low activity of K^+ in the hydrothermal fluid, as well as high Fe/(Fe + Mg) content of the host rock.

The K_2O composition in stilpnomelane (Table 3.3) is highly variable with the degree of oxidation, ranging from about 1.0 wt % in the reddish-brown stilpnomelane to about 4.4 wt % in the green variety at the Kalahari Goldridge deposit. Generally, the K_2O composition in stilpnomelane has been found to be higher in ferro-stilpnomelane compared to ferri-stilpnomelane (Brown, 1971; Gole, 1980). Brown (1971) reported leaching of potassium in stilpnomelane during its oxidation as the main cause of low potassium composition which may be attributed to replacement of K that is loosely held in the zeolite structure of stilpnomelane by water molecules during oxidation or alteration processes (Eggleton, 1972; Floran and Papike, 1975).

Table 3.3. Microprobe data of stilpnomelane in various lithologies in the orebody at the Kalahari Goldridge deposit.

	Interbedded schist						Mineralized quartz vein			Mineralized BIF							
Sample number	452/25B-1	452/25B-2	452/25B-3	525/20-1	525/20-2	NQH-19B	532/11A	DD17/183-1	DD17/183-2	52[illegible]/12A	531/9B	524/8	13175/2C-1	13175/2C-2	589/4	589/1F-1	589/1F-2
							Group IIB	Group IIB	Group IIB								
No. of analyses	3	2	3	3	1	1	1	2	2	2	1	3	3	1	3	6	2
Colour	Green	Green	Brown	Reddish brown	Brown	Brown	Brown	Dark brown	Dark brown	Brown	Brown	Pale brown	Green	Brown	Reddish Brown	Reddish Brown	Reddish Brown
SiO_2	46.27	47.05	45.02	43.92	44.97	46.62	41.41	45.10	45.57	45.79	49.91	43.70	46.77	47.81	46.81	48.40	46.90
TiO_2	0.01	0.00	0.01	0.00	0.01	0.02	0.09	0.01	0.00	0.01	0.00	0.02	0.01	0.00	0.00	0.08	0.00
Al_2O_3	4.94	5.12	6.51	7.28	6.74	6.64	8.30	4.90	5.02	5.55	6.46	5.35	5.45	5.50	6.38	8.40	5.83
FeO*	32.33	32.28	32.80	35.51	35.06	34.18	35.19	32.78	32.50	34.07	32.80	34.89	31.94	33.71	33.34	29.72	33.49
MnO	0.24	0.17	0.19	0.08	0.07	0.19	0.21	0.02	0.02	0.08	0.09	0.14	0.13	0.12	0.09	0.08	0.09
MgO	4.15	4.55	4.45	3.23	3.11	3.12	4.23	3.38	3.58	3.30	4.30	2.68	4.23	4.20	4.64	4.67	4.78
CaO	0.23	0.30	0.35	0.07	0.05	0.48	0.10	0.17	0.29	0.26	0.26	0.67	0.14	0.17	0.16	0.17	0.10
Na_2O	0.34	0.25	0.18	0.39	1.14	0.51	0.10	0.33	0.31	0.38	0.22	0.81	0.39	0.10	0.64	0.54	0.59
K_2O	3.22	2.74	1.87	1.64	2.07	1.97	1.69	1.16	0.99	1.56	1.84	3.22	3.41	1.55	1.09	1.20	1.10
Total	91.72	92.47	91.40	92.13	93.22	93.73	91.31	87.85	88.28	91.00	95.88	91.46	92.47	93.16	93.16	93.26	92.88
Cations per formula unit based on 11 oxygens																	
Si	3.71	3.71	3.59	3.53	3.58	3.65	3.38	3.74	3.75	3.69	3.74	3.59	3.70	3.73	3.64	3.66	3.67
Al (iv)	0.29	0.29	0.41	0.47	0.42	0.35	0.62	0.26	0.25	0.31	0.26	0.41	0.30	0.27	0.36	0.34	0.33
Tetrahedral total	4.00	4.00	4.00	4.00	4.00	4.00	4.00	4.00	4.00	4.00	4.00	4.00	4.00	4.00	4.00	4.00	4.00
Al (vi)	0.17	0.19	0.21	0.22	0.21	0.26	0.18	0.22	0.23	0.22	0.31	0.11	0.21	0.24	0.23	0.41	0.20
Ti	0.00	0.00	0.00	0.00	0.00	0.00	0.01	0.00	0.00	0.00	0.00	0.00	0.00	0.00	0.00	0.00	0.00
Fe	2.17	2.13	2.20	2.39	2.33	2.24	2.40	2.27	2.23	2.30	2.06	2.40	2.11	2.20	2.17	1.89	2.19
Mn	0.02	0.01	0.01	0.01	0.00	0.01	0.01	0.00	0.00	0.01	0.01	0.01	0.01	0.01	0.01	0.01	0.01
Mg	0.50	0.53	0.53	0.39	0.37	0.36	0.51	0.42	0.44	0.40	0.48	0.33	0.50	0.49	0.54	0.53	0.56
Octahedral total	2.85	2.87	2.96	3.00	2.91	2.87	3.11	2.91	2.91	2.91	2.85	2.85	2.83	2.93	2.95	2.83	2.96
Ca	0.02	0.03	0.03	0.01	0.00	0.04	0.01	0.02	0.03	0.02	0.02	0.06	0.01	0.01	0.01	0.01	0.01
Na	0.05	0.04	0.03	0.06	0.18	0.08	0.02	0.05	0.05	0.06	0.03	0.13	0.06	0.01	0.10	0.08	0.09
K	0.33	0.28	0.19	0.17	0.21	0.20	0.18	0.12	0.10	0.16	0.18	0.34	0.35	0.15	0.11	0.12	0.11
Totals	0.40	0.34	0.25	0.23	0.39	0.31	0.20	0.19	0.18	0.24	0.23	0.53	0.42		0.22		
Fe/(Fe + Mg)	0.81	0.80	0.81	0.86	0.86	0.86	0.82	0.84	0.84	0.85	0.81	0.88	0.81	0.82	0.80	0.78	0.80

Table 3.4. Summary of microprobe analysis of intermediate biotite-stilpnomelane at the Kalahari Goldridge deposit.

Sample number	589/4		532-11A		525-12A
Host rock	BIF		qtz-vein		qtz-vein
	Mean	std	Mean	std	
No. of analyses	3		3		2
Wt %					
SiO_2	29.71	1.15	30.12	0.87	27.41
TiO_2	1.33	0.17	1.48	0.18	1.20
Al_2O_3	15.30	0.50	14.40	0.76	15.79
FeO	31.91	0.37	34.39	0.07	37.11
MnO	0.06	0.01	0.05	0.03	0.05
MgO	8.54	0.19	6.94	0.70	6.25
CaO	0.03	0.02	0.06	0.03	0.04
Na_2O	0.06	0.01	0.02	0.01	0.04
K_2O	5.31	0.60	3.41	0.93	2.22
Total	92.25		90.88		90.11
Cations per formula unit based on 11 oxygens					
Si	2.49		2.56		2.38
Al (iv)	1.50		1.43		1.62
Tetrahedral total	3.98		3.99		4.00
Al (vi)	0.01		0.02		0.00
Ti	0.08		0.09		0.08
Fe	2.23		2.45		2.70
Mn	0.00		0.00		0.00
Mg	1.07		0.88		0.81
Octahedral total					
Ca	0.00		0.01		0.00
Na	0.01		0.00		0.01
K	0.57		0.37		0.25
Inter-layer total	0.58		0.38		0.26
X_K					
Fe/(Fe + Mg)	0.68		0.74		0.77

std = one standard deviation

3.2.4: Minnesotaite

Minnesotaite has a minor occurrence and has been observed mainly in samples from borehole GDP 527. The minnesotaite grains were identified in samples in less altered chert-magnetite mesobands (527/3A and 527/4) where it occurs typically as fine- to medium-grained rosettes (bow-tie) and colourless grains. In sample 527/3A, minnesotaite is associated with quartz, siderite, and pyrite-pyrrhotite in individual magnetite-rich microbands and shows evidence as a secondary product from reactions between siderite and quartz, and pyrrhotite and quartz. Similar assemblages have been observed in sample 527/4. However, in certain bands, green stilpnomelane may be intergrown with minnesotaite in addition to the observed assemblages. The paragenetic relationship between the stilpnomelane and minnesotaite is unclear due to lack of clear-cut textural evidence. X-ray powder diffraction patterns show d-spacing values from 9.17 to 9.55 Å for minnesotaite (Appendix V).

Figures 3.6A-D illustrates the textural relationship between minnesotaite and other mineral assemblages in sample 527/3A. In Figure 3.6A and B, minnesotaite occurrence at the interface between siderite and quartz (chert) shows its development by reaction between the two minerals. Relics of magnetite in the siderite bands and the occurrence of sulphides (pyrite and pyrrhotite) in the siderite bands (Fig. 3.6A and B) show a replacement of the original magnetite microbands by siderite and sulphides. In Figures 3.6C and D, coarse-grained minnesotaite sheaves and rosettes are intergrown with sulphides in the original magnetite microband. Pyrite and pyrrhotite shows annealing textures with no evidence of mutual replacement, which may be indicative of coeval precipitation from the replacement of magnetite.

Minnesotaite, on the other hand, replaces isolated pyrrhotite grains or selectively replaces pyrrohotite where it coexists with pyrite, which suggests that minnesotaite postdates both pyrite and pyrrhotite. These reactions are envisaged to have occurred through two intermediate steps for each assemblage as shown by equations [3.1] and [3.2].

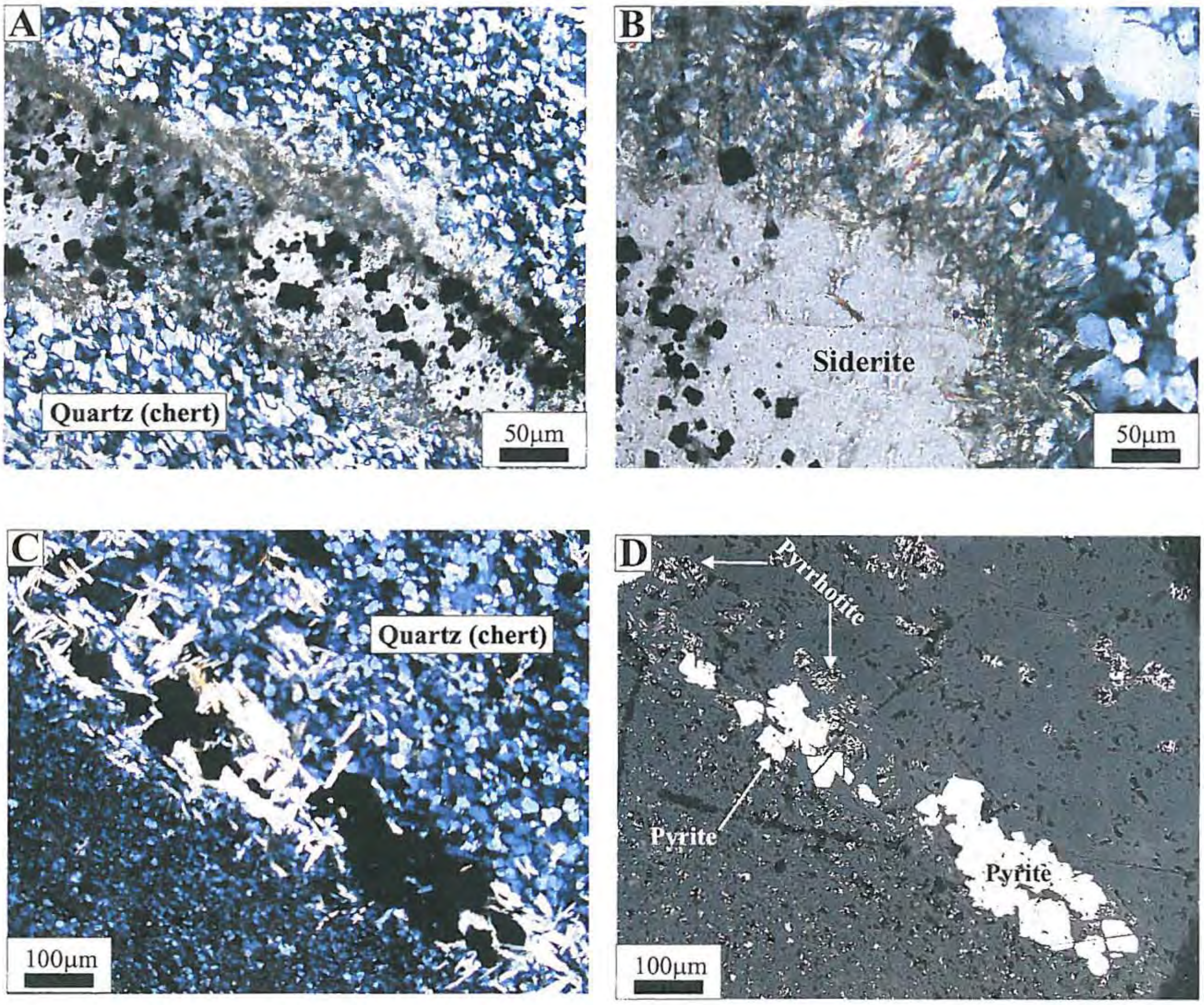

Figure 3.6. Photomicrographs showing minnesotaite occurrences in less altered BIF mesoband (sample 527/3A). Photomicrographs **A** and **B** show development of minnesotaite (acicular grains) along siderite-quartz boundary. Opaque minerals in **A** and **B** are relics of magnetite in nearly complete replacement. Crossed polarized light. Photomicrograph **C** taken in crossed polarized light, shows minnesotaite (sheaves and rosettes) growth in an originally magnetite microband. The magnetite is replaced by pyrite and pyrrhotite (**D**, reflected light) while the minnesotaite selectively replaces pyrrhotite.

$Fe_3O_4 + 3CO_2 = 3FeCO_3 + 1/2O_2$ [3.1A]
Magnetite siderite

$3FeCO_3 + 4SiO_2 + H_2O = Fe_3Si_4O_{10}(OH)_2 + 3CO_2$ [3.1B]
siderite quartz minnesotaite

$Fe_3O_4 + 3H_2S = 3FeS + 3H_2O + 1/2O_2$ [3.2A]
magnetite pyrrhotite

$3FeS + 4SiO_2 + 4H_2O = Fe_3Si_4O_{10}(OH)_2 + 3CO_2$ [3.2B]
pyrrhotite quartz minnesotaite

These reactions suggest that the path taken for the production of minnesotaite is largely dependent on the activity of CO_2 and H_2S in the fluid as represented by the intermediate steps [3.1A] and [3.2A] at low fO_2. The occurrence of these assemblages in the same thin section suggests that local variation of CO_2 and H_2S activity prevailed during the mineralization. It is not possible, however, to determine whether the minnesotaite is associated with ladder vein or large vein stage of the mineralization. Also, it is not clear whether the minnesotaite formed from a prograde or retrograde reaction due to lack of clearly defined minnesotaite-stilpnomelane reaction textures.

Microprobe analyses of six minnesotaite grains in sample 527/3A show compositions consisting primarily of SiO_2, FeO and MgO with minor amounts of Al_2O_3 and MnO, generally less than 1 wt% (Table 3.5). Fe/(Fe+Mg) ratios show a range from 0.67 to 0.88. The average composition of the minnesotaite is represented by the formula $Fe_{2.23}Mg_{0.77}Si4O_{10}(OH)_2$.

Table 3.5. Summary of microprobe analysis of minnesotaite (sample 527/3A) at the Kalahari Goldridge deposit.

			Sample	527/3A		
Grain	1	2	3	4	5	1
Wt %						
SiO_2	48.05	51.08	49.97	51.33	51.66	52.72
TiO_2	0.00	0.00	0.01	0.00	0.03	0.01
Al_2O_3	0.46	0.78	0.57	0.66	0.43	0.67
FeO	39.83	31.60	34.88	32.04	34.73	32.24
MnO	0.06	0.16	0.16	0.19	0.19	0.16
MgO	3.05	7.61	6.30	8.09	6.39	8.75
CaO	0.02	0.03	0.04	0.02	0.03	0.01
Na_2O	0.02	0.09	0.06	0.01	0.10	0.11
K_2O	0.03	0.51	0.34	0.47	0.26	0.53
Total	91.54	91.86	92.32	92.82	93.82	95.21
Cations per formula unit based on 11oxygens						
Si	3.92	3.96	3.93	3.94	3.97	3.94
Al (iv)	0.04	0.07	0.05	0.06	0.04	0.06
Tetrahedral total	3.96	4.03	3.98	4.00	4.01	4.00
Al (vi)	0.00	0.00	0.00	0.00	0.00	0.00
Ti	0.00	0.00	0.00	0.00	0.00	0.00
Fe	2.72	2.05	2.29	2.06	2.23	2.01
Mn	0.00	0.01	0.01	0.01	0.01	0.01
Mg	0.37	0.88	0.74	0.93	0.73	0.97
Octahedral total	3.09	2.94	3.04	3.00	2.98	3.00
Ca	0.00	0.00	0.00	0.00	0.00	0.00
Na	0.00	0.01	0.01	0.00	0.01	0.02
K	0.00	0.05	0.03	0.05	0.03	0.05
Inter-layer total	0.01	0.07	0.05	0.05	0.04	0.07
Fe/(Fe+Mg)	0.88	0.70	0.76	0.69	0.75	0.67

3.2.5: Muscovite

Muscovite has a minor occurrence in the veins and BIF and occurs as flaky or tabular coarse grains. Much higher proportions occur in the schists as fine-grained sericite intermixed with chlorites. Most commonly, muscovite occurs as replacement of chlorite schist resulting in the assemblage quartz-chlorite-carbonate±muscovite±stilpnomelane in the interbedded schist. Sericites are particularly widespread in the footwall schist units and consist of the assemblage sericite-carbonate-quartz±chlorite. Microprobe analyses show that the muscovite is phengitic in composition (Table 3.6). Average formulae for the muscovites in the various lithologies are represented as:

Interbedded schist: $(K,Na)_{0.92}Fe_{0.33}Mg_{0.14}Al_{2.63}Si_{3.04}O_{10}(OH)_2$

BIF: $(K,Na)_{0.79}Fe_{0.40}Mg_{0.11}Al_{2.43}Si_{3.20}O_{10}(OH)_2$

Goup IIA: $(K,Na)_{0.77}Fe_{0.31}Mg_{0.09}Al_{2.52}Si_{3.21}O_{10}(OH)_2$

Group IIB: $(K,Na)_{0.92}Fe_{0.31}Mg_{0.20}Al_{2.46}Si_{3.13}O_{10}(OH)_2$

Table 3.6. Summary of microprobe analysis of muscovite at the Kalahari Goldridge deposit.

	Mean	std	Mean	std	Mean	std	
No. of analyses	10		7		9		2
Host rock	qtz-vein		qtz-vein		BIF		schist
Wt %							
SiO_2	46.58	1.03	46.06	1.41	45.69	1.18	45.95
TiO_2	0.64	0.13	0.25	0.04	0.35	0.08	0.42
Al_2O_3	31.12	0.98	30.69	0.65	29.36	0.92	33.61
FeO*	5.51	0.26	5.29	0.38	6.82	2.21	6.00
MnO	0.01	0.01	0.03	0.02	0.01	0.01	0.03
MgO	2.04	0.25	0.84	0.10	1.07	0.27	1.40
CaO	0.03	0.02	0.03	0.02	0.03	0.01	0.03
Na_2O	0.20	0.02	0.16	0.01	0.15	0.02	0.22
K_2O	10.45	0.20	8.43	0.14	8.54	0.35	10.47
Total	96.57		91.77		92.02		98.13
Cations per formula unit based on 11 oxygens							
Si	3.13		3.21		3.20		3.04
$Al_{(iv)}$	0.87		0.79		0.80		0.96
Tetrahedral total	4.00		4.00		4.00		4.00
$Al_{(vi)}$	1.59		1.72		1.63		1.67
Ti	0.03		0.01		0.02		0.02
Fe	0.31		0.31		0.40		0.33
Mn	0.00		0.00		0.00		0.00
Mg	0.20		0.09		0.11		0.14
Octahedral total	2.14		2.13		2.16		2.16
Ca	0.00		0.00		0.00		0.00
Na	0.03		0.02		0.02		0.03
K	0.90		0.75		0.76		0.88
Inter-layer total	0.92		0.77		0.79		0.92
X_K	0.97		0.97		0.97		0.97
Na/(Na + K)	0.03		0.03		0.03		0.03
Fe/(Fe + Mg)	0.60		0.78		0.78		0.71

std = one standard deviation

3.3: Carbonate minerals

Carbonate alteration is a characteristic feature associated with most lode gold deposits hosted in Archaean greenstones. The most common carbonates in these greenstones include siderite, ankerite, dolomite, magnesite and calcite (e.g., Phillips, 1986; Kishida and Kerrich, 1987; Golding and Wilson, 1983). The precipitation of the carbonates has been attributed to a reaction between CO_2-bearing hydrothermal fluid and Ca-, Fe-, Mg-, Mn-bearing silicates or oxides in the host rocks (Kerrich and Fyfe, 1981). The type of carbonate present in a particular deposit is therefore largely dependent on the host lithologies. Fe-rich varieties such as siderite and ankerite are dominant in BIF and mafic rocks whereas dolomite and magnesite preside in unltramafic lithologies.

Carbonate occurrence at the Kalahari Goldridge deposit is widespread and is dominated by siderite and ankerite series with minor amounts of dolomite and calcite. Due to the close resemblance of carbonates under the microscope, the identification of the carbonates was done in conjunction with X-ray powder diffraction and electron microprobe analyses. In most samples, carbonate in the deposit commonly occurs as replacement of quartz, magnetite, chlorite and sulphides (Fig. 3.7).

Siderite constitutes the largest proportion of carbonates in the BIF and occurs at selvedges of veins in contact with the BIF. In less altered and less deformed BIF, siderite occurs in narrow and continuous microbands replacing magnetite in magnetite mesobands. In more altered BIF samples, siderite occurs mostly as

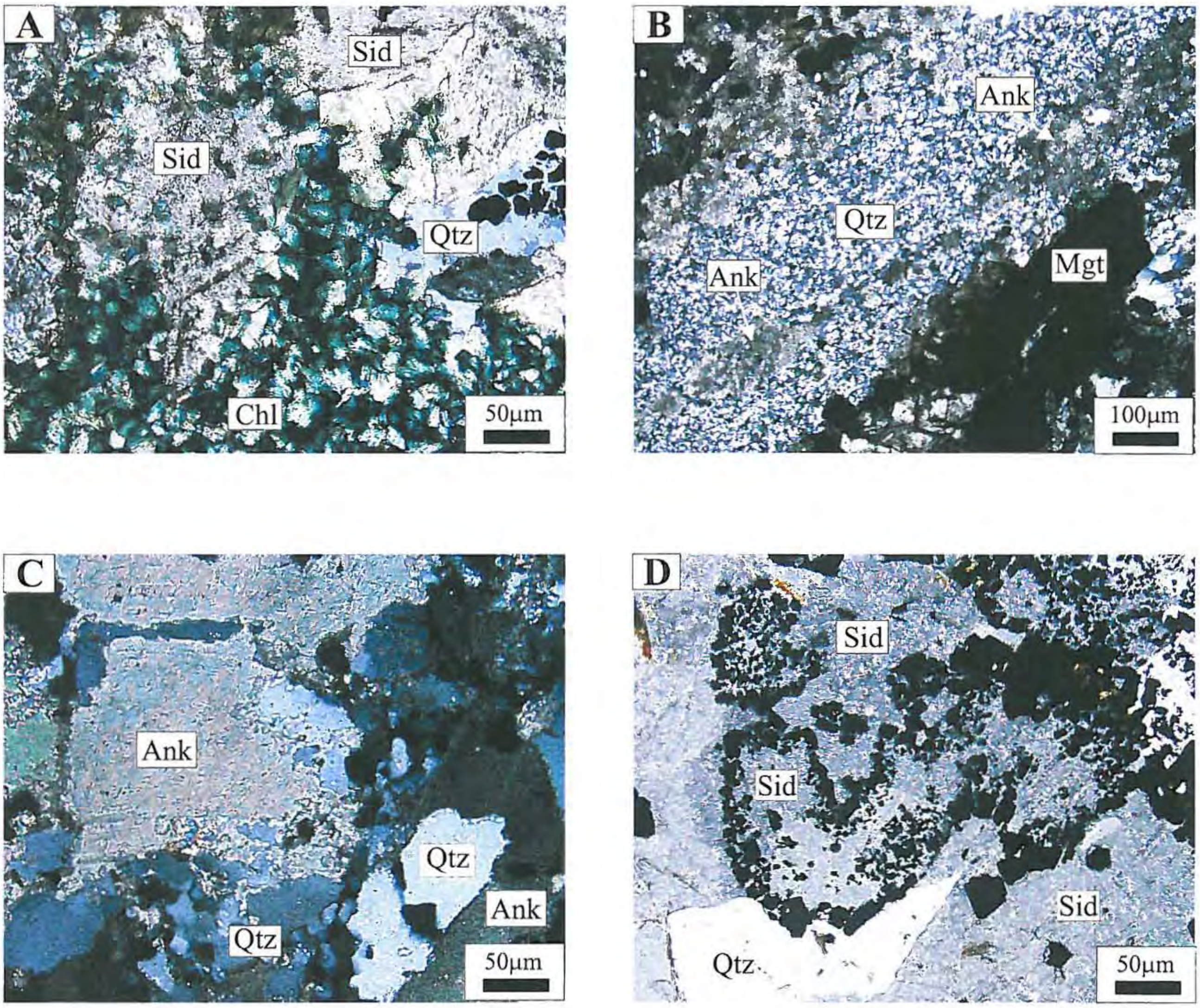

Figure 3.7. Photomicrographs (crossed polarized light) showing carbonate alteration at the Kalahari Goldridge deposit. **A**. Replacement of chlorite (Chl) by siderite (Sid) in BIF. B. Replacement of quartz (Qtz) in chert microband by ankerite (Ank). **C**. Quartz (Qtz) replacement by ankerite (Ank) in mineralized vein. **D**. Magnetite (opaque grains) replacement by siderite (Sid) in BIF.

coarse anhedral to euhedral granules or as massive aggregates, mainly as replacements of magnetite, sulphides or chlorite. The replacement by siderite is commonly recognized by the occurrence of magnetite relicts in the siderites, retention of pseudomorphic shapes of the opaque minerals or incomplete replacement textures. Along the vein selvedges, siderite may form mosaic aggregates with quartz.

Ankerite phases are associated with the schist units and quartz veins in the ore body. They range from medium- to coarse-grained in equigranular matrix in the quartz veins and as a fine-grained matrix in the schist units. In the veins, ankerite is generally more abundant than siderite and commonly replaces quartz. In some BIF samples, ankerite replaces quartz in certain chert microbands (e.g. Fig. 3.7B). In places, the entire chert band is replaced by ankerite. Ankerite also shows high modal abundance in the schists where it occurs in bands, primarily as a replacement of chlorite in discrete bands pseudomorphic of the original chlorite bands. Calcite is of minor importance in the BIF and the orebody schist, but occurs mainly as fine-grained anhedral grains in the footwall contacts and hanging-wall schist, and in late veins in the deposit.

The composition of the carbonates (siderite and ankerite) determined by electron microprobe analyses are given in Appendix XI and summarized in Tables 3.7, and Figure 3.8 illustrates the carbonate composition in ternary plot. Calcite was determined only qualitatively by X-ray powder diffraction.

Microprobe analyses of 33 siderite grains in veins and host BIF (Table 3.7) exhibit some compositional variations. Siderites associated with Group IIA and Group IIB quartz veins exhibit similar compositions containing 0 to 10 mole %

$MnCO_3$, 22 to 40 % $MgCO_3$ and up to 3.19 mole % $CaCO_3$ in solid solution. In the less altered BIF samples (527-3A and 13175/2A), there is enrichment in $MnCO_3$ and $MgCO_3$ relative to the more altered samples. $MnCO_3$ contents range between 1 and 18 mole %, whilst $MgCO_3$ varies from 30 and 40 mole %. $CaCO_3$ contents vary from 1.05 to 1.96 mole %. Most Fe-rich siderites are associated with the altered BIF samples with compositions showing a range from 64.57 to 93.0 mole % $FeCO_3$, 1.0 to 7.14 mole % $MnCO_3$, 11.28 to 32.23 mole % $MgCO_3$ and up to 2.52 mole % $CaCO_3$ in solid solution. Calculated average formulae of the siderite are represented as:

Group IIA veins: $Fe_{0.61}Mg_{0.35}Mn_{0.02}Ca_{0.02}CO_3$,
Group IIB veins: $Fe_{0.57}Mg_{0.33}Mn_{0.08}Ca_{0.02}CO_3$,
Less altered BIF: $Fe_{0.56}Mg_{0.36}Mn_{0.07}Ca_{0.01}CO_3$,
Altered BIF: $Fe_{0.74}Mg_{0.21}Mn_{0.03}Ca_{0.02}CO_3$.

Summaries of microprobe analyses for 24 ankerite grains from mineralized quartz-carbonate veins and the schist units are shown in Tables 3.7. Ankerite compositions from the three schist samples (452/25B, 525/20, DD17/17) analyzed, indicate a range from 9.4 to 28.11 mole % $FeCO_3$, and 15.9 to 36.69 mole % $MgCO_3$. A relatively restricted variation occurs in the ankerite associated with the veins, which contains 14.14 to 22.58 mole % $FeCO_3$, 23.12 to 36.98 mole % $MgCO_3$ and up to 5.54 mole % $MnCO_3$. Average formulae of the ankerite were determined approximately as follows:

Interbedded schist: $CaFe_{0.4}Mg_{0.5}Mn_{0.1}(CO_3)_2$,
Group IIA veins: $CaFe_{0.5}Mg_{0.5}(CO_3)_2$,
Group IIB veins: $CaFe_{0.4}Mg_{0.6}(CO_3)_2$.

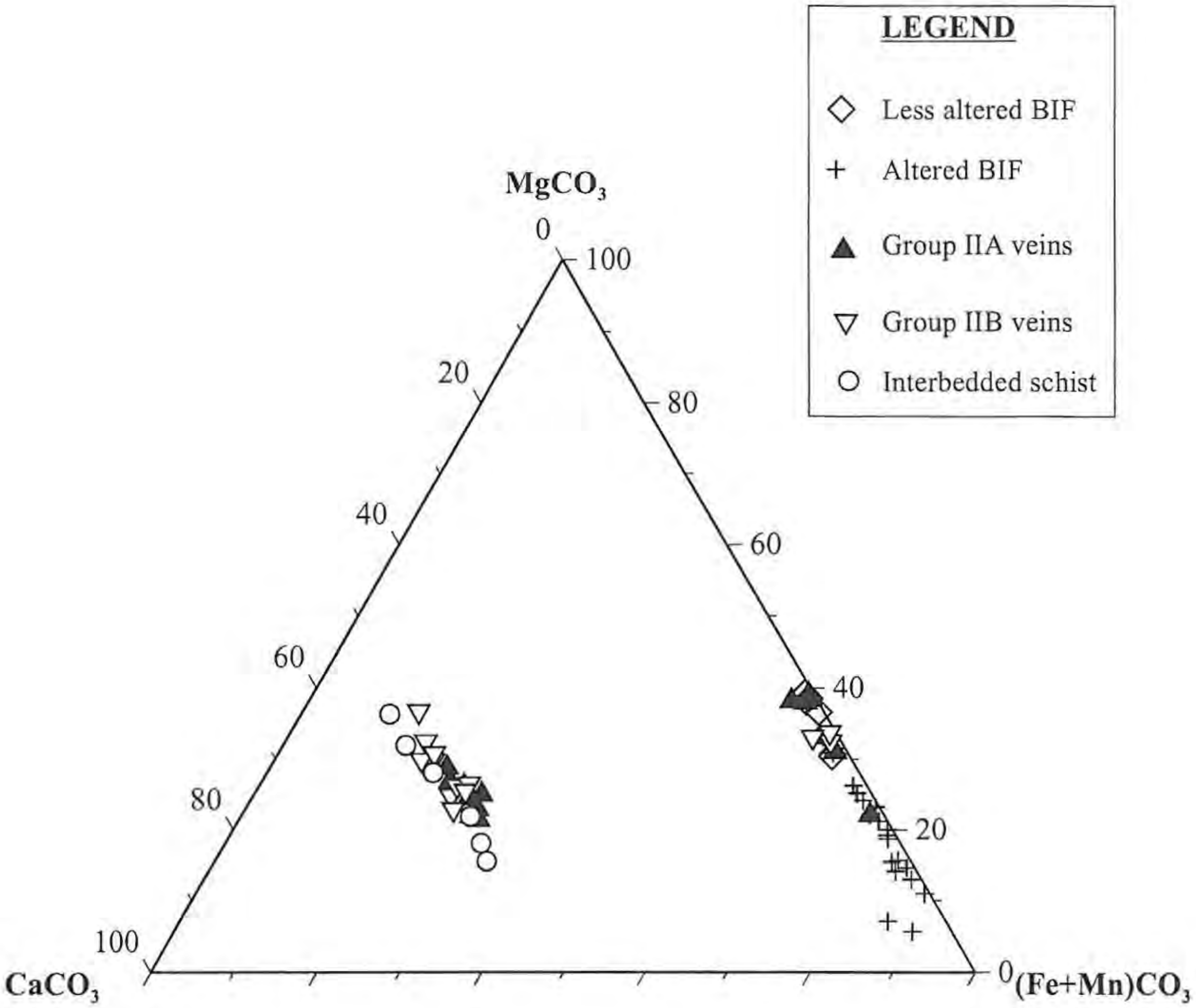

Figure 3.8. Ternary plot of compositions of carbonate occurring in different lithologies in the orebody at the Kalahari Goldridge deposit.

The dominant occurrence of the carbonates in the deposit is generally consistent with most Archaean gold deposits reported worldwide (e.g., Golding and Wilson, 1983; Phillips and Groves, 1984; Phillips, 1986; Kishida and Kerrich, 1987). Replacement reactions between carbonates and other primary mineral assemblages and (stable isotope signatures) suggest that carbonate precipitation in the BIF and other lithologies resulted primarily from fluid interaction with the host rocks. This is discussed in further detail in Chapters 4 and 6. The genetic implication of the carbonate in the BIF is considered using samples 13175/2A and 13175/2B as examples (see Fig.4.2). Sample 13175/2A corresponds to a less altered BIF band whilst sample 13175/2B represents a significantly altered band that is characterized by extensive ladder veining. The relative degree of alteration and bulk composition of the two rocks, discussed in Chapter 4, indicates higher carbonate content and a corresponding higher degree of volatile composition in the more altered sample. The carbon and oxygen stable isotope signatures of carbonates taken from these samples show a range of 0.02 ‰ and 0.35 ‰ respectively (see Chapter 6, Table 6.2). These observations constitute ample evidence that the minor carbonates observed in the less altered BIF samples can be attributed to limited fluid interaction with the BIF.

3.4: Sulphides and other Opaque Minerals

Magnetite, pyrite, pyrrhotite and chalcopyrite constitute the main opaque minerals associated with the mineralization at Kalahari Goldridge. Pyrite and pyrrhotite form the dominant sulphide phases making probably > 95 volume percent of the ore minerals.

3.4.1: Magnetite

Magnetite occurs as fine-grained disseminations to coarse-grained euhedral crystals. It is generally intergrown with quartz, carbonate, silicates and sulphides. In less altered BIF samples, magnetite occurs as small octahedra, generally along monomineralic layers, and as disseminations (Fig. 3.9). Coarse-grained euhedral crystals are common where significant recrystallisation has occurred. Scattered euhedral and granular aggregates are also common at the boundaries between magnetite mesobands and quartz veins in some samples.

In altered BIF samples, recrystallization is very significant and magnetite occurs as coarse subhedral to euhedral granular aggregates in the magnetite mesobands, as discrete grains or as individual lenses (Fig. 3.9B). In most samples, coarse and well developed octahedral magnetite grains characterize recrystallization. Extensive reaction and replacement textures are characteristic features associated with the deformed or brecciated BIF units. Pyrite, pyrrhotite and siderite are the main replacement minerals commonly occurring along foliation planes. Incomplete replacement is commonly seen as relicts of the magnetite in the associated minerals. In the interbedded schist, magnetite occurs as disseminated grains in a chlorite matrix. Microprobe analyses reveal that the magnetite is essentially pure containing relatively low amounts of MgO, Al_2O_3, TiO_2, Cr_2O_3 and MnO, which total less than 2 wt percent (Table 3.9).

Table 3.9. Microprobe analyses of magnetite from the Kalahari Goldridge Deposit.

Sample No.	531/9B-1	531/9B-2	524/8-1	524/8-2	13175/2C	13175-2C
No. of analyses	2	2	2	2	3	2
Wt %						
SiO_2	1.16	0.92	1.15	0.74	0.73	0.17
TiO_2	0.11	0.13	0.05	0.05	0.07	0.02
Al_2O_3	0.05	0.05	0.02	0.07	0.07	0.00
Cr_2O_3	0.00	0.00	0.02	0.00	0.01	0.01
Fe_2O_3	66.27	67.21	66.14	67.14	66.75	67.91
FeO	31.63	31.68	31.54	31.39	31.18	31.07
MnO	0.00	0.06	0.01	0.02	0.02	0.01
MgO	0.04	0.03	0.02	0.06	0.07	0.02
CaO	0.01	0.00	0.01	0.02	0.01	0.01
Total	99.26	100.08	98.97	99.49	98.92	99.21

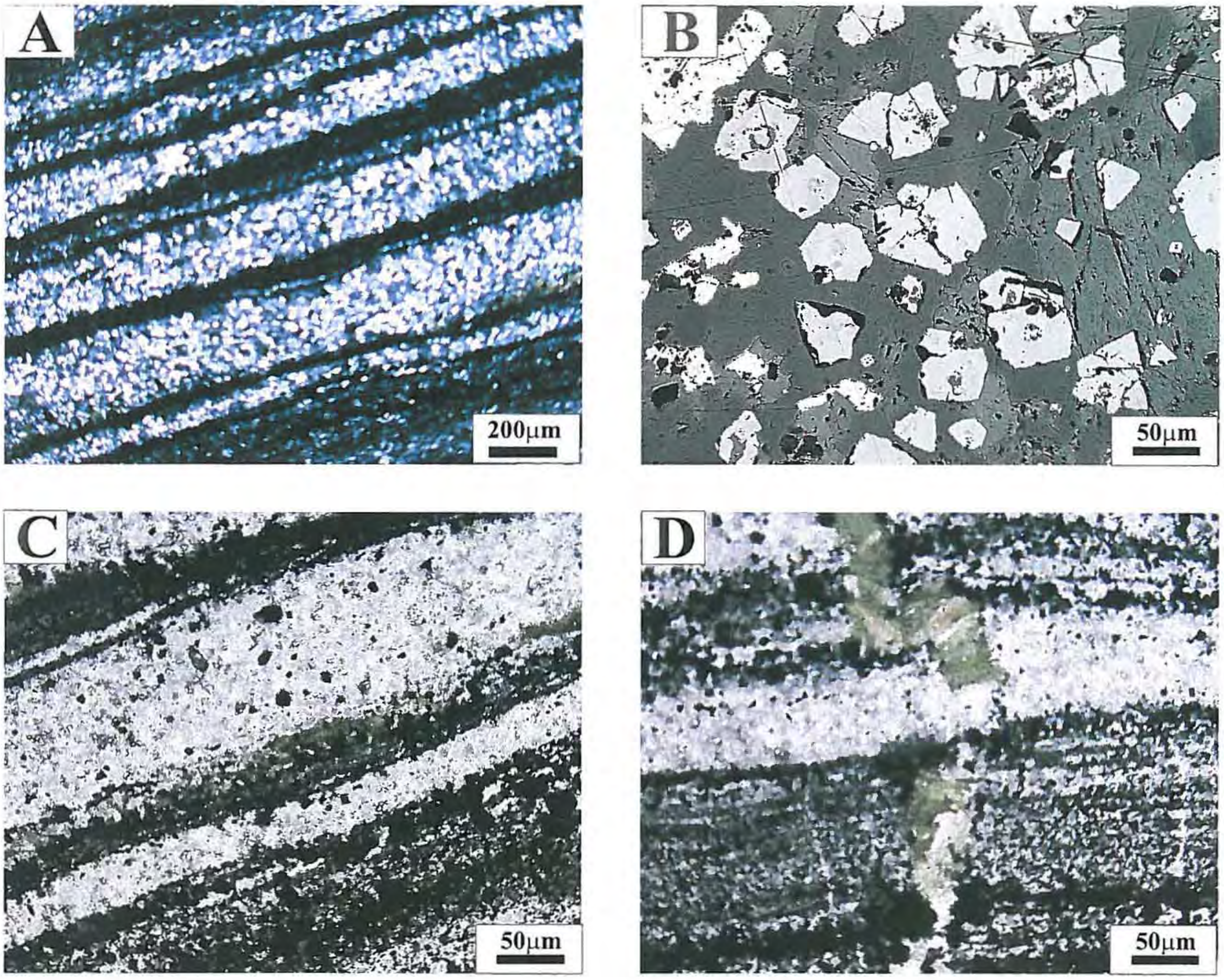

Figure 3.9. A. Photomicrograph of fine-grained magnetite microbands (black) interlayered with chert in less altered chert-magnetite mesobands (sample 116/05/1; Crossed nicols). **B**. Recrystallized magnetite grains in altered chert-magnetite mesoband (sample 588/10B; reflected light).
C. Photomicrograph showing fine-grained stilpnomelane in magnetite microbands in less altered BIF (sample 116/05/1; plane polarised light). **D.** Green stilpnomelane growing in magnetite microbands along a micro-ladder vein cutting subperpendicular to the magnetite microband in a less altered chert-magnetite mesoband (sample 116/05/1; plane polarized light). NB: Less altered and altered chert-magnetite mesobands are shown in Figure 2.

3.4.2: Pyrrhotite

Pyrrhotite shows almost similar abundance as pyrite at the Kalahari Goldridge deposit. It occurs as anhedral to subhedral grains ranging in size up to 2cm. It commonly occurs replacing magnetite in the BIF (Fig. 3.10A) or magnetite disseminations in the interbedded schist. To a lesser degree, pyrrhotite replacement of chlorite also occurs in the interbedded schist, commonly associated with dark brown stilpnomelane, carbonate and pyrite assemblages. Gold is visibly associated with the pyrrhotites. However, the modal proportion of its occurrence is observed to be less than with pyrite grains, despite high assay values in pyrrhotite-rich samples. Under such circumstances, the gold may be occurring at submicroscopic levels or in lattice sites of the pyrrhotite. The modal proportion of pyrrhotite associated with the Group IIA veins is higher than with the Group IIB veins.

3.4.3: Pyrite

Pyrite is ubiquitous in the deposit occurring in the BIF and schist in the orebody. Pyrite also occurs in the meta-pelites and volcanic clasts in the hanging-wall sediments. Minor amounts of pyrite are also observed in mineralized veins occurring particularly along the contacts with the BIF. Pyrite occurrence in the footwall schist is rare.

In the interbedded schist, pyrite occurs as subhedral to euhedral grains in continuous stratiform bands or semi-discrete layers sub-parallel to the foliation plane in the schist. The pyrites generally range in size between 100μm and 0.5mm, and exhibit cubic to irregular shapes.

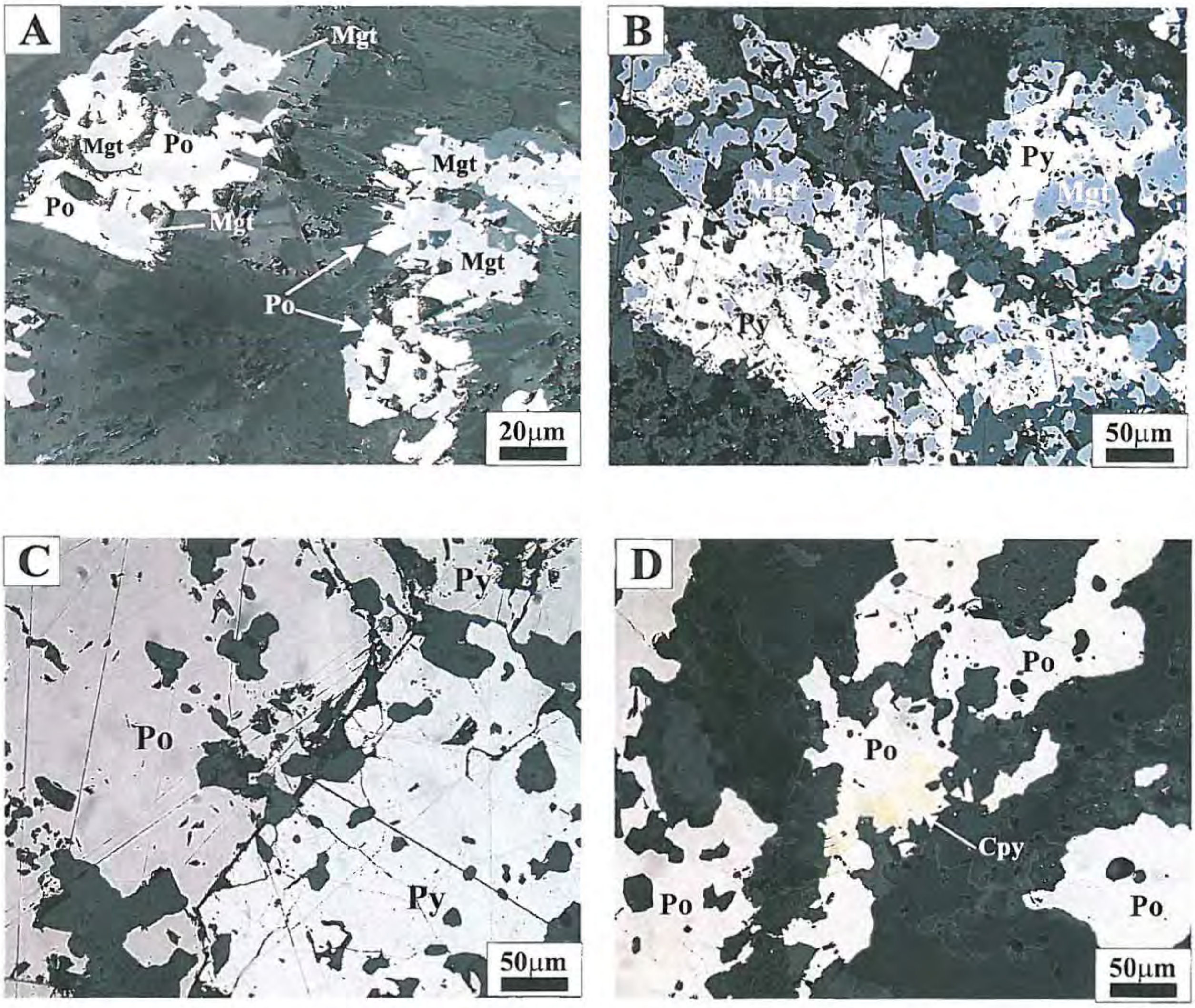

Figure 3.10. Reflected light photomicrographs illustrating textural relationship of opaque minerals associated with gold at the Kalahari Goldridge deposit. **A.** Replacement of magnetite (Mgt) by pyrrhotite (Po), sample 589/4. **B.** Replacement of magnetite (Mgt) by pyrite (Py). **C.** Textural equilibrium between pyrite (Py) and pyrrhotite (Po). **D.** Replacement of pyrrhotite (Po) by chalcopyrite (Cpy), sample DD18/18/1.

Pyrite in the BIF occurs as coarse subhedral to euhedral and ranges in size up to 5mm. Pyrite typically occurs as replacement of magnetite (Fig. 3.10B) and chlorite in these rock units. Replacement occurs along the foliation planes and laminated bands. The replacement of chlorite by pyrite occurs where evidence of fluid interaction is present. Pyrites in the schist generally contain inclusions of gangue minerals, which commonly occur in the cores of the pyrite.

In the BIF, pyrite replacement of magnetite is typically characterized by sub-rounded pyrrhotite inclusions, and is commonly associated with inclusions of visible gold. Coexisting pyrite and pyrrhotite exhibit annealing textures and show no clear evidence of mutual replacement between the two minerals in most samples (Fig. 3.10C). However, small inclusions of pyrrhotite in the pyrites suggest pyrrhotite may have preceded pyrite in the crystallization sequence.

Pyrite in the altered BIF is commonly intergrown with other gangue minerals (e.g., stilpnomelane, chlorite, carbonate), giving evidence of their contemporaneous growth from fluid interaction with magnetite. Some pyrites have been fractured in places, which is indicative of brittle deformation. Some of these fractures and related cracks may be filled with gold grains. No visible gold has been identified with pyrites in the schist.

3.4.4: Chalcopyrite

Chalcopyrite forms a minor component of the sulphides and represents the only Cu-bearing sulphide present at Kalahari Goldridge. It consistently occurs as anhedral replacements of pyrrhotite along grain boundaries and rarely as replacement of pyrite (Fig. 3.10D). Few isolated inclusions have occurred in pyrite, some of which are replacements of pyrrhotite in the pyrite in the altered

BIF. Anhedral masses of chalcopyrite also occur as discrete grains or as replacement of pyrrhotite in the schist.

3.4.6: Bismuth telluride series

This group of minerals occurs in very minor amounts and were identified from one sample (588/10B). They commonly occur as anhedral isolated grains or associated with pyrrhotite and/or gold along grain boundaries. Where it is associated with pyrrhotite, it replaces the latter along grain boundaries or occurs as inclusions.

The microprobe analyses of 6 grains are presented in Table 3.10 and, illustrated in a Bi-S-Te ternary plot (Fig. 3.11), show compositions ranging from native Bi to Bi tellurides in the tetradymite series, which occur at temperatures ranging from 200 to 400°C (Marcoux et al., 1996). Minor amounts of Fe ranging up to 1.67 wt % occur in all analyzed samples. The lack of sulphur in these minerals and the close association with pyrrhotite suggests their deposition possibly occurred under conditions of relatively low sulphur activity.

Table 3.10. Microprobe analysis of bismuth minerals at the Kalahari Goldridge deposit.

Grain	1	2	3	4	5	6
No. of analyses	1	1	1	1	1	2
Element (Wt %)						
Au	0.28	0.08	0.00	0.10	0.00	0.01
S	0.00	0.08	0.02	0.92	0.00	0.15
Se	0.00	0.00	0.00	0.00	0.07	0.03
Cu	0.02	0.02	0.00	0.02	0.00	0.01
Te	5.55	0.00	0.00	0.00	18.02	8.41
Fe	0.64	1.27	0.72	0.70	0.77	1.67
Ag	0.06	0.00	0.00	0.00	0.02	0.00
Pb	0.00	0.00	0.00	0.00	0.00	0.00
Bi	92.08	96.67	99.10	97.62	81.59	90.38
Total	98.62	98.11	99.84	99.36	100.46	100.65

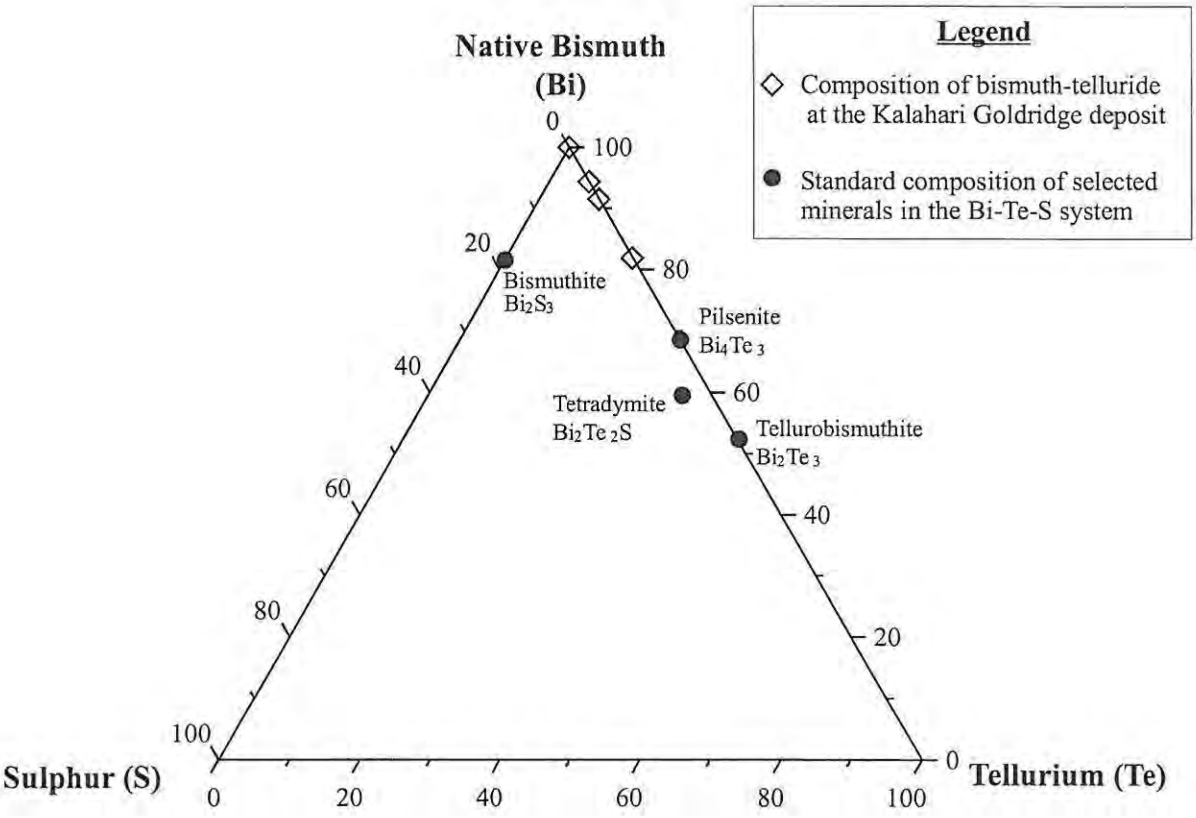

Figure 3.11. Ternary plot showing the compositional range of bismuth minerals (open squares) at the Kalahari Goldridge deposit in the Bi-Te-S system. Shown for reference are common bismuth minerals in the ternary system (Marcoux et al., 1996).

3.4.7: Gold

Gold occurs as isolated grains or closely associated with sulphides and gangue minerals notably carbonates, mainly in the altered BIF. The gold association with the sulphides commonly occurs as inclusions in pyrite (Fig. 3.12), as blebs or coarse grains along boundaries of pyrrhotite pyrite and gangue minerals (Fig. 3.13), as discrete grains (Fig. 3.13C), or as microcrack fillings in pyrite (Fig. 3.14). Gold is also commonly found together with pyrrhotite (and less commonly with gangue and magnetite) as inclusions in pyrite (Fig. 3.15). Minor amounts of more Ag-rich gold have been found associated with bismuth minerals (native bismuth and bismuth tellurides). The grain size of the gold is highly variable from less than 1 to about 130μm in diameter and subrounded to angular in shape. The microscopic investigation showed that nearly 80 percent of visible gold identified is associated with pyrite grains that replace magnetite. No gold has been identified with pyrite associated with the schist.

Microprobe analyses of 14 gold grains (Table 3.11) showed only trace amounts of Fe, Cu and S. Fineness of the gold grains [1000*(Au/(Au + Ag)] ranges from 823 to 931 (Fig. 3.16) with the lowest values associated with bismuth tellurides (823-830). The fineness data have been useful to characterize the environment of mineralization. High average and restricted fineness ranges (890-960) have been documented (Morrison et al., 1991) to characterize the Archaean lode deposits. In particular, Morrison et al. (1991) stated a range below 900 for fineness associated with BIF-hosted deposits although individual deposits may fall outside this range.

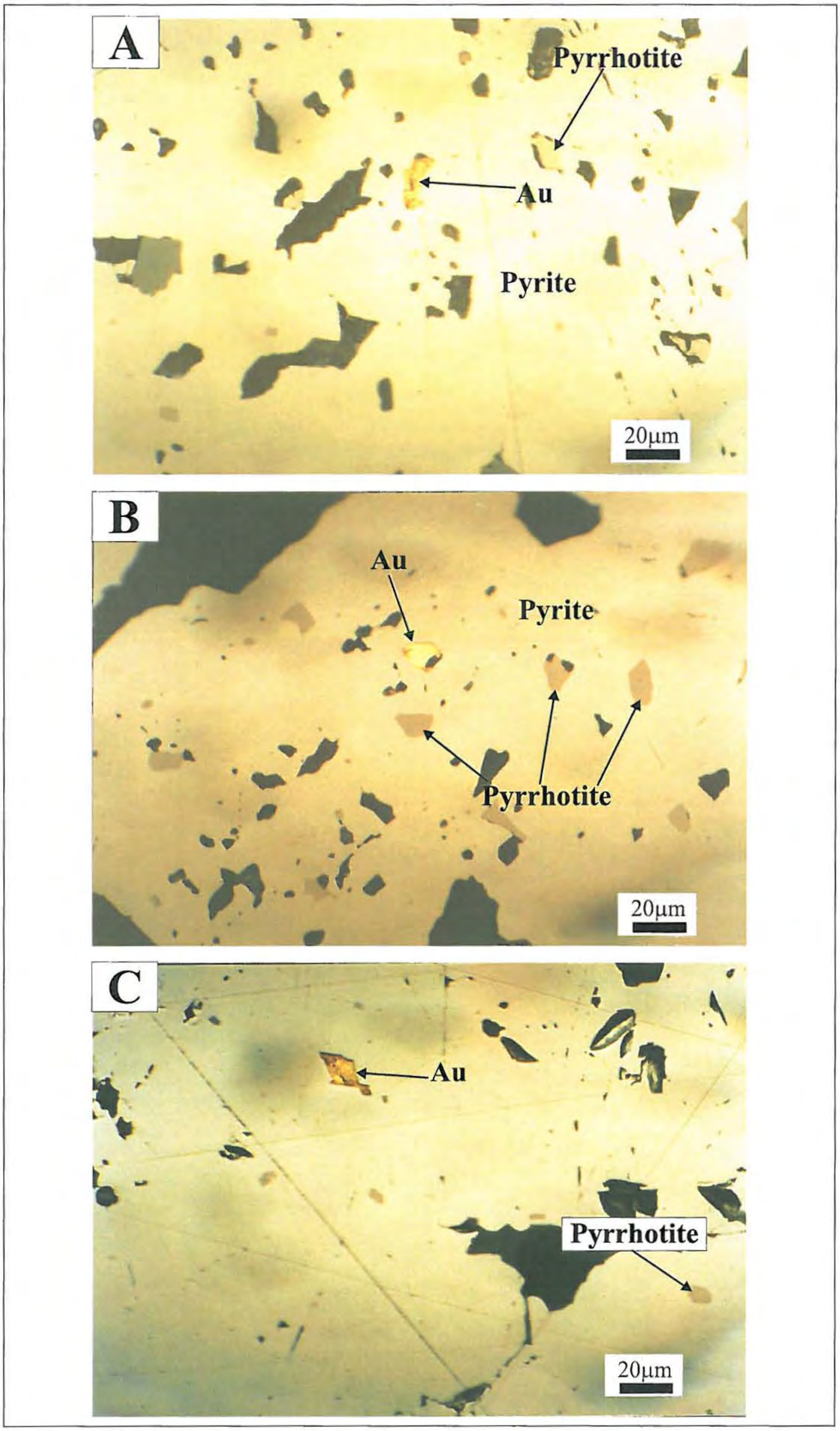

Figure 3.12. Photomicrographs of gold (Au) inclusions in pyrite in BIF at the Kalahari Goldridge deposit.

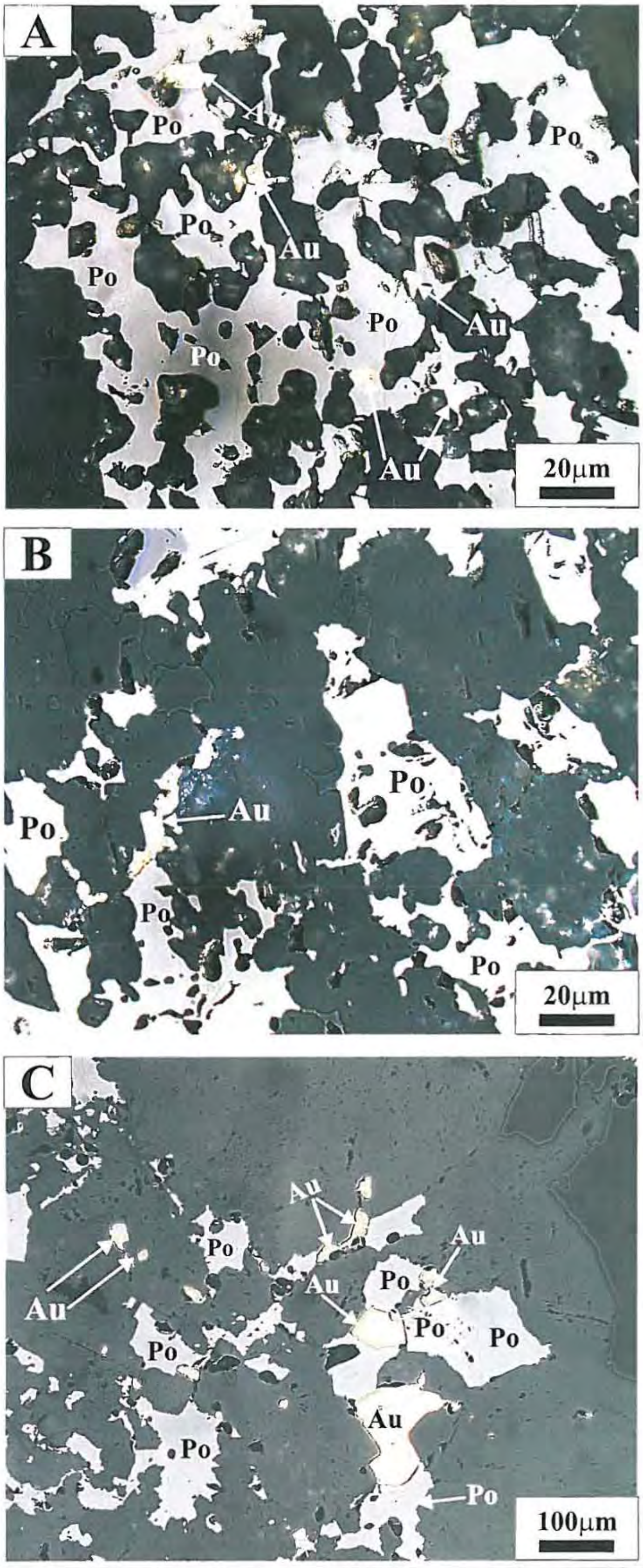

Figure 3.13. Photomicrographs of gold (Au) associated with pyrrhotite (Po) in BIF at the Kalahari Goldridge deposit. Fig. **C** also shows the occurrence of discrete Au grains.

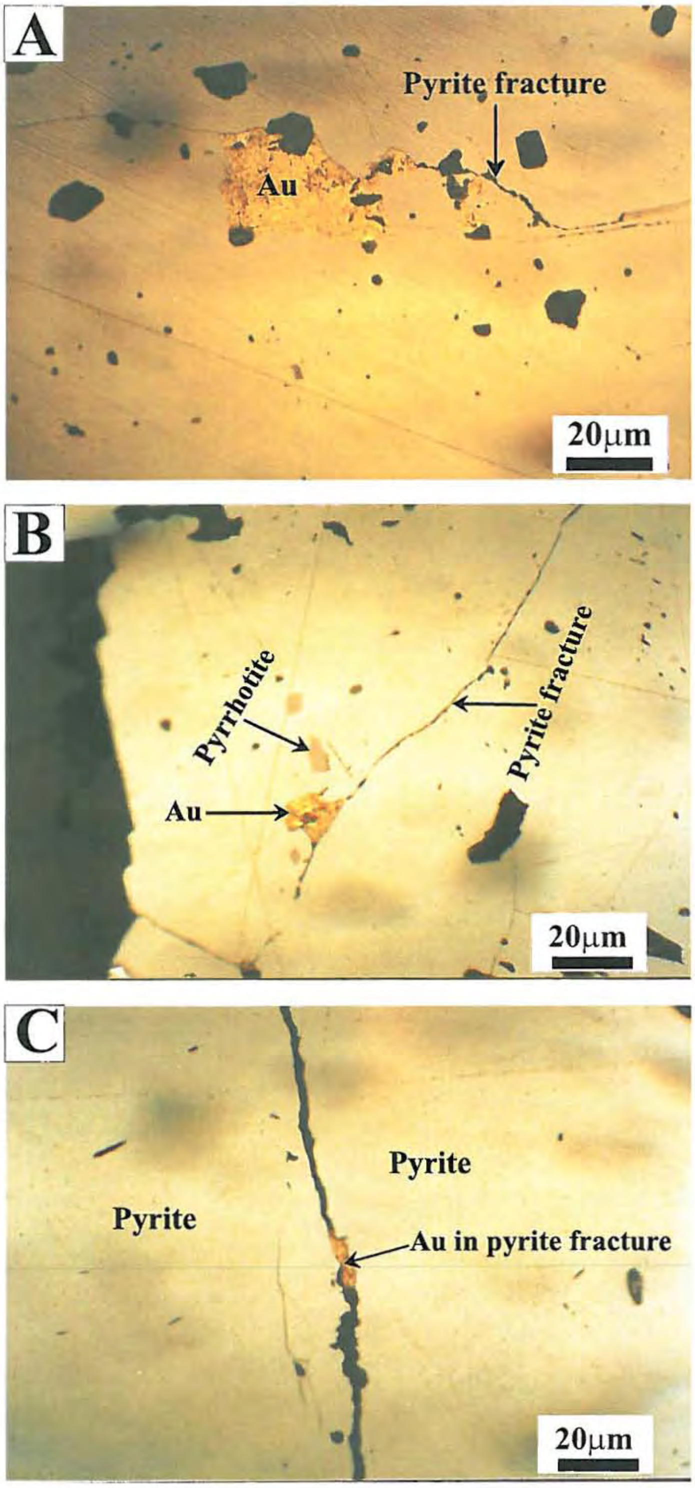

Figure 3.14. Photomicrographs of gold (Au) in microfractures in pyrite at the Kalahari Goldridge deposit.

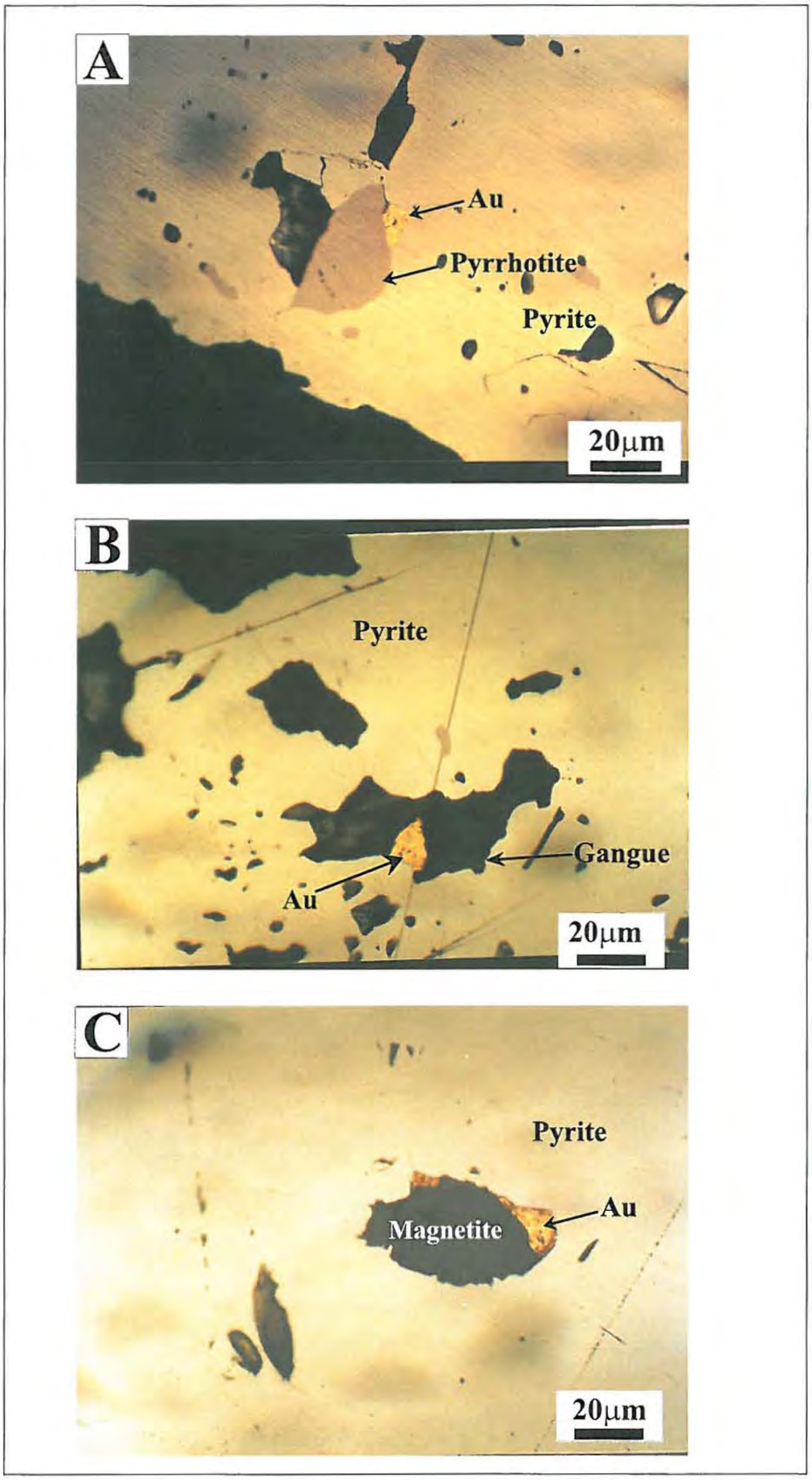

Figure 3.15. Photomicrographs showing textural relationship between gold (Au) and other opaque and gangue minerals at the Kalahari Goldridge deposit. **A**. Coexisting Au and pyrrhotite hosted in pyrite. **B**. Coexisting Au and gangue (carbonate) hosted in pyrite and **C**. Au coexisting with magnetite in pyrite host.

Table 3.11. Microprobe analyses of gold grains associated with ore minerals at the Kalahari Goldridge deposit.

Gold grain	1		2	3	4	5		6		7	
No of analyses	4		1	1	1	5		3		5	
	Mean	std				Mean	std	Mean	std	Mean	std
Wt %											
Au	81.28	0.58	82.57	81.96	80.82	85.57	0.48	88.70	0.40	89.54	0.84
Ag	16.59	0.14	17.04	17.30	17.34	13.96	0.59	11.09	0.82	10.65	0.27
Cu	0.01	0.02	0.01	0.04	0.00	0.02	0.01	0.00	0.00	0.02	0.01
Fe	0.23	0.16	0.39	0.83	1.29	0.06	0.04	0.15	0.11	0.11	0.01
Bi	0.00	0.00	0.00	0.00	0.00	0.00	0.00	0.00	0.00	0.00	0.00
As	0.00	0.00	0.00	0.00	0.00	0.00	0.00	0.00	0.00	0.00	0.00
Te	0.00	0.00	0.00	0.04	0.02	0.00	0.00	0.00	0.00	0.00	0.00
S	0.12	0.05	0.16	0.00	0.00	0.14	0.12	0.17	0.09	0.13	0.06
Total	98.24		100.17	100.18	99.46	99.75		100.11		100.43	
Fineness	830.49		828.91	825.69	823.35	859.75		888.83		893.71	

Gold grain	8		9		10		11		12		13
No of analyses	2		2		2		2		2		1
	Mean	std	Mean	std	Mean	std	Mean	std	Mean	std	
Element											
Au	91.96	0.45	92.11	0.08	91.41	0.14	91.77	0.90	86.68	0.07	91.52
Ag	6.74	0.09	8.13	0.01	8.14	0.32	7.89	0.65	11.60	0.34	8.99
Cu	0.01	0.01	0.11	0.01	0.04	0.02	0.02	0.02	0.00	0.00	0.02
Fe	0.89	0.36	0.14	0.03	0.13	0.01	0.12	0.01	0.21	0.10	0.15
Bi	0.00	0.00	0.00	0.02	0.00	0.00	0.00	0.00	0.00	0.00	0.00
As	0.00	0.00	0.00	0.00	0.00	0.00	0.00	0.00	0.00	0.00	0.00
Te	0.00	0.00	0.00	0.00	0.00	0.00	0.00	0.00	0.00	0.00	0.00
S	0.12	0.06	0.00	0.00	0.14	0.01	0.13	0.02	0.12	0.01	0.11
Total	99.73	0.05	100.51	0.15	99.86	0.48	99.92	0.24	98.61	0.37	100.67
Fineness	931.69		918.88		918.23		920.87		881.97		910.55

Gold grain	13	14	
No of analyses	1	3	
		Mean	std
Element			
Au	91.52	91.67	0.26
Ag	8.99	7.99	0.39
Cu	0.02	0.01	0.02
Fe	0.15	0.13	0.00
Bi	0.00	0.00	0.00
As	0.00	0.00	0.00
Te	0.00	0.03	0.01
S	0.11	0.08	0.08
Total	100.67	99.91	0.48
Fineness	910.55	919.85	

std = one standard deviation

Comments:

1-4 (From sample 588-10B) Au coexisting with bismuth-telluride
5 (From sample 525-20A) Au inclusion in pyrite
6-8 (From sample 117/018/1) Au inclusion in pyrite
9 (From sample 118/21/7) Au-pyrrhotite inclusion in pyrite
10-11 (From sample 118/21/7) Au in pyrite fracture
12 (From sample 118/2/11) Au-pyrrhotite inclusion in pyrite
13 (From sample 118/21/6 Au-pyrrhotite inclusion in pyrite
14 (From sample 118/21/6) Au-carbonate inclusion in pyrite

In specific examples, Saager et al. (1987) reported a range from 6.69 to 8.12 for Ag content in Au grains at the Vubachikwe BIF-hosted deposit in Zimbabwe, corresponding to fineness of 933 to 919. Pretorius et al. (1988) reported the composition of Au grains, which corresponds to a fineness range from 930 to 970 at the Fumani BIF-hosted deposit in South Africa. At Mt. Morgan BIF-hosted deposit, Vielreicher et al. (1994) indicated a fineness range from 851 to 889.

Morrison et al. (1991) attributed the high fineness of gold in Archaean systems to sulphidization associated with gold deposition. They showed that Ag transport in hydrothermal solution is favoured by the $AgCl^-$ whereas gold is favoured by the $Au(HS)_2^-$ complex. Furthermore, a decreased a_{SO_4}/a_{H_2S} ratio in the hydrothermal fluid favours the precipitation of Au rather than Ag (McCuaig and Kerrick, 1998). This also implies that higher a_{SO_4}/a_{H_2S} ratios in the ore fluid would favour Ag precipitation. Higher-temperature deposits also show greater abundances of Ag than lower-temperature deposits. Morrison et al. (1991) also associated the consistency in the fineness of gold in Archaean terranes to three possible reasons: (1) a unique origin for the style of mineralization, (2) unique source of the gold and (3) a mechanism of homogenizing the fineness values through post-mineralization and metamorphism. Anhaeusser (1986) stated that consistency of gold fineness in general is characteristic of gold that precipitated in a single stage in the paragenesis of the ore. Therefore, as pointed out earlier, the close association of the bismuth minerals with pyrrhotite (which precipitates at low a_{H_2S}) and the lower fineness in gold (higher Ag) associated with the bismuth mineral suggests that their precipitation occurred at higher temperatures.

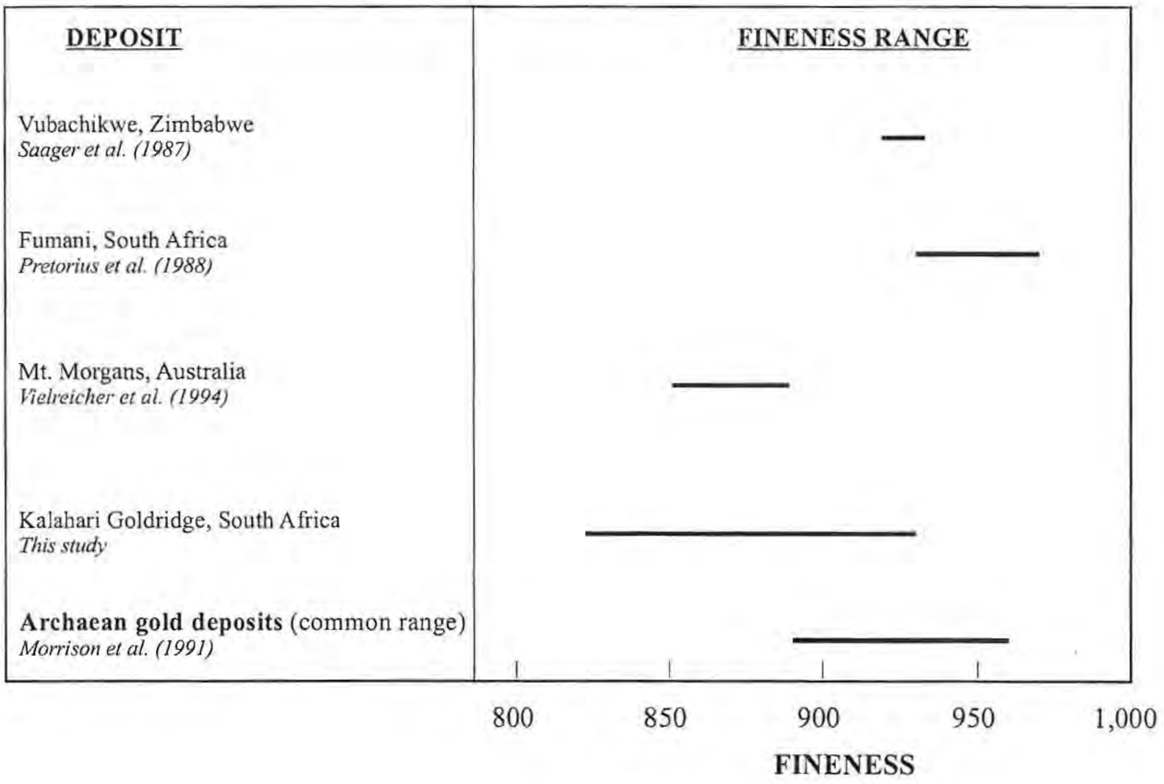

Figure 3.16. Gold fineness data of selected BIF-hosted gold deposits in Archaean greentones. Common fineness range for Archaean gold deposits in general is included for comparison.

3.5: Mineral Paragenesis

Figure 3.17 summarizes the paragenetic sequence of the mineral assemblages found at Kalahari Goldridge. The sequence has been divided into pre-ore, main stage and post-gold mineralization. These relationships establish a generalized sequence of deposition of the minerals identified in the ore deposit.

Minerals associated with the pre-ore stage were identified in less altered BIF and schist due to low or minimal fluid-rock interaction and may reflect the primary mineralogy associated with metamorphism. Earliest minerals include minnesotaite, ferro-stilpnomelane, magnetite and quartz (chert) in the BIF and chlorite, pyrite and pyrrhotite in the schist. Early formed chlorite occurs throughout the pelitic schist in the orebody and hanging-wall. Trace amounts of chlorite are also found in the footwall. Early formed stilpnomelane and minnesotaite occur in minor amounts in less altered BIF samples.

The main stage represents the hydrothermal event and the main episode of the gold mineralization as well as the formation of the bulk of silicates, carbonates and opaque minerals present in the deposit. This stage is characterized by brittle deformation and the subsequent introduction of the hydrothermal fluid and equilibration with host rocks. Gold-bearing sulphides (pyrite and pyrrhotite), bismuth minerals (native bismuth and bismuth tellurides), carbonates (siderite, ankerite) and silicates such as white mica, stilpnomelane and chlorite, recrystallised magnetite, and quartz are also associated with this stage. This stage is further subdivided into Stages I and II, which are associated with the mineralized quartz veining in the deposit.

The absence of any evidence of mutual replacement between pyrite and pyrrhotite at their grain boundaries (e.g. Fig. 3.10C) makes it difficult to define the time relationship between the two minerals. However, high proportions of pyrrhotite associated with the ladder veins and the inclusions of pyrrhotite in pyrite as described earlier make it clear that it predates pyrite. The high proportion of pyrite associated with the Group IIB veins on the other hand, also suggests that stage II accounts for the majority of the pyrites at the Kalahari Goldridge deposit. Textural relationships show that chlorite and stilpnomelane formed throughout the entire mineralization stage. Native gold appears to be coeval with sulphides and other gangue minerals in both stages I and II.

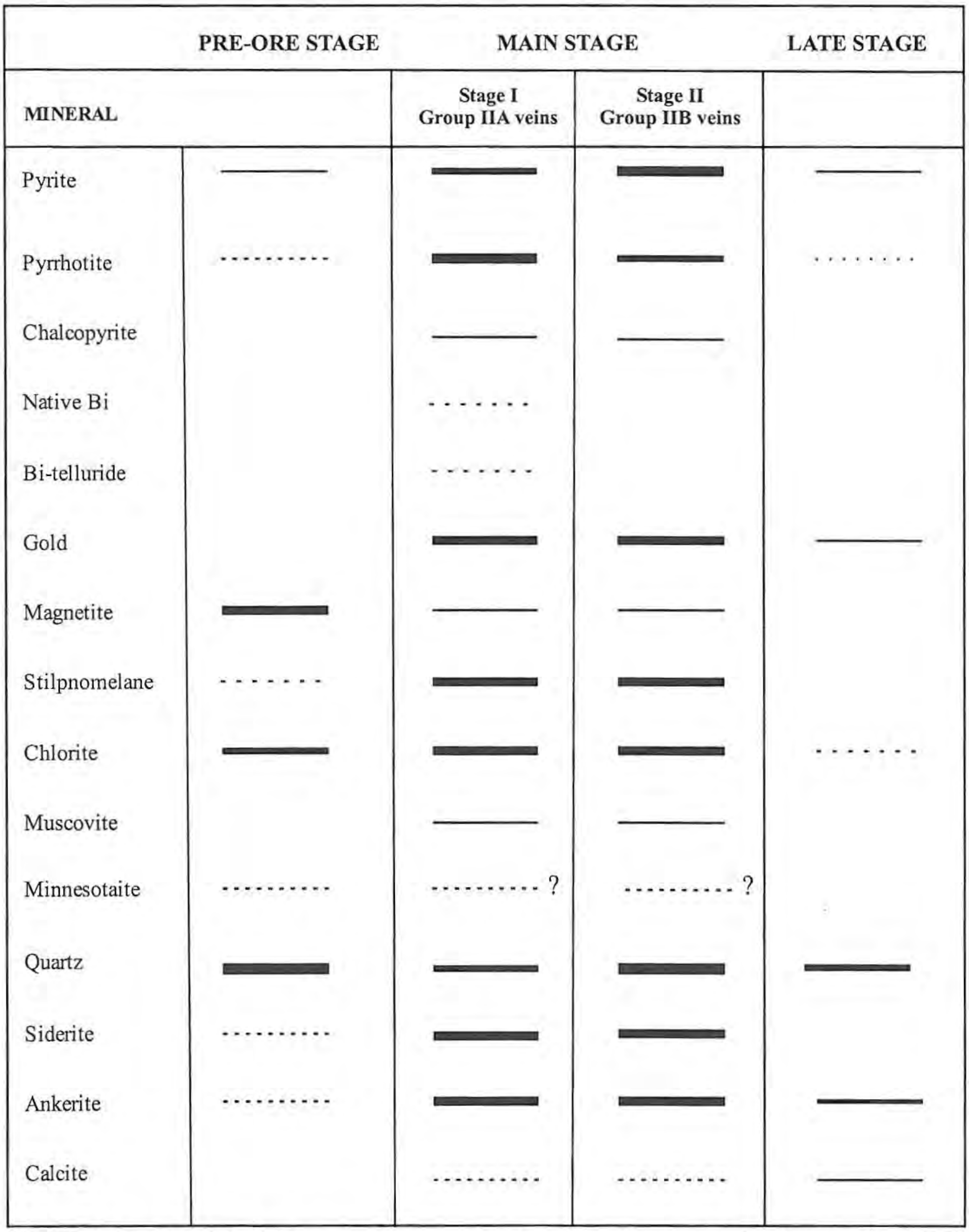

Figure 3.17. Simplified paragenetic sequence for mineralization at the Kalahari Goldridge deposit.

However, gold in pyrite fractures may be associated with a later stage phenomenon where gold is likely to be derived from lattice sites of pyrite or by a supergene process.

Stage III is characterized by late carbonates consisting of calcite and dolomite in veins, and sulphides consisting dominantly of pyrites.

3.6: Metamorphic Implications of the Mineral Assemblage

Studies reported in literature on the metamorphic grades of BIFs hosting gold deposits (Saager et al. 1987; Pretorius et al. 1988; Lhotka and Nesbitt, 1989; Vielreicher et al. 1994) indicate a range from sub-greenschist facies to medium-grade. For example, Vielreicher et al. (1994) reported a magnetite-quartz-carbonate-minnesotaite mineral assemblage at the Mt. Morgan BIF-hosted gold deposit, Western Australia, which is characteristic of temperatures below 300°C (Miyano and Klein, 1989, see below). Saager et al. (1987) indicated a medium grade of metamorphism (400 to 600°C) for BIF at the Vubachikwe deposit in Zimbabwe. They described a metamorphic assemblage consisting of cummingtonite-grunerite, tremolite, chlorite, quartz, and carbonates (siderite, ankerite and calcite). Lhotka and Nesbitt (1989) reported a range of metamorphic grades from a low grade (sub-biotite) to medium grade consisting of biotite, garnet, grunerite and pyroxene as the prominent mineral assemblage associated with BIF at the Contwoyoto Lake-Point Lake gold deposit in the Lupin area, Abitibi greenstone belt, Canada. Pretorius et al. (1988) indicated an upper amphibolite facies grade (620±70°C) for BIF at the Fumani mine in the Sutherland greenstone belt in South Africa.

The rare occurrence of outcrops, together with the high degree of alteration associated with the host rocks at Kalahari Goldridge makes it difficult in constraining the precise metamorphic conditions of the host rocks. The mineralogy of a less altered mafic schist sample taken within about 30km of the mine consists essentially of chlorite, epidote, actinolite, quartz and minor amounts of plagioclase. As documented by Laird (1982), the mineral assemblages such as observed in these mafic units, are representative of greenschist to lower amphibolite facies grades of metamorphism. Figure 3.18 shows the experimentally derived stability relations of common minerals in iron-formation (Miyano and Klein, 1989). Minnesotaite and greenalite have been identified as index minerals in very low-grade metamorphism possibly within the zeolite or prehnite-pumpellite facies in iron formations (French, 1973; Klein and Flink, 1975; Floran and Papike, 1975, 1978; Frost, 1979). According to these authors, minnesotaite stability persists until near the greenschist-amphibolite facies transition where it converts to grunerite.

At Kalahari Goldridge deposit, minnesotaite has been identified in less altered BIF as a secondary product from magnetite and siderite. Grunerite on the other hand, has not been identified in any of the studied samples. The occurrence of minnesotaite and the absence of grunerite in the mineral assemblages in BIF samples at the Kalahari Goldridge deposit, therefore, can be used to constrain approximately the upper thermal limits during metamorphism prior to mineralization. This ranged approximately up to 350°C and pressures less than 7 kbars. In the absence of retrograde reaction in the altered mineral assemblage, the coexistence of chlorite and stilpnomelane in the altered samples suggests maximum temperatures of 430°C were attained in the host rocks. Furthermore, the absence of chlorite in less altered BIF samples possibly suggests that peak metamorphism was synchronous with the mineralization.

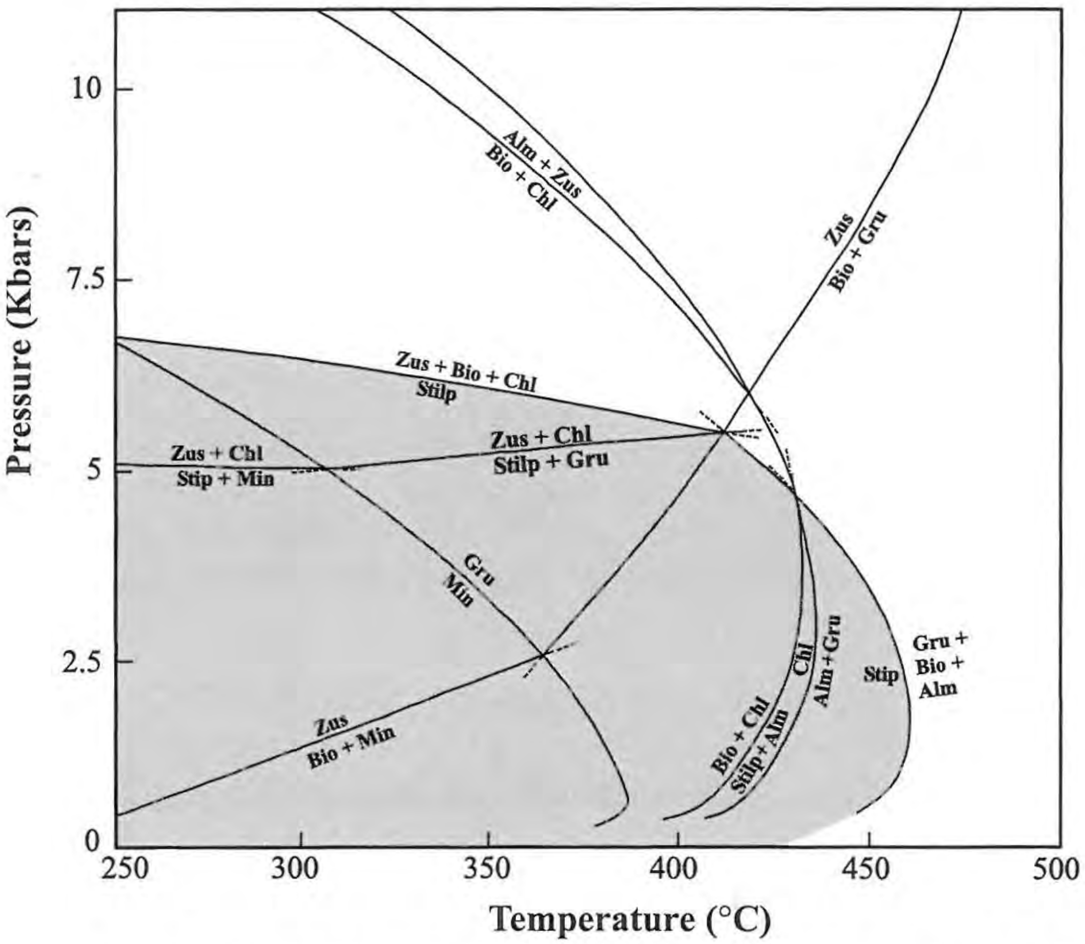

Figure 3.18. Phase relations of Fe-endmember Al-bearing silicates in Fe-rich rocks (redrawn from Miyano and Klein, 1989).
Abbreviations: Stilp, stilpnomelane; Bio, biotite; Chl, chlorite; Alm, almandine; Min, minnesotaite; Gru, grunerite; Zus, zussmasite. Shaded area represents stability field of stilpnomelane.

Chapter 4: HYDROTHERMAL ALTERATION AND BULK ROCK GEOCHEMISTRY

4.1 Hydrothermal Alteration

4.1.1: Introduction

The process of hydrothermal alteration involves the interaction of transgressing hydrothermal fluid with wall rock. The patterns of hydrothermal alteration associated with many ore deposits have been useful tools in exploration to delineate mineralized areas. In gold-related hydrothermal alteration, the mineralization may display a lateral variation of mineral assemblage away from the fluid source. Various studies (e.g. Phillips and Groves, 1984; Phillips and Brown, 1987; Kishida and Kerrick, 1987; Bohlke, 1989) have shown that index mineral assemblages commonly define the variation from local to regional scale. The mineralogical variations as demonstrated in most of these studies are largely dependent on the initial composition of the hydrothermal fluid, the chemical composition and the mineralogy of the host rock, the degree of interaction between the transgressing fluid and host rock, and pressure and temperature changes during the alteration process.

Hydrothermal alteration at the Kalahari Goldridge deposit is very pervasive and extends into the surrounding wallrocks in both the footwall and hanging wall. The extensive wall-rock alteration has overprinted the regional metamorphic assemblage. The associated mineralogy shows marked relationship with the intensity of the alteration and the bulk composition of host rock. Important metasomatic changes associated with the alteration include potassic alteration, carbonation, sulphidation and chloritization.

The vein systems (Chapter 2) suggest at least two episodes of gold mineralization existed at the Kalahari Goldridge deposit. Therefore, the associated mineralogy observed in the deposit may be associated with multiple episodes of fluid interaction with host rock. However, the consistency in the alteration assemblages and textural relationships throughout the deposit indicates that the wall rock experienced a uniform alteration history from a unique fluid source. In the following sections, the various alteration processes and their relation to the gold mineralization at Kalahari Goldridge are described.

4.1.2: Potassic alteration

Potassic metasomatism at Kalahari Goldridge is characterized by the development of stilpnomelane and muscovite (sericitisation) as the main hosts of K in the alteration assemblages. The degree of K-metasomatism is greatly influenced by the amount of Al in the host rock. Muscovite is commonly associated with the replacement of chlorite and is best developed in the schists within the orebody, footwall and hanging-wall and to lesser extent in the BIF. The degree of the sericite alteration is apparently controlled by the extent of fluid influx. In the footwall and hanging-wall schists, the alteration is most intense in areas proximal to the orebody, which have a characteristic bleached appearance. The intense alteration is also recognized by the presence of well defined foliation in the schist. The degree of alteration is generally uniform in the footwall and hanging-wall schist and subparallel to the orebody, with complete obliteration of primary mineralogy in the footwall mafic schist proximal to the orebody that decreases away from the orebody. Sericitisation in the interbedded schist exhibits variable intensity, which apparently resulted from variable fluid access, as demonstrated by the intensity of quartz veining.

Stilpnomelane development is restricted to lithologies in the orebody, both interbedded schist and BIF. However, the modal proportion of stilpnomelane in the BIF is generally higher than in the schist. The intense K-metasomatism at the Kalahari Goldridge deposit suggests the introduction of K by the hydrothermal fluid. Equations 4.1 to 4.3 represent typical reactions that may be associated with K-metasomatism at the Kalahari Goldridge deposit.

$$\underset{\text{magnetite}}{7/3Fe_3O_4} + \underset{\text{quartz}}{13SiO_2} + 21/4H_2O + \underset{\text{chlorite}}{Fe_5Al_2Si_3O_{10}(OH)_8} + 5/4K^+ = \underset{\text{stilpnomelane}}{2K_{0.625}Fe_6AlSi_3O_{21}(OH)_2 \bullet 3/2H_2O} + 7/6O_2 + 5/4H^+ \quad [4.1]$$

4.1.3: Sulphidation

Sulphidation at the Kalahari Goldridge deposit is typically marked by the abundance of pyrite and pyrrhotite and minor amounts of chalcopyrite. The sulphidation is represented by the selective replacement of magnetite by the pyrite and pyrrhotite along Fe-rich foliation planes in the BIF as well as in the schist. Pervasive replacement can be seen adjacent to contacts of the large quartz-carbonate veins with Fe-rich bands of the host BIF, creating cm-scale sulphide haloes along the vein contacts (Fig. 4.1). Typical reactions representing the sulphide replacement can be represented as follows:

$$\underset{\text{chlorite}}{3Fe_5Al_2Si_3O_{10}(OH)_8} + 2K^+ + 30H_2S + 22O_2 = \underset{\text{quartz}}{3SiO_2} + \underset{\text{muscovite}}{2KAl_3Si_3O_{10}(OH)_2} + \underset{\text{pyrite}}{15FeS_2} + 18H_2O \quad [4.2]$$

$$\underset{\text{chlorite}}{3Fe_5Al_2Si_3O_{10}(OH)_8} + 2K^+ + 15H_2S = \underset{\text{quartz}}{3SiO_2} + \underset{\text{muscovite}}{2KAl_3Si_3O_{10}(OH)_2} + \underset{\text{pyrrhotite}}{15FeS} + 24H_2O + 2H^+ \quad [4.3]$$

$$\underset{\text{Magnetite}}{Fe_3O_4} + 6H_2S + O_2 = \underset{\text{Pyrite}}{3FeS_2} + 6H_2O \quad [4.4]$$

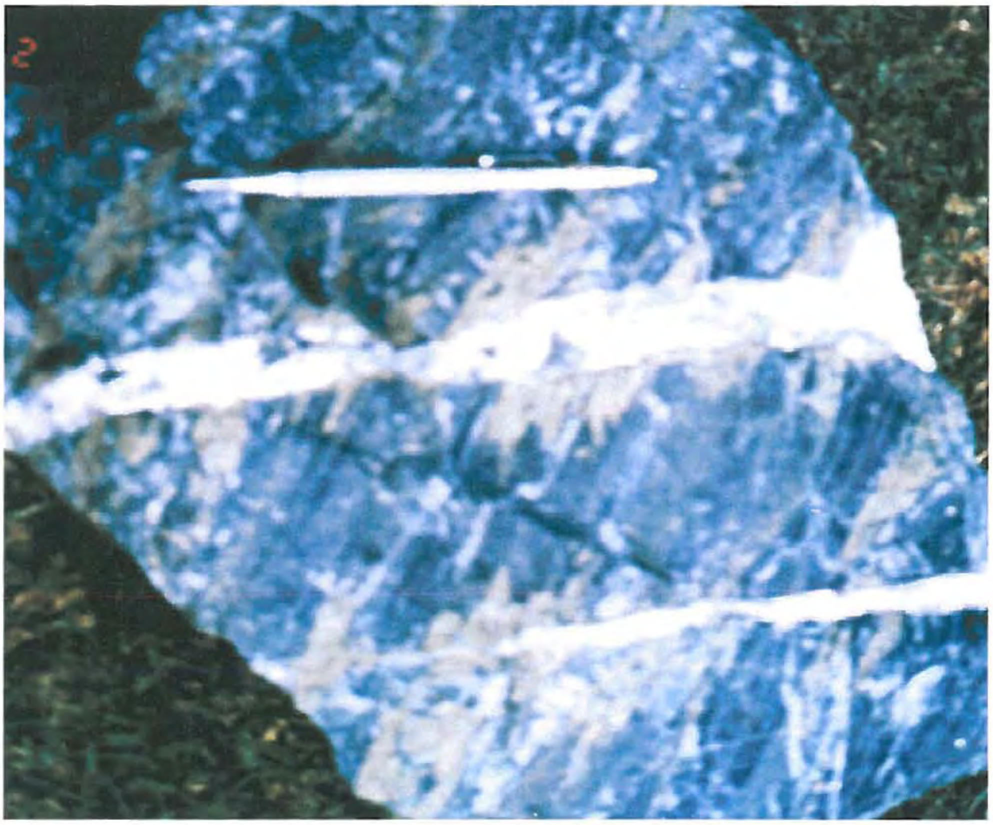

Figure 4.1. Sulphide haloes along margins of vein with BIF.

$$\underset{\text{Magnetite}}{Fe_3O_4} + 3H_2S = \underset{\text{Pyrrhotite}}{3FeS} + 3H_2O + 1/2O_2 \qquad [4.5]$$

4.1.4: Carbonate alteration

Carbonate alteration is widespread at the Kalahari Goldridge deposit and is marked by the replacement of magnetite layers, chlorite and quartz. The carbonate alteration pattern at the Kalahari Goldridge deposit is influenced by the lithological variation in the deposit with distribution of the carbonates showing a strong association with the Fe content in the host rock. Siderite, ankerite-dolomite, and calcite are the major carbonate alteration minerals identified in the deposit. Calcite and siderite have not been identified together, but individually both co-exist with ankerite.

Calcite alteration is restricted to the footwall and to a lesser extent in the hanging-wall and can be attributed to the breakdown of epidote and plagioclase, which is common in less altered mafic schist. Siderite alteration on the other hand is limited to the BIF from replacement of magnetite and pyrite. Carbonatization by ankerite forms the main mineralogical change in the schist in the orebody by the replacement of chlorite as the major metasomatic change. Ankeritization also occurs by replacement of quartz in chert bands and veins. The modal abundance of ankerite and siderite in the orebody shows a close association with increasing intensity of alteration as demonstrated qualitatively by X-ray powder diffraction reflecting a greater fluid access. This is illustrated in Figure 4.2A and B showing the peak intensities of the carbonates in the X-ray pattern of two samples 13175/2A (least altered) and 13175/2B (altered) from adjacent bands (Fig. 4.2C).

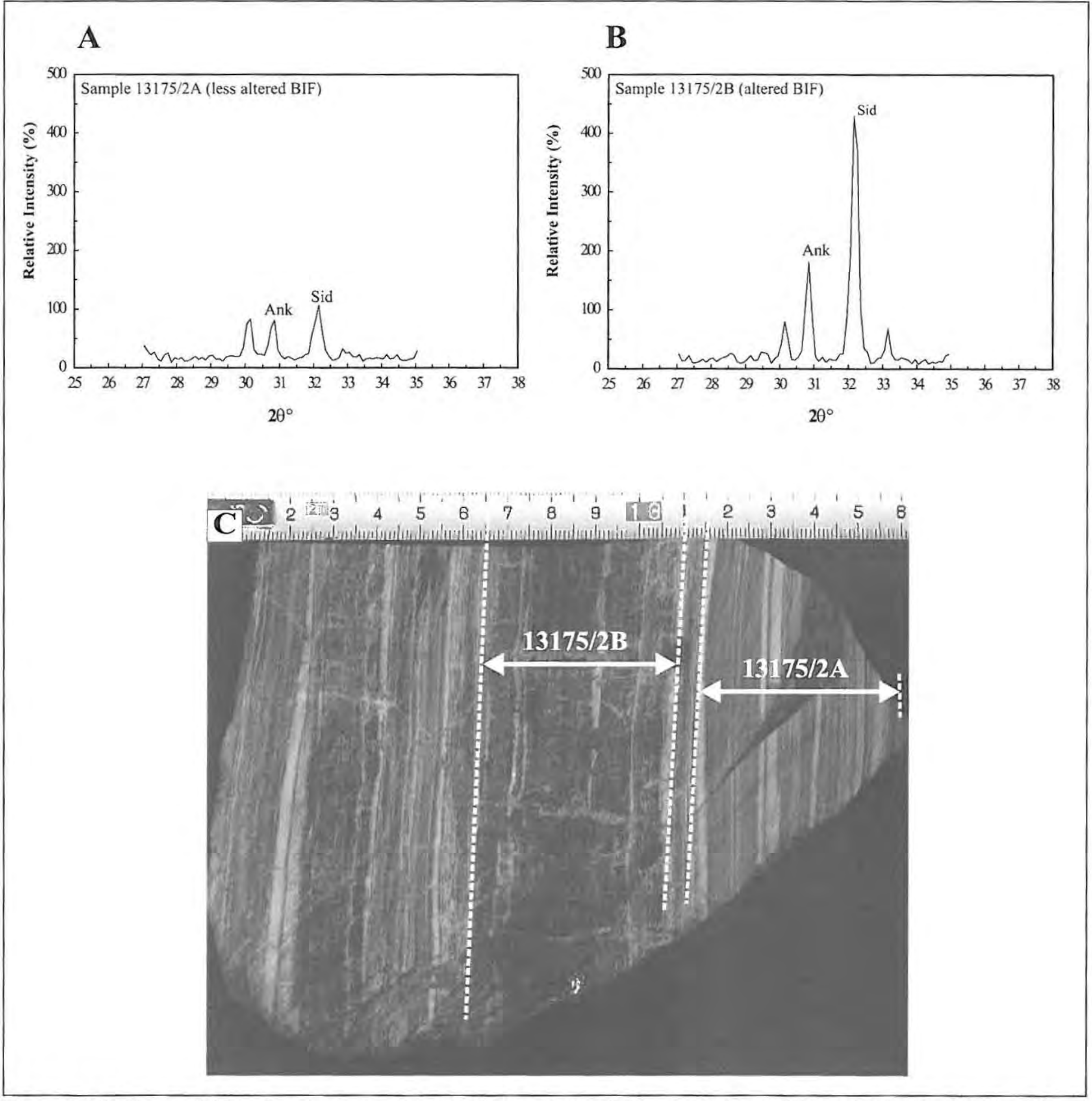

Figure 4.2. X-ray diffraction patterns (**A** and **B**) showing relative peak intensities of ankerite (ank) and siderite (sid) in adjacent mesobands in sample 13175/2 shown in **(C)**. **A**, (13175/2A, less altered) and **B** (13175/2B, altered). The intensity of the peaks demonstrates the degree of carbonation associated with ladder veining in the mesobands.

Textural relationships between carbonate and other alteration minerals typically, chlorite, pyrite and pyrrhotite indicate at least two generations of carbonate occurs at the Kalahari Goldridge deposit. The spatial relationship between these minerals (pyrite, pyrrhotite and chlorite) and magnetite suggest that they formed as products of interaction of ore fluid with magnetite in the altered BIF samples. However, significant replacements of these latter minerals by carbonates also occur in some samples. This observation might therefore indicate that, despite similarities in vein mineral compositions during the two gold mineralization episodes, the textural relationship indicates significant overprints of a later fluid evolution, possibly associated with the second episode of mineralization.

At the Kalahari Goldridge deposit, the high abundance of carbonate alteration assemblages is generally a reflection of high activity of CO_2 equilibrating with the host rock and is similar to many gold deposits in Archaean settings described in literature (e.g., Phillips and Groves, 1984; Phillips and Brown, 1987; Kishida and Kerrick, 1987; Bohlke, 1989).

4.1.5: Chloritization

Apart from the schist units which host a significant proportion of the chlorite in the Kalahari Goldridge deposit, chlorite alteration is commonly associated with the altered BIF. Chlorite is generally rare in the least altered BIF samples, which is consistent with the general lack of Al-bearing silicates in most iron-formations worldwide. This also suggests chloritization in the BIF was attributed predominantly to hydrothermal alteration. Iron and silica are documented (Klein 1983), to be the most dominant components in BIFs with average Al contents being generally less than 1 wt %, hence chlorite and other Al-bearing in low-being generally less than 1 wt %, hence chlorite and other Al-bearing in low-grade metamorphic iron-formation are thus rare. Therefore, significant chloritization associated with the altered BIF units at Kalahari Goldridge deposit can be associated with in situ enrichment of Al in detrital components (e.g. aluminous clay minerals) resulting leaching of silica in the BIF during alteration. Evidence for the leaching of silica is demonstrated by the mass-balance calculation (see section 4.3 on Bulk Rock Geochemistry), which shows consistent depletion in all analyzed samples.

4.2 Bulk Rock Geochemistry

4.2.1: Background

Comparison of unaltered and altered equivalents of host rocks, based on relative chemical variations in major and trace elements provides a basis on which to decipher the chemical composition of the original fluid composition, due to subsequent gains and losses of elements during the hydrothermal process. In many gold deposits, the distribution and variation of the major and trace elements also serve to delineate the geochemical haloes around the deposit and subsequently to identify pathfinders for the mineralization. Furthermore, the variable mobility of the elements during hydrothermal alteration and regional metamorphism can be used to define the protoliths of the host lithologies, as well as the hydrothermal and metamorphic history. In particular, mobile elements provide information about the alteration process, whilst immobile elements retain the geochemical characteristics of the protolith. In any given suite of rocks representing the various stages of alteration, the mobile elements results in changes by real gain or loss in absolute abundance. The immobile elements, on the other hand, change by dilution during addition of new components, or by concentration through leaching of soluble components, such that simple inspection is not sufficient for deducing chemical changes.

Summaries on the mobility of elements during hydrothermal alteration, (e.g. Lesher et al. 1991; Niu and Lesher, et al. 1991) indicates that major elements including Si, Al, Fe, Mg, Mn, Ca and Na are hosted in rock-forming minerals that are dissolved or precipitated in reduced, saline hydrothermal fluids of low pH, and hence, are relatively mobile in such fluids. In low-grade metamorphic derived-fluids, however, these elements are less mobile due to the slightly acidic to near neutral pH and H_2O-CO_2-rich composition of these fluids. The rare elements (As, Se, Sb, Te, Bi and B), large ion lithophile elements (LILE: Ba, Cs, Rb, Sr, Tl, K and Li), volatiles (H_2O, CH_4, CO_2, H_2S) and precious metals (Au, Ag) are generally mobile in both hydrothermal and metamorphic fluids. They show enrichment in most lode gold deposits relative to their enclosing host rock. The low charge to radius ratios of the precious metals and the LILE enhance complex formation by these elements, and hence their ability to be transported readily in such fluids. The high field strength elements (HFSE: Th, Nb, Ta, Zr, Y, P, Al, Hf and Ga) and rare earth elements (REE: La-Lu) are insensitive to alteration. These elements are characterized by high charge to radius ratios and hence are not readily complexed for transport in hydrothermal fluids. The transition metals including Sc, Ti, V, Cr, Ni, Co, Cu, and Zn on the other hand, exhibit variable mobilities depending on the prevailing condition of the hydrothermal fluid. At low- to intermediate-grade metamorphic conditions, Cr, Sc, V, Ni, and Ti are relatively more mobile than Cu and Zn (Kerrich, 1983; Leitch and Lentz, 1994).

4.2.2: Sampling and description of samples

Sampling for the bulk rock analyses at the Kalahari Goldridge deposit were derived from 8 diamond-drill holes from the northern (GDP-452, GDP-529, GDP-527), central (GDP-525, GDP-531, GDP-587, GDP-588) and southern (DD-17) parts of the deposit as well as grab samples at cross-sections in the open-pit (13175/2A, 13175/2B and 13175/2C) in the D-zone orebody extending about 1km north-south. A total of 45 samples have been analyzed for major and trace elements. These samples represent the major lithological units found at the Kalahari Goldridge deposit namely footwall mafic schist, orebody schist, BIF and the hanging-wall sediments consisting of schist, phyllite and graywacke. All the analyzed samples have undergone variable degrees of alteration, which is generally reflected by the modal abundance of the dominant alteration minerals, associated with each lithology.

Samples from the footwall schist (DD17/8, DD17/17, 588/26, 527/12A, 525/25A) were taken close to the orebody primarily because drill intersection with the footwall was limited to within 5 meters of the ore body, except for borehole DD17 in the southern end of the orebody, which intersected deeper into the footwall. Most of these samples have undergone intense alteration. DD17/8 and DD17/17 represent samples from the same drill core but different stratigraphic depths and exhibit some differences in their degree of alteration. DD17/8 was sampled near the contact with the orebody. This sample is very altered and its mineralogy consists essentially carbonate, sericite, and quartz and trace amounts of chlorite. Sample DD17/17 occur about 20 meters into the footwall and contains significant chlorite, quartz, micas and relicts of plagioclase feldspar, which is characteristic of the primary (metamorphic) mineralogy.

Samples from the interbedded schist (588/7, 588/20A, 525/11B, 525/19, 452/19B, DD17/7) represent pelitic sediments interbedded with the BIF in the orebody. Mineralogically, these samples consist of chlorite and quartz with variable amounts of sulphides (pyrite and pyrrhotite), stilpnomelane, muscovite, carbonate and magnetite. The modal proportions of chlorite, stilpnomelane, carbonate and sulphide in these samples vary, and depend on the degree of interaction of the rock with the ore fluid.

Sixteen BIF samples from the orebody were analyzed for major and trace element composition. Six of these consist of least altered samples separated from slabs showing very little effect of alteration resulting from selective veining of quartz-carbonate ladder sets in adjacent bands (e.g., Figs 2.8A and 4.2C). These samples are described further in a later section (subsection 4.2.7). The altered samples show variable degree of alteration

Selected samples from the hanging wall consist of two graywackes (452/1B and 525/1), three schist (588/Q2, 527/X-1 and 527/4), and four shale samples (DD-17/X1, 527/1, 525/10 and 452/3A). The hanging-wall sediments, particularly the schist and the phyllites are flooded with chert clasts. Therefore careful selection was done to avoid such samples as much as possible.

4.2.3: Analytical methods

X-ray fluorescence (XRF) of ten major oxides (SiO_2, Al_2O_3, Fe as Fe_2O_3, MgO, MnO, CaO, TiO_2, Na_2O, K_2O and P_2O_5) and volatiles as loss on ignition (LOI), and trace elements Zn, Cu, Ni, Co, Cr, V, Ba, Sr, Rb, Sc, Ce, Nd, Nb, Zr, Y and La were analyzed on the representative samples using lithium tetraborate fusion disks and powdered pellets at the Department of Geology, Rhodes University.

The LOI includes sulphur, CO_2, H_2O and all volatile constituents. The analytical measurement is according to the procedure of Norrish and Hutton (1969). Inductively coupled plasma-mass spectrometry (ICP-MS) of the above-stated trace elements and additional elements (Au, Ag, Bi, As, W, Sb and Te) was also analyzed on the representative BIF samples at the Department of Geological Sciences, University of Cape Town. Detailed descriptions of the analytical procedures for the XRF and ICP-MS are given in Appendix IIA and IIB respectively. The bulk compositional data of analyzed samples are given in Tables 4.1 to 4.4.

Table 4.1. Chemical analyses of hanging-wall sediments at the Kalahari Goldridge deposit.

	Graywacke		Schist			Phyllite			
Sample No.	452/1B	525/1	588/Q2	527/X-1	525/4	DD17/X-1	527/1	525/10	452/3A
Wt (%)									
SiO_2	70.56	70.36	59.32	58.42	45.44	64.15	64.37	62.43	63.24
TiO_2	0.19	0.22	0.52	0.56	0.78	0.54	0.57	0.56	0.65
Al_2O_3	15.27	12.01	13.21	8.12	11.63	14.37	13.56	13.63	15.06
$Fe_2O_{3\ total}$	1.99	3.75	10.57	11.56	22.84	6	6.78	9.26	8.29
MnO	0.05	0.08	0.15	0.21	0.41	0.09	0.09	0.08	0.12
MgO	0.76	1.39	3.56	6.15	3.5	3.01	3.84	3.93	2.49
CaO	2.01	2.75	3.63	4.67	4.31	1.82	1.8	1.61	1.42
Na_2O	4.32	2.23	0.73	0.1	0.08	1.66	0.28	0.06	2.36
K_2O	2.31	2.24	1.69	0.54	1.21	3.09	3.1	2.65	2.04
P_2O_5	0.03	0.04	0.11	0.07	0.1	0.06	0.08	0.11	0.06
H_2O-	0.3	0.12	0.21	0.13	0.24	0.1	0.13	0.25	0.45
LOI	2.82	4.34	5.52	8.74	8.27	5.02	5.2	5.23	4.49
Total	100.59	99.51	99.21	99.27	98.81	99.91	99.81	99.79	100.67
ppm									
Zn	27	100	126	130	130	120	175	145	94
Cu	16	39	84	125	194	45	59	43	67
Ni	18	43	157	127	170	135	187	160	129
Co	5	13	32	35	42	19	27	29	25
Cr	60	106	345	271	482	355	466	300	346
V	30	53	138	186	279	136	144	133	170
Sc	<5	7	17	25	35	19	20	19	23
Ba	575	459	306	140	251	292	399	427	448
Sr	498	262	94	124	145	138	82	84	229
Rb	63	62	65	22	38	114	115	99	68
Ce	25	24	20	10	21	11	15	30	17
Nd	5	11	10	<5	12	7	9	14	12
La	12	12	12	<5	6	6	8	14	8
Nb	<5	<5	5	<5	5	6	8	<5	5
Zr	72	57	82	32	63	82	78	110	102
Y	5	6	17	13	23	19	21	13	13

Both major and trace elements were analyzed by XRF analytical technique.

Table 4.2. Chemical analyses of interbedded schist at the Kalahari Goldridge deposit.

	Interbedded schist					
Sample No.	527/11	452/19B	588/20A	525/11B	525/19A	DD/17-7
Wt %						
SiO_2	48.70	46.42	39.28	42.57	60.71	67.80
TiO_2	0.43	0.14	0.20	0.47	0.28	0.34
Al_2O_3	7.07	2.18	7.53	6.70	4.97	6.82
Fe_2O_{3total}	25.75	19.53	30.90	31.49	23.22	16.56
MnO	0.26	0.30	0.87	0.61	0.21	0.08
MgO	3.12	2.75	3.92	3.48	2.03	2.41
CaO	3.46	12.63	4.07	2.77	2.94	1.05
Na_2O	0.06	0.01	0.04	0.04	0.02	0.00
K_2O	0.67	0.14	0.83	0.71	0.27	0.01
P_2O_5	0.14	0.13	0.14	0.12	0.09	0.08
H_2O	0.23	0.34	0.34	0.32	0.26	0.05
LOI	8.57	13.50	11.82	9.59	4.69	4.20
Total	98.46	98.06	99.93	98.86	98.06	99.39
ppm						
Zn	142	75	146	172	180	107
Cu	93	45	73	40	68	68
Ni	134	138	128	165	97	113
Co	24	18	15	22	16	58
Cr	249	566	136	547	178	231
V	146	59	81	161	84	360
Sc	18	11	22	33	13	13
Ba	120	51	147	412	68	3
Sr	69	111	98	49	32	15
Rb	37	8	24	32	18	<5
Ce	28	14	40	18	23	23
Nd	11	4	16	9	12	11
La	13	7	21	7	9	10
Nb	<5	<5	<5	<5	<5	5
Zr	53	11	68	33	41	66
Y	19	10	22	15	12	15

Table 4.3. Chemical analyses of BIF samples from the Kalahari Goldridge deposit

	Least altered samples					Altered samples										
	13175/2A-1	587/19-1	13175/2C-1	531/2B-1	527/4	531/2B-2	13175/2B	13175/2C-2	527/6D	452/9BC	452/10B	452/14	588-3B	588/9A	588/14A	588/25B
Wt % oxide																
SiO_2	72.68	62.72	76.90	83.28	55.58	24.82	32.00	32.04	46.95	41.96	34.14	43.84	71.33	34.89	62.20	53.53
TiO_2	0.02	0.02	0.02	0.02	0.02	0.22	0.03	0.06	0.02	0.18	0.05	0.05	0.05	0.04	0.04	0.02
Al_2O_3	0.08	0.00	0.07	0.00	1.03	1.90	0.37	0.67	0.25	2.23	1.03	0.70	0.68	0.35	0.36	0.07
$Fe_2O_{3\ total}$	20.02	33.64	21.56	13.33	38.25	48.25	45.44	46.96	35.57	37.40	40.25	33.52	19.60	50.30	25.45	26.78
MnO	0.35	0.30	0.14	0.20	0.04	0.96	0.96	1.07	0.70	0.41	0.68	0.52	0.25	0.74	0.45	0.64
MgO	0.90	0.77	0.45	0.53	1.16	4.18	2.94	3.36	2.30	3.61	3.70	3.41	1.85	3.00	2.55	2.56
CaO	1.62	0.65	0.23	0.50	0.84	3.96	3.16	4.10	2.48	3.27	3.27	3.27	2.22	1.09	0.73	5.62
Na_2O	0.02	0.00	0.00	0.00	0.03	0.10	0.05	0.12	0.04	0.02	0.02	0.11	0.18	0.02	0.01	0.01
K_2O	0.05	0.00	0.01	0.01	0.06	0.54	0.10	0.29	0.07	0.04	0.06	0.17	0.25	0.02	0.01	0.00
P_2O_5	0.31	0.09	0.07	0.04	0.07	0.61	0.22	0.29	0.09	0.18	0.11	0.11	0.27	0.24	0.09	0.10
LOI	4.16	1.16	0.86	2.19	3.73	11.96	12.59	10.95	11.06	11.00	15.82	13.90	4.17	9.29	8.69	8.71
H_2O-	0.10	0.10	0.15	0.20	0.06	0.34	0.08	0.11	0.27	0.43	0.29	0.35	0.28	0.41	0.30	0.34
Total	100.29	99.46	100.44	100.29	100.88	97.83	97.93	100.02	99.79	100.73	99.42	99.95	101.12	100.39	100.86	98.38
ppm																
Zn	25.8	36.66	15.21	46.27	47.5	188.47	32.0	38.82	115	79.2	72.4	70.3	17.3	80.9	73.2	310
Cu	28.5	3.33	3.65	5.14	71.5	5.50	71.4	2.05	104	26.4	18.0	25.3	8.66	10.0	5.64	15.1
Ni	5.79	12.98	5.50	9.51	7.90	27.68	7.93	6.10	13.4	31.6	6.18	18.1	17.9	15.6	7.71	12.3
Co	1.69	3.09	0.84	1.31	2.46	4.48	6.52	1.22	4.86	9.40	0.89	3.40	3.18	7.04	3.22	6.36
Cr	11.6	14.09	14.82	12.01	9.97	38.88	10.5	25.58	22.3	83.0	11.0	21.8	22.8	14.7	25.8	9.94
V	4.25	5.67	4.89	4.24	4.81	28.18	5.30	7.21	33.8	37.9	13.9	14.9	15.7	8.30	10.6	6.67
Sc	0.13	0.19	*lld*	*lld*	0.19	5.79	0.68	1.12	2.55	3.94	0.33	1.16	1.99	0.68	1.84	5.53
Ba	13.3	1.14	5.06	6.76	9.89	168.81	30.5	38.22	36.2	29.1	26.3	71.5	107	8.50	10.8	42.5
Sr	17.9	6.95	2.93	5.26	16.9	54.68	33.9	47.37	51.8	65.8	36.5	50.8	35.6	12.1	9.31	0.54
Rb	1.68	0.10	0.64	0.97	2.45	40.42	4.86	6.90	3.76	2.73	4.32	9.68	14.8	1.74	1.12	1.11
Ce	7.90	6.98	2.45	1.65	5.58	15.92	9.96	11.25	7.31	8.49	9.58	12.3	7.01	9.01	6.92	5.48
Nd	4.71	3.77	1.45	0.85	2.80	11.16	5.76	6.46	3.73	4.66	4.33	6.45	3.90	4.58	3.83	3.30
La	4.16	3.35	1.18	0.95	2.66	7.89	5.11	5.48	3.77	4.11	5.27	6.38	4.35	4.66	3.36	2.56
Nb	0.10	0.15	0.11	0.06	0.16	0.76	0.07	0.11	0.22	0.90	0.18	0.20	0.23	0.29	0.22	0.24
Zr	1.27	0.92	0.43	0.62	1.08	10.14	3.38	3.68	5.19	13.9	1.71	4.00	3.89	3.89	2.97	4.62
Y	8.39	5.57	1.63	1.20	2.84	13.02	7.04	7.31	4.75	6.41	3.83	5.31	8.53	5.77	3.26	6.43
Ag	0.026	0.01	0.03	0.02	0.11	0.13	0.34	0.08	0.43	0.23	0.53	0.64	0.057	0.35	0.048	0.12
Sb	0.22	0.38	0.21	0.19	0.64	0.19	0.37	0.16	0.18	0.23	0.32	0.36	0.34	0.51	0.25	1.50
As	1.33	0.49	0.53	0.73	2.47	4.22	4.05	0.40	0.43	5.47	6.36	3.19	0.65	3.20	0.60	1.12
W	0.57	0.81	1.26	0.69	1.35	1.09	0.45	0.35	0.38	1.78	0.36	1.01	0.86	0.62	0.71	1.24
Bi	1.88	*lld*	*lld*	0.14	10.1	*lld*	4.75	*0.00*	7.75	1.72	10.0	36.5	2.18	10.8	6.78	3.93
Te	0.021	*lld*	*lld*	*lld*	0.60	*lld*	0.15	*0.00*	0.38	0.12	0.21	2.80	0.016	0.70	0.66	0.12
Au	0.014	0.01	0.06	0.04	*lld*	0.18	0.57	0.26	*lld*	*lld*	0.041	0.14	0.013	0.076	0.037	0.23

lld = below detection limit Major elements analysed by X-ray flourescence and trace elements by ICP-MS technique.
Lower limit of detection for ICP-MS is based on 3 standard deviations of background
LOI = Loss on ignition

Table 4.4. Chemical analyses of footwall mafic schist at the Kalahari Goldridge deposit.

	Footwall mafic schist					
	DD17/8	DD17/16	588/26	525/25A	527/12A	452/28A
Wt %						
SiO_2	45.55	45.87	50.56	53.77	48.43	44.48
TiO_2	0.35	1.66	1.23	1.33	1.15	1.32
Al_2O_3	10.85	14.07	16.41	14.13	15.39	17.56
Fe_2O_{3total}	10.23	14.95	12.24	13.15	8.93	14.3
MnO	0.13	0.17	0.28	0.24	0.13	0.16
MgO	11.85	6.77	2.12	1.91	4.15	3.46
CaO	8.55	6.87	5.39	5.4	8.3	6.82
Na_2O	0	1.46	2.66	1.64	0.91	0.08
K_2O	0.01	0.02	0.61	0.4	2.39	3.06
P_2O_5	0.04	0.2	0.13	0.12	0.12	0.14
H_2O	0.23	0.23	0.37	0.16	0.1	0.16
LOI	11.63	6.45	7.21	5.89	9.29	9.3
Total	99.41	98.72	99.21	98.13	99.27	100.84
ppm						
Zn	112	165	90	107	99	116
Cu	64	104	151	101	135	10
Ni	339	150	68	47	167	114
Co	53	15	24	17	103	41
Cr	809	213	165	61	156	187
V	199	101	404	443	387	437
Sc	39	43	44	49	46	51
Ba	<5	11	52	25	257	229
Sr	50	75	101	108	88	59
Rb	<5	<5	20	15	72	68
Ce	<5	16	8	10	7	8
Nd	<5	10	5	8	5	<5
La	<5	<5	<5	<5	<5	<5
Nb	<5	<5	<5	<5	<5	<5
Zr	17	80	54	74	68	71
Y	9	34	24	30	22	25

4.2.4: Inter-element correlations

The correlation coefficients for some of the elements pairs in the various lithologies are given in Table 4.5. A negative correlation between Fe_2O_3 and SiO_2 (Fig. 4.3A) is consistent with the general observation in iron-formation as a consequence of their bimodal composition such that any variation in one major component (e.g. SiO_2) is reflected in the other major components, otherwise known as the closure effect. Similarly, an antithetic relationship between SiO_2 and MnO (Fig. 4.3B) is indicative of closure effect between carbonate and quartz

Table 4.5. Correlation coefficient for selected elements pairs in rock units at the Kalahari Goldridge deposit

		Orebody	Footwall
Element pair	BIF	Interbedded schist	Mafic schist
Y-P_2O_5	0.52	0.46	0.92
MgO-LOI	0.91	0.66	0.68
Fe_2O_3-SiO_2	-0.93	0.78	0.1
MnO-SiO_2	-0.85	0.84	0.73
TiO_2-V	0.67	0.98	0.99
Cr-V	0.77	0.15	0.54
MgO-CaO	0.49	0.11	0.75
MnO-Fe_2O_3	0.71	0.86	0.34
Sr-CaO	0.85	0.79	0.70
Au-Ag	0.30		
Au-Sb	0.27		
Au-As	0.36		
Au-W	0.27		
Au-Bi	0.34		
Au-Te	0.18		
K-Rb	0.94		
K-Ba	0.92		
Rb-Ba	0.96		
Rb-Sr	0.55		
Co-Ni	0.82		
Al_2O_3-Zr	0.83		
TiO_2-Al_2O_3	0.88		
Ce-La	0.99		
Ce-Nd	0.96		
TiO_2-Zr	0.87		

in the BIF. A strong positive correlation is displayed between LOI and MgO (r = 0.91, Fig. 4.3C) in rocks in the orebody (BIF and schist) and this is indicative of significant proportions of CO_2 in the volatile phase resulting from carbonate alteration.

Figure 4.3D illustrates the scatter plot between P_2O_5 and Y in all the various sample groups. A strong positive correlation between P_2O_5 and Y in the BIF provides evidence for the environment of formation as deep-sea sediments shown by the line representing the trend for deep-sea sedimentation (Marchig et al. 1982). These authors showed that phosphorous in the deep-sea is hosted in detrital apatite with enrichments in Sc, Y and rare earth elements, providing a typical positive correlation between P and Y, Sc or La in the deep-sea sediments. In contrast, metalliferous sediments or exhalates do not have correspondingly high Y values because of the mobilization of P by hydrothermal leaching and coprecipitation with iron-hydroxide excluding Sc, Y and La.

Figure 4.4A-D illustrates overall positive correlations between the following pairs in all the lithologies: V- TiO_2 (r = 0.98), V-Cr (r = 0.78), MgO-CaO (r = 0.52) and MnO-Fe_2O_3 (r = 0.82). The correlation between MgO and CaO (Fig. 4.4A) is attributed to Ca-Mg substitution during carbonate crystallization. Variable degrees of alteration and mobilities of the two elements in each lithology possibly account for the dispersion of the data. In Figure 4.4B, a strong positive correlation between Fe_2O_3-total and MnO in the ore body lithologies (schist, r = 0.85; BIF, r = 0.71) possibly reflects formation of Fe-rich carbonates (ankerite and siderite) in these lithologies.

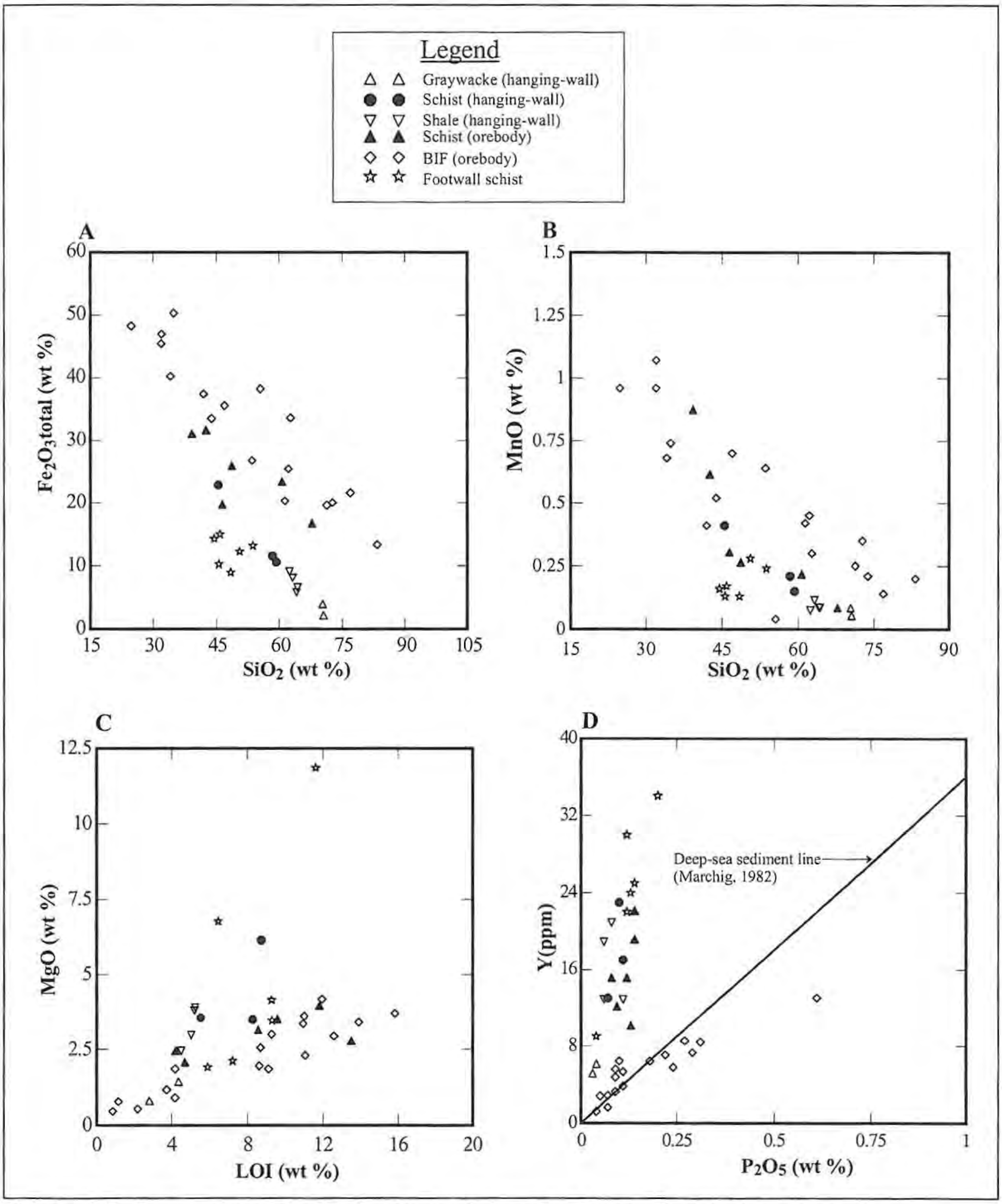

Figure 4.3. Elemental variation in lithologies at the Kalahari Goldridge deposit. A. SiO_2 versus Fe_2O_3total . B. SiO_2 versus MnO, C. LOI versus MgO and D. P_2O_5 versus Y

V-TiO_2 and V-Cr plots (Fig. 4.4C and 4.4D respectively), display an overall coherent correlation. Excluding one sample point, V and TiO_2 display very strong positive correlation in both the interbedded schist (r =0.98) and footwall mafic schist (r =0.99).

Several element pairs, including Sr-CaO, K_2O-Ba, K_2O-Rb, Ni-Co, and Ba-Rb exhibit significant positive correlations in the BIF (Figs. 4.5A-D). These elemental pairs exhibit similar geochemical properties and significant mobilities in hydrothermal fluids. In general, the plots display significant increases in these elements in the altered units in comparison with the least altered units, which is consistent with the mobility of the elements during hydrothermal alteration. High positive correlation exists in K_2O-Ba (r = 0.92), Rb-Ba (r = 0.96) and K_2O-Rb (r = 0.94) variations in the mineralized BIF (Figs. 4.5A-C). These elements are hosted by K-bearing minerals (e.g., biotite, muscovite) and makes significant substitution among each other due to their similar ionic radii (Ba, 1.34Å; Rb, 1.45 Å and K, 1.33Å). At the Kalahari Goldridge deposit, stilpnomelane and muscovite constitute the main K-bearing mineral in the deposit. Therefore significant increases of these minerals in the altered units suggest that they were derived from the hydrothermal fluid. Variations between Rb and Sr (Fig. 4.5E) show much scattering, which indicates limited co-enrichment or depletion between the two elements.

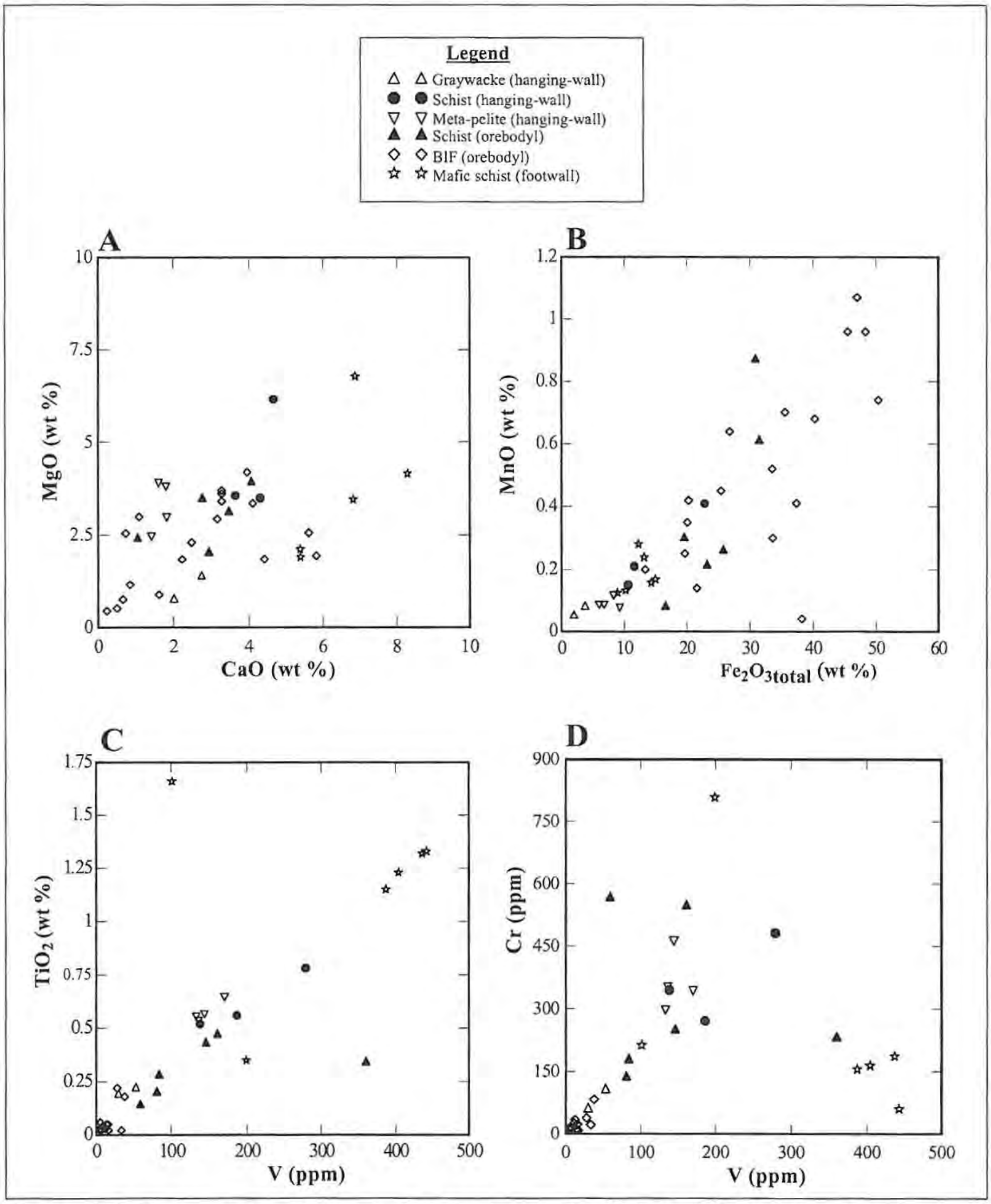

Figure 4.4. Elemental variation in lithologies at the Kalahari Goldridge deposit. A. CaO versus MgO, B. Fe_2O_3total versus MnO, C. V versus TiO_2 and D. V versus Cr.

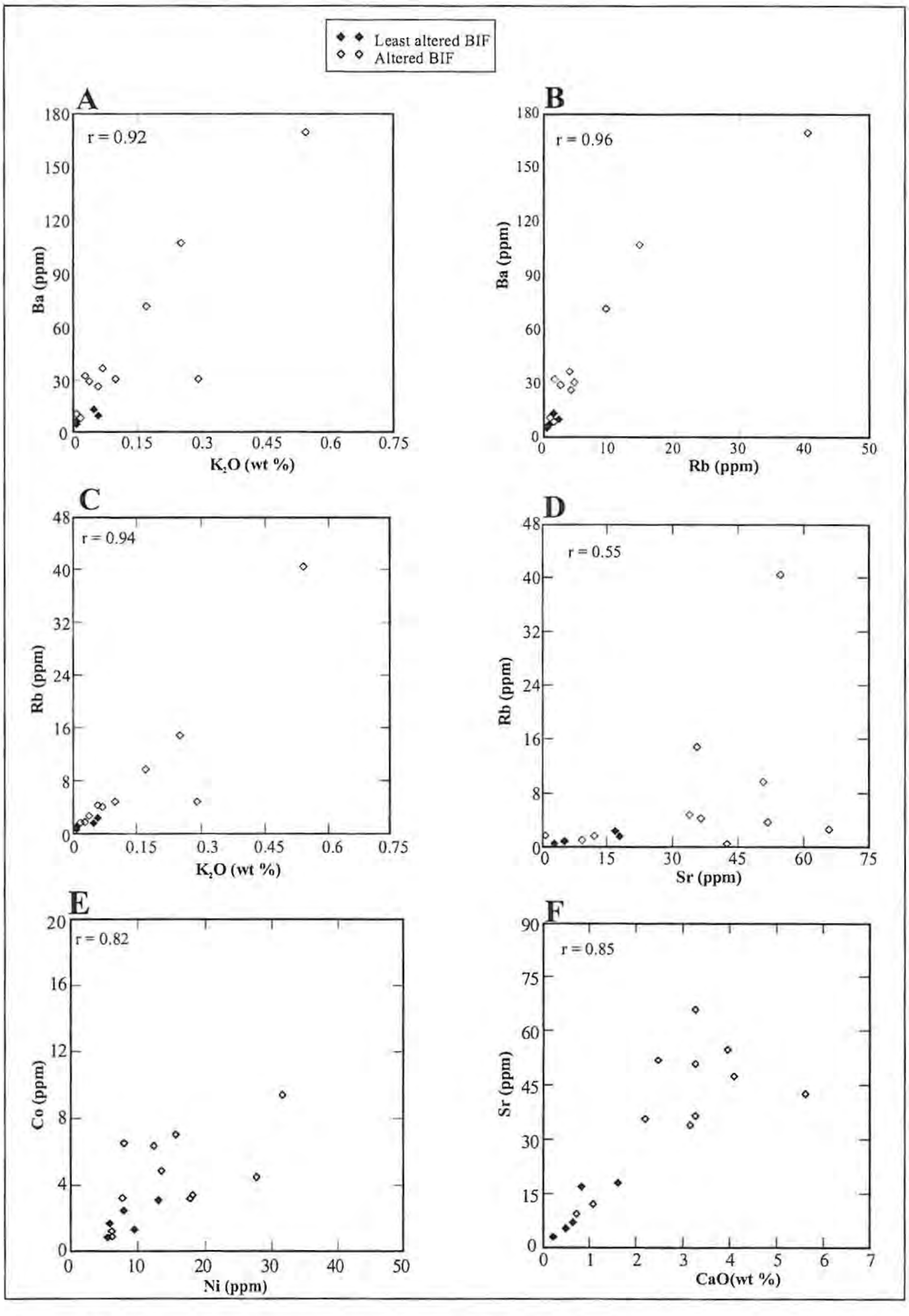

Figure 4.5. Elemental variation in orebody (BIF) at the Kalahari Goldridge deposit. A. K_2O versus Ba. B. CaO versus Sr. C. Ni versus Co. D. Rb versus Ba. E. K_2O versus Rb,and F. Sr versus Rb.

Figure 4.5F illustrates a well defined positive correlation between Sr and CaO, which is indicative of crystallographic substitution of Sr (ionic radius 1.18Å) for Ca (ionic radius 1.01Å) in the carbonates. The two elements show enrichments and some degree dispersion in the more altered samples. The enrichment is consistent with increased carbonation in the more altered BIF samples whereas the dispersion can be attributed to variable mobility of the two elements during alteration.

Co and Ni exhibit a significant positive correlation ($r = 0.74$). The two elements also exhibit higher abundances in the samples showing higher degrees of alteration (Fig. 4.5E), and may be attributed to partitioning of these elements into the sulphides associated with the altered magnetite mesobands, resulting from substitution for Fe in the sulphides.

The scatter plots between Au and other rare elements (As, Bi, W, Te, Ag and Sb) shown in Figures 4.6A-F are erratic and indicate no apparent correlations. The lack of correlation between Au and these elements is quite uncertain. However, Au shows an overall co-enrichment in Bi, Te and Ag (see next section). As pointed out by Eilu et al. (1997), these elements exhibit variable geochemical dispersion in different environments or deposits. In other words, an element useful as a pathfinder in one deposit may not be useful in another deposit. Such variations, they concluded, reflect the nature of the fluids, solute sources and/or fluid-rock exchange during subsequent transport from source region to depositional site.

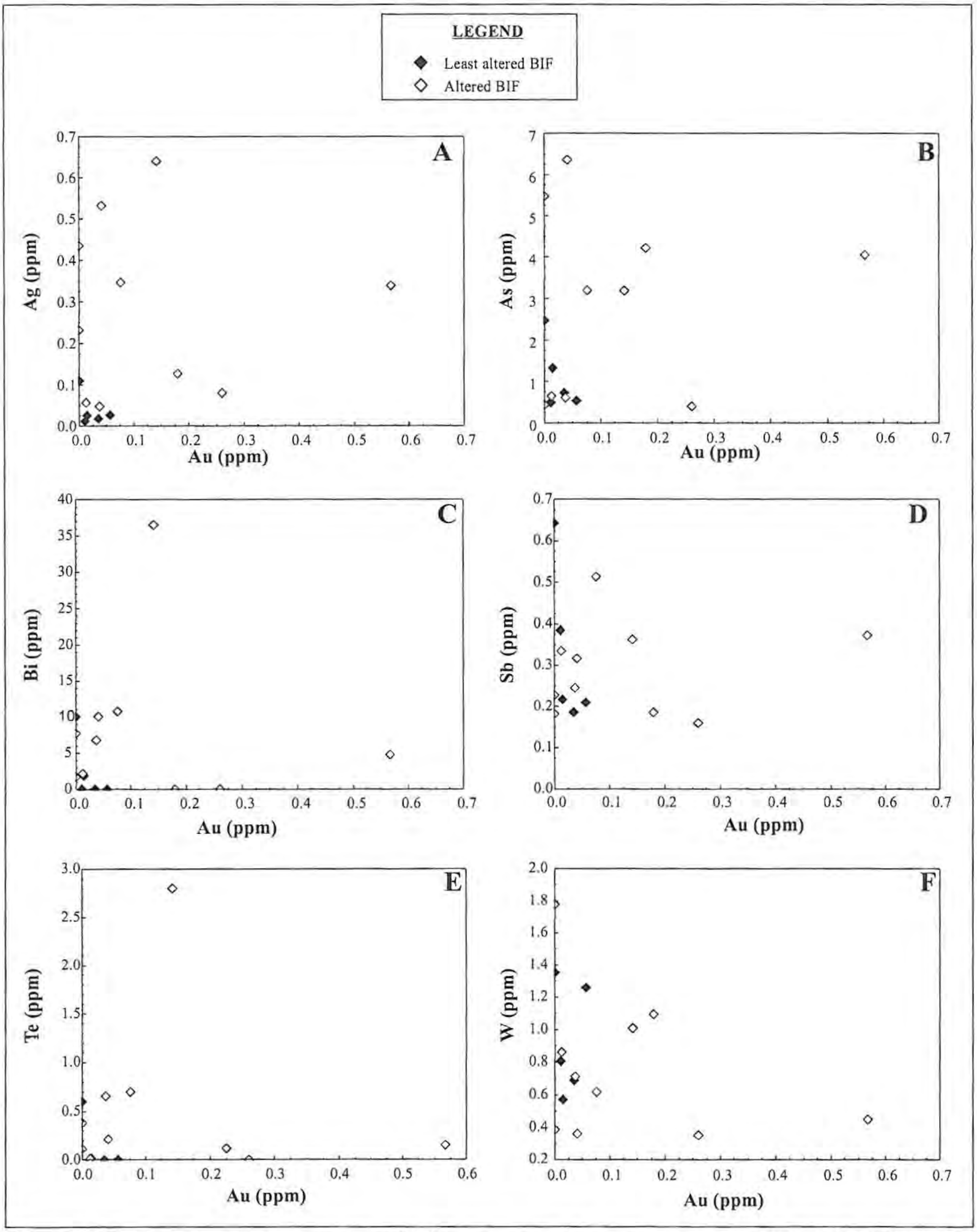

Figure 4.6. Variation between gold (Au) and other rare elements in BIF at the Kalahari Goldridge deposit. A. Au versus Ag, B. Au versus As, C. Au versus Bi, D. Au versus Sb, E. Au versus Te and F. Au versus W

4.2.5: Chemical comparison of Kalahari Goldridge BIF with other iron-formations

The comparisons between BIFs have always been wrought with several problems based on the fact that banded iron-formations are very inhomogeneous, resulting from various scales of banding and the diversity of assemblages that can occur with fairly similar bulk compositions (Klein, 1983). On this basis, only general comparisons can be made.

At the Kalahari Goldridge deposit, a comparison of the less altered BIF samples with major element compositions of other worldwide BIFs, summarized in Klein (1983), indicates relatively high SiO_2 contents against a common range up to 68 wt % in most worldwide BIFs. In some isolated cases, higher SiO_2 ranging up to 88 wt % has been documented in some BIFs (e.g. 16.1 to 87.2 wt %, Klein, 1978; 26.6-86.5 wt %, Lesher, 1978; 6-88 wt %, Dymek and Klein, 1988; 30.51- 90.43 wt %, Manikyaba et al., 1993). The high variability in SiO_2 in these samples reflect variation in chert- or quartz-rich banding associated with the BIF. On the basis of Fe as Fe_2O_3-total and SiO_2 as major constituents, Manikyaba et al., (1993) classified as ferruginous cherts, samples containing < 15 wt % Fe_2O_3-total and the rest SiO_2, and cherty BIF for samples containing > 15 wt % Fe_2O_3-total and the remainder silica. On this basis, the BIF at Kalahari Goldridge with an average Fe_2O_3-total 25.36 ± 10.28 wt % and 70.23 ± 11.09 wt % for SiO_2 may be classified as cherty BIF. It should however be noted that, despite the restricted range in composition of the less altered BIF samples, due to the limited data points, the range may not represent the complete spectrum of compositions that are likely to occur in the area.

In an attempt to classify the environment of depositions for the BIF hosting the gold at Kalahari Goldridge deposit, the average concentration of the transition elements metals in the Kalahari Goldridge samples are compared to average Algoma- and Superior-type BIF (Fig 4.7) based on the data of Gross and McLeod, (1980), which are summarized in Table 4.6. The Kalahari Goldridge plot shows a close resemblance in shape with that of Algoma-type BIF indicating that the BIFs at Kalahari Goldridge were deposited in a similar environment to Algoma-type BIF. The subparallel relationship between the Kalahari Goldridge transition elements with the Algoma type also suggests uniform dilution of the Kalahari Goldridge BIF samples. This could be attributed to silica dilution by cherty bands given their high concentration in the Kalahari Goldridge BIF.

Table 4.6. Average transition metal data from the Algoma- and Superior-type BIFs (Gross and McLeod, 1980) and Kalahari Goldridge (this study).

	Algoma	Superior	Kalahari Goldridge (this study)
Sc	8	18	0.2
V	109	42	4.8
Cr	118	112	12.5
Co	41	28	1.9
Ni	103	37	8.3
Cu	149	14	22.4
Zn	330	40	34.3

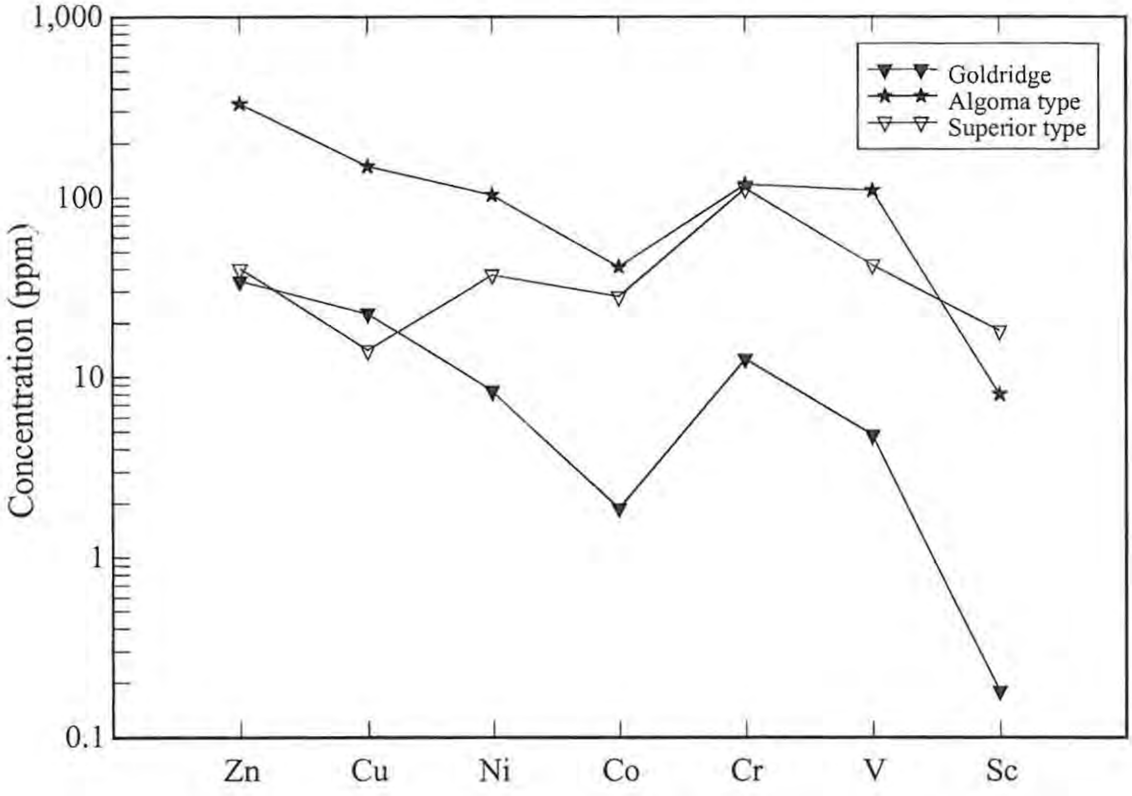

Figure 4.7. Comparison of average transition element concentrations of less altered Kalahari Goldridge BIFs and those in Canadian Algoma- and Superior-type BIFs. Data for Algoma and Superior types are from Gross and McLeod (1980). The Kalahari Goldridge BIFs show general depletion in transition metals but exhibit a similar pattern with the Algoma-type indicating a similar environment of deposition.

4.2.6: Mass balance analysis of alteration

4.3.6.1: Method of calculation

The method of Grant (1986) was used for mass balance calculations to determine chemical changes resulting from metasomatic reaction at the Kalahari Goldridge deposit. The Grant's isocon approach is a modification of the original by Gresens (1967) and is defined by the equation,

$$C_i^A = M^O/M^A\ [C_i^O + \Delta C_i] \qquad [4.5]$$

Where C_i^A and C_i^O represent the concentrations of the component i in the altered and original rocks respectively. M^O and M^A represent the masses of rock contained in an equal-sized rock volume before and after alteration respectively and ΔC_i is the change in mass of the component i during alteration relative to the initial mass of the system.

Grant (1986) deduced that $\Delta C_i = 0$ for an immobile element. Therefore identification of immobile elements reduces equation [4.5] to $C_i^A = M^O/M^A\ [C_i^O]$ and plots on a straight line through the origin where C_i^A and C_i^O represent the x and y coordinates respectively, and the slope M^O/M^A is equivalent to the ratio of equivalent masses of immobile components in the original and altered samples. When the slope of the isocon is determined, the mass change ΔC_i for each component can be calculated by the rearrangement of equation [4.5] as,

$$\Delta C_i = M^A/M^O C_i^A - C_i^O \qquad [4.6]$$

A positive mass change indicates addition of that component and a negative mass change indicates a depletion of that component.

As the application of mass balance calculations in alteration assemblages requires the knowledge of the chemical and mineralogical composition of both primary host rock and its altered equivalent, a great drawback was presented at Kalahari Goldridge due to the lack of totally unaltered samples for comparison with the altered equivalents. This is primarily due to the following reasons:

(i). an intense hydrothermal alteration affecting the entire host assemblages in the mine area, and

(ii). thick overburden of Kalahari sand and limited diamond drilling in the Kraaipan volcanic belt which hosts the Kalahari Goldridge deposit. However, attempts were made to separate least altered samples from certain BIF bands, defined by a lack of ladder quartz veining in these bands as shown for example, in Figs. 2.8A and 4.2C. These samples are characterized by fine and undeformed layering of magnetite and chert. Their petrography also shows conspicuous differences in mineralogy from the altered equivalents that show evidence of intense metasomatism. Furthermore, the volatile constituent (LOI) is consistent with the minimal occurrence of hydrous silicates, carbonates and sulphides compared to the altered equivalents.

In this study, sixteen selected BIF samples consisting of five least altered were compared with eleven altered samples for the mass balance calculations. The average composition of the five least altered BIF samples was used to evaluate the net mass change of major and trace elements for each of the eleven altered BIF samples as described above. The immobile elements were determined based on the method of MacLean and Kranidiotis (1987) who proposed that binary plots of typical immobile elements (Ti, Zr, Y, Nb, Al and REE) should yield linear arrays, with high correlation coefficients ($r = 0.90 - 0.99$) that pass through the origin and bulk composition. In this study, a series of binary plots of these immobile elements (Fig. 4.8A-F) identified Ce and La as the most immobile pair as their binary plot showed a high correlation coefficient ($r = 0.99$) and the linear regression through the bulk composition passes through the origin (Fig. 4.8A). La or Ce could therefore be used for the mass change calculations.

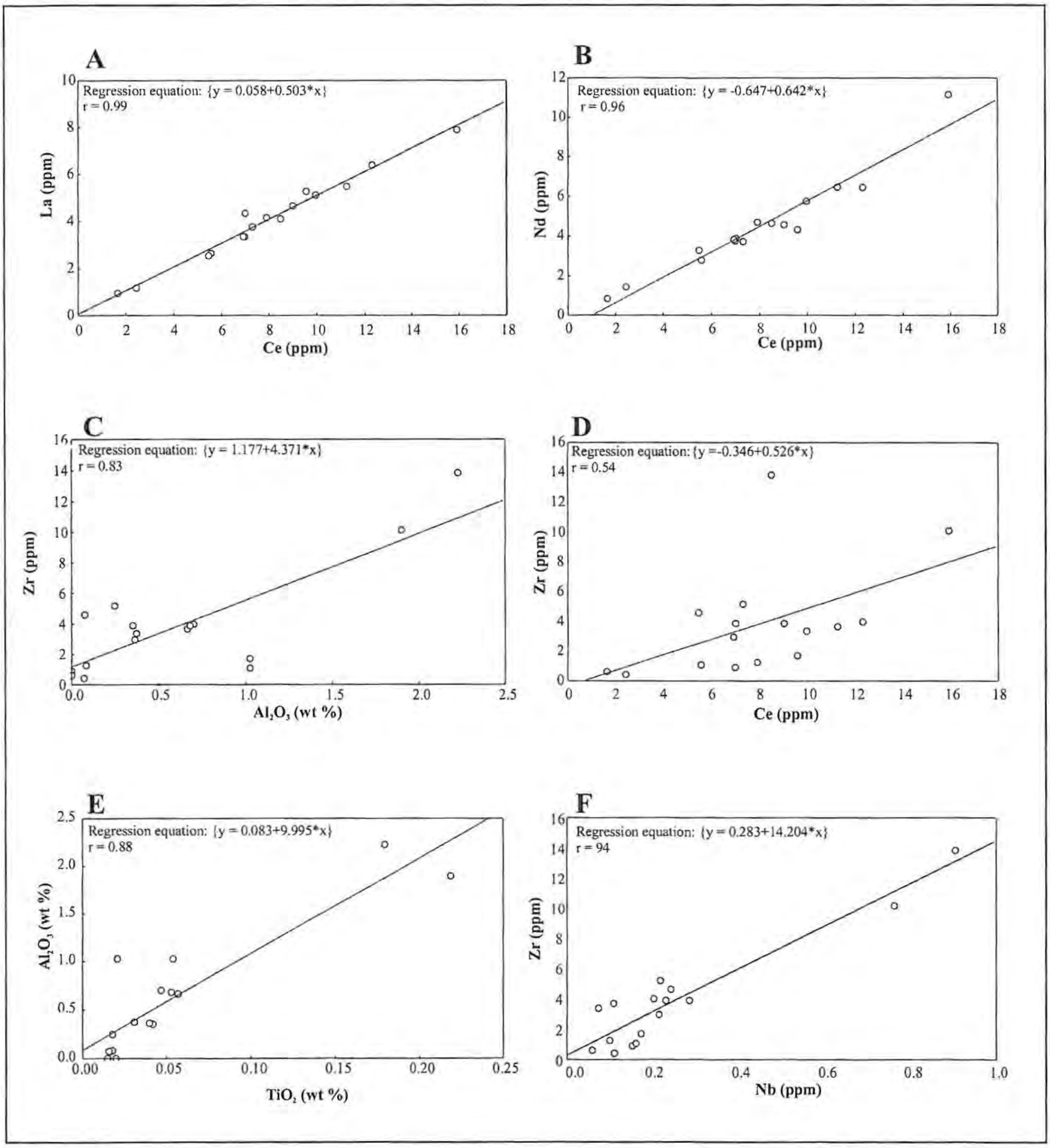

Figure 4.8. Binary plots of immobile elements in BIF at the Kalahari Goldridge deposit. A. Ce versus La, B. Ce versus Nd, C. Al_2O_3 versus Zr, D. Ce versus Zr, E. TiO2 versus Al_2O_3 and F. Nb versus Zr. Also shown are the linear regression lines through the bulk composition of the rock

4.3.7.2: Mass changes in altered BIF

Using the Grant (1986) approach in equation [4.5], the mass balance calculation was done assuming constant Ce. Therefore, the mass change is calculated such that $M^O/M^A = C^A_{Ce}/C^O_{Ce}$ for constant Ce is, $\Delta C_i = C^O_{Ce}/C^A_{Ce} C_i^A - C_i^O$. The elemental changes, calculated as gains (positive symbol) and losses (negative symbol) of each element in the individual altered BIF samples, initially expressed in g/100g (for major elements) and mg/100g (for trace elements) of unaltered rock, and converted to percentage mass change relative to the unaltered rock is presented in Table 4.7 and illustrated in Figure 4.9.

It is important to note that the calculated mass balance does not represent absolute changes as would be determined if the parent rock was homogeneous and chemically unaltered. The BIF samples may be heterogeneous due to the fact that each band may contain variable proportions of chert (quartz) and magnetite. Secondly, some of the altered BIF samples contain cm-scale ladder quartz veins, which could not be separated physically.

Inspection of percentage mass change for individual samples indicates that silica is consistently depleted in significant amounts whilst MgO and LOI experienced enrichment in all samples. The depletion of silica can be attributed to significant leaching by the hydrothermal fluid and deposition in open-space fractures in addition to quartz precipitated from the hydrothermal fluid. Evidence for the leaching of SiO_2 is provided by the significant replacement of quartz by carbonates in chert bands and recrystallized quartz in altered BIF. MnO, CaO, Na_2O, K_2O and H_2O experienced enrichment in most of the samples and on average showed enrichments of 74%, 122%, 203%, 143% and 38% respectively.

Table 4.7. Calculated mass change (%) in altered BIF using the equation of Grant (1986) assuming constant Ce.

	Least altered	Altered BIF												
Sample No.	Mean of 5 samples (Table 4.3)	531/2B-2	13175/2C-2	13175/2B	527/6D	452/9BC	452/10B	452/14	588-3B	588/9A	588/14A	588/25B	Mean	std
	Wt %													
SiO_2	70.23	-89	-80	-78	-55	-67	-75	-75	-29	-73	-37	-31	-63	21
TiO_2	0.02	276	38	-16	-33	457	53	4	106	26	58	-20	86	150
Al_2O_3	0.24	149	23	-22	-29	430	122	19	102	-19	10	-72	65	139
$Fe_2O_{3\ Total}$	25.36	-41	-19	-12	-6	-17	-19	-47	-46	7	-29	-5	-21	18
MnO	0.21	44	127	128	129	10	68	2	-14	93	54	178	74	62
MgO	0.76	70	93	89	103	166	148	79	70	113	138	203	116	43
CaO	0.77	59	133	101	116	138	117	70	102	-23	-33	558	122	156
Na_2O	0.01	206	391	121	125	13	8	334	1112	19	-45	-48	203	335
K_2O	0.03	535	386	86	80	-13	10	152	558	-61	-68	-93	143	240
P_2O_5	0.11	65	13	-7	-46	-12	-51	-61	64	15	-45	-22	-8	44
LOI	2.42	53	98	155	206	154	233	129	21	107	155	224	140	68
H_2O^-	0.12	-13	-61	-68	50	99	23	13	61	80	75	154	38	67
	ppm													
Zn	34.27	70	-51	-54	124	29	8	-18	-65	27	52	714	76	219
Cu	22.43	-92	-96	56	211	-34	-59	-55	-73	-76	-82	-40	-31	90
Ni	8.33	2	-68	-53	7	112	-62	-13	50	1	-34	33	-2	54
Co	1.88	-26	-72	70	74	181	-76	-28	19	103	22	205	43	94
Cr	12.49	-4	-11	-59	20	272	-55	-31	28	-36	47	-28	13	92
V	4.77	82	-34	-46	375	344	49	24	131	-6	57	26	91	142
Sc	0.10	1644	377	223	1566	2053	63	350	1260	259	1171	4754	1247	1349
Ba	7.24	620	131	106	235	125	85	294	933	-37	6	428	266	292
Sr	10.00	69	107	66	247	269	86	103	149	-35	-34	-95	85	112
Rb	1.17	971	159	104	116	31	89	232	787	-19	-32	-14	220	338
Ce	4.91	0	0	0	0	0	0	0	0	0	0	0	0	0
Nd	2.71	27	4	4	-8	-4	-19	-5	1	-9	0	9	0	12
La	2.46	-1	-3	2	3	-6	9	4	24	2	-3	-6	2	9
Nb	0.12	99	-59	-69	25	329	-24	-31	38	31	31	87	42	110
Zr	0.86	262	86	92	302	798	1	85	216	143	144	381	228	219
Y	3.92	2	-19	-12	-19	-8	-50	-46	52	-21	-41	48	-10	34
Ag	0.04	2	-9	332	659	238	607	566	3	388	-12	176	268	261
Sb	0.33	-83	-79	-44	-63	-61	-51	-56	-28	-15	-47	313	-19	112
As	1.11	17	-84	79	-74	176	192	15	-59	55	-61	-10	22	96
W	0.94	-64	-84	-77	-73	6	-80	-57	-36	-64	-46	19	-50	35
Bi	2.42	-100	-100	-4	115	-60	112	503	-37	141	99	46	65	170
Te	0.13	-100	-100	-41	105	-48	-13	794	-91	203	273	-15	88	266
Au	0.02	136	384	1084	-100	-100	-11	141	-63	75	13	763	211	385

Gains and losses of major oxides and selected trace elements in hydrothermally altered BIF is expressed as percentage relative to abundances in least altered BIF (column 2). Std = one standard deviation.

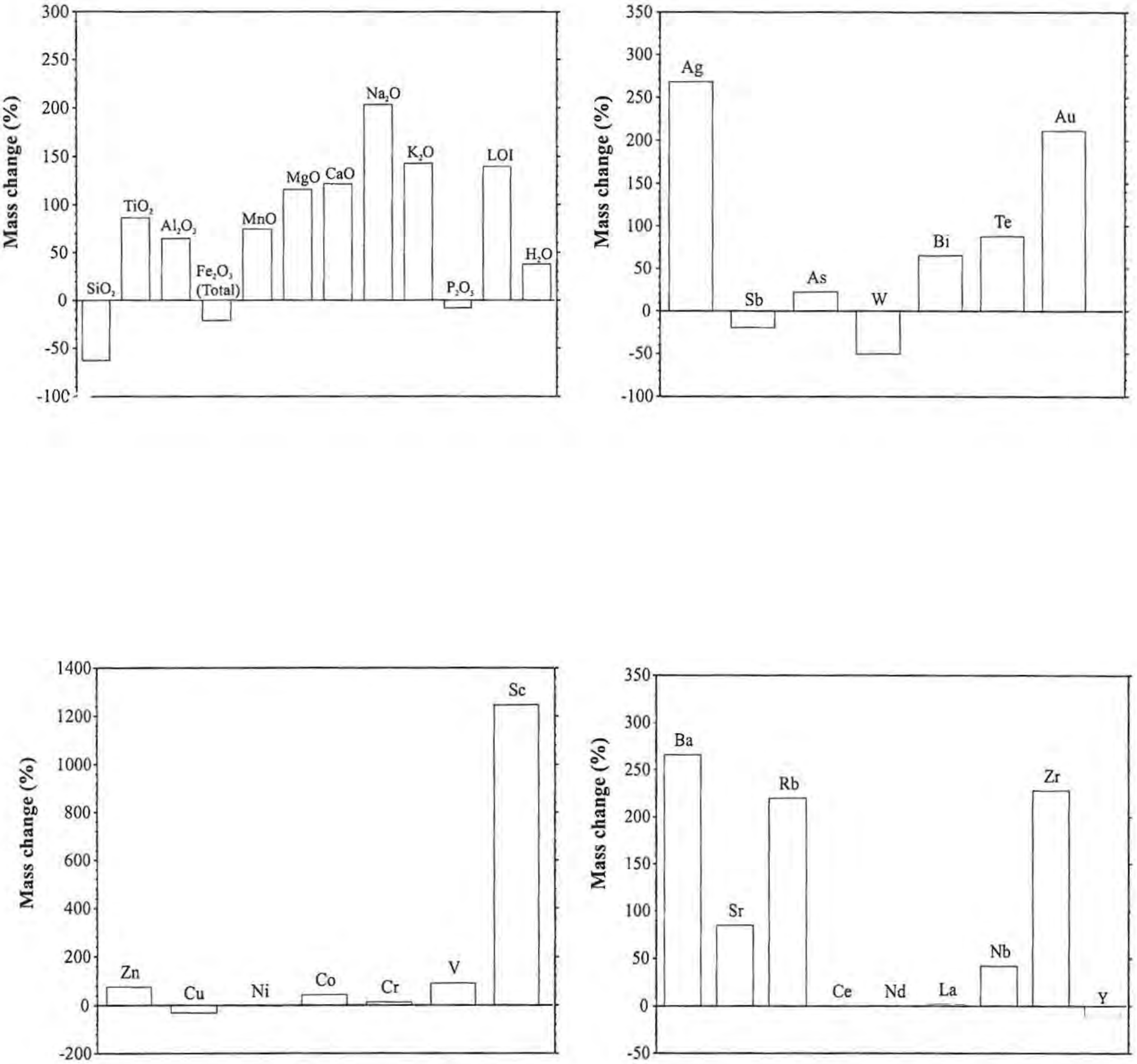

Figure 4.9. Mass changes of major and trace elements during hydrothermal alteration at the Kalahari Goldridge deposit. Gains and losses are expressed in percentage relative to least altered samples.

The consistent enrichment of volatiles (LOI), which consist dominantly of CO_2, H_2S and CH_4, is a reflection of intense carbonate and sulphide precipitation in the deposit, whilst H_2O enrichment is associated with hydrous phases such as chlorite and stilpnomelane. Gains in MgO, CaO and MnO are also consistent with the intense carbonate alteration associated with the deposit. Na_2O and K_2O enrichment is ascribed to the presence of stilpnomelane and muscovite, as the main hosts in the deposit. Fe_2O_3-total experienced minor depletion in all samples with average values of approximately 20%, whilst P_2O_5 remained relatively unchanged on average. The minor depletion of Fe suggests that a large proportion of Fe in the host rock has been retained as sulphides and carbonates in the altered BIF. The Fe released is attributed to have been and deposited in the quartz veins mostly as sulphides, carbonates and chlorites.

The transition elements Ni and Cr were generally insensitive to alteration at the Kalahari Goldridge deposit. Cu was depleted moderately while Co, Zn, V and Sc experienced enrichments, with Sc showing consistent and very high relative enrichment ranging up to 4754% absolute enrichment (average, 1349 %). The rare elements and precious metals are characterized by variable average enrichments in Au (211%), Ag (268%), Bi (65%), Te (88%) and As (22%), while Sb and W were depleted by approximately 19% and 50% respectively.

The large ion lithophile elements, Ba, Sr and Rb have been added from the hydrothermal fluid. Enrichment of Sr (91%) can be ascribed to ankerite formation sympathetically with CaO, while Ba and Rb, which alongside with K_2O, may be attributed to the extensive K-metasomatism, with these elements being incorporated in muscovite and stilpnomelane.

Of the high field-strength elements (Zr, Y and Nb) and rare earth elements (Nd and La), which are traditionally considered immobile, the rare-earth elements Nd and La were generally unchanged, which is consistent with their isochemical behaviour. However, the high field strength elements Zr, Y and Nb experienced some mobility. Zr and Nb showed enrichments of approximately 228 and 42 % respectively, whilst Y experienced a minor depletion of 10 %. Typical immobile elements Al (as Al_2O_3) and Ti (as TiO_2) exhibit variable and co-varying mass changes with average enrichments of 86% and 65% respectively. Their co-variation suggests that these elements were derived from a common source.

A number of studies (Ludden et al. 1984; Golding et al., 1990; Moritz and Crocket, 1991; Eilu et al., 2001) have demonstrated that the mobile behaviour of these "immobile" elements during alteration in Archaean lode gold deposits. In these studies, the mobile behaviour of these elements was attributed to the intense carbonatization association with these alterations. This contention has been demonstrated by Langmuir (1979) who showed that in fluids containing high levels of CO_2, these "immobile" elements, due to their high valence favour the formation of stable carbonate complexes, and hence are easily transported in the hydrothermal fluid. These observations and the extensive carbonate alteration at the Kalahari Goldridge deposit provide ample evidence for significant mobility of Zr, which may be hosted in accessory phases particularly zircon. Given the paucity of Al in pristine BIFs and its low solubility in hydrothermal solution, its enrichment in the altered BIF units, as evidenced by the presence of Al-bearing phyllosilicates such as stilpnomelane, chlorite and muscovite, indicates that Al may have been sourced from detrital components (e.g. aluminous clay minerals) in the terrigenous sediments interbedded with the BIF by in-situ enrichment through leaching of silica from these clay minerals.

5.1 Fluid Inclusion Geochemistry

5.1.1: Introduction

Fluid inclusion application has been an integral part in the study of ore genesis for decades. The primary aim of the study is to characterise the P-T-X evolution of the vein-forming hydrothermal fluids. These studies are based on the assumption by Roedder (1984), that the volume and composition of the examined fluid inclusion have remained constant since the entrapment of the inclusion.

The interpretation of the P-T-X characteristics of the fluid inclusion requires careful measurement of phase changes in the inclusion during freezing-heating runs. These phase changes, namely, (i) final melting temperature of CO_2 (Tm_{CO_2}), (ii) final melting temperature of ice (Tm_{ice}), (iii) dissociation temperature of clathrate ($Tm_{clathrate}$), (iv) homogenization temperature of CO_2 and CH_4 ($ThCO_2$/$ThCH_4$) and (v) final homogenisation of the CO_2-H_2O-NaCl and H_2O-NaCl inclusions (Th_{total}) are compared with published experimental data to calculate composition, salinity and density of the fluid. The $TmCO_2$ determines the purity of CO_2 phase in the inclusion. The triple point of pure CO_2 is -56.6°C. The Tm_{ice} was used to determine salinity of H_2O-NaCl (type III) inclusions (Hall et al., 1988). In the presence of CO_2 vapour, CO_2 liquid and aqueous liquid, the clathrate dissociation temperature serves as an alternative for the salinity estimate of CO_2-H_2O-NaCl inclusions to avoid the high salinity estimates using

Tm_{ice} in the CO_2-H_2O-NaCl system (Bozzo et al., 1975, Collins 1979, Diamond, 1992). The addition of NaCl to the pure CO_2-H_2O system shifts the CO_2-H_2O clathrate melting point (10°C) to lower temperatures. In contrast, the presence of other volatiles, such as CH_4, causes the opposite effect to that of NaCl, resulting in the dissociation temperatures above 10°C. Therefore all salinities calculated from clathrate melting temperatures for CH_4-bearing inclusions represent minimum values.

The temperature of total homogenization of an inclusion defines its bulk density. In addition, the total homogenization temperature of fluid inclusions generally provides minimum temperature estimates. Assuming immiscibility did not occur, trapping temperature can only be estimated if a pressure correction is applied. However, where evidence of immiscibility is present, the total homogenization temperature equals the temperature of trapping (Touret, 1977; Ramboz et al., 1982).

5.1.2: Sampling and classification of inclusions

The selection of samples formed an important part of the fluid inclusion study, since the samples to be studied must be representative of the mineralization event. Therefore, for the purpose of this study, emphasis was laid on quartz veins associated with the gold mineralization. The quartz samples were restricted to those, which showed minimal effects of deformation, in order to minimise post-entrapment modifications of fluid inclusions. Also, microthermometric data were collected on inclusions, which showed no necking characteristics. A total of twenty mineralized quartz vein samples (8 from Group IIA and 12 from Group IIB veins) and two samples, one each from the unmineralized steeply-dipping veins (thus, Group I and the Group III veins) were selected for the fluid inclusion petrography and microthermometry. Microthermometry was restricted to primary or pseudo-secondary fluid inclusions, based on the general assumption that the volume and composition of the original trapped fluid (primary or pseudo-secondary inclusions) have remained constant since their entrapment (Roedder, 1984; Sterner and Bodnar, 1984). Therefore primary and pseudosecondary inclusions provide information about the mineralizing fluids. Secondary inclusions on the other hand, may provide information on the later geological history of a crystal. The criteria for classifying the inclusions were based on the work of Roedder (1984). The term "primary" was used for inclusions that occur in random clusters or in isolation. The term "pseudo-secondary" was applied to inclusions that generally occur in orientated arrays within grain boundaries, whilst "secondary" was applied to all inclusions that occur in abundance as trails along healed fractures.

5.1.3: Inclusion Petrography

In this study, three main types of fluid inclusions were identified based on their composition from microthermometry and number of phases present at room temperature (21-22°C). These are designated as type I, type II and type III inclusions.

Type I inclusions are represented by one-phase carbonic liquids at room temperature. The inclusions consist of variable mixtures of CO_2 and CH_4, ranging from CO_2-dominant to CH_4-dominant fluids. Type I inclusions occur as clear to dark inclusions and commonly exhibit characteristic negative crystal shapes. Some inclusions contain a thin film of water between the carbonic fluid and the inclusion walls. CO_2-rich inclusions nucleate a bubble on cooling below room temperature. CH_4-rich inclusions have been identified in one sample (525/21) taken in close proximity to the footwall black shale unit. They nucleate a bubble at temperatures below -100°C. The type I inclusions occur in subordinate amounts compared to type II and III inclusions.

Type II inclusions contain two- (e.g., Fig 5.1A,B) or three-phase aqueous-carbonic fluids at room temperature. The three-phase inclusions consist of aqueous liquid, carbonic liquid and vapour. The two-phase fluid inclusions are the most abundant of type II inclusions, and consist of aqueous and carbonic liquids. The type II constitutes the majority of inclusions occurring in the mineralized (Group II) veins. The carbonic phase nucleates a bubble on cooling below room temperature. Their shapes range from irregular and ellipsoidal to nearly rounded. The volume proportion of the carbonic phase is generally variable from 50 to 95 percent.

Type III inclusions consist of aqueous liquid and vapour phases at room temperature (Fig. 5.1C). They have degree of fill (F_{H_2O}) in the range of 80 to 95 volume percent liquid in the mineralized veins, and about 50 to 85 volume percent in the Group III veins. One-phase aqueous inclusions were identified in some mineralized quartz veins. However, due to the absence of a vapour phase and their inability to nucleate a bubble on cooling, phase transition measurements could not be carried out on these inclusions. Most type III are secondary in origin and exhibit degree of fill (> 95 %). The inclusions are generally subrounded to irregular elongated shapes with size varying from 5 to 25µm. Type III inclusions form the dominant population in the late quartz veins.

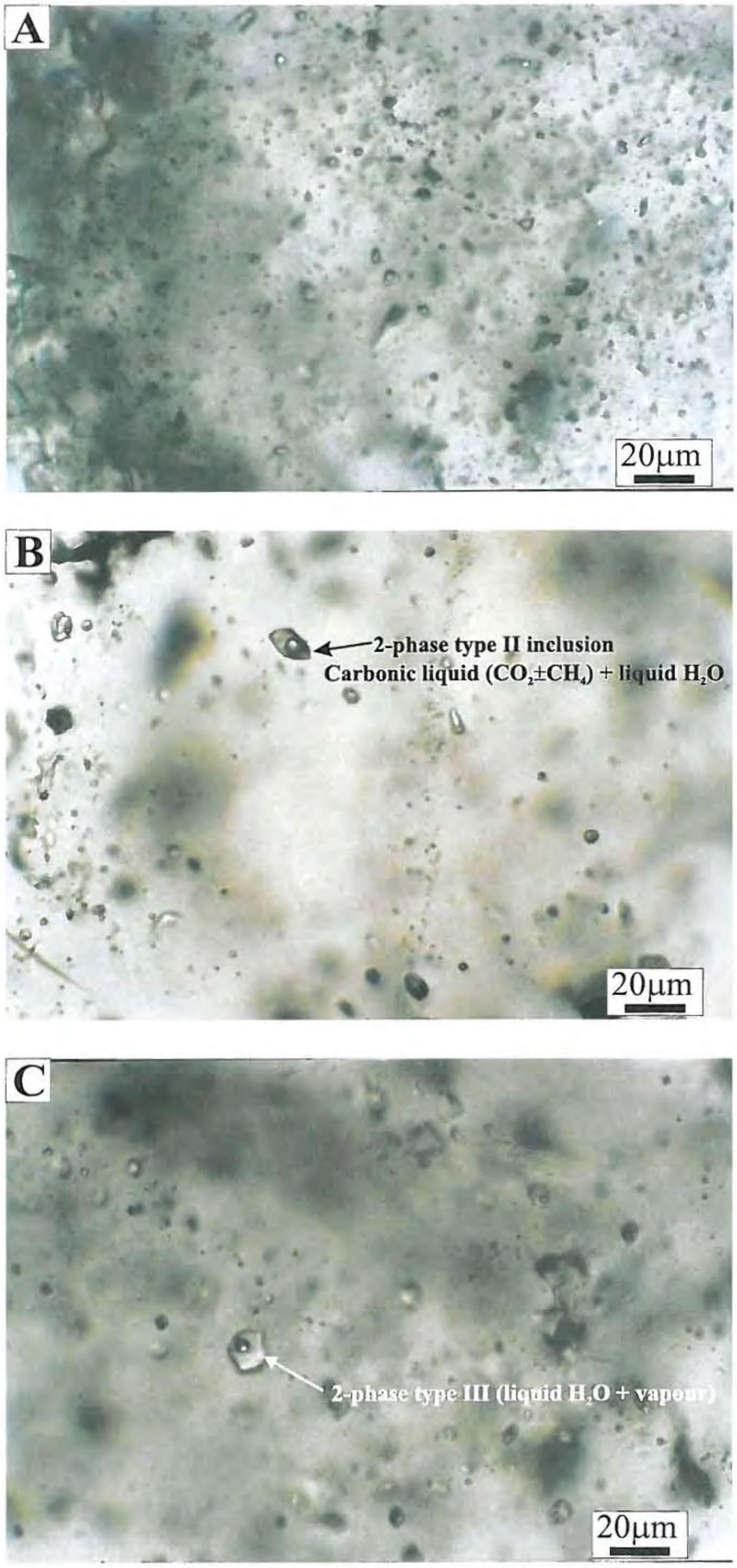

Figure 5.1. Photomicrographs of fluid inclusions in mineralized veins at the Kalahari Goldridge deposit. **A.** Types I and II inclusions in Group IIA (ladder) vein. **B**. 2-phase type II (liquid carbonic and aqueous phases) in Group IIB veins. **C**. 2-phase type III inclusions (liquid H_2O and vapour) in Group IIB vein.

5.1.4: Microthermometry

5.1.4.1 Analytical methods

Microthermometry was conducted on 178 primary fluid inclusions from twenty mineralized quartz veins and two non-mineralized quartz veins. Microthermometry was performed at the Department of Geology, Rhodes University using a Linkam THMS 600 heating/freezing stage attached to a Nikon microscope with a X50 objective lens. Freezing runs were done using liquid nitrogen aided by a LNP cooling pump connected to the stage while heating runs were performed by a thermal resistor with a TM-93 control unit. The lower and upper limits of the stage are respectively -180° and +600°C. Calibrations were performed using pure water and CO_2 inclusions and potassium dichromate provided by the manufacturer.

Samples were first frozen rapidly to temperatures below -100°C and then heated slowly at a rate of 0.5 to 1.0°C/min at temperatures below 31°C. Heating rate was increased to 5 to 10°C/min until total homogenization. The accuracy is estimated to be within ± 0.5°C for phase transition temperatures below -20°C, ± 0.2°C between -20°C and 31°C and up to ± 5°C for temperatures above 150°C. Freezing of inclusion was done rapidly to below -100°C to avoid the nucleation of meta-stable phases.

In this study, the following six phase transition temperatures were measured during heating runs: (i) final melting temperature of CO_2 (Tm_{CO_2}), (ii) final melting temperature of ice (Tm_{ice}), (iii) dissociation temperature of clathrate ($Tm_{clathrate}$), (iv) homogenization temperature of CO_2 and CH_4 ($ThCO_2/ThCH_4$) and (v) final homogenization of the CO_2-H_2O-NaCl and H_2O-NaCl inclusions (Th_{total}).

5.1.4.2: Microthermometry results

The results of the microthermometric data for all the veins are given in Appendices VI to IX and summarized in Tables 5.1 to 5.5.

i. Early quartz vein (Group I)

Fluid inclusions from the samples of Group I quartz veins were generally too small to be examined. Their size ranged up to 5μm. Inclusions consist dominantly of type I and type II. Measurements were made on twelve inclusions in the Group I quartz samples. These consist of 6 type I inclusions and 6 type II inclusions. The melting temperature of one solid CO_2 in type I inclusion occurred at −60.3°C. The melting temperatures of solid CO_2 in the type II inclusions showed depressed values (−59.5 to −62°C) in comparison to the melting temperature of pure CO_2. Homogenization of CO_2 for both type I and II inclusions was to the liquid phase. Th_{CO2} values vary from 9.7 to 14.5°C, and from 9.4 to 14.0°C for type I and type II inclusions respectively. Clathrate melting temperatures range from 9.0 to 16°C. Six homogenization temperatures were attempted for type II inclusions: three inclusions homogenised to the vapour phase between 280 and 290°C and three inclusions decrepitated prior to homogenization at temperatures between 247 to 263 °C.

Table 5.1. Summary of microthermometric data of inclusions in Group I quartz veins at the Kalahari Goldridge deposit.

Inclusion type	Type I $CO_2 \pm CH_4$	Type II CO_2-CH_4-H_2O-NaCl
Tm_{CO_2} (°C)	-60.3 n= 1	-60.0 to -59.5 n=6
Tm_{ice} (°C)		
$Th_{clathrate}$ (°C)		9 to 16.0 n=6
Th_{CO_2} (°C) L/V	9.7 to 14.5 (L) n=6	9.4 to 14.2 n=6
Th_{total}L/V (°C)		280 to 290 (V) n=3
$T_{decrepitation}$ (°C)		247 to 263 n=3
ρ_{CO_2} (g/cm^3)	0.79 to 0.82 n=6	0.79 to 0.82 n=6
$\rho_{aqueous}$ (g/cm^3)		1.005 n=2
ρ_{bulk} (g/cm^3)		nd
Salinity (wt % NaCl)	2.03 n=2	2.03 n=2

L = homogenization to liquid phase, V = homogenization to the vapour phase.
n = number of observations nd = not determined

ii. Ladder quartz vein (Group II A)

Fluid inclusions in the Group IIA quartz veins are not common. Petrographic studies shows that most of the samples are free of fluid or contain inclusions generally not suitable for microthermometric measurements (less than 2µm). The Group IIA veins samples are dominated by type I and II inclusions.

Microthermometric measurements were conducted on 56 inclusions in Group IIA quartz veins. Because of the small size of the inclusions and poor optical visibility at low temperatures, Tm_{CO_2} could only be measured on 23 of the 56 inclusions. Only one type I inclusion was identified in the Group IIA veins, and indicated Tm_{CO_2} of -59.5°C. The Tm_{CO_2} of the type II inclusions range from -61.9 to -57.2°C (Fig. 5.2A).

Table 5.2. Summary of microthermometry data of fluid inclusions in ladder mineralized vein (Group IIA) at the Kalahari Goldridge deposit.

Inclusion type	Type I CO_2 or CH_4	Type II CO_2-CH_4-H_2O-NaCl	Type III H_2O-NaCl
Tm_{CO2} (°C)	-59.5	-61.9 to -57.2, n = 22	
Tm_{ice} (°C)			-3.9 to -2.5, n = 10
$Th_{clathrate}$ (°C)		7.5 to 15, n = 42	
Th_{CO2} (°C)	10.1 to 15.9, (L) n = 4	-4.3 to 21.9 (L), n = 42	
$ThCH_4$ (°C)			
$Th_{total}L/V$ (°C)		268 to 307 (V), n = 13	255 to 283 (L/V), n = 4
$T_{decrepitation}$ (°C)		210 to 284, n = 22	245 to 268, n = 5
ρ_{CH4} (g/cm^3)			
ρ_{CO2} (g/cm^3)	0.82 to 0.78, n = 4	0.89 to 0.73, n = 42	
$\rho_{aqueous}$ (g/cm^3)		0.992 to 1.029, n = 25	1.021 to 1.036, n = 10
ρ_{bulk} (g/cm^3)		0.83 to 0.88, n = 9	
Salinity (wt % NaCl)		0 to 5.41, n = 25	4.18 to 6.3, n = 10

L = homogenization to the liquid phase. V = homogenization to the vapour phase.
n = number of observations

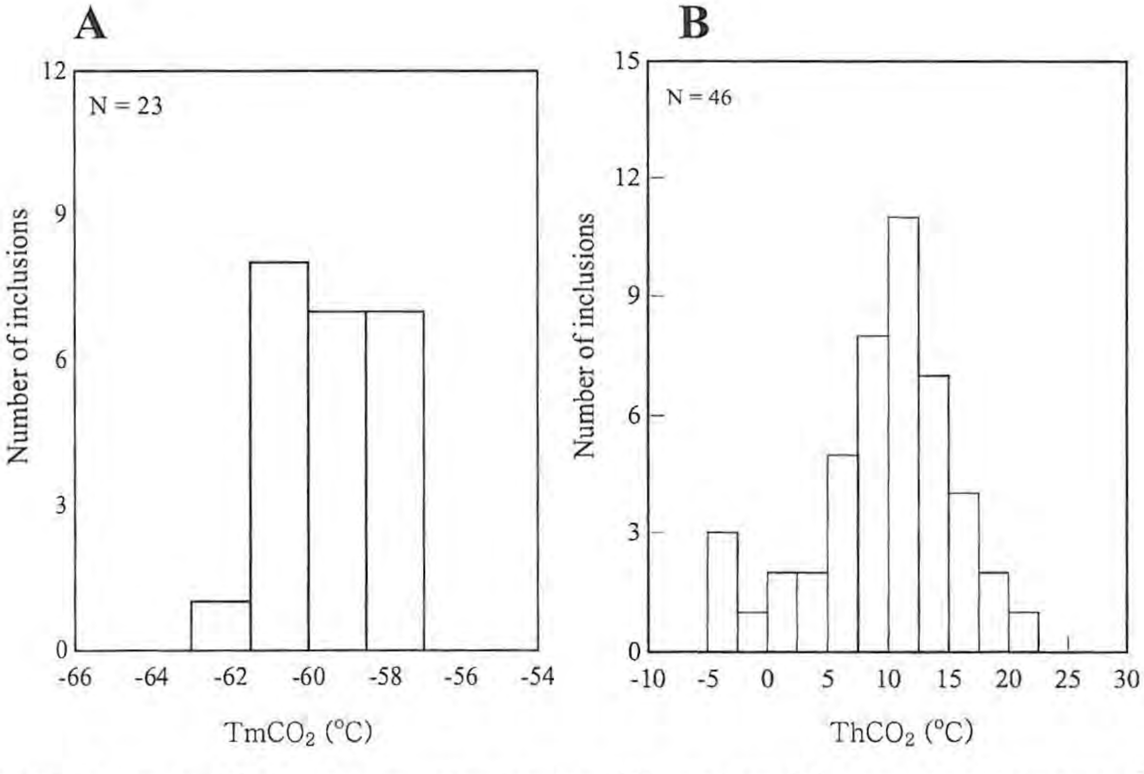

Figure 5.2. Histograms showing the CO_2 melting (A) and homogenization temperatures (B) in Group IIA veins.

The rang from

-4.3 to 2 sions

shows a discrete mode between 10 and 12.5°C (Fig. 5.2B). The range of Th_{CO2} corresponds to CO_2 densities from 0.88 to 0.73g/cm^3 based on the data of Ely et al. (1989).

Clathrate dissociation temperatures in type II inclusions yielded values from 6.4 to 14.8°C (Fig. 5.3A). Fluid salinity estimates were calculated for inclusions with clathrate melting temperatures lower than 10°C (6.4 to 9.8°C) after the data of Bozzo et al. (1975). These correspond to minimum salinities ranging from 0.41 to 5.41 wt% NaCl equivalent (Fig. 5.3B). Salinity cannot be determined on type II inclusions with $Tm_{clathrate}$ higher than 10°C. The type II inclusions with depressed Th_{CO2} show corresponding higher $Tm_{clathrate}$, greater than 10°C, which indicates the presence of significant amounts of CH_4 in the inclusions. The presence of CH_4 in these inclusions has been confirmed by Raman spectroscopy (discussed in section 5.1.4).

Salinities calculated from the Tm_{ice} of the type III inclusions (-2.5° to -3.9°C, Fig. 5.4A) indicate a range from 4.18 to 6.3 wt % NaCl equivalent (Fig. 5.4B), using the data of Hall et al. (1988). Most type II inclusions decrepitated prior to total homogenization, which indicates high pressures generated by the volatiles notably $CO_2 \pm CH_4$. Decrepitation occurred in the range from 210 to 270°C (Fig. 5.5A) with some inclusions decrepitating close to homogenization. Total homogenization occurred from 270 to 307°C (Fig. 5.5B), and occurs dominantly in the vapour phase. The total homogenization temperatures of the two type III inclusions occurred in the range from 270 to 283°C (Fig. 6B) into the liquid or vapour phase but mostly in the vapour phase.

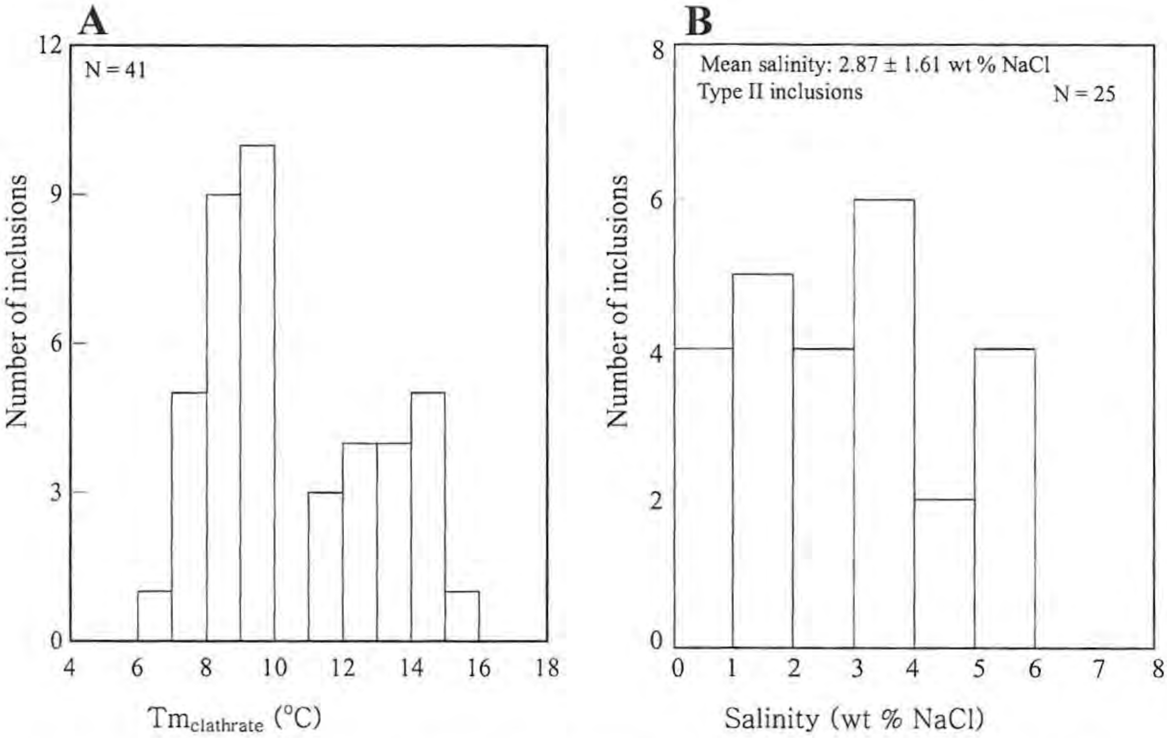

Figure 5.3. Histograms showing clathrate melting temperatures (A) and corresponding salinity (B) in type II inclusions, Group IIA veins.

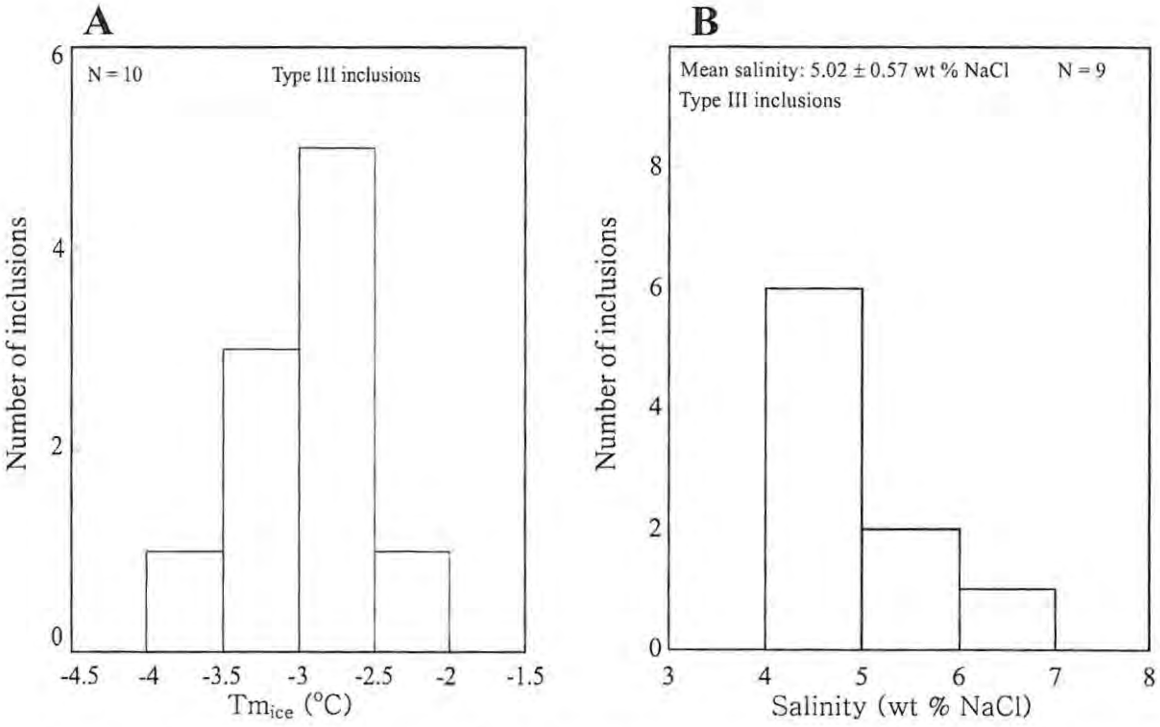

Figure 5.4. Histograms showing the melting temperature of ice (A) and corresponding salinity (B) in type III inclusions, Group IIA veins.

iii. Large quartz vein (Group IIB)

The Group IIB quartz veins contain type I, II and III fluid inclusions. The type II inclusions form the largest population of inclusions in the veins. The size of the inclusions is variable from about 5 to 20μm with a mean of about 10μm. Most of the observed type III inclusions in the veins occurred as secondary inclusions.

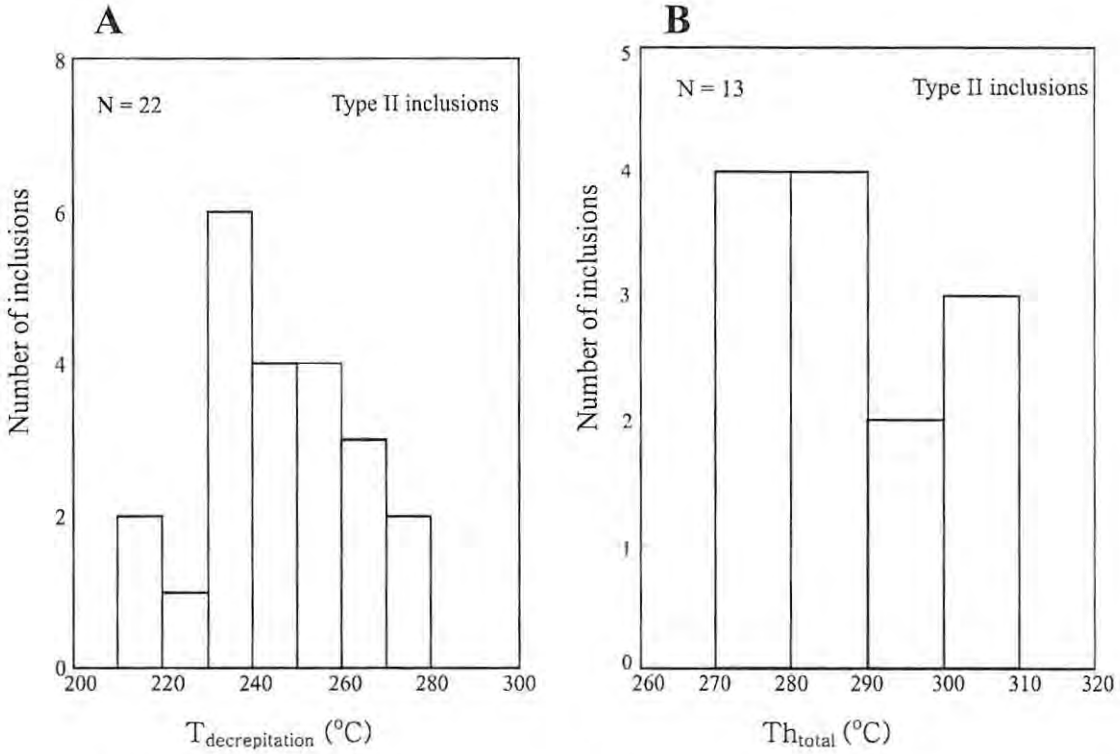

Figure 5.5. Histograms showing decrepitation and total homogenization temperatures of type II inclusions in Group IIA veins

Melting temperatures of solid CO_2 showed significant depression from the triple point value of -56.6°C. Values range from -56.8 to -64.3°C (Fig. 5.7A), indicating the presence of other volatiles (CH_4) in the inclusions. The homogenization of CO_2 occurred dominantly in the liquid phase and showed a wide spread from 8.4 to 24.2°C with three distinct modes (10 - 12.5°C; 15.0 -

17.5°C; and 20 - 22.5°C; Fig. 5.7B). The range of homogenization temperatures corresponds to CO_2 densities from 0.70 to 0.87 g/cm^3. Homogenization temperatures of three CH_4-rich inclusions vary between -95 to -97.0°C in the liquid phase.

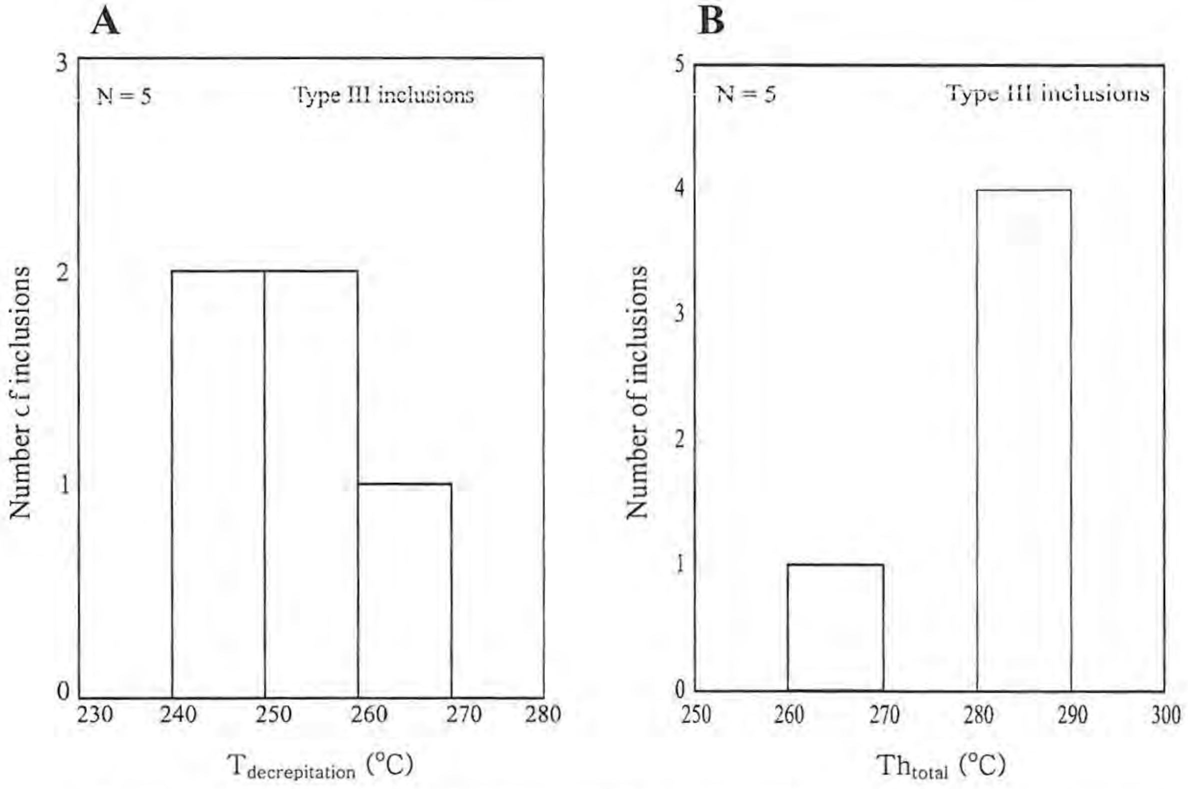

Figure 5.6. Histograms showing decrepitation and total homogenization temperatures of type III inclusions in Group IIA veins.

No solid phases were observed in these inclusions on further warming beyond the triple point of pure CO_2 (-56.6°C), which indicates that the inclusions were essentially pure methane. Clathrate melting temperatures of most type II inclusions (Fig. 5.8A) occurred from 7.0 to 13.3°C. The fluid salinities from the clathrate temperatures range from pure water to 5.77 wt % NaCl equivalent (Fig. 5.8B). Ice melting temperatures of the type III inclusions vary from -1.9 to -3.1°C (Figure 5.9A), corresponding to salinity estimates from 3.23 to 5.11 wt% NaCl equivalent (Fig. 5.9B).

Table 5.3 Summary of microthermometric data of Group IIB veins at the Kalahari Goldridge deposit

Inclusion type	Type I CO_2 or CH_4	Type II CO_2-CH_4-H_2O-NaCl	Type III H_2O-NaCl
Tm_{CO2} (°C)	-64.3 to -58.5, n = 6	-61.0 to -57.0, n = 56	
Tm_{ice} (°C)			-3.1 to -1.9, n = 9
$Th_{clathrate}$ (°C)		7 to 13.3, n = 80	
Th_{CO2} (°C) L/V	8.4 to 14.8 (L), n = 6	9.1 to 24.2 (L) n = 80	
Th_{CH4} (°C)			
Th_{total}L/V (°C)		248 to 310 (V), n = 41	271 to 306 (L or V), n = 6
Tdecrepitation (°C)		195 to 275 n = 39	235 to 255, n = 3
ρ_{CH4} (g/cm^3)			
ρ_{CO2} (g/cm^3)	0.83 to 0.79, n = 6	0.82 to 0.70, n = 80	
$\rho_{aqueous}$ (g/cm^3)		0.992 to 1.025, n = 77	1.014 to 1.027, n = 9
ρ_{bulk} (g/cm^3)		0.76 to 0.89, n = 36	
Salinity (wt % NaCl)		0.0 to 5.77, n = 77	3.71 to 5.11, n = 9

L = homogenization to liquid phase. V = homogenization to vapour phase.
n = number of observations

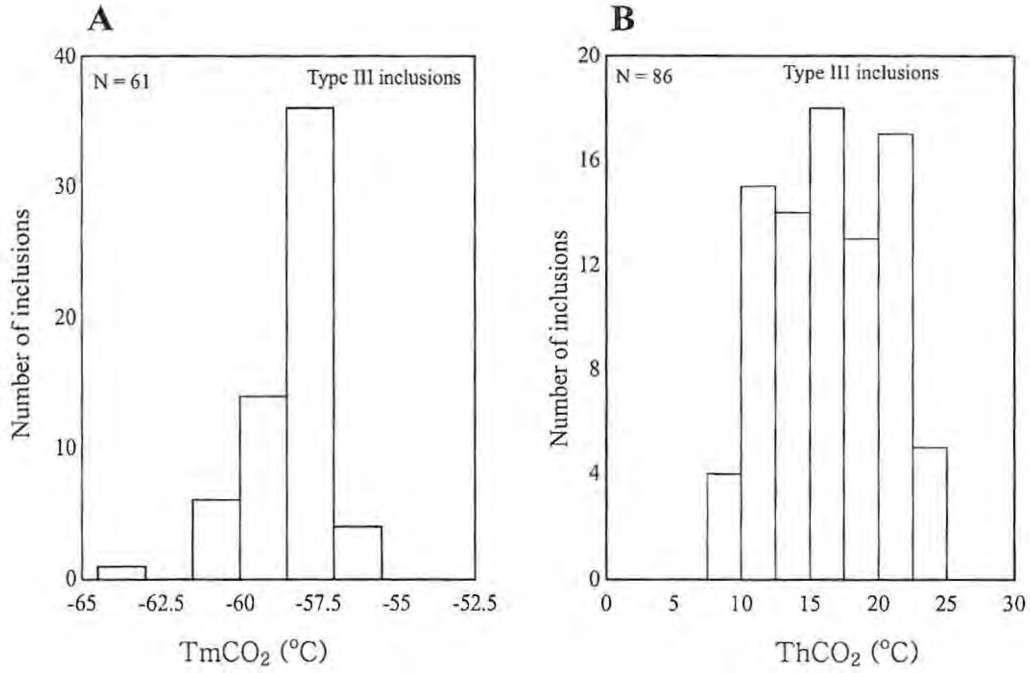

Figure 5.7. Histograms showing CO_2 melting (A) and CO_2 homogenization temperatures (B) in Group IIB veins.

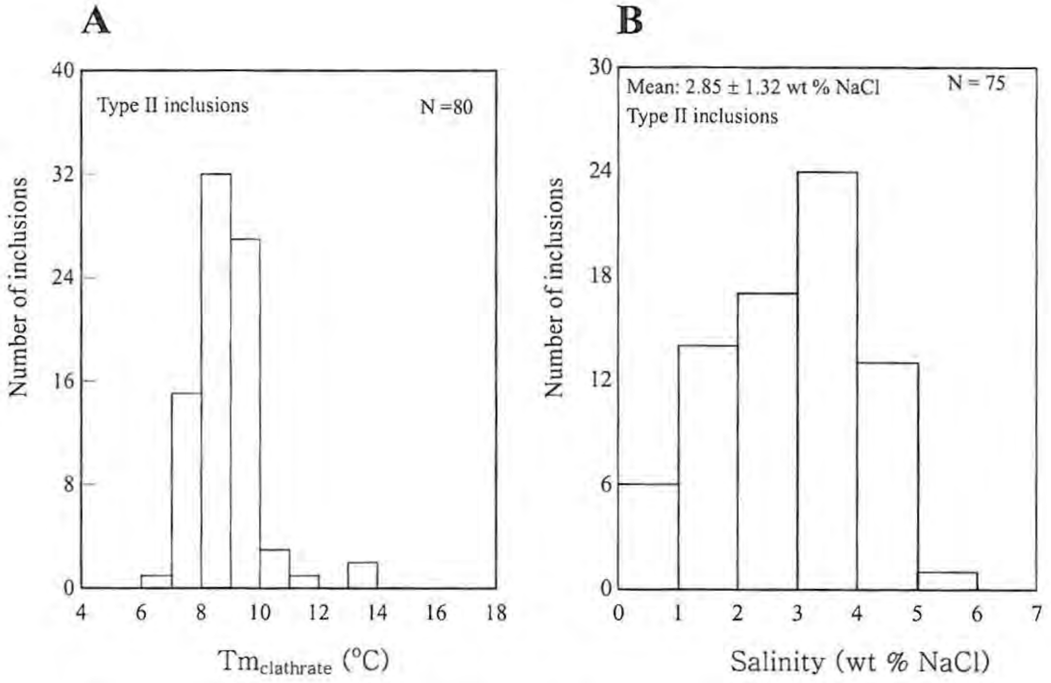

Figure 5.8. Histograms showing clathrate melting temperatures and corresponding salinity estimates in type II inclusions, Group IIB veins.

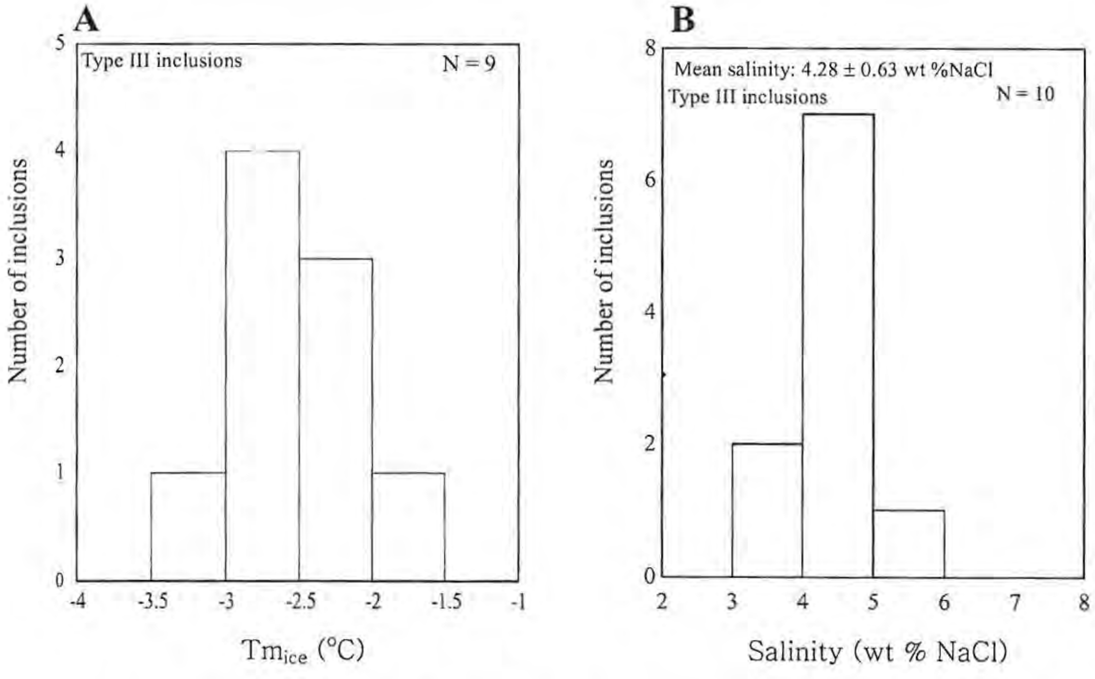

Figure 5.9. Histograms showing the melting temperature (A) and corresponding salinity (B) in type III inclusions, Group IIB veins.

As with the Group IIA veins, several type II inclusions decrepitated before reaching homogenization. The decrepitation temperatures vary from 214 to 270°C (Fig. 5.10A). The total homogenization temperatures showed a range from 254 to 310°C, mainly to the vapour phase (Fig. 5.10B). Primary type III inclusions yielded temperatures from 271 to 306°C (Fig. 5.11B). Some of the inclusions decrepitated before homogenization, suggesting that the inclusions may contain minor amounts of volatiles. No clathrates were observed in the type III inclusions. However, Bodnar et al. (1985) showed that clathrate formation in inclusions with CO_2 contents less than 4 mole percent might be optically invisible. Some type III inclusions, which show similar features to primary inclusions, homogenised at low temperatures between 122 to 220°C. These inclusions were, however, considered to be secondary due to the low temperatures and may reflect late-trapped fluids.

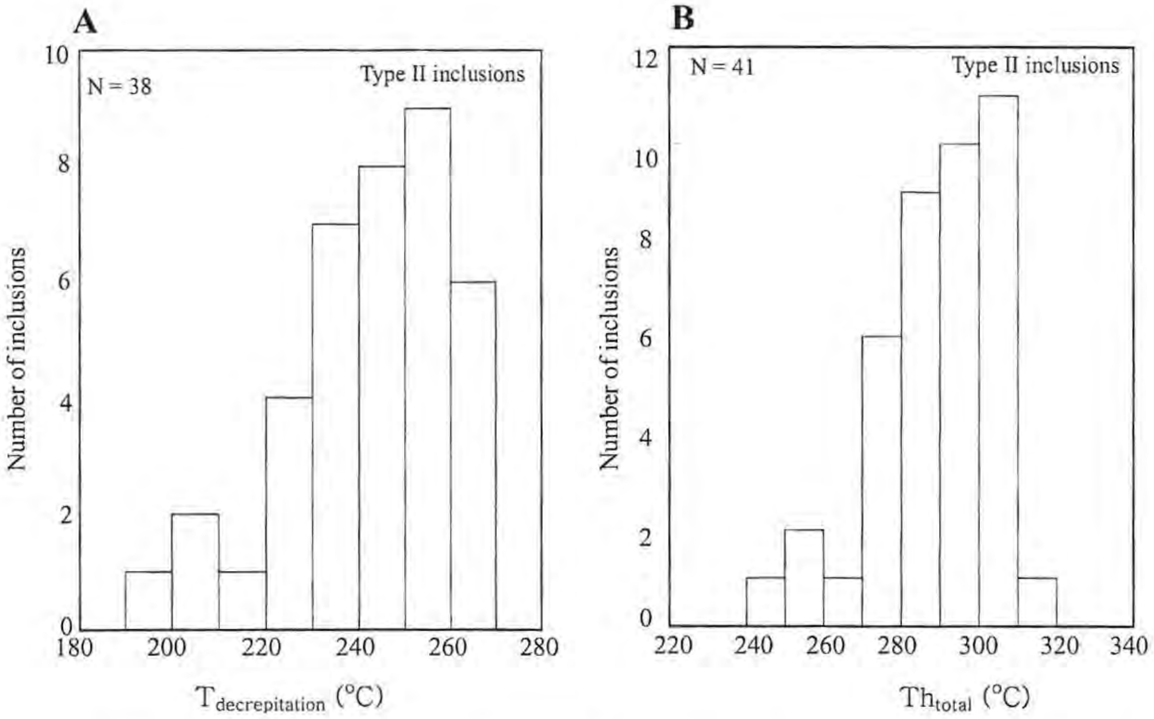

Figure 5.10. Histograms showing decrepitation and total homogenization temperatures of type II inclusions in Group IIB veins.

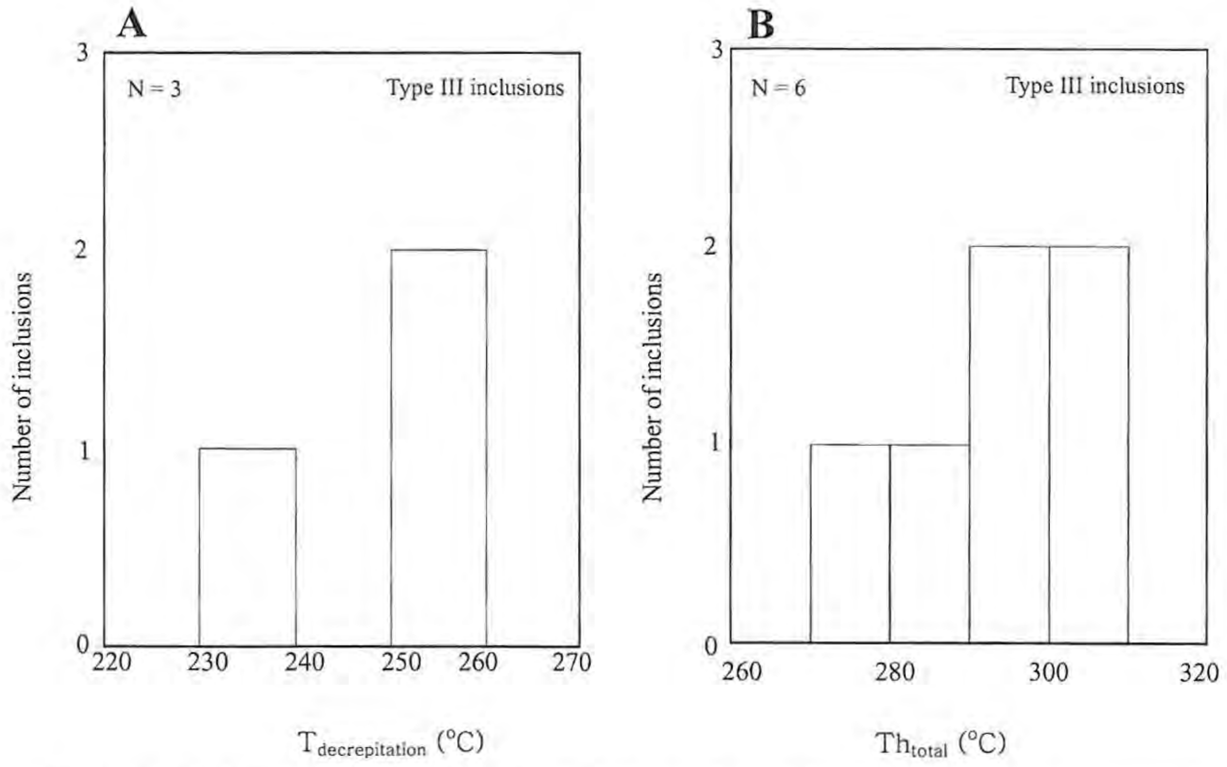

Figure 5.11. Histograms showing decrepitation and total homogenization temperatures of type III inclusions in Group IIB veins.

iv. Late quartz vein (Group III)

The Group III veins contain all three types of inclusions. However, type III inclusions form the dominant population. Table 5.4 shows the summary of microthermometric data of the late veins. The Tm_{CO2} in three analyzed inclusions shows significant depression from -60.1 to -70.0°C. Ice melting temperatures range from 0.5 to -3.5°C and are equivalent to fluid salinities in the range from 0.8 to 5.71 wt % NaCl. The dissociation temperature of clathrates exceeds 10°C, consistent with significant CH_4 contents as recorded in the Tm_{CO2}. Observed CO_2 homogenization temperatures range from 0.7 to 9.9°C. Total homogenization temperatures of the type III inclusions show a relatively wide range from 217° to 362°C, either in the liquid or vapour phase. Of the two type II inclusions, one homogenized in the vapour phase at 220°C, whilst the other decrepitated at 249°C.

Table 5.4. Summary of microthermometric data of inclusions in Group III veins at the Kalahari Goldridge deposit

Inclusion type	Type I $CO_2 \pm CH_4$	Type II CO_2-CH_4-H_2O-NaCl	Type III H_2O-NaCl
Tm_{CO2} (°C)	-70.0, n = 1	-65.0 to -60.1, n = 2	
Tm_{ice} (°C)			0.3 to -3.5, n = 9
$Th_{clathrate}$ (°C)		11.5 to 13.0, n = 2	
Th_{CO2} (°C) L/V	9.7 to 14.5 (L), n = 6	1.6 to 9.9 (L), n = 2	
Th_{total} L/V (°C)		220 (V), n = 1	217 to 355 (L or V), n = 9
$T_{decrepitation}$ (°C)		249, n = 1	
ρ_{CO2} (g/cm^3)	0.88, n = 1	0.83, n = 1	
$\rho_{aqueous}$ (g/cm^3)		nd	0.998 to 1.022, n = 9
ρ_{bulk} (g/cm^3)		nd	
Salinity (wt % NaCl)		nd	1.05 to 5.71, n = 9

L = homogenization in the liquid phase. V = homogenization to vapour phase.
n = number of observations. nd = not determined.

5.1.5: Laser Raman Spectroscopy

Twenty fluid inclusions in 6 quartz vein samples were analysed by laser Raman microprobe at the Department of Physics, University of Witwatersrand for volatile species including CO_2, CH_4, H_2S and N_2. The fluid inclusions are representative of samples from the Group IIA and Group IIB quartz veins.

5.1.5.1: Analytical method

The analyses were carried on a Jobin-Yvon T64000 Raman microprobe using an Olympus BX40 microscope attachment and a liquid N_2-cooled CCD detector. An Ar ion laser of 514.5nm was used as the excitation radiation and source power of 500mW. Spectral resolution was better than $2cm^{-1}$. The beam was focused to a spot size of approximately 3μm using an Olympus objective with a 100X magnification and numerical aperture of 0.9. A small confocal pinhole size (0.5mm) was used to reduce the vertical dimension of the laser focus and thus minimize the quartz mineral host bands. A spectrum of the quartz adjacent to the inclusion but at same depth was recorded as a sample to serve as a blank for atmospheric N_2, because the optical path of the laser in the atmosphere can give atmospheric N_2 signals.

5.1.5.2: Results

The Raman spectral regions enabled analysis of CO_2, N_2, H_2S, CH_4 and H_2O. The calculated compositions from the Raman spectra are given in Table 5.5 and examples of the spectra for samples PH/6-004 and 525/25-002 in the Group IIA and Group IIB veins respectively in Figures 5.12 and 5.13.

CO_2 displayed two peaks, the strongest peak occurring from 1375 to 1376 cm^{-1} and the second peak from 1287 to 1291 cm^{-1}. The Raman spectra for CH_4 showed peaks ranging from 2912 to 2916 cm^{-1}. Broad bands in the region around 3200 cm^{-1} and 3400 cm^{-1} indicated fluid inclusions containing water and dissolved salts respectively. Neither N_2 nor H_2S was detected in any of the fluid inclusions. CO_2, N_2, H_2S and CH_4 were not detected in the aqueous inclusions.

Table 5.5 Raman microprobe data for fluid inclusion in mineralized veins at the Kalahari Goldridge deposit

Quartz sample			Gaseous phases (mol %)				
	Inclusion No.	Inclusion type	CO_2	CH_4	N_2	H_2S	CO_2/CH_4
Group IIA							
EH/6S	EH/6S-001	2-phase type II	77.6	22.4	—	—	3.5
	EH/6S-002	2-phase type II	89.6	10.4	—	—	8.6
	EH/6S-003	2-phase type II	73.3	26.7	—	—	2.7
	EH/6S-004	2-phase type II	87.8	12.2	—	—	7.2
PH/6S	PH/6-001	2-phase type II	54.4	45.6	—	—	1.2
	PH/6-002	2-phase type II	87.1	12.9	—	—	6.8
	PH/6-003	2-phase type II	86.4	13.6	—	—	6.4
	PH/6-004	1-phase type I	57.1	42.9	—	—	1.3
Group IIB							
531/16B	531/16B-001	2-phase type II	82.0	18.0	—	—	4.6
	531/16B-002	2-phase type II	84.8	15.2	—	—	5.6
	531/16B-003	1-phase type I	31.9	68.1	—	—	0.5
	531/16B-004	1-phase type I	94.6	5.4	—	—	17.5
532/11A	532/11A-001	1-phase type I	66.1	33.9	—	—	1.9
	532/11A-002	2-phase type II	82.4	17.6	—	—	4.7
	532/11A-003	1-phase type I	91.3	8.7	—	—	10.5
525/21	525/21-001	2-phase type II	55.8	44.2	—	—	1.3
	525/21-002	2-phase type II	42.0	58.0	—	—	0.7
	525/21-003	2-phase type II	24.2	75.8	—	—	0.3

The Raman analyses show that the carbonic phase of the inclusions consists of a mixture of CO_2 and CH_4. Estimates of CO_2 and CH_4 contents in inclusions in the Group IIB veins ranged from 24 to 95 mol % and 5 to 76 mol % respectively. In the Group IIA veins, the CO_2 content is variable between 54 and 90 mol % whilst CH_4 ranges between 13 and 45 mol %. The CO_2/CH_4 ratio in the fluid inclusions is highly variable from CO_2-dominant to CH_4-dominant, even within a single sample. The inclusions in the Group IIB veins show a wider variation in the CO_2/CH_4 ratios from 0.3 to 17.5, in comparison to the inclusions in the Group IIA veins, which varied from 1.2 to 8.6 (Table 5.5).

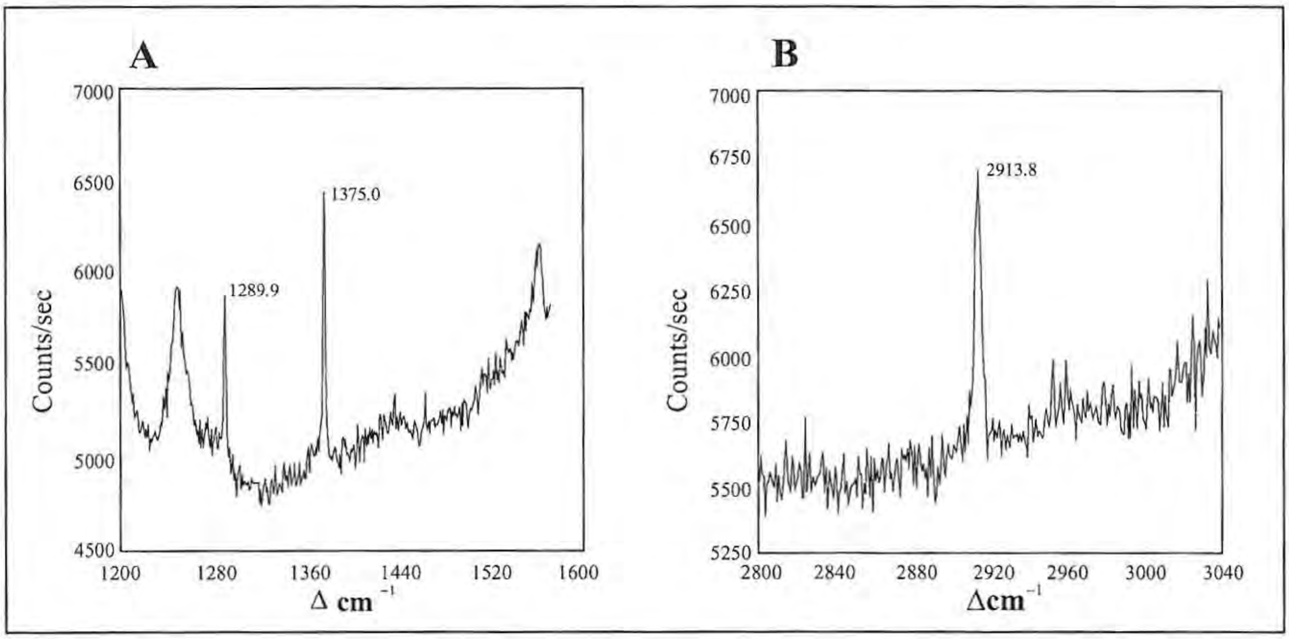

Figure 5.12. Raman spectrum of CO_2 (A) and CH_4 (B) in fluid inclusion in Group IIA vein (sample PH/b-004).

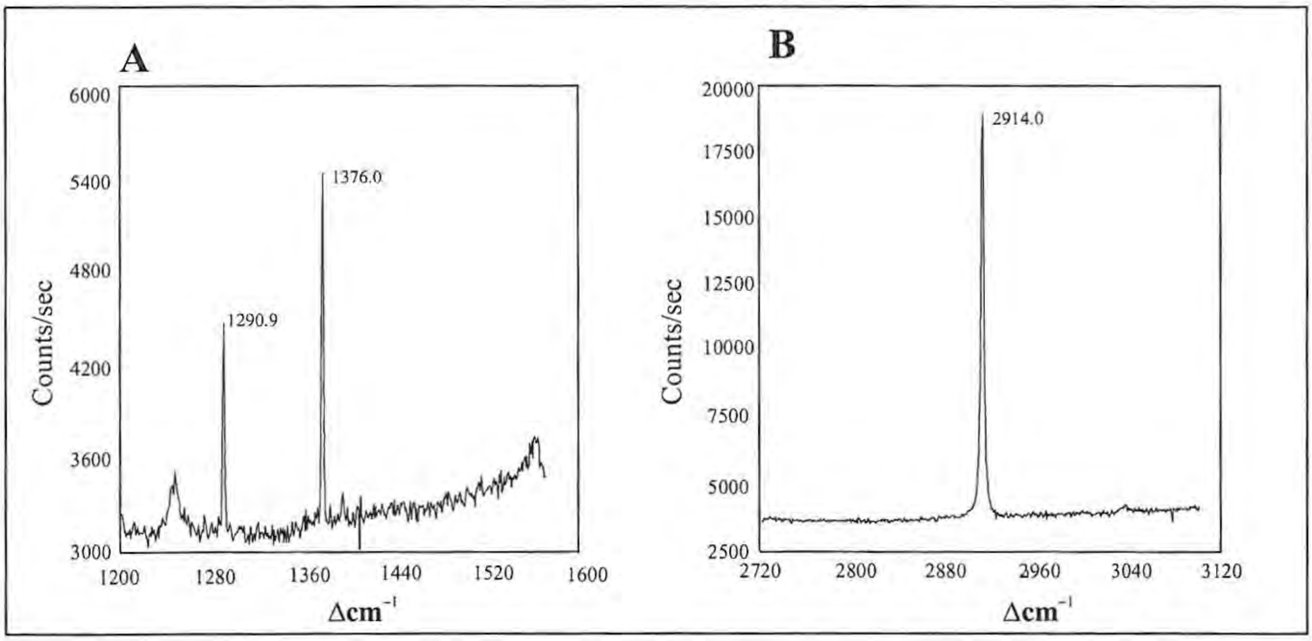

Figure 5.13. Raman spectrum of CO_2 (A) and CH_4 (B) in fluid inclusion in Group IIB vein (sample 525/25-002).

Petrographic, microthermometric and laser Raman investigations of the fluid inclusions suggests that the ore fluid responsible for the vein formation associated with gold mineralization at the Kalahari Goldridge deposit was of low salinity and consists of a mixture of aqueous and carbonic (CO_2 + CH_4) components. The presence of minor amounts of volatiles ($CO_2 \pm CH_4$) in the aqueous inclusions is indicated by the frequent decrepitation of these inclusions prior to total homogenization. The presence of these volatiles may also account for the relatively higher salinities in the aqueous inclusions in comparison with the aqueous-carbonic inclusions. As explained previously, minor amounts of $CO_2 \pm CH_4$ (< 4 mol %) in aqueous inclusions may cause optically invisible clathrates (Bodnar et al., 1985), and hence cause an increase in the salinity of the residual fluid due to the exclusion of electrolyte (e.g., NaCl, KCl, $CaCl_2$) from the clathrate structure. These salinity estimates therefore represent maximum values for the ore fluid.

The wide Th_{CO2} range between 7.5 and 25°C with three distinct modal populations (10 - 12.5°C, 15 - 17.5°C and 20 - 22.5°C) associated with the large veins apparently corresponds to an extended pressure range during fluid entrapment. The modal peak of the Th_{CO2} (10 - 12.5°C) in the Group IIA veins on the other hand, shows a restricted range giving an indication of a protracted pressure range. Giving consideration to the similarity of the fluid compositions and overlapping total homogenization temperatures of the type II and type III primary inclusions in both the Group IIA and IIB veins, it can be deduced that the ore fluid from which the veins crystallized possibly evolved from a single parental source under isothermal conditions. The time relationship between mineralization associated with the Group IIA and Group IIB veins is considered to be a progressive event based on the overlapping of the modal Th_{CO2} peak in the Group IIA veins and that of the first modal Th_{CO2} peak of the Group IIB veins.

The wide variation of CO_2 densities has also been attributed to heterogeneous trapping and fluid unmixing resulting from fluctuation of fluid pressure during hydraulic fracturing (Touret, 1977; Ramboz et al., 1982; Sibson et al. 1988), differential leakage of H_2O from aqueous-carbonic inclusions (Watson and Brenan, 1987; Hollister, 1990) or partial mixing of variable amounts of two homogeneous fluids of different compositions (Pichavant et al., 1982; Ramboz et al, 1982).

Criteria proposed by Ramboz et al., (1982) for identifying the presence of fluid unmixing include:

(i) the two types of inclusions must occur in the same region and must show clear evidence that the fluids were trapped contemporaneously;

(ii) the two members of fluids suspected to have been trapped contemporaneously, must homogenize at the same temperature (or within the same temperature range). One must homogenize to the liquid phase ($L + V \Rightarrow L$), and the other to the vapour phase ($L + V \Rightarrow V$);

(iii) if one inclusion type decrepitates before homogenising, the other must behave similarly.

The situation at Kalahari Goldridge, meets the criteria (ii) and (iii). However, it is unlikely that fluid unmixing dominated the observed variation in CO_2 densities in the Group IIB veins considering the dominant occurrence of the aqueous-carbonic inclusions and the rare occurrence of immiscible end-member pairs, which characterize the presence of fluid immiscibility.

An effect of mixing of different compositions as a possible cause for the wide spread in CO_2 density is likely to be reflected in a similar variation in the oxygen isotopic signatures of fluids from these veins. However, the oxygen isotope signatures suggest uniform fluid composition (see section 6.2 on carbon stable isotopes), whilst post-entrapment modification through loss of H_2O is not supported by textural evidence. Furthermore, field evidence indicates that the Group IIB veins post-date the Group IIA veins. Therefore a post-deformational event capable of producing such variation of fluid density in the Group IIB veins would produce a similar fluid inclusion assemblage in the Group IIA veins.

The significant occurrence of CH_4 and the wide variation of the CO_2/CH_4 ratios in the ore fluids bring into question the source of the CH_4 and whether it played any role in the precipitation of the gold. Possible sources of CH_4 can be attributed to fluid interaction with dispersed organic materials, which characterise diagenetic to low-grade sedimentary units such as the BIF units hosting the gold at Kalahari Goldridge (e.g. Mullis, 1987) and/or the thin discontinuous carbonaceous phyllitic units sandwiched between the footwall and the orebody. The significant variation in the CO_2/CH_4 ratio can be attributed to local fluctuation in fO_2 promoted by variable fluid pressures during trapping.

As noted earlier, aqueous inclusions at Kalahari Goldridge have minor occurrence in comparison with carbonic or mixed carbonic-aqueous inclusions. This observation can be attributed to extraction of H_2O for hydration of phyllosilicates (e.g. chlorite, stilpnomelane and muscovite), particularly stilpnomelane, which hosts extra water molecules in its zeolite structure. In addition, hydrolysis reactions between ore fluid and carbonaceous materials in the host rocks ($2C + 2H_2O = CO_2 + CH_4$) could also result in the loss of H_2O in inclusions.

5.2: Pressure-Temperature Constraints on Au Mineralization

A combination of fluid inclusion data and composition of mineral assemblage can be used for the P-T estimates associated with the Au mineralization at Kalahari Goldridge. The pressure and temperature existing during hydrothermal alteration and quartz vein formation are important parameters to constrain the physico-chemical conditions during gold precipitation. These estimates are based on the assumption that the alteration mineral assemblage was synchronous with the gold precipitation. Another assumption is that the P-V-T-X characteristics of the original fluids were preserved after trapping. Changes in the composition of the inclusion after trapping can render the interpretation of fluid inclusion data difficult or impossible. Such changes can be effected by post-trapping deformational events, which can be accompanied by recrystallization and fluid re-equilibration (Roedder, 1984). At Kalahari Goldridge, compelling evidence points to the fact that most of mineral assemblages particularly in the BIF, resulted from hydrothermal alteration, and thus were synchronous with the gold precipitation, whilst analyzed fluid inclusions show no evidence of post-entrapment modifications.

5.2.1: Temperature estimate

Temperature estimates during mineralization are derived from the fluid inclusion data and compositional variations of chlorite in the alteration assemblages and mineralized veins. The total homogenization temperature of fluid inclusions provides minimum temperature estimates, in the absence of fluid immiscibility, and therefore a correction factor based on an independent geothermometer is required.

At the Kalahari Goldridge deposit, overlapping total homogenization temperatures of inclusions in the mineralized veins in the range of 255 to 310°C and the rare evidence of fluid immiscibility suggest that minimum temperatures remained in this range during vein formation. In view of the widespread occurrence of chlorite in the alteration assemblages, chlorite geothermometry has been used to obtain the temperature existing during hydrothermal alteration. The experimental work of Cathelineau and Nieva (1985) and Cathelineau (1988) showed that the Al content in the tetrahedral sites of chlorite correlates positively with temperature. These experiments also documented that the effect of pressure on the geothermometer is negligible.

Microprobe analyses of chlorites in Au-quartz veins, BIF and interbedded schist yielded mineralization temperatures from 345 to 400°C (Table 3.4A-C, Figs. 5.14 and 5.15). A general observation of the estimated temperature is that the highest values exist in the altered BIF samples, whilst the lowest temperatures are recorded in the veins. The low values in the veins would suggest that these temperatures represent final filling temperatures, as vein crystallization is associated with the waning stages of the hydrothermal fluid during mineralization. Further constraints on the temperature are based on the coexistence of siderite-pyrite-pyrrhotite-magnetite assemblage in the alteration zone. The assemblage defines the upper stability limit of the temperature during the alteration process, based on the experimental data of Seguin (1971) of phase relations in the Fe-C-O-S system. The data of Seguin (1971) documented that this assemblage are stable up to a temperature of 382 ± 13°C at 2kbar.

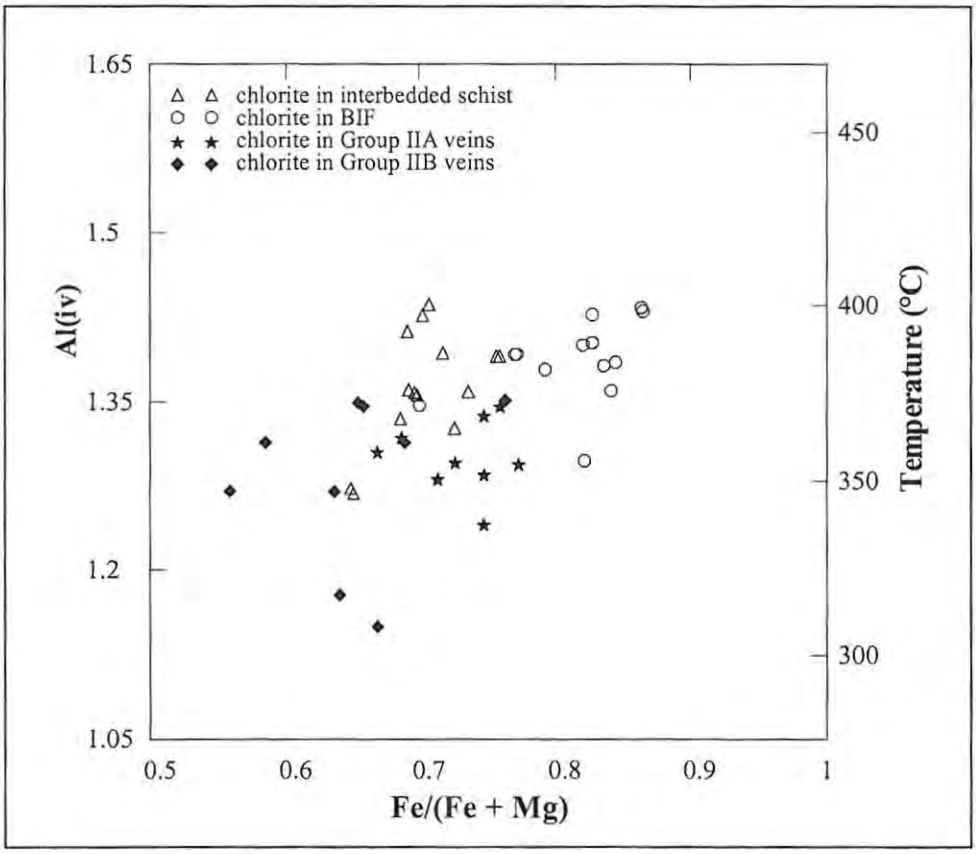

Figure 5.14. Plot showing Al(iv)-Fe/(Fe + Mg)-Temperature variations in chlorites in the alteration zone at the Kalahari Goldridge deposit. See also Figure 5.15.

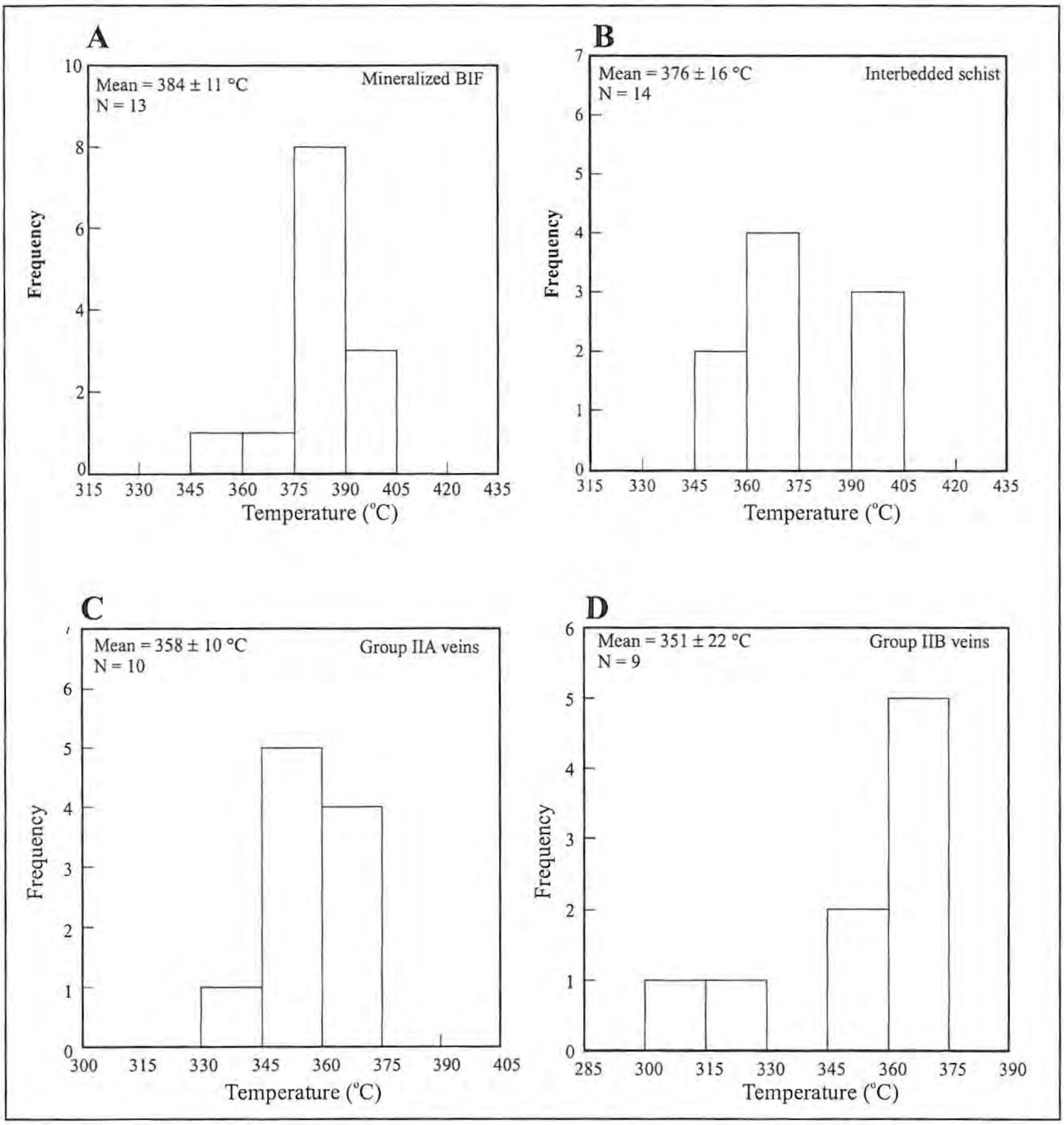

Figure 5.15. Histograms of temperature estimates based on chlorite geothermometry from various lithologies at the Kalahari Goldridge deposit. A. Mineralized BIF, B. Interbedded schist, C. Group IIA veins and D. Group IIB veins.

5.2.2: Pressure estimates

The pressures existing during the mineralization at Kalahari Goldridge can be constrained using calculated isochores of primary inclusion densities from representative fluid inclusion compositions in the mineralized veins, in conjunction with independent temperature estimates from chlorite crystallization temperatures in the mineralized quartz veins and alteration assemblages. The isochores define the trajectory in P-T space along which the fluid was trapped and are generally calculated based on the assumption that the inclusions are a closed system. They are thus a constant-volume and constant-mass system so that independent temperatures or pressures allow for the interpolation of other variables.

The isochores for aqueous inclusions were calculated using the equation of Zhang and Frantz (1987) with average values of Th_{total}. Isochores for one-phase carbonic inclusions (CO_2-rich, CH_4-rich or CO_2-CH_4) were calculated using the modified Redlich-Kwong (MRK) equation of Holloway (1981), based on average fluid densities, giving consideration to the tight clustering of the homogenization temperatures. The geometrical ideal mixing procedure of Brown and Lamb (1989) was used to construct isochores for the mixed aqueous-carbonic (CO_2-CH_4-H_2O-NaCl) inclusions. In this method, the location of the mixed fluid isochore is assumed to lie between the intersection of isochores of the end-member fluids H_2O-NaCl and CO_2, which constitute the ternary fluid system (CO_2-H_2O-NaCl), scaled to the volume percent CO_2. In determining the position of the end-member isochores in the CO_2-H_2O-NaCl system, Brown and Lamb (1989) used the MRK equation of Kerrick and Jacob (1981) for the CO_2 phase, and the formulation of Zhang and Frantz (1987) for the H_2O-NaCl phase for aqueous densities < $1 gm^{-3}$, or their modified version of the Zhang and Frantz (1987) equation for aqueous densities > $1 gm^{-3}$.

In this study, the isochore for the aqueous end-member was determined using the Zhang and Frantz (1987) equation modified by Brown and Lamb (1989) and the MRK equation of Holloway (1977, 1981) for the CO_2 end-member isochore, instead of the Kerrick and Jacob (1981) equation, because the former takes into account the CH_4 contents in CO_2. Furthermore, Duane et al. (1992) demonstrated that incorporating about 4% CH_4 into CO_2 causes error in pressure estimates in the range of 15 to 20%. The volume percent of the carbonic phase was calculated based on the graphical data of Schwartz (1989), which is itself based on the experimental data of Gehrig (1980) and Bowers and Helgerson (1983) at 40°C, and utilizes the CO_2 density, Th_{total} measurements of the CO_2-H_2O-NaCl inclusions and salinity of the inclusions. This approach eliminates the visual estimation of the volume fraction, which can be associated with significant uncertainties due to irregular shape of the inclusion, extent in the third dimension and optical effects related to differences in the refractive indices of the various phases (Brown and Lamb, 1989). Furthermore, the choice of 40°C by Schwartz (1989) is based on the observation by Burrus (1981) that, at temperatures slightly above the critical point of CO_2 ($\approx +31° < T < 50°C$), coexisting phases of CO_2 and H_2O-NaCl act as pure end members since solubility of H_2O in CO_2 is less than 0.6 mole percent and that of CO_2 in H_2O is less than 3 mole percent at these temperatures and pressures below 500 bars. However, errors due to the mutual solubility of CO_2 and H_2O have been corrected for in the graphical approach.

On the basis of the wide Th_{CO_2} for inclusions in the Group IIB veins, the lowest and highest bulk density data were applied to determine the isochores, whilst average values were used for inclusions associated with the Group IIA veins, due to the tight clustering of Th_{CO2}. The calculated isochores for the various fluids associated with the mineralization at the Kalahari Goldridge deposit are presented in Figures 5.16A and B. Given the temperature interval 345 to 400°C determined from the chlorite compositions, projected entrapment pressures range from approximately 0.75 to 2.0 kbars for the large mineralized veins, and 1.0 to 2.0 kbars for the ladder veins.

The projected pressures for the given temperature range (345 - 400°C) consistently show overlapping values for the carbon-containing inclusions from 1.7 to 2.0 kbars for both mineralized veins. Such tight pressure constraints for the carbon-bearing inclusions in both mineralized vein systems suggest that the fluids must have equilibrated under similar P-T conditions during mineralization. The aqueous inclusions, on the other hand, show steep isochores with lower entrapment pressures ranging from approximately 1.0 to 1.5 kbars in the Group IIA veins and, 0.7 to 1.3 kbars in the Group IIB veins, suggesting that they were trapped during the later stages of the veining.

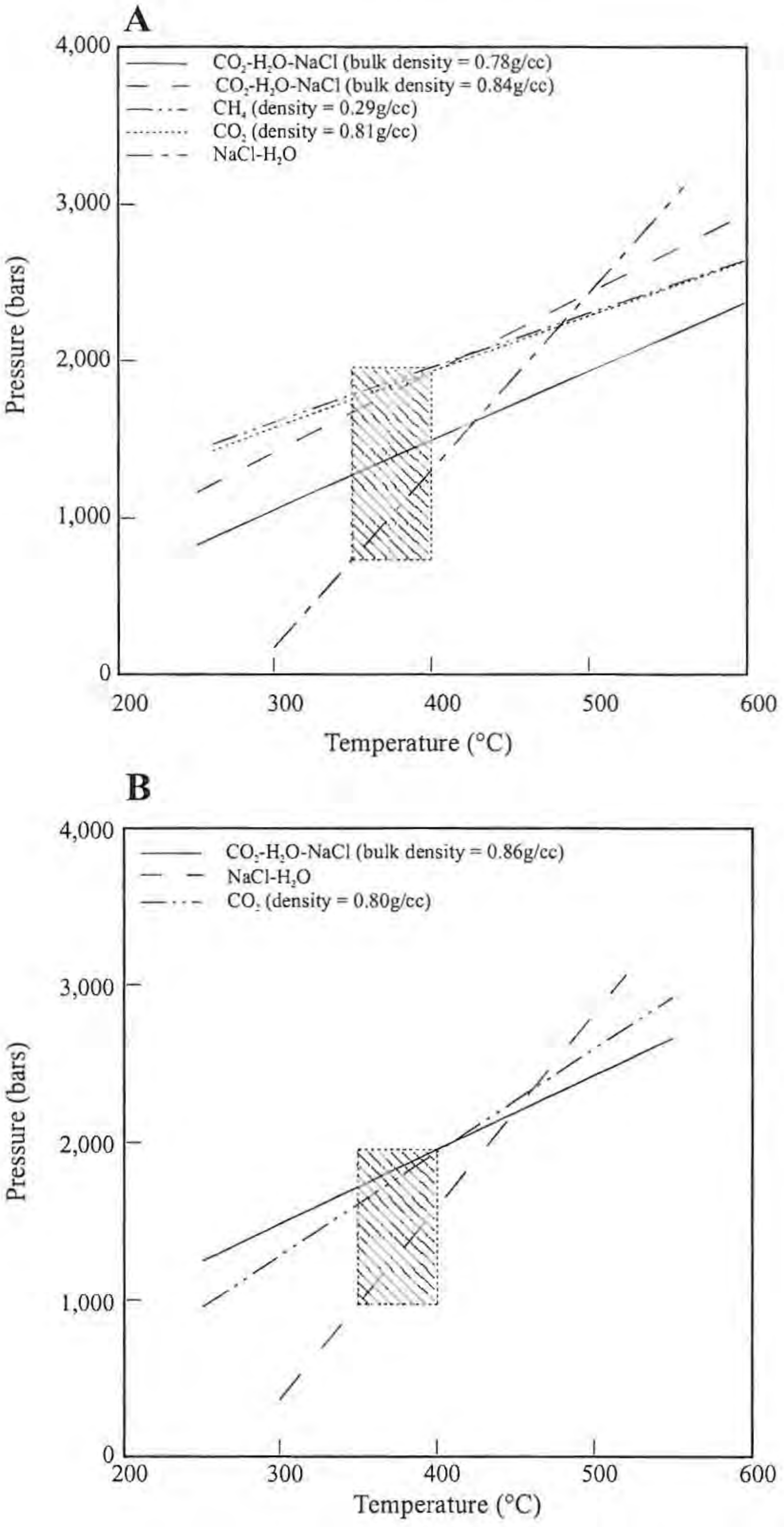

Figure 5.16. Pressure-temperature plots showing conditions (boxed area) associated with gold mineralization at the Kalahari Goldridge deposit. A. represents conditions associated with the Group IIB veins, and B. the conditions associated with Group IIA veins. See text for isochore derivation and discussion

5.3: Physico-chemical Conditions of the Ore Fluid System

One of the major aims of this study is to define the composition of the ore fluid responsible for gold deposition at Kalahari Goldridge as well to as constrain the physicochemical parameters, which controlled the transport and deposition of the gold. Combinations of mass action relationships are useful for the calculation of such thermodynamic parameters as fO_2, ΣS, XCO_2 and pH of the fluid system. These parameters provide a fundamental understanding of the fluid composition, mode of transport and depositional mechanism of the gold. Defined conditions can also be compared with fluid associated with gold deposition in other Archaean systems worldwide.

At Kalahari Goldridge, mass action relationships of end-member compositions of alteration assemblages, as well as fluid inclusion compositions were used to constrain the thermodynamic parameters. (e.g., Neall and Phillips, 1987; Böhlke, 1989; Cassidy and Bennet, 1993; Zhou et al., 1994). Mineral reactions written from three chlorite end-members, clinochlore {$Mg_5Al_2Si_4O_{10}(OH)_8$ - Chl-1}, daphnite {$Fe_5Al_2Si_4O_{10}(OH)_8$) - Chl-2} and Al-free chlorite {$Mg_6Si_4O_{10}(OH)_8$, - Chl-3}, the Fe end-members of carbonate ($FeCO_3$) and stilpnomelane ($K_{0.625}Fe_6AlSi_8O_{21}(OH)_{5.625}\cdot3/2H_2O$) were used for the calculation of the physicochemical parameters.

5.3.1: Basis for the thermodynamic calculation

Thermodynamic data for the calculations were taken from Walshe (1986) for chlorites, Miyano and Klein (1989) for stilpnomelane, and Robie et al. (1978) for siderite, magnetite and hematite. Data for pyrite, pyrrhotite and siderite were taken from Helgeson (1969). Assuming ideal mixing, the activities of the end-member compositions are calculated from microprobe data using the activity models of Walshe (1986) for chlorite, and Miyano and Klein (1989) for stilpnomelane. The activity of siderite is calculated from the Fe/(Fe+Mg) ratio. Magnetite, pyrite and pyrrhotite show nearly ideal composition and therefore a unit activity is assumed. Unit activity is also assumed for liquid water. Fugacity coefficients of gaseous species are taken from the data of Ryzhenko and Volkov (1971). Activity coefficient of aqueous species (e.g. γ_{H2S}) is calculated using the modified Debye-Hückel equation and data in Helgeson et al. (1981) and Truesdell (1984). Expressions and formulae used for calculating activities and activity coefficients are listed in Appendix III.

5.3.2: Oxygen fugacity (fO_2) and total sulphur content ($a_{\Sigma S}$)

The fO_2 and $a_{\Sigma S}$ at Kalahari Goldridge are constrained using mass action relationships involving the mineral assemblage carbonate, magnetite, pyrite, and pyrrhotite, and fluid inclusion compositions at 350°C and 1.7 kbar (e.g. Neall and Phillips, 1987). Mineral reactions for the calculations are represented as:

$$\underset{\text{magnetite}}{Fe_3O_4} + 3CO_2 = \underset{\text{siderite}}{3FeCO_3} + 1/2O_2 \qquad [5.1]$$

$$\underset{\text{siderite}}{FeCO_3} + H_2S_{(g)} = \underset{\text{pyrrhotite}}{FeS} + CO_2 + H_2O(l) \qquad [5.2]$$

$$\underset{\text{Chl-3}}{5/6Mg_6Si_4O_{10}(OH)_8} + \underset{\text{Chl-2}}{Fe_5Al_2Si_4O_{10}(OH)_8} + 5CO_2 =$$

$$\underset{\text{Siderite}}{5FeCO_3} + \underset{\text{Chl-1}}{Mg_5Al_2Si_4(OH)_8} + \underset{\text{quartz}}{10/3SiO_2} + 10/3H_2O \qquad [5.3]$$

The fO_2 and a_{H_2S} are calculated with equations (5.1) and (5.2) respectively. The fCO_2 used in the reaction is calculated from equation (5.3). The calculated values for the BIF, Group IIA and IIB veins are presented in Table 5.6. The calculated fO_2 ranges give an overall range from $10^{-29.98}$ to $10^{-31.24}$ (Group IIA veins, $10^{-30.72}$ to $10^{-30.47}$; Group IIB veins, $10^{-30.92}$ to $10^{-29.90}$ and BIF, $10^{-31.24}$ to $10^{-30.34}$). In view of the common occurrence of CH_4 and CO_2 in fluid inclusions in mineralized veins, the fO_2 can also estimated according to the reaction:

$CO_2 + 2H_2O = CH_4 + 2O_2$ [5.4]

Assuming equilibrium is established among the involved species. The equilibrium constant for the reaction is calculated from the equation of Ohmoto and Kerrich (1977). The XCH_4 and XCO_2 were derived from the Raman data for fluid inclusions. Given that high CH_4/CO_2 ratios occur in inclusions proximal to carbonaceous meta-pelites, which is attributed to the hydrolysis reaction between carbon and the ore fluid, the lowest CH_4/CO_2 ratios are assumed to represent the original ratios prior to fluid interaction with the carbonaceous rocks. Therefore, XCH_4 and XCO_2 in the fluid are calculated using CH_4/CO_2 ratios of 1.2 and 0.3 for the Group IIA and Group IIB veins respectively. This gives fO_2 values of $10^{-32.96}$ for the Group IIA veins and $10^{-32.12}$ for the Group IIB veins. These estimates provide minimum fO_2 conditions of the ore fluids associated with mineralization. The combined data give fO_2 for ore fluid conditions associated with gold mineralization ranging from $10^{-29.98}$ to $10^{-32.96}$. These estimated redox conditions of the ore fluid bracket the CO_2-CH_4 buffer ($10^{-33.5}$) and pyrite-pyrrhotite-magnetite buffers ($10^{-30.80}$) as shown in Figure 5.17. The overall a_{H_2S} varies from $10^{-2.44}$ to $10^{-2.23}$ (BIF: $10^{-2.44}$ to $10^{-2.29}$; Group IIA veins: $10^{-2.39}$ to $10^{-2.23}$ and Group IIB veins: $10^{-2.36}$ to $10^{-2.32}$). Using an activity coefficient of 0.32 for H_2S, this corresponds to an overall range of 0.018 to $0.011m_{\Sigma S}$ in the ore fluid. The estimated ΣS contents are consistent with most sub-amphibolite facies Archaean gold-ore fluids, which fall in the range $10^{-3.5}$ to $10^{-1}m_{\Sigma S}$ (Mikucki and Ridley, 1993).

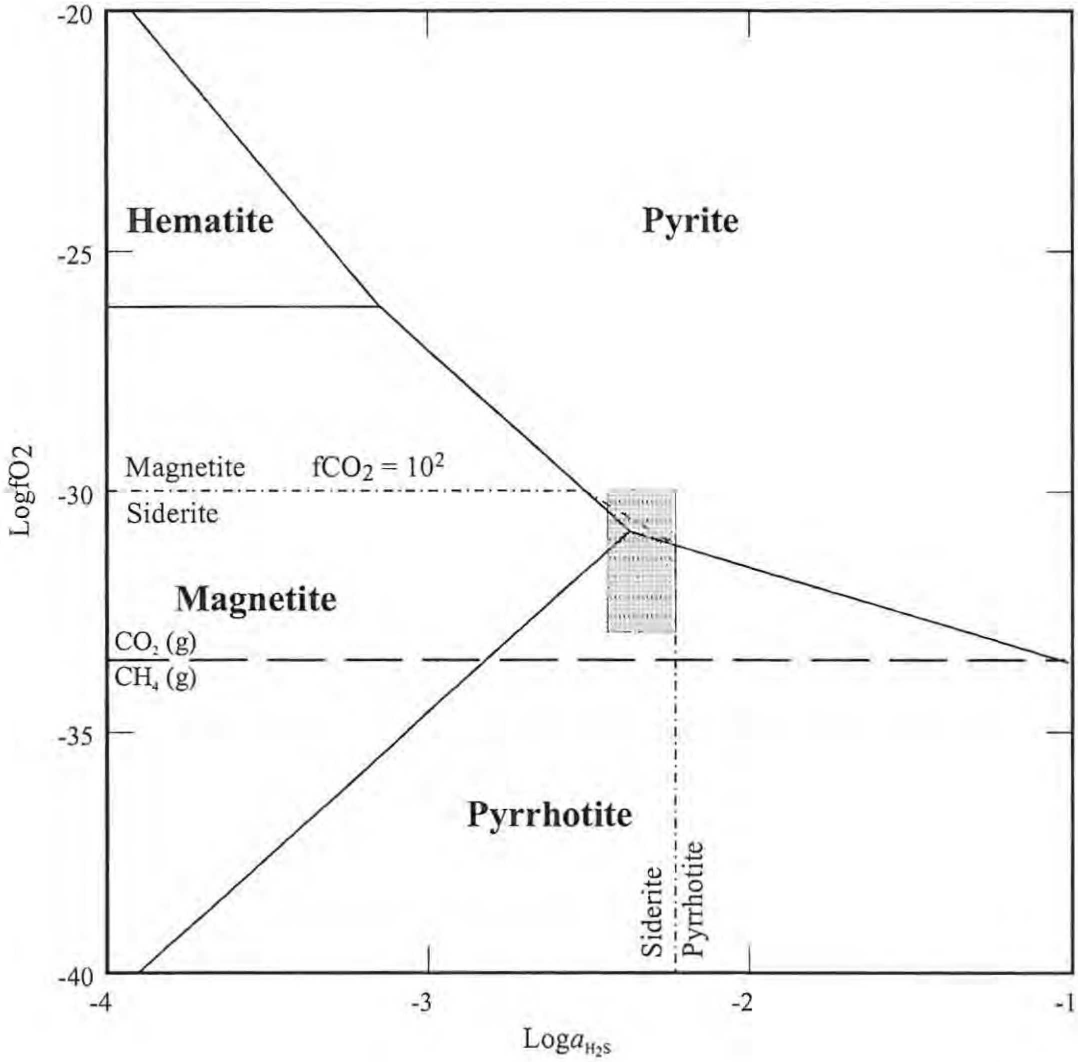

Figure 5.17. Stability field of selected mineral phases as a function of $\log aH_2S$ and $\log fO_2$ at 350°C and 1.7kbars. Thick lines represents reaction boundaries between Fe-oxides and sulphide phases. The CO_2-CH_4 redox buffer is shown as heavy dashed lines. Shaded area represents ore fluid condition at the Kalahari Goldridge deposit and is constrained by the siderite-pyrite-pyrrhotite assemblage and fluid inclusion composition.

5.3.3: CO_2 composition in ore fluid

During progressive interaction of CO_2-rich ore fluid with wallrock, the original mineral assemblage in the wallrock commonly buffers the onset of hydrothermal alteration to low CO_2 values of the ore fluid. Increasing alteration is marked by an increase in the CO_2 composition in the ore fluid, reaching the initial composition in the most altered units. The initial CO_2 composition can therefore be represented by the mineral assemblage in the most intensely altered wallrock in the deposit. On this basis, the composition of CO_2 in the ore fluid at the time of mineralization have been calculated for a number of mesothermal lode gold systems using isobaric T-XCO_2 univariant curves (e.g., Kishida and Kerrich 1987; Clark et al. 1989; Neall and Phillips 1987) or isobaric-isothermal activity-XCO_2 univariant curves (e.g., Kishida and Kerrich 1987; Cassidy and Bennet 1993) with mineral compositions in the alteration assemblage.

At Kalahari Goldridge, the mineral assemblages associated with each mineralized veining event (Groups IIA and IIB) cannot be distinguished due to the broad similarities in the mineral composition in the host rock. To avoid any ambiguity, the XCO_2 in this study is calculated independently based on coexisting carbonate and chlorite in each vein under isobaric conditions of 1.7 kbars for the Group IIA veins and a range of 1.3 to 1.7kbars for the Group IIB veins. An equilibrium reaction in the system FeO-Al_2O_3-SiO_2-H_2O-CO_2-MgO of end-member composition is derived to constrain the composition of CO_2 in the ore fluid at the time of mineralization according to equation 5.3.

Isobaric T-XCO_2 curves for the mineralized veins (Fig. 5.18) at the temperature range for the mineralization (350 - 400°C) at Kalahari Goldridge gives XCO_2

ranges of 0.06 to 0.16 for the ore fluid associated with Group IIA veins and 0.05 to 0.14 for the Group IIB veins.

The estimated composition at Kalahari Goldridge is consistent with the calculated XCO_2 compositions for most Archaean gold systems, spanning from 0.05 to 0.25 (Mikucki and Ridley, 1993). For BIF-hosted gold deposits, XCO_2 values ranging from 0.09 to 0.22 have been determined (Mikucki and Groves, 1990). The range of estimated composition for both sets of veins shows that the fluid associated with veining possibly evolved from the same homogenous parental source. The estimated fCO_2 shows higher magnitude in the BIF than the veins and may be attributed to the fact that fluid infiltration and equilibration with the host BIF resulted in the significant loss of the CO_2 to the host BIF during carbonation.

Table 5.6. Calculated $\log fCO_2$, $\log fO_2$ and $\log a_{H_2S}$ in mineralized veins and BIF at the Kalahari Goldridge deposit.

Lithology	Sample No.	$\log fCO_2$	$\log fO_2$	$\log H_2S$
Group IIA veins	525/12A	2.40	-30.47	-2.32
	13175 /2C	2.29	-30.70	-2.35
	531/184	2.05	-30.70	-2.35
	PH/6	2.04	-30.72	-2.36
	588-10C	2.55	-30.67	-2.35
Group IIB veins	532-11A	2.48	-30.44	-2.31
	585-20	1.98	-29.98	-2.23
	587/2C-4	1.98	-30.92	-2.39
	DD17/183	2.11	-30.35	-2.30
BIF	NQH/10A	2.54	-30.55	-2.33
	525/12A	2.53	-30.34	-2.29
	524/8	2.52	-30.78	-2.37
	13175 /2C	2.53	-30.84	-2.38
	532/9	2.50	-31.24	-2.44

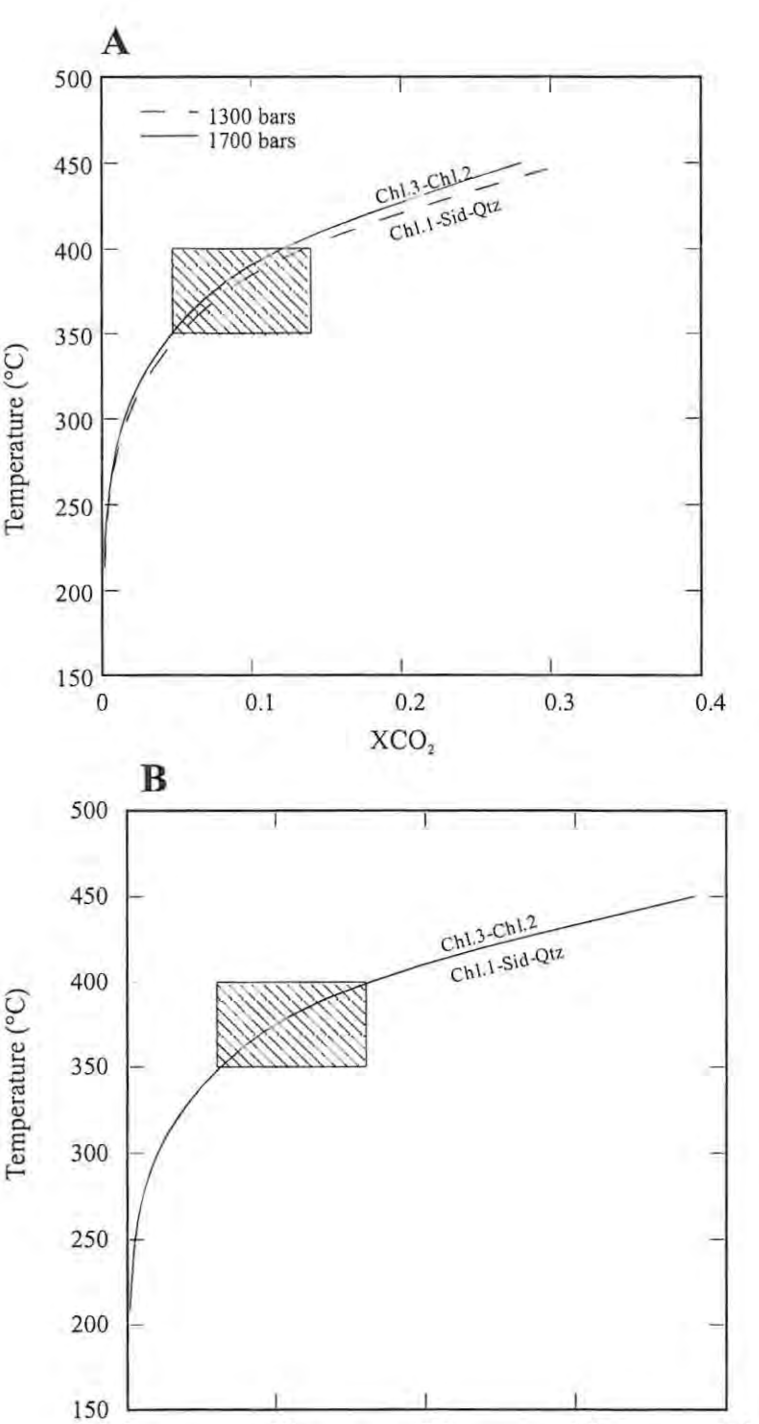

Figure 5.18. Isobaric T-XCO$_2$ diagrams for the alteration assemblage associated with Group IIA and IIB mineralized veins at the Kalahari Goldridge deposit. A. Group IIA veins and B. Group IIB veins. Box represents conditions of mineralization. Equilibrium curves were calculated using end-member compositions of chlorite-carbonate assemblage. Activities for solid-solution end-members were calculated assuming ideal site-mixing models (see text). Abbreviations: Chl.1 = clinochlore, Chl.2 = daphnite, Chl.3 = Al-free chlorite, Sid = siderite and Qtz = quartz.

5.3.4: pH estimate

Derivation of the pH conditions of the fluid during gold precipitation require the salinity estimate from fluid inclusion data and ratios of main cations notably Na^+/K^+ from cation exchange equilibria involving mineral assemblages in the altered wall rock. The salinity data assume K^+ and Na^+ as the dominant cation species in the solution. The molal concentrations of Na^+ and K^+ are thus generally approximated to equal the salinity of the ore fluid:

$$mNa^+ + mK^+ = mCl^- \qquad [5.5]$$

The quantitative estimate of the pH at Kalahari Goldridge cannot be estimated due to the absence of Na-bearing minerals in the deposit, making the Na^+/K^+ ratio estimate impossible. Therefore, based on the available information, only the direction of the pH can be deduced. In this case, two major metasomatic reactions can be used to define the shift in the pH during mineralization. This involves the assemblage stilpnomelane-chlorite-quartz-carbonate represented by equations 5.6 and 5.7.

$$125/3SiO_2 + 35/6Chl\text{-}3 + 35/12H_2O + 12Chl\text{-}2 + 25/4K^+ =$$
$$10Stilp + 25/4H^+ + 7Chl\text{-}1 \qquad [5.6]$$

$X^{2+} + CO_2 + H_2O = XCO_3 + 2H^+$ [5.7], where $X = Fe + Mg + Mn$

In the above reactions, the formation of stilpnomelane (stilp) and carbonate is associated with the consumption of K^+ and CO_2 from the fluid and the concomitant release of H^+ in both reactions to the fluid. The net consequence is the lowering of the pH of the fluid, which plays a significant role in the gold solubility (see Chapter 7).

CHAPTER 6: STABLE ISOTOPE GEOCHEMISTRY

6.1: Introduction

Recent advancement in the understanding of stable isotope systematics such as the fractionation behaviour of the isotopes in a variety of geological environments has brought significant insight into the genesis of fluids associated with lode gold deposits in sub-amphibolite facies terranes (e.g., Ohmoto and Rye, 1979; Taylor, 1974, 1979). Prior to this, the origins of hydrothermal fluids from which mesothermal lode gold deposits in low-grade metamorphic terrains were generated have been a subject of constant debate for decades. As the main constituents in most of these high-temperature fluids, the stable isotopes of carbon (C), sulphur (S), hydrogen (H) and oxygen (O) have been used extensively in these studies, based on gases extracted from mineral phases associated with these deposits.

As part of this study, gases were extracted from alteration minerals to analyze for S, C and O isotopic compositions in these minerals. Minerals prepared for isotopic analysis include quartz (O-isotopes), carbonate (O- and C-isotopes), pyrite and pyrrhotite (S-isotopes), and fluid inclusions (C-isotopes). These studies aimed to (i) characterize the isotopic composition of the minerals and to investigate any variation in the different host lithologies, (ii) determine whether isotopic equilibrium was established during the mineralization and (iii), identify the source of the hydrothermal fluid as well as the source of sulphur and carbon in the fluid.

6.2: Sulpur Isotope Geochemistry

6.2.1: Sampling and analytical technique

Forty sulphide samples (including 14 pyrrhotites and 26 pyrites) from the mineralized veins and host rocks at the Kalahari Goldridge deposit were examined for their sulphur isotope signatures. Optically pure samples of the sulphides were handpicked with the aid of a binocular microscope from coarsely crushed vein and host rocks. Sulphides from the vein and host BIF consist of large euhedral grains measuring up to 4mm. Samples from schist interbedded with BIF were separated from thin sulphide laminations or in some cases from massive sulphide aggregates.

Following the procedure of Yanagisawa and Sakai (1983), the sulphides were first decomposed with HNO_3 and the resultant aqueous sulphate precipitated as $BaSO_4$. The $BaSO_4$ was heated with vanadium pentoxide (V_2O_5) and silica glass in a highly evacuated glass line to liberate the sulphur as SO_2. The sulphur isotopic ratio of the SO_2 gas derived was determined using a Finnigan MAT delta E mass spectrometer at the Geological Institute, University of Tokyo by Dr. Akira Imai. The isotopic compositions are expressed in $\delta^{34}S$ ‰ relative to Canõn Diablo Troilite (CDT).

6.2.2: Results

The S-isotope data are given in Table 6.1 and graphically illustrated in Figures 6.1 to 6.3. Pyrites in the BIF show a $\delta^{34}S$ range from +2.93 to +4.94 ‰ whilst the pyrrhotite range is from +2.71 to +3.69 ‰. Two analyzed pyrite samples from the Group IIA veins showed $\delta^{34}S$ values of +2.8 to +4.25 ‰ whilst the pyrrhotite samples showed a restricted range from +3.64 to +4.24‰ for the three sample analyses. The $\delta^{34}S$ signatures of pyrite in the Group IIB veins vary from +2.69 to +4.25 ‰ whilst pyrrhotite ranges from +1.95 to +4.05 ‰.

Lightest $\delta^{34}S$ values were found in sulphide associated with the schist interbedded with BIF, and are less than +2.0‰. Four of the seven samples showed depleted values from -1.23 to -0.47 ‰, and the other three samples showed slightly positive values from +0.78 to +1.85 ‰. The observed isotopic values of the sulphides in the veins and the host BIF fall within the range of +1 to +6 ‰ exhibited by most Archaean mesothermal gold deposits derived from reduced hydrothermal fluids (Kerrich, 1989).

In isotopic studies of sulphides in black shales in Maine, USA, Oliver et al. (1992) pointed out that at low fluid fluxes, kinetic effects may be important operating parameters which would result in reactive mineral species such as pyrrhotite equilibrating with the fluid, whilst less reactive minerals like pyrite retain their isotopic values prior to the fluid interaction. On the other hand, they noted that when large fluid fluxes of sulphur-bearing fluids infiltrate sulphide-bearing rocks with isotopic composition distinct from the average sulphur values of the host rock, there is potential for considerable change and homogenization of the sulphur isotopic values. On this basis, it can be concluded that the slightly positive S-isotopic values of sulphides in the schist can be attributed to precipitation of remobilized diagenetic sulphides in the schist by the hydrothermal fluid during gold precipitation.

Table 6.1. Sulphur isotope composition of sulphides from the Kalahari Goldridge deposit.

Sample No.	$\delta^{34}S_{pyrite(py)}$ (‰)	$\delta^{34}S_{pyrrhotite(po)}$ (‰)	$\Delta\delta^{34}S_{py-po}$ (‰)	Isotopic Temp (°C)	Sample Source
587-8F	+3.27	+4.05	-0.78		Group IIB vein
NQH-10B	+3.98	+3.78	0.2	952	Group IIB vein
587-7	+3.36	+2.88	0.48	518	Group IIB vein
589-13C		+3.55			Group IIB vein
NQH-10A		+1.95			Group IIB vein
585-7A	+2.69				Group IIB vein
585-10B	+3.80				Group IIB vein
DD17-4A	+3.84				Group IIB vein
532-7B	+4.25	+3.71	0.54	472	Group IIA vein
532-7A	+2.80				Group IIA vein
588-10/5		+4.24			Group IIA vein
589-6C		+3.64			Group IIA vein
534/300	+4.94				BIF
534/318	+4.20				BIF
NQH-5	+4.45				BIF
527 10B	+3.65				BIF
MSH-W	+4.15				BIF
585-BD	+3.71				BIF
588-10B	+3.10	+3.40	-0.3		BIF
587-18B		+2.71			BIF
525-18A		+2.69			BIF
KLG/W-7	+4.55				BIF
MSH/W-4	+4.36				BIF
MSH/3	+4.56	+3.69	0.87	314	BIF
13175-2B	+2.93				BIF
MSH/W-1	+3.90				BIF
588-21A		-0.54			Massive pyrrhotite in interbedded chlorite schist
529-16A	-0.59				Pyrite vein perpendicular to foliation in interbedded chlorite schist
529-16B/PD	-1.23				Pyrite vein perpendicular to foliation in interbedded chlorite schist
529-16B/PL	-0.47				Pyrite parallel to foliation in interbedded chlorite schist
587-18A		+1.25			Chlorite schist trapped in quartz vein
452-24B	+0.78				Pyrite parallel to foliation in interbedded chlorite schist
MSH/W-6	+1.85				Pyrite parallel to foliation in interbedded chlorite schist

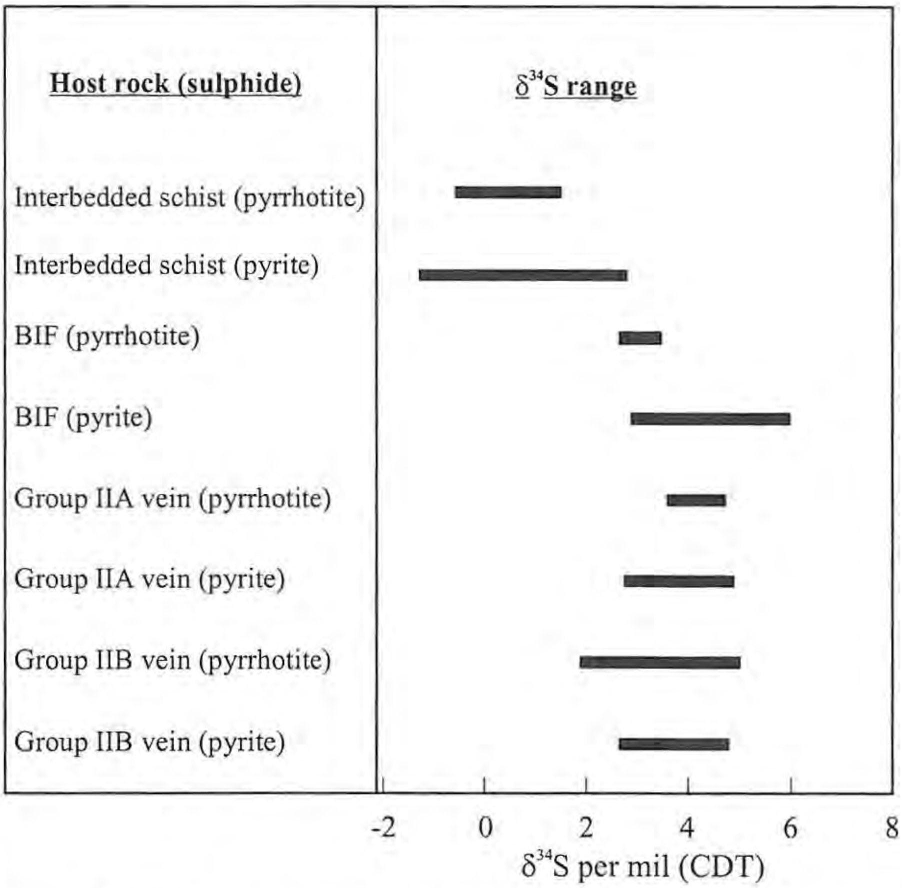

Figure 6.1 δ^{34}S range for sulphides in various lithologies at the Kalahari Goldridge deposit.

6.2.3: Sulphur isotope geothermometry

The temperature of the mineralization at the Kalahari Goldridge deposit may be evaluated based on coexisting pyrite and pyrrhotite in several parts of the ore assemblage. Because the application of the sulphide geothermometry is based on equilibrium sulphur-isotope fractionation between coexisting sulphur-bearing phases (Ohmoto and Rye, 1979), it provides a base to determine whether equilibrium was attained during sulphidization at the Kalahari Goldridge deposit.

Ohmoto and Rye (1979) noted that successful application of the geothermometer depends most importantly on the contemporaneous crystallization of the mineral pair and furthermore, the mineral pairs must be formed in equilibrium with solution under uniform temperature and chemical conditions (e.g., pH, fO_2).

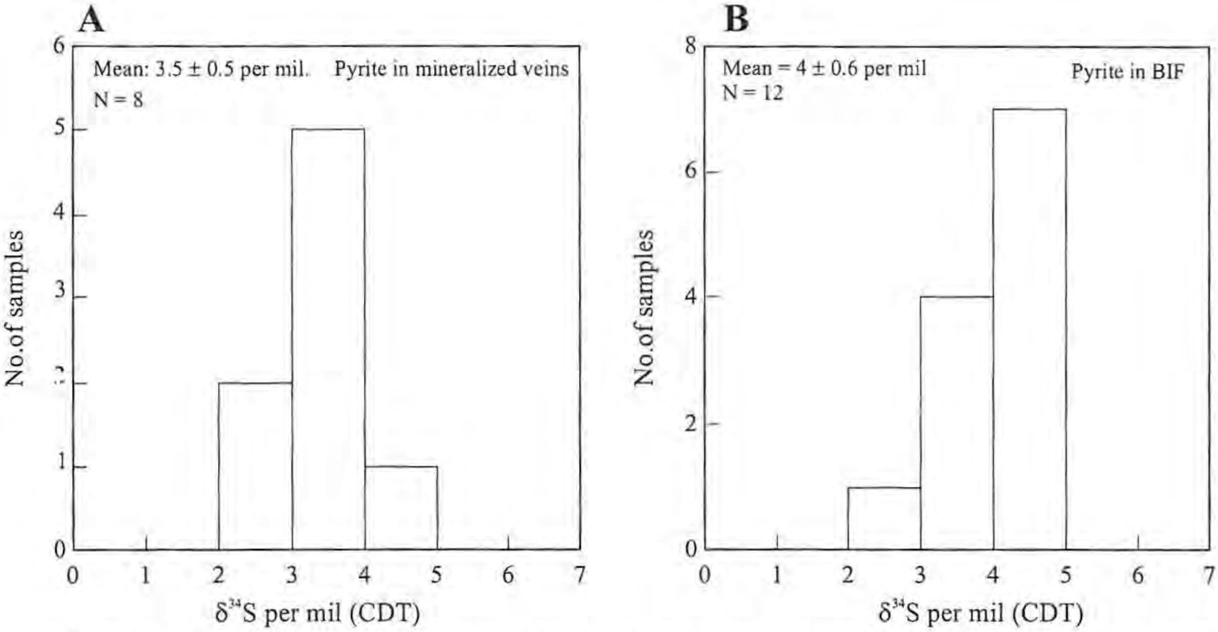

Figure 6.2. Histograms showing sulphur isotope composition of pyrite in mineralized veins (Group IIA and Group IIB veins) "A" and BIF "B", Kalahari Goldridge deposit.

The fractionation between pyrite and pyrrhotite ($\Delta\delta^{34}S_{py-po}$) derived from $\delta^{34}S$ signatures of the sulphides show a scattered range from -0.78 to 0.87 ‰ (Table 6.1). Using the experimental data of Ohmoto and Rye (1979), most of the pairs yielded anomalously high temperatures from 472 to 951°C outside the range obtained from chlorite geothermometry (350 to 400°C) except one sample, which yielded a temperature of 315°C. This observation suggests that although the pyrite-pyrrhotite pair exhibits textural equilibrium in most of the ore mineral assemblages examined, their precipitation may have occurred out of isotopic equilibrium with the ore fluid.

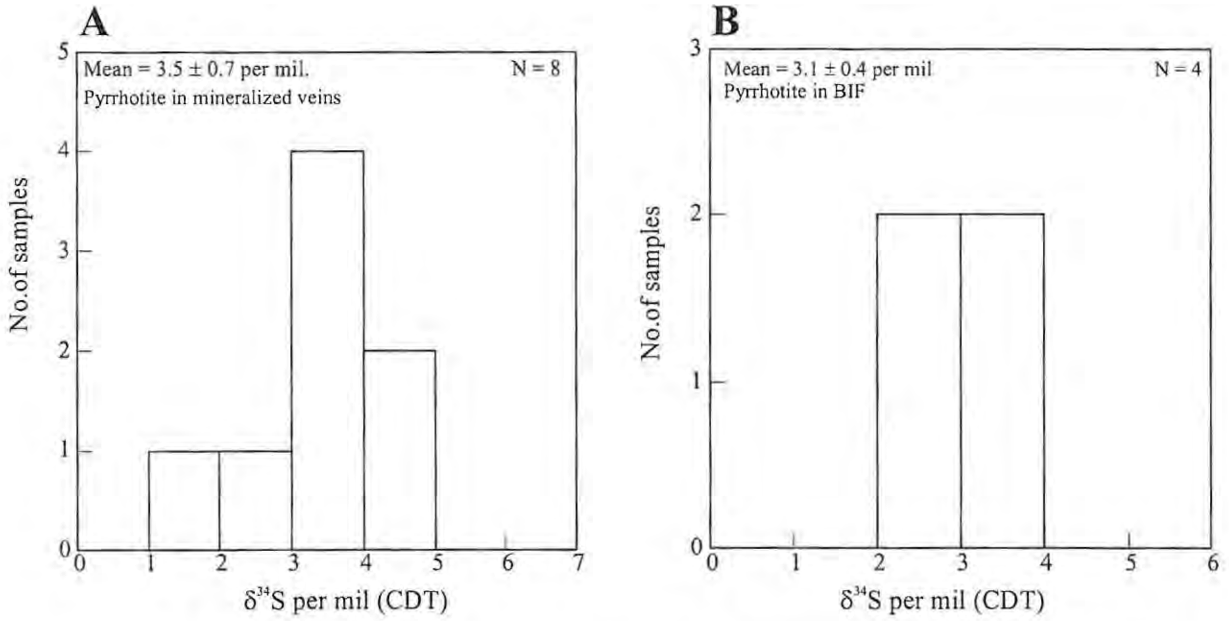

Figure 6.3. Histograms of sulphur isotope composition of pyrrhotite in mineralized veins "A", and BIF "B" at the Kalahari Goldridge deposit.

Such disequilibrium could be the result of (i) isotopic exchange from fluids of variable source, (ii) continued isotopic exchange between the sulphide-pair after precipitation, or (iii) the crystallization of the sulphide-pair occurring at temperatures below 200°C (Ohmoto and, Rye 1979).

At the Kalahari Goldridge deposit, giving consideration to the restricted estimated total sulphur composition shown in Chapter 6, the high temperature estimate of the mineralization (350-400°C) and the overlapping paragenetic relationship between pyrite and pyrrhotite, it can be concluded that continued isotopic exchange between the sulphide-pair after precipitation is the most probable cause of the isotopic disequilibrium between the sulphides.

6.2.4: Estimate of $\delta^{34}S$ of the primary ore fluid ($\delta^{34}S_{(\Sigma S)}$).

The sulphur isotope composition of the hydrothermal sulphides reported above can be used to define the source of the sulphur responsible for sulphidation at the deposit. The experimental work of Ohmoto and Rye (1979) showed that the S-isotopic composition of the sulphides is controlled primarily by the ambient temperature, fO_2 and pH as well as the sulphur isotopic composition of the original fluid, $\delta^{34}S_{(\Sigma S)}$. Therefore, interpretation of the source of the sulphur must take into consideration these parameters.

At the estimated temperature range for the mineralization at the Kalahari Goldridge deposit (350 - 400°C), the fractionation between the pyrite and H_2S ($\Delta\delta^{34}S_{py-H_2S}$), and between pyrrhotite and H_2S ($\Delta\delta^{34}S_{po-H_2S}$), according to the data of Ohmoto and Rye (1979), ranges from 1.03 to 0.98 ‰ and 0.26 to 0.22 ‰ respectively. Therefore, given the estimated $\delta^{34}S$ composition of the sulphides, it can be deduced that the pyrite and pyrrhotite precipitated from fluids with $\delta^{34}S_{H_2S}$ of approximately +1.69 to +3.94 ‰ and +1.72 to +4.00 ‰ respectively (i.e., $\delta^{34}S_{H_2S} = \delta^{34}S_i - \Delta i$, where Δi is the fractionation between sulphide species i and H_2S). The isotopic relationship between the $\delta^{34}S_{(\Sigma S)}$ and H_2S given by the equation of Ohmoto and Rye (1979) is summarized as;

$$\delta^{34}S_{(\Sigma S)} = \delta^{34}S_{H_2S} + \Delta_{SO_4^{2-}-H_2S} * (R/(1+R)) \qquad [6.1]$$

where R is the mole ratio $\Delta SO_4^{2-}/\Delta H_2S$ in the fluid, and $\Delta_{SO_4^{2-}-H_2S}$ is the fractionation between SO_4^{2-} and H_2S given as $\delta^{34}S_{SO_4^{2-}} - \delta^{34}S_{H_2S}$ (Ohmoto and Rye (1979).

At 350 and 400°C, the fractionation between SO_4^{2-} and H_2S is 19.5 and 17.6 respectively, according to the data of Ohmoto and Rye (1979). The R factor in the equation depends on the ambient pH and the fO_2 and can be derived from the following equation 6.2,

$$H_2S_{(aq)} + 2O_2 = SO_4^{2-} + 2H^+ \qquad [6.2]$$

As discussed in Chapter 5, the quantitative estimation of the pH has not been possible due to lack of some parameters. However, the low oxidation state of the fluid estimated from fluid inclusion data and stable alteration mineral assemblage suggests that H_2S would be the predominant species in the ore fluid. Furthermore, Ohmoto (1986) showed that when pyrrhotite occurs as a stable phase at temperatures less than 500°C, ore fluid pH is < 6 and H_2S is the dominant sulphur species in the fluid and $R < 0.01$. It may therefore be concluded that the isotopic composition of the ore fluid would have $\delta^{34}S_{(\Sigma S)}$ approximately equal to $\delta^{34}S_{H_2S}$ (i.e. $\delta^{34}S_{(\Sigma S)} \approx \delta^{34}S_{H_2S}$). In this case, the fluid from which the sulphides precipitated would have $\delta^{34}S_{H_2S}$ ranges from approximately +1.69 to +3.94‰ and +1.72 to +4.0 ‰ respectively for pyrite and pyrrhotite. This therefore concludes that the sulphides in the veins and BIF were deposited from a fluid with a unique S-isotopic composition with $\delta^{34}S_{(\Sigma S)}$ of the fluid varying from +1.69 to +4.0‰.

6.2: Carbon and Oxygen Isotope Geochemistry of Carbonates

6.2.1: Sampling and analytical procedure

Forty three carbonates derived from veins and whole-rock samples at the Kalahari Goldridge deposit were analyzed for C- and O-isotopes. The veins consist of seven mineralized (8 Group IIA and 5 Group IIB veins) and nine non-mineralized late (2 Group I and 7 Group III) vein samples. Whole-rock samples were taken from footwall (5 samples), BIF (7 samples) and the hanging wall units (2 meta-greywackes, 5 schists and 2 phyllites).

Sample preparation was according to the procedure of McCrea (1950). 10 to 50 mg of powdered sample were reacted with 100% H_3PO_4 in a Y-tube and CO_2 was evolved at different temperatures depending on the carbonate phase present in the sample. CO_2 was evolved in a steam bath for calcite and ankerite-dolomite at 25 and 50°C respectively for at least 4 hours. CO_2 from siderite was evolved in a paraffin bath at 100°C for at least 6 hours. The evolved CO_2 was analyzed for C- and O-isotopic composition using a Finnigan MAT 252 mass spectrometer at the Department of Geological Sciences, University of Cape Town. The C- and O-isotopic data are presented in the standard notation of $\delta^{13}C$ and $\delta^{18}O$ respectively. Measurements are made with respect to the Pee Dee Belemnite (PDB) for carbon and Standard Mean Ocean Water (SMOW) for oxygen.

6.2.2: Results

The carbon isotope data are given in Table 6.2 and illustrated in Figures 6.4 and 6.6. The $\delta^{13}C$ range for carbonates in the mineralized veins varies from -8.0 to -5.6 ‰ (-8.0 to -6.8 ‰ for the Group IIA veins, and -6.5 to -5.6 ‰ for the Group IIB veins). The non-mineralized late (Group III) veins indicate a $\delta^{13}C$ range from -3.7 to -1.0 ‰ (average -2.0 ± 0.9 ‰, 1σ). The isotopic composition of one fluid inclusion sample derived from the Group IIB vein (sample NQH16A) indicated a $\delta^{13}C = -6.9$ ‰.

The $\delta^{13}C$ signatures of carbonates from the whole-rock samples show the following ranges: BIF (-6.7 to -4.8 ‰; average, -6.1 ± 0.5 ‰), hanging-wall meta-sediments (-6.9 to -5.0 ‰; average, -6.1 ± 0.7 ‰), and footwall schist (-6.1 to -3.3 ‰; average, -4.8 ± 1.3 ‰), Table 6.2. These ranges broadly overlap the data for the mineralized veins except for minor excursions to higher values in two of the footwall samples (529/21 and 525/25A). It is possible that the higher isotopic signatures in some of the footwall samples could be attributed to fluid equilibration at lower temperatures or an interaction with later fluids of different isotopic character.

Table 6.2. Carbon and oxygen isotope composition of vein and whole-rock carbonates from the Kalahari Goldridge deposit.

Sample	Comments	Carbonate	$\delta^{13}C_{carbonate}$(‰)	$\delta^{13}C_{fluid}$ (‰)	$\delta^{18}O_{carbonate}$ (‰)	$\delta^{18}O_{fluid}$ (‰)
		VEIN SAMPLES				
Mineralized veins						
MSH/W-3A	Group IIA	ankerite	-7.6	-7.1 to -7.7	9.8	5.2 - 6.3
13175/2C	Group IIA	ankerite	-7.2	-6.7 to -7.3	9.1	4.4 - 5.6
QH/21A	Group IIA	ankerite	-7.5	-7.0 to -7.62	10.5	5.9 - 7.0
QH/21B	Group IIA	ankerite	-7.2	-6.7 to -7.32	10.2	5.6 - 6.7
QH/22A	Group IIA	ankerite	-8.0	-7.5 to -8.12	9.3	4.7 - 5.8
QH/22B	Group IIA	ankerite	-7.8	-7.3 to -7.9	10.0	5.4 - 6.5
QH/22C	Group IIA	ankerite	-6.8	-6.3 to -6.92	9.9	5.3 - 6.4
531/9C	Group IIA	siderite	-6.9	-6.4 to -7.0	11.5	6.9 - 8.0
PH/010	Group IIB	ankerite	-5.6	-6.2 to -6.7	10.0	5.4 - 6.5
NQH/16A	Group IIB	ankerite	-6.5	-7.1 to -7.6 (-6.91, F.I)	8.8	4.2 - 5.3
531/16B	Group IIB	siderite	-6.1		10.8	6.2 - 7.2
589/12	Group IIB	siderite	-5.9		10.8	6.2 - 7.2
588/X5	Group IIB	siderite	-6.3		12.2	7.6 - 8.7
Non-mineralized veins						
DD17/X6	Group III	dolomite	-1.9		16.3	
534/295m	Group III	dolomite	-1.0		17.0	
13175/2D	Group III	dolomite	-1.6		16.2	
529/6B	Group III	dolomite	-1.5		16.5	
529/7B	Group III	ankerite	-3.7		14.6	
NQH/005	Group III	ankerite	-2.9		14.7	
NQH/007	Group III	ankerite	-1.5		15.3	
529/15	Group I	calcite	-1.9		12.8	
NQH/013	Group I	dolomite	-2.7		11.7	
		WHOLE-ROCK SAMPLES				
BIF (orebody)						
13175/2A	less altered	ankerite	-6.7		10.0	5.0 - 6.1
13175/2B	altered BIF	ankerite	-6.6		10.3	5.3 - 6.5
525/23CWR	altered BIF	ankerite	-5.4		9.3	4.3 - 5.5
529/13	altered BIF	ankerite	-5.8		11.8	6.7 - 8.0
588/19B	altered BIF	siderite	-6.0		12.1	8.1 - 8.8
531/9CWR	altered BIF	siderite	-6.7		12.7	8.7 - 9.4
529/298	less altered	siderite	-5.8		13.3	9.3 - 10.0
Hanging-wall sediments						
529-3	schist	ankerite	-6.6		9.4	
525-5B	schist	ankerite	-6.3		9.5	
527-X1	schist	ankerite	-5.4		12.4	
588-1	schist	ankerite	-5.0		11.6	
588-1	schist	calcite	-6.9		8.7	
525-1	graywacke	ankerite	-6.2		9.6	
529-1A	graywacke	ankerite	-6.5		9.3	
525-10	meta-pelite	ankerite	-5.2		10.6	
DD17-X1	meta-pelite	ankerite	-6.6		11.4	
Footwall sediments						
DD17-8	schist	calcite	-5.9		9.8	
525/25A	schist	calcite	-3.5		10.5	
529-21	schist	calcite	-3.3		12.5	
527-12A	schist	calcite	-6.1		10.5	
588-26	schist	calcite	-5.1		10.9	

$\delta^{18}O_{fluid}$ was calculated using a temperature range of 350 to 400°C with the fractionation equations of Becker and Clayton (1976) for siderite-water and Mathews and Katz (1977) for ankerite-water.

F.I = Fluid inclusion

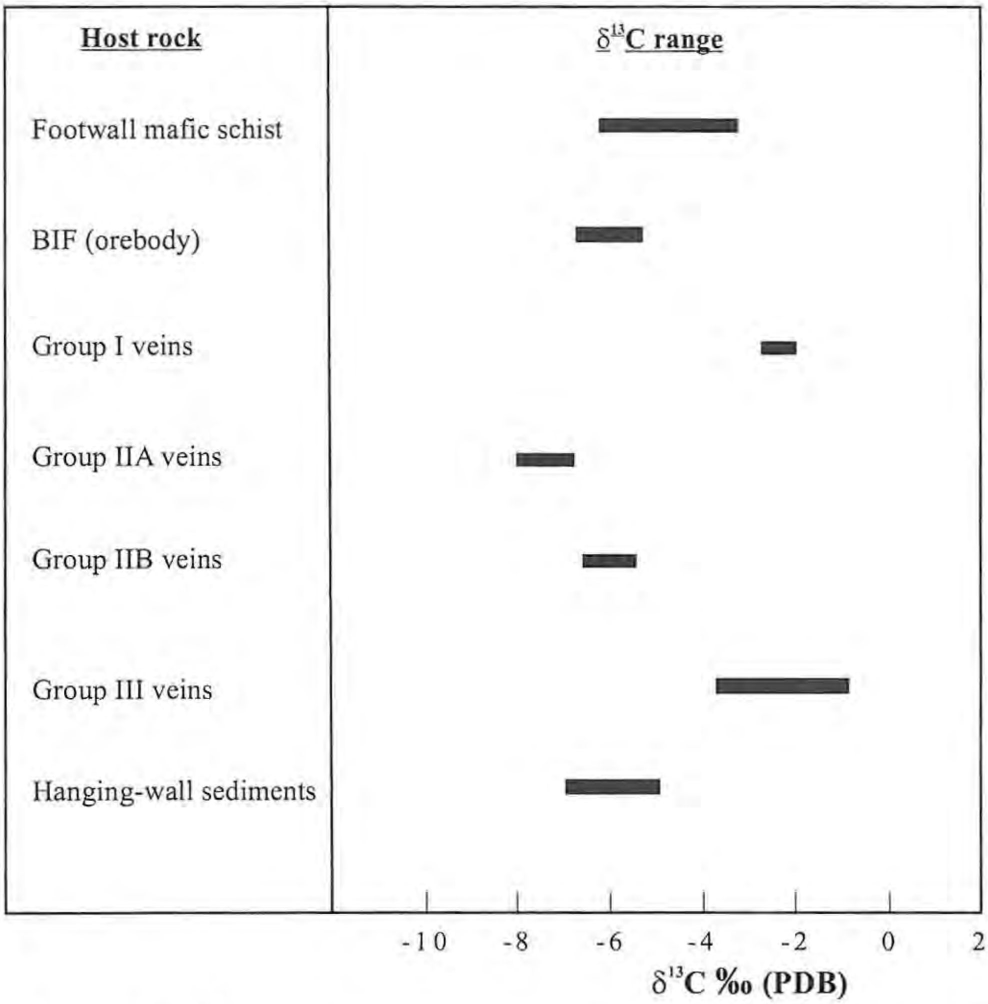

Figure 6.4. $\delta^{13}C$ range of carbonates in veins and host rocks at the Kalahari Goldridge deposit.

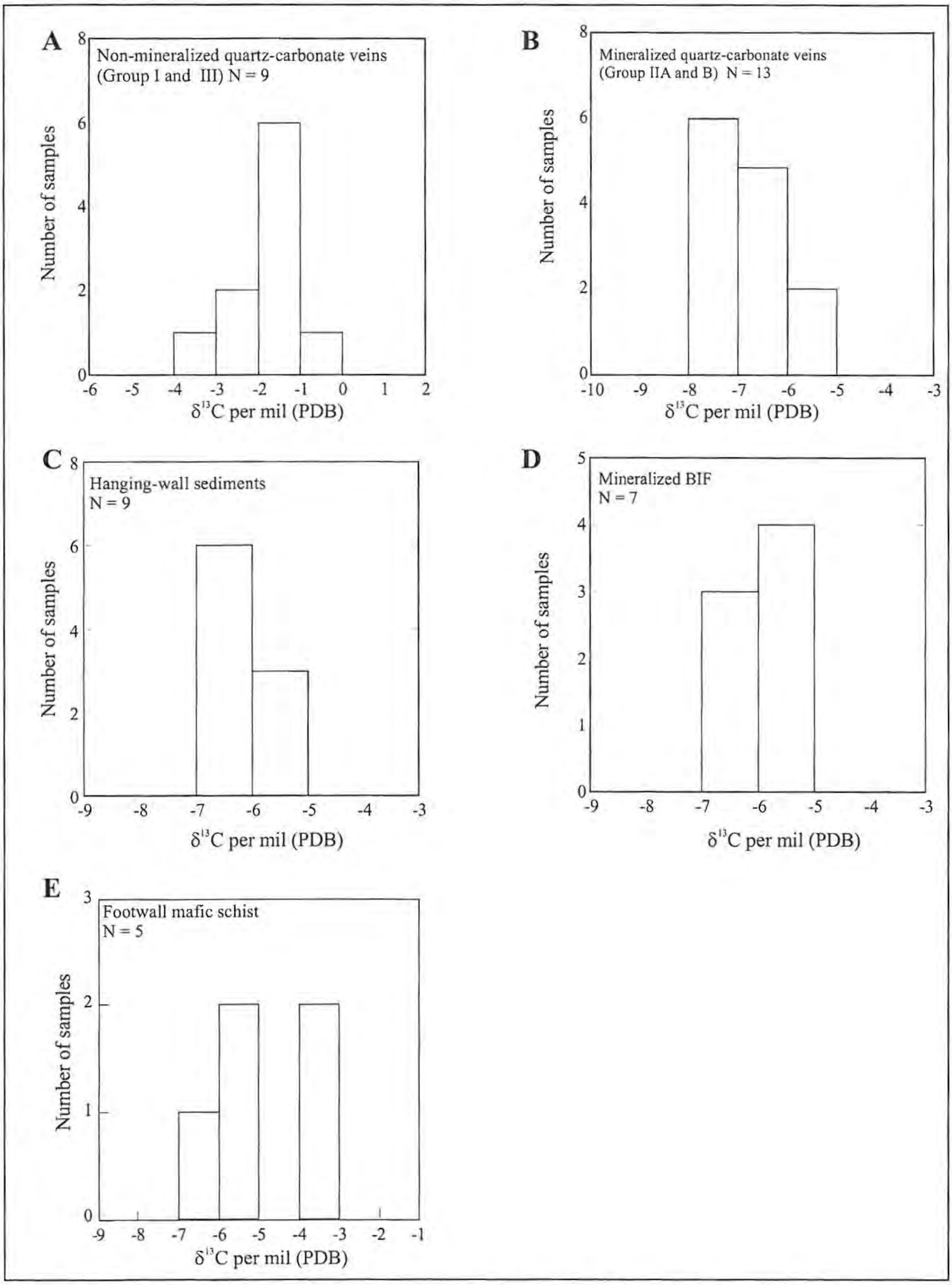

Figure 6.5. Histograms of carbon isotope composition of carbonates in veins and host rocks at the Kalahari Goldridge deposit: A. Non-mineralized quartz-carbonate veins, B. Mineralized quartz-carbonate veins, C. Hanging-wall sediments, D. Mineralized BIF and E. Footwall mafic schist.

6.2 3: Estimate of $\delta^{13}C$ of the primary ore fluid ($\delta^{13}C_{\Sigma C}$)

The source of carbon in most lode gold deposits can be traced by the $\delta^{13}C$ of carbonates due to their widespread occurrence in these deposits. The widespread carbonation in these deposits also shows the significant occurrence of oxidized carbon species in these fluids. The oxidized species in the hydrothermal fluid may originate from a magmatic source, from oxidation or hydrolysis of reduced carbon species in sediments, metamorphic rocks, or from leaching of carbonate minerals (Ohmoto and Rye, 1979).

As with the sulphur isotopes, the carbon isotope composition is also controlled by the temperature, fO_2, pH at deposition, and the carbon isotopic composition of the source fluid, $\delta^{13}C_{\Sigma C}$ (Ohmoto, 1972; Ohmoto and Rye, 1979). The isotopic fractionation between the oxidized species (CO_2, H_2CO_3, HCO_3^- and CO_3^{2-}) is generally minimal. However, fractionation between the reduced (CH_4) and oxidized carbon species can be very large because the proportions of these species are affected by changes in the physico-chemical conditions of the fluid system (Ohmoto, 1972).

In aqueous fluids, Ohmoto (1972) demonstrated that CO_2 is present as the CO_2 molecule and H_2CO_3 and their sum expressed as $H_2CO_{3\,(apparent)}$. However, CO_2 occurs as the predominant species in solution above 100°C, therefore:

$$\delta^{13}C_{H_2CO_{3(apparent)}} = \delta^{13}C_{\Sigma CO_2} \qquad [6.3]$$

The isotopic composition of other carbon species in solution is related to $\delta^{13}C_{\Sigma CO_2}$ by the expression:

$$\delta^{13}C_{\Sigma CO_2} = \delta^{13}C_i - \Delta i \qquad [6.4]$$

where Δi = relative isotopic enrichment between the specie i and $H_2CO_{3(app)}$ (Ohmoto, 1972; Ohmoto and Rye, 1979; Ohmoto, 1986). As noted previously, siderite and ankerite form the dominant carbonates in the mineralized veins and show uniform $\delta^{13}C$ values. There are no experimental fractionation values for these carbonates and CO_2. However dolomite fractionation data can be used for ankerite because of the similarities in their crystal structure and acid fractionation factor.

At 350 and 400°C, the fractionation between ankerite and CO_2 is 1.8 and 2.1‰ respectively. In this case, the ankerite in the Group IIA veins would have precipitated from a fluid with $\delta^{13}C_{\Sigma CO_2}$ ranging from −10.1 to −8.6 ‰ at these temperatures. Ankerite in the Group IIB veins would have precipitated from a fluid with $\delta^{13}C_{\Sigma CO_2}$ values ranging from = −8.6 from −7.4 ‰.

Under conditions of equilibrium, the principal carbon species in hydrothermal solution CH_4 and CO_2, can be related to $\delta^{13}C_{\Sigma C}$ according to the expression,

$$\delta^{13}C_{\Sigma C} = \delta^{13}C_{\Sigma CO_2} + \Delta_{CH_4\text{-}CO_2} /(1+R) \qquad [6.5]$$

where R is the mole ratio of CO_2/CH_4 in the fluid, and $\Delta_{CH_4\text{-}CO_2}$ is the equilibrium fractionation factor between CO_2 and CH_4 (Ohmoto, 1972; 1986).

$\Delta_{CO_2\text{-}CH_4}$ at Kalahari Goldridge is calculated to be 22 ‰ at 350°C and 19 ‰ at 400°C using the data of Bottinga (1969). The CO_2/CH_4 ratio in fluid inclusions examined by Raman microprobe ranges from 1.3 to 8.6 in the Group IIA veins, and 0.3 to 17.5 for inclusions in the Group IIB veins (Chapter 5, Table 5.4). However, at Kalahari Goldridge, a general observation indicates that much of the CH_4 may be derived locally by partial reduction of H_2O-CO_2 hydrothermal fluid by organic materials in the meta-pelites underlying the orebody and in host BIF and therefore may not represent an intrinsic component of the original ore fluid. The highest CO_2/CH_4 ratio would most possibly reflect the original content of the fluid. This is based on a comparison with isotopic studies of fluid inclusions by Kruelen and Schuiling (1982), which demonstrated that, in a closed system, the ^{13}C enrichment of CO_2 in fluid inclusions closely depends on the CO_2/CH_4 ratio during equilibration. Therefore, the absence of CH_4 in the fluid tends to preserve the original $\delta^{13}C$ value in the fluid. Kruelen and Schuiling (1982) also noted that, at low CO_2/CH_4 ratios, ^{13}C enrichment corresponds to an increase in isotopic fractionation.

On this note, the calculated $\delta^{13}C_{\Sigma C}$ of the ore fluid associated with Group IIA vein mineralization would range from -7.8 to -6.3 ‰, and from -7.6 to -6.0 ‰ for mineralization associated with the Group IIB veins. The close overlap of the estimated $\delta^{13}C_{\Sigma C}$ of the ore fluids associated with both mineralized vein sets suggests that the fluid evolved from a homogenous parent source. Further evidence supporting this conclusion comes from the $\delta^{13}C$ of fluid inclusions derived from the one Group IIB vein sample (NQH/16) with $\delta^{13}C = -6.9$ ‰ and gives an indication of the consistency of the fluid isotopic composition.

The $\delta^{18}O$ values of carbonates in the Group IIB veins show a restricted range from 8.8 to 12.2 ‰ with an average of 10.5 ± 1.2 ‰ (1σ). The $\delta^{18}O$ values for the Group IIA vein carbonates vary from 9.1 to 11.5 ‰ with an average of 10.0 ± 1.3 ‰. The $\delta^{18}O$ for the non-mineralized late veins (Group III) are isotopically heavier, ranging from 12.8 to 17.0 ‰ (average 15.4 ± 1.4, 1σ). One non-mineralized early vein (Group I) indicated $\delta^{13}C$ and $\delta^{18}O$ values of -2.7 ‰ and 11.7 ‰ respectively.

The $\delta^{18}O$ values of carbonates derived from the whole-rock samples show a restricted range with no obvious distinction from the mineralized veins samples. The whole-rock samples give the following $\delta^{18}O$ ranges: BIF (9.3 to 13.3 ‰; average, 11.4 ± 1.4 ‰), hanging wall sediments (8.6 to 12.4 ‰; average, 10.3 ± 1.3 ‰) and footwall schist (9.8 to 12.5 ‰; average, 10.8 ± 1.0 ‰.). The carbon and oxygen isotopic compositions of these carbonates fall within the range reported in most Archaean gold deposits, which show a range from -11.0 to +0.5 and 9.1 to 15.4 ‰ respectively (Kerrich, 1989).

The whole-rock carbonates are more enriched in ^{18}O than the vein carbonates. A major factor controlling this phenomenon may have been heavy host-rock $\delta^{18}O$ composition buffering the ore fluid composition through fluid-rock interaction. Supporting this interpretation is the highest $\delta^{18}O$ isotopic value recorded by the least altered whole-rock BIF sample (529/298) suggesting a low fluid-rock interaction. Siderite also shows consistent enrichment in ^{18}O over ankerite in the deposit. A similar enrichment pattern is observed in other lithologies where different carbonates have been analyzed. For example, carbonates in the late veins show ^{18}O enrichment in the order dolomite>ankerite>calcite (Table 6.2).

Assuming isotopic equilibrium in the temperature range 350° to 400°C, and using the siderite-water fractionation equation of Becker and Clayton (1976), sample 531/9C in the Group IIA veins indicates that the $\delta^{18}O$ of the hydrothermal fluid ($\delta^{18}O_{H_2O}$) ranges from 6.9 to 8.0 ‰ and from 6.2 to 8.7 ‰ for the siderite samples in the Group IIB veins. The calculated $\delta^{18}O_{H_2O}$ exhibited by the $\delta^{18}O_{siderite}$ in the BIF shows relatively higher $\delta^{18}O$ values from 7.5 to 9.8 ‰.

Also, using the dolomite-water fractionation equation of Mathews and Katz (1977) for ankerite, the $\delta^{18}O_{H_2O}$ established from samples MSH/W-3A and 13175/2C in the Group IIA veins varies from 4.4 to 6.3 ‰. The Group IIB vein ankerite samples (PH/010 and NQH/16A), on the other hand, indicate a calculated $\delta^{18}O_{H_2O}$, ranging from 4.2 to 6.5 ‰. The fluid isotopic composition in the BIF, using the ankerite-water fractionation, also shows relative enrichment in ^{18}O ranging from 4.7 to 8.3 ‰. The $\delta^{18}O$ value of the hydrothermal fluid in equilibrium with ankerite calculated using the dolomite-water fractionation equation of Mathews and Katz (1977) indicated a range from 4.4 to 7.0 ‰ for the hydrothermal fluid from which crystallization took place in the Group IIA veins, and a range from 4.2 to 6.5 ‰ for fluid associated with the Group IIB veins. Similar calculations for ankerite from the BIF whole-rock samples showed enrichment in ^{18}O with $\delta^{18}O$ ranging from 4.7 to 8.3 ‰. The variance in the calculated $\delta^{18}O$ values of the ore fluid from the siderite-water and ankerite-water fractionation equations suggests the two minerals were in disequilibrium.

A comparison between vein carbonates at the Kalahari Goldridge deposit indicates a progressive increase in the $\delta^{13}C$ signatures from the mineralized to late veins in the order Group IIA veins (-8.0 to -6.8 ‰) < Group IIB veins (-6.5 to -5.6 ‰) < late veins (Group III) (-3.7 to -1.0 ‰). A summary by Rye and Ohmoto (1974) and Ohmoto and Rye (1979) revealed that such variation has been observed at several studied deposits, where an increasing trend of $\delta^{13}C$ occurs in carbonates formed late in the paragenetic sequence of the mineralization. Ohmoto and Rye (1979) attributed this sequence to (i) decreasing temperature,

(ii) increasing CO_2/CH_4 ratios in an evolving fluid system, and/or (iii) contribution of CO_2 from other sources resulting in a progressive increase in the $^{13}C/^{12}C$ ratio.

Temperature gradient is an unlikely factor for the observed trend at the Kalahari Goldridge deposit, since temperature estimates from both fluid inclusion total homogenization and alteration assemblage minerals (chlorite) suggest temperatures were fairly constant during the veining system (Chapter 5). The relatively narrow ranges of the $\delta^{13}C$ of carbonates in the mineralized veins and host BIF also suggest that the possibility of mixing of varied fluids is also unlikely. Therefore, a possible cause of the systematic variation of $\delta^{13}C$ in the veins could be attributed to an increase in the oxidation state of an evolving fluid (increasing CO_2/CH_4 ratio) system, resulting from local fluid interaction with the graphitic rocks or immiscible separation of CO_2 + CH_4 in the hydrothermal fluid.

During fluid unmixing, the reduced species (CH_4), being more volatile, partitions favourably into the vapour phase relative to the oxidized species (CO_2) and acts to oxidize the residual aqueous fluid. In this way, the later evolved fluids would be enriched in the heavier isotopic carbon, ^{13}C, due to the fact that the heavier isotopes are fractionated into the higher molecular weight species under uniform conditions. Ohmoto and Rye (1979) also noted that in fluid-graphite interaction where redox conditions favourably control the fractionation between $\delta^{13}C_{\Sigma C}$ and $\delta^{13}C_{carbonate}$, the precipitated carbonates yield $\delta^{13}C$ signatures at low oxygen fugacity conditions resulting from an increasing proportion of the reduced (CH_4) to oxidized aqueous carbon species and a subsequent increase in the CO_2/CH_4.

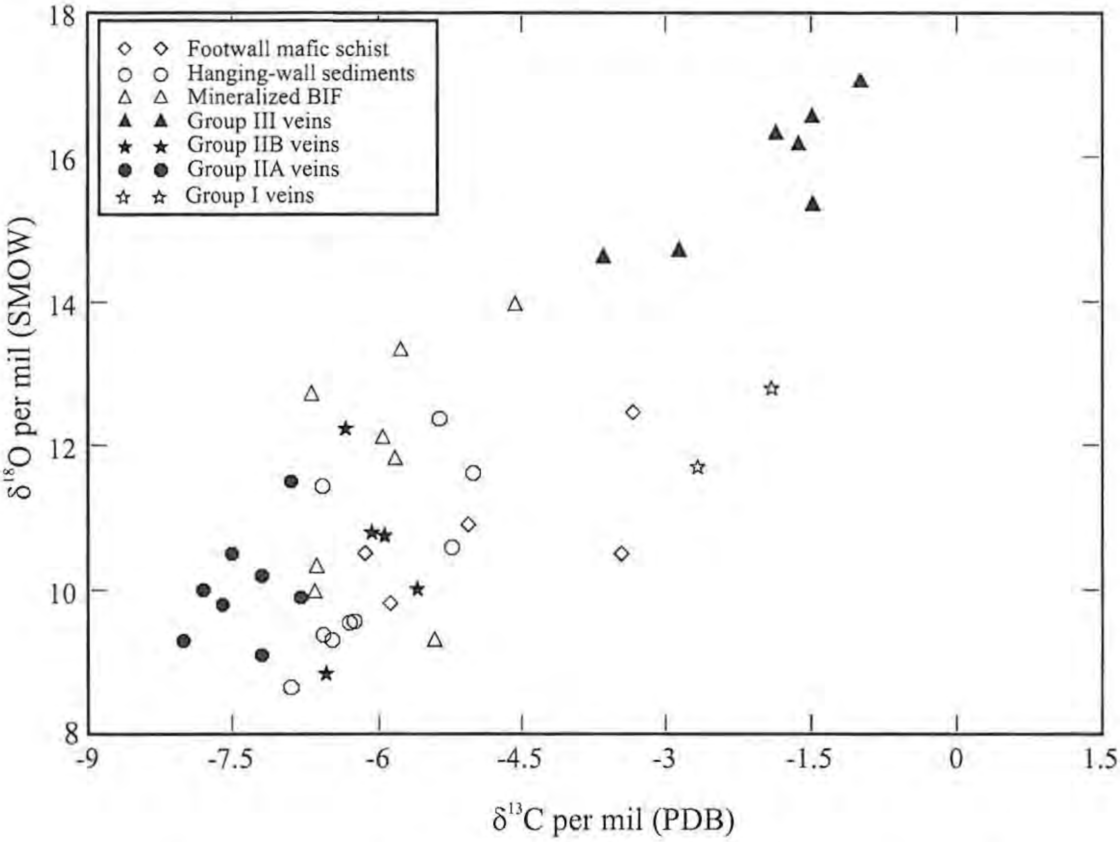

Figure 6.6. Variation of carbon and oxygen isotope composition of carbonates in veins (filled symbols) and whole-rocks (open symbols) at the Kalahari Goldridge deposit.

Evidence supporting this interpretation is illustrated in Figure 6.6, which shows a positive correlation between $\delta^{13}C$ and $\delta^{18}O$ of these carbonates. Further supporting evidence is the observed increasing pyrite contents from the Group IIA to the Group III (late) veins. In addition, although no CO_2/CH_4 ratio data are available for the Group III veins, a comparison between the Group IIA and the Group IIB veins show highest CO_2/CH_4 ratios in the Group IIB veins. Furthermore, the Group IIA veins being paragenetically earlier than the Group IIB veins, Figure 6.6 shows that samples from the Group IIA veins indicate lowest isotopic values, implying the original fluid had lowest CO_2/CH_4 ratios due to the fact that temperatures during crystallization were fairly uniform and hence, uniform fractionation between CO_2 and CH_4 took place.

The tight clustering of carbon isotope compositions of the whole-rock samples throughout orebody (BIF), footwall and hanging-wall units suggests that hydrothermal alteration during the mineralization was highly pervasive under uniform temperature. Furthermore, as observed in most Archaean lode gold systems, the host rocks contained minor amounts of carbonates prior to mineralization, due to earlier alteration events such as metamorphism. As a result, the carbon isotope composition of the carbonates associated with gold mineralization in these rocks may represent mixtures of carbon isotope composition of varied origin and therefore attempts to constrain the source of the carbon in these deposits can be misleading. However, the closely uniform $\delta^{13}C$ signatures of carbonates in the mineralized veins and the host rocks throughout the deposit at Kalahari Goldridge suggests that the host rocks contained little or no carbonate prior to mineralization. This also indicates that the carbon in the ore fluid was derived from the same source, therefore the $\delta^{13}C$ of the carbonates can be used to trace the primary $\delta^{13}C$ of the ore fluid.

6.3: Oxygen Isotope Geochemistry of Quartz

6.3.1 Sampling and analytical procedure

Ten vein-quartz samples consisting of nine samples from the mineralized vein system (2 Group IIA and 7 Group IIB veins) and one from a non-mineralized late (Group III) veins were analyzed for oxygen isotope composition.

According to the method of Borthwick and Harmon (1982), 10mg of powdered quartz sample (<200mesh) were reacted with ClF_3 at 600°C overnight. The purified oxygen produced was converted to CO_2 by hot platinized carbon rod. The CO_2 produced was measured by a Finnigan MAT252 mass spectrometer at the Department of Geological Sciences, University of Cape Town. The oxygen isotope ratio $\delta^{18}O$ is reported relative to SMOW and analytical precision is 0.2 ‰ (1σ).

6.3.2: Results

The results of $\delta^{18}O$ are shown in Table 6.3 and illustrated in Figure 6.7. The two mineralized vein samples MSH/W-3 and 525/23C show $\delta^{18}O$ signatures of 12.3 and 14.5 ‰ respectively. Samples from the Group IIB veins range from 12.0 to 14.1 ‰. The late non-mineralized vein (Group III) sample DD17/X6 indicated significant enrichment in ^{18}O, with a $\delta^{18}O$ value of 19.2 ‰. Within the Kalahari Goldridge deposit no significant difference exists between the values for Group IIA and the Group IIB veins.

Using the quartz-water fractionation equation of Matsuhisa et al. (1979), and assuming a temperature range of 350 to 400°C, the $\delta^{18}O$ of the hydrothermal fluid responsible for the Group IIA vein mineralization varies from 7.0 to 10.5 ‰, and ranges from 6.9 to 10.0 ‰ for the fluid responsible for mineralization associated with the Group IIB veins.

Table 6.3. Oxygen isotope composition of quartz from quartz-carbonate veins at the Kalahari Goldridge deposit.

Sample	Source lithology	$\delta^{18}O_{quartz}$(‰)	$\delta^{18}O_{fluid}$ (‰)
MSH/W-3	Group IIA	12.3	7.0 - 8.3
525/23C	"	14.5	9.2 - 10.5
PH/010	Group IIB	13.2	7.9 - 9.1
NQH/10A	"	12.6	7.3 - 8.6
588/12	"	13.0	7.7 - 9.0
NQH/16A	"	12.0	6.7 - 7.9
589/12	"	12.0	6.7 - 7.9
PH/011	"	14.1	8.7 - 10.0
531-16B	"	12.5	7.2 - 8.4
588/X5	"	12.2	6.9 - 8.1
DD17-X6	Group III	19.2	

$\delta^{18}O_{fluid}$ calculated using the quartz-water fractionation data of Matsuhisa et al. (1979).

6.3.3: Mineral-pair geothermometry

Quartz-carbonate pairs in the alteration assemblage have been used to calculate fluid temperatures during mineralization. The quartz-carbonate mineral pairs also served to establish if equilibrium was maintained during the precipitation of the minerals. The data for the coexisting quartz-carbonate pairs are shown in Table 6.4. Combining the siderite-water fractionation equation of Becker and Clayton (1976) and the quartz-water fractionation equation of Matsuhisa et al. (1979), gives temperatures estimates of 182 and 208°C for the two quartz-siderite pairs derived from the Group IIB veins. The quartz-ankerite pairs were also calculated combining the data of Matsuhisa et al. (1979) and the dolomite-water data of Mathews and Katz (1977). The calculated temperatures from the quartz-ankerite pairs indicate very low temperature ranging from 20 to 56°C (Table 6.4).

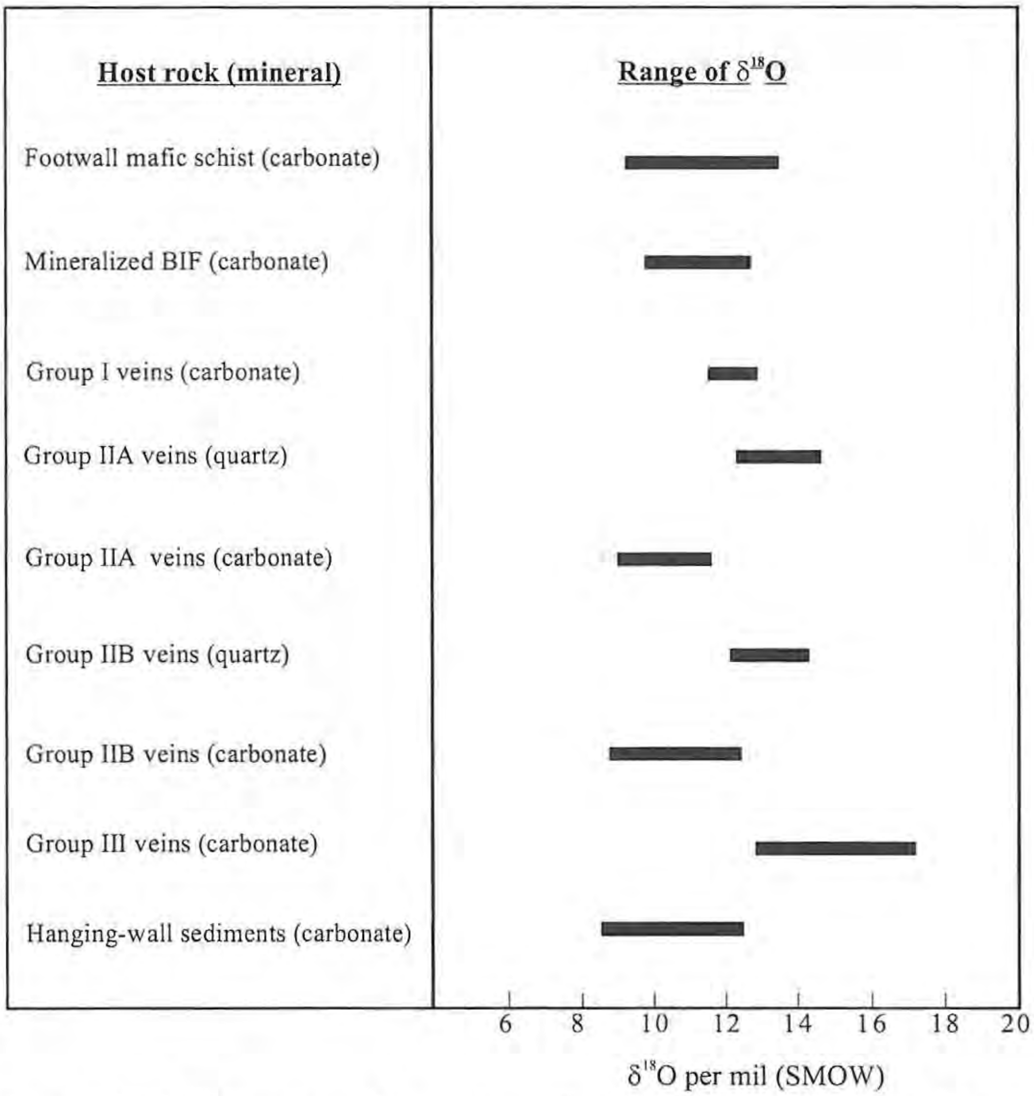

Figure 6.7. $\delta^{18}O$ ranges of quartz and carbonates in vein and host rocks at the Kalahari Goldridge deposit.

Table 6.4: Oxygen isotope composition and fractionation of coexisting quartz-carbonate pairs.

Sample	Source lithology	$\delta^{18}O_{quartz}$ (‰)	$\delta^{18}O_{carbonate}$(‰)	Mineral pair	$\Delta_{quartz-carbonate(‰)}$	Temp. (°C)
MSH/W-3	Group IIA	12.3	9.8	quartz-ankerite	2.5	56
PH/010	Group IIB	13.2	10.0	quartz-ankerite	3.2	21
NQH/16A	"	12.0	8.8	quartz-ankerite	2.1	22
531-16B	"	12.5	10.8	quartz-siderite	1.7	182
588/X5	"	12.2	10.8	quartz-siderite	1.4	209
DD17-X6	Group III	19.2	16.3	quartz-dolomite	2.9	36

The lower temperature estimates relative to the independent temperature estimates which range from 350 to 400°C from chlorite geothermometry may reflect retrograde equilibration of the quartz-carbonate fractionation during cooling. This is consistent with the observation by Clayton et al. (1968) that carbonates are texturally less resistant than quartz to retrograde isotope exchange.

Chapter 7: GENETIC MODEL FOR MINERALIZATION

7.1: Existing Genetic Models

A wide consensus of opinion based on data from many Archaean greenstone belts (Perring et al., 1987; Groves, et al., 1987b; Groves, et al., 1988; Colvine et al., 1988) has documented that gold mineralization in these terranes has been formed from low-salinity CO_2-H_2O-rich hydrothermal fluids channelled from laterally continuous and deep-seated ductile shear zones at approximate depths of 10-15km (Groves et al., 1987b), during the late stages of greenstone belt deformation and metamorphism. For economic viable deposits within these major fault systems, these models propose that large volumes of the gold-bearing fluid must be focussed through chemically favourable host-rock sequences of variable permeability and competence. The low tensile strength of the competent rocks induces hydraulic fracturing which serves as conduits for vein crystallization and associated mineralization (Phillips and Groves, 1983; Houstoun, 1987; Cox et al., 1991; Ridley, 1993). In relatively impermeable lithologies, such as shales, there may be obstruction of hydrothermal circulation and enhancement of gold deposition where ore fluids are ponded (Groves et al., 1987b).

These conceptual models have been inferred from the structural disposition of many gold deposits in Archaean greenstone belts, which is the most important feature controlling the distribution and geometry of Archaean lode gold deposits (Groves et al., 1987b). These structures reflect movement on trans-craton shear zones and different structural styles of the mineralization resulting from variation in the orientation of the regional stress field and strength of the host rock (Groves and Foster, 1993). In particular, the gold deposits occur in, or close to, extensional fractures and shear zones, which are characterized by quartz-vein sets, laminated veins and breccias (Groves et al., 1988). The gold-bearing shear zones, which can be traced for hundreds of meters up to tens of kilometers, are essentially secondary or tertiary structures related to the more ductile craton-scale shears.

Several models have been proposed to account for the mechanism of deposition of gold in mesothermal lode gold systems (see section 7.3.2). In Archaean greenstone belts, the deposition of the gold is induced by Fe-sulphide precipitation, which destabilizes gold sulphur-complexes, causing gold precipitation in Fe-rich lithologies such as BIF, tholeiitic basalts and dolerites. Also, a change in fO_2 and/or pH resulting from fluid interaction with wallrock or phase separation, induces gold precipitation. Fluid inclusion studies suggest that the emplacement temperature of the lode gold deposits was in the range 200-450°C with most available data clustering around 250-350°C, and pressures ranging from 1-4.5 kbars, but mostly 1-2 kbars (see Perring et al., 1987 for summary).

Despite the general agreement on the conceptual models stated above, there exists divergence of opinion on the source of the ore fluids and the ore fluid components. Various models have been proposed to account for the origin of gold mineralization in Archaean greenstones. These include metamorphic (Kerrick and Fryer, 1979; Kerrick and Fyfe, 1981; Groves and Phillips, 1987), magmatic (Burrows et al. 1986; Wood et al. 1986; Burrows and Spooner, 1987; Cameron and Hattori, 1987) or by a submarine volcanic activity (exhalative model, Hutchinson et al., 1971; Seyfried and Janecky, 1985; Boyle, 1987). These are summarized below.

7.1.1: Metamorphic model:

The metamorphic fluid model (Fig. 7.1A), proposed by Groves et al. (1984) and Groves and Phillips (1987) was based on several studied deposits in Western Australia, in which they observed that the vast majority of gold deposits occurs in volcanic-dominated sequences of greenstone belts, with most of the large deposits hosted by Fe-rich units such as tholeiitic basalts, dolerites, and BIFs, and a few deposits hosted by granitoids-gneissic terranes enclosing the greenstone belts. They also observed that major deposits are remotely emplaced from voluminous granitoids surrounding the greenstone belts. In addition, the contacts between the granitoids and the greenstones were characterized by limited alteration. The fluid associated with the mineralization is envisaged to have been generated by devolatization reactions in deep-seated volcanic piles near the brittle-ductile transition under greenschist to amphibolite facies metamorphism. These fluids are focused and channeled upwards into structural conduits such as shear zones, faults or hydraulic fractures by stress-controlled dilation (seismic pumping). In this process, fluid is drawn into the source region of an "earthquake" and expelled along structural conduits when rapture occurs (Sibson, 1987). The model advocates that gold was an indigenous constituent of the deep-seated volcano-sedimentary rocks and that extensive fluid interaction with host rocks during passage of the fluid scavenged trace metals from the enclosing rocks and deposited in chemically conducive sites where they may form economic deposits. These fluids have been documented (e.g. Ho et al., 1990) as being characterized by low salinities (< 2 wt % NaCl equivalent) due to low concentrations of halogens in rock-forming minerals, H_2O-CO_2-rich (15-25 mol % CO_2), alkaline to near-neutral in pH, with densities of 0.7 to 0.8g/cm^{-3}.

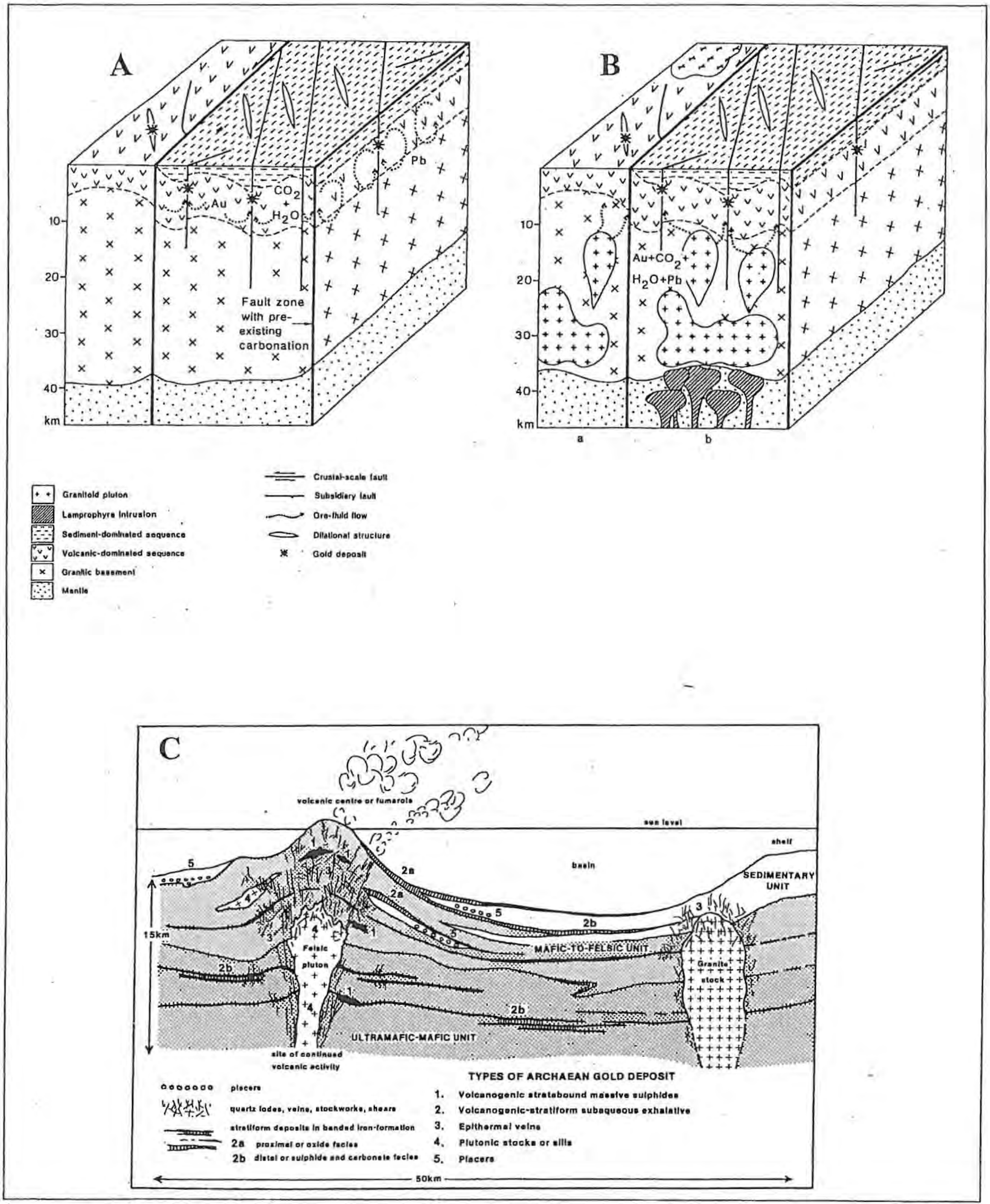

Figure 7.1. Schematic diagrams showing the genesis of gold mineralization in Arcahean greenstone belts. **A.** Metamorphic model showing evolution of H_2O-CO_2-Au fluids from devolatization of amphibolite-facies greenstones and convection in fault zones that penetrate granitic basement (after Perring et al.,1987). **B.** Magmatic-granitoid model showing the generation of granitoids above mantle plume (a) and above lamprophyric magmas (b), evolving H_2O-CO_2-Au-Pb fluids throughout diapiric ascent. **C.** Possible gold-sulphide mineralization based on the exhalative model in submarine environment (reproduced from Anhaeusser, 1986).

7.1.2: Magmatic model:

The magmatic model (Fig. 7.1B) is based on evidence from the close spatial association of several of these deposits with felsic igneous intrusions as well as from stable isotope studies and ore fluid compositions. This model, argued by Burrows et al. (1986) and Wood et al. (1986), showed close geochemical similarities of ore fluid associated with granitoid-related Mink Lake and Hollinger-McIntyre deposits respectively in the Abitibi greenstone belt in Canada (i.e. both are H_2O-CO_2-rich, salinities of 4.0 ± 2.0 and 5.6 ± 1.2-wt. % NaCl equiv.; $\delta^{18}O_{H_2O} = +4.7 \pm 0.5‰$ and $+6.0 \pm 1.9‰$ and $\delta^{13}C = -3.0 \pm 1.5$ ‰ and -3.3 ± 0.4‰). In addition, basing their argument on comparable carbon isotope signatures of 14 other gold deposits (-3.1 ± 1.3‰) in the Timmins area in Canada, with the Hollinger-McIntyre and Mink Lake deposits, these authors proposed a magmatic fluid source for Archaean lode deposits. Their conclusion was further supported by comparable data with those of the largest greenstone-hosted gold deposit, Golden Mile in Kalgoorlie, Western Australia whose carbon isotope signature (-3.4 ± 0.4 ‰) is indistinguishable from the Canadian deposits.

The conclusion of Burrows et al. (1986) and Wood et al. (1986) is further supported by Burnham (1979) who documented that CO_2-rich fluids, commonly associated with metamorphic fluids, can be generated in first evolved hydrothermal fluids from felsic magmas at pressures below 2kbars. These fluids, according to Burnham (1979), should also be enriched in brine as the halogens are strongly partitioned into the aqueous phase of the hydrothermal fluid. However, this effect is counteracted by small amounts of CO_2 in the aqueous phase which tend to suppress the concentration of alkalis in the fluid, resulting in relatively CO_2-rich and halogen-poor fluids. This model assumes that gold and related ore-forming elements have been partitioned into silicate magmas generated by anatexis of either mantle or crust, and transported to the upper crust where they are partitioned into exsolved H_2O-CO_2 magmatic fluids.

7.1.3: Exhalative model

This model postulates that deposition of ore was the result of exhalation of the ore constituents through hot springs and fumaroles during volcanism and subsequent sedimentation on the sea floor of the volcanic basins (Hutchinson et al., 1971; Seyfried and Janecky, 1985; Boyle, 1987). The exhalative model originally advocated to account for massive sulphide deposits, has been extended to the formation of certain gold deposits in Archaean greenstone terranes, typically gold mineralization in chemical sediments such as banded iron-formation (e.g. Hutchinson and Burlington, 1984; Saager et al., 1987). In this model (Fig. 7.1C), the extrusion of lava to shallow depths beneath the seafloor is thought to have provided heat for deep convection of seawater resulting in water-rock interaction at high temperatures up to 400°C. Sustained water-rock interaction leaches base and precious metals in volcanic rocks in large enough volumes to produce ore-forming fluids. High concentrations of H_2S from a combination of sources are leached along with the metals. Sulphides, sulphates, silica and gold are then precipitated from fluids exhaled on the seafloor in response to decreasing temperature and increasing pH resulting from conductive cooling and mixing with ambient seawater at or near the seafloor.

7.2: Genetic Models for the Kalahari Goldridge Deposit

In the preceding chapters, discussions based on field observations, analytical and empirical data have been presented and aspects of the mineralization at Kalahari Goldridge were considered. In the subsequent sections, an attempt is made to integrate these data to propose a genetic model for the Kalahari Goldridge deposit. In particular, the geochemical constraints and the source(s) of the ore fluid and gold, major controlling factors on the gold transport and depositional processes are considered, as well as implications for mineral exploration. In addition, a comparison is made with other BIF-hosted gold deposits in other Archaean greenstone terranes worldwide.

7.2.1: Fluid Evolution

7.2.1.1: Ore fluid characteristics

Evidence from fluid inclusions and stable isotopes in the two sets of mineralized veins indicates a homogeneous fluid chemistry during mineralization at Kalahari Goldridge and that precipitation occurred under relatively isothermal conditions (350-450°C) during both stages of mineralization at high fluid pressures ranging from 0.7 to 2.0 kbars. Assuming a lithostatic fluid-pressure gradient, this corresponds to depths from 2.5 to 7.0 km. Microthermometric and Raman analyses of fluid inclusions indicate that the hydrothermal fluid consisted of a low-salinity aqueous-carbonic mixture. The ore-fluid salinities estimated from clathrate and ice-melting temperatures show values less than 7 wt % equivalent NaCl (average, 3 wt % NaCl equivalent). The calculated fO_2, ranging from $10^{-33.85}$

to $10^{-29.98}$, lies between the CH_4-CO_2 and pyrite-pyrrhotite-magnetite buffers, indicating the relatively reduced nature of the ore fluid. Estimated ΣS of the ore fluid ranges from 0.011 to 0.018m and lies in the range prescribed for Archaean gold-ore fluids in sub-amphibolite facies.

The fluid is characterized by a wide variation of CH_4/CO_2 ratios, as determined from fluid inclusions, with highest ratios observed in veins within carbonaceous phyllites. Based on this observation, the increased CH_4 content in the fluid is attributed to localized hydrolysis reactions between hydrothermal fluid and carbonaceous phyllites underlying the orebody. Hence, fluids containing lowest CH_4/CO_2 ratios are inferred to represent the primary source fluid that migrated through hydrofractures at the onset of mineralization. Similar variation in the CH_4/CO_2 ratios has been reported in a number of gold deposits worldwide (e.g., Guilhaumou et al., 1990; Cox et al., 1991; Ridley and Hagemann, 1999). In most cases, these deposits are hosted in graphitic or carbonaceous environments. The variations in the CH_4/CO_2 ratios have been attributed to one or a combination of the following factors:

1. unmixing of an originally mixed CO_2-CH_4-H_2O fluid.
2. heterogeneous mixing of end-member CH_4-rich and CO_2-H_2O-rich fluids under isobaric conditions.
3. variable degrees of interaction of CO_2-H_2O fluids with carbonaceous sediments.

Taking into consideration the factors discussed above, the very restricted overall range in the $\delta^{13}C$ values of the mineralized vein carbonates (~2‰) at Kalahari Goldridge indicates that the fluids from which carbonates were deposited, were similar in composition and origin and therefore militates against a mixing model for the CH_4/CO_2 ratio variation. At the temperatures considered for deposition for the mineralized veins (350 to 400°C), it is unlikely that fluid unmixing played a significant role considering the small shift in $\delta^{13}C$. The variable CH_4/CO_2 ratios pertaining to the fluids at Kalahari Goldridge is more likely to reflect incomplete re-equilibration of primary inclusions with carbonaceous sediments due to continuous deformation. In which case, some of the original vein-forming fluid composition would be preserved.

7.2.1.2: Source(s) of fluid and ore components

The stable isotopic data from the alteration mineral assemblages at the Kalahari Goldridge deposit provide important constraints to define the possible sources of the fluids and the components associated with the gold mineralization. Calculations of the $\delta^{34}S_{H_2S}$ value of using pyrite-H_2S and pyrrhotite-H_2S fractionation factors and independent temperature estimates, indicate that primary ore-fluid isotopic $\delta^{34}S_{\Sigma S}$ varies from +1.69 to +3.94 ‰ and +1.72 to +4.0 ‰ respectively. The overlapping and restricted $\delta^{34}S_{\Sigma S}$ values suggest that the sulphides were precipitated from a homogenous fluid. In samples containing co-existing pyrite and pyrrhotite assemblages, fractionation between the sulphides varies widely and may indicate precipitation occurred out of isotopic equilibrium. The calculated $\delta^{34}S_{\Sigma S}$ values fall within the range for magmatic sulphides (-3 to 3 ‰, Ohmoto and Rye, 1979). In the light of the calculated range for $\delta^{34}S_{\Sigma S}$ of the ore fluid, the sulphides at Kalahari Goldridge could have been derived directly from a magmatic source, or by dissolution of magmatic-derived sulphides in volcanic terranes such as greenstones by reduced metamorphic fluids traversing through the volcanic sequence (e.g., Lambert et al., 1984; Kerrich, 1987).

The carbon isotope composition of the hydrothermal fluids ($\delta^{13}C_{\Sigma C}$), calculated from $\delta^{13}C$ of the carbonates in the auriferous veins at Kalahari Goldridge has a range from -6.0 to -7.8 ‰. This overlaps with the values provided by Ohmoto and Rye (1979) for average crustal carbon (-5 ± 3 ‰) and carbon derived from the mantle (-5 ± 2 ‰). Thus, the estimated $\delta^{13}C_{\Sigma C}$ range for the Kalahari Goldridge deposit does not provide a definitive source for the carbon. The carbon in the hydrothermal fluid may therefore be due to either a magmatic contribution, or alternatively, it may be attributed to metamorphic reworking of mantle-derived carbonation developed along major faults or shear zones (Groves and Phillips, 1987; Groves and Foster, 1993).

The $\delta^{18}O$ isotopic compositions of quartz and carbonates from the auriferous veins provide constraints on the isotopic composition of the hydrothermal fluid ($\delta^{18}O_{H_2O}$) associated with the gold mineralization at the Kalahari Goldridge deposit. The $\delta^{18}O_{H_2O}$, based on the $\delta^{18}O$ of quartz showed a narrow range from 7.0 to 10.5 ‰ (mean, 8.2 ± 1 ‰) for the hydrothermal fluid from which the Group IIA quartz veins crystallized, and 6.7 to 10.0 ‰ for the Group IIB veins. The calculated $\delta^{18}O_{H_2O}$ from $\delta^{18}O$ of siderite from the Group IIB veins indicated a comparable range from 6.9 to 8.4 ‰ (mean, 7.3 ± 0.8 ‰). Similar calculations based on the $\delta^{18}O$ of ankerite yielded lower $\delta^{18}O_{H_2O}$ values (5.4 ± 0.8 ‰). The calculated $\delta^{18}O_{H_2O}$ value of the hydrothermal fluid from the oxygen isotope data of carbonates and quartz from the mineralized veins overlap the range for magmatic (+6 to +11 ‰) and metamorphic (+5 to +25 ‰) fluids (Taylor, 1974; 1997).

7.2.2: Gold transport and deposition model

7.2.2.1: Gold solubility and transport

Gold is known to occur in two oxidation states (Au^+ and Au^{3+}) in solutions. Seward (1973; 1984) showed that Au^+ is the most dominant species in high-temperature geological solutions due to its high stability in low oxidation potential solutions that characterize these fluids, while Au^{3+} is negligible. Experimental studies by several workers (e.g., Henley, 1973; Seward, 1973; Shenberger and Barnes, 1989; Zotov et al., 1989; Hayashi and Ohmoto, 1991; Benning and Seward, 1996; Gibet et al., 1998) have documented mechanisms for transporting gold in high-temperature geological systems associated with gold deposits. Important complexes identified in these experiments responsible for gold transport include the chloro-complex, $AuCl_2^-$ (Henley, 1973; Zotov et al., 1989) and sulphide complexes ($Au(HS)_2^-$, Seward, 1973; Shenberger and Barnes, 1989; Hayashi and Ohmoto, 1991; $AuHS^o$, Benning and Seward, 1989; Gibet et al., 1998; and $HAu(HS)^o{}_2$, Hayashi and Ohmoto, 1991). The experimental work demonstrated that the transporting ability of gold as sulphide complexes occurs at low salinities and fO_2 but at variable pH conditions. These studies documented that the $Au(HS)_2^-$ complex, for example, is predominant in neutral to slightly acidic pH conditions, whilst the $AuHS^o$ and $HAu(HS)_2^o$ complexes are stable in acidic conditions.. In contrast, the $AuCl^-$ complex is important in more acidic and high salinity H_2S-poor conditions at relatively high fO_2. The solubilities of these species are expressed by the reactions:

$$Au + 2H_2S_{(aq)} = Au\,(HS)_2{}^-{}_{(aq)} + H^+{}_{(aq)} + 1/2H_2 \qquad [7.1]$$

$Au + 2H_2S_{(aq)} = HAu(HS)_2^o{}_{(aq)} + 1/2H_2$ [7.2]

$Au + 2H_2S_{(aq)} = Au(HS)^o{}_{(aq)} + 1/2H_2$ [7.3]

$Au + 2Cl^-{}_{(aq)} = AuCl_2^-{}_{(aq)}$ [7.4]

Other Au complexes considered by Seward (1993) to be of potential importance in high-temperature hydrothermal fluids include tellurium-bearing ligands ($Au(Te_2)HS^{2-}$, $Au(Te_2)_2^{2-}$, $Au(TeS)_2^{3-}$ and $AuTe_2^{3-}$), $Au(NH_3)_2^+$, and $Au(CN)_2^-$. The ubiquitous presence of CO_2 in fluid inclusions in Archaean gold deposits has also led some authors (e.g. Kerrick and Fyfe, 1981; Phillips et al. 1983) to suggest that the gold carbonate complex, $(Au(HCO_3)_2^-$, may be important in hydrothermal ore-forming solutions. However, experimental data are lacking to validate these suggestions. Giving consideration to the close association of the gold with sulphides, and the chemical conditions of the ore fluid derived from the fluid inclusion studies and the alteration mineral assemblage at the Kalahari Goldridge deposit, gold transport in ore fluids is likely to have occurred as $Au(HS)_2^-$.

Figure 7.2 illustrates the gold solubility contours of the $Au(HS)_2^-$ complex as a function of fO_2 and pH for the Kalahari Goldridge deposit constructed at 350°C, with average ΣS composition in ore fluid = 0.014m (Table 5.6), and average salinity ΣCl of 0.5m from fluid inclusion data (Tables 5.1 and 5.2), using an activity coefficient for the $Au(HS)_2^-$ complex ($\gamma_{Au(HS)_2^-}$) ≈ 1, calculated by the method of Renders and Seward (1989). The concentration of gold in the fluid can be calculated given the fO_2 and pH conditions. However, the lack of data for calculating the pH for Kalahari Goldridge ore fluids precludes calculation of the precise gold solubility. Therefore, this can only be speculated based on the general assumption that the pH of hydrothermal ore fluids typically ranges from 5 to 6.5 (Seward, 1993). On this basis, the concentration of gold in the Kalahari

Goldridge ore fluids would fall within the range from 0.1 to 5μmg/kg (0.1 to 5ppb) at the estimated fO_2 range from $10^{-32.96}$ to $10^{-29.98}$.

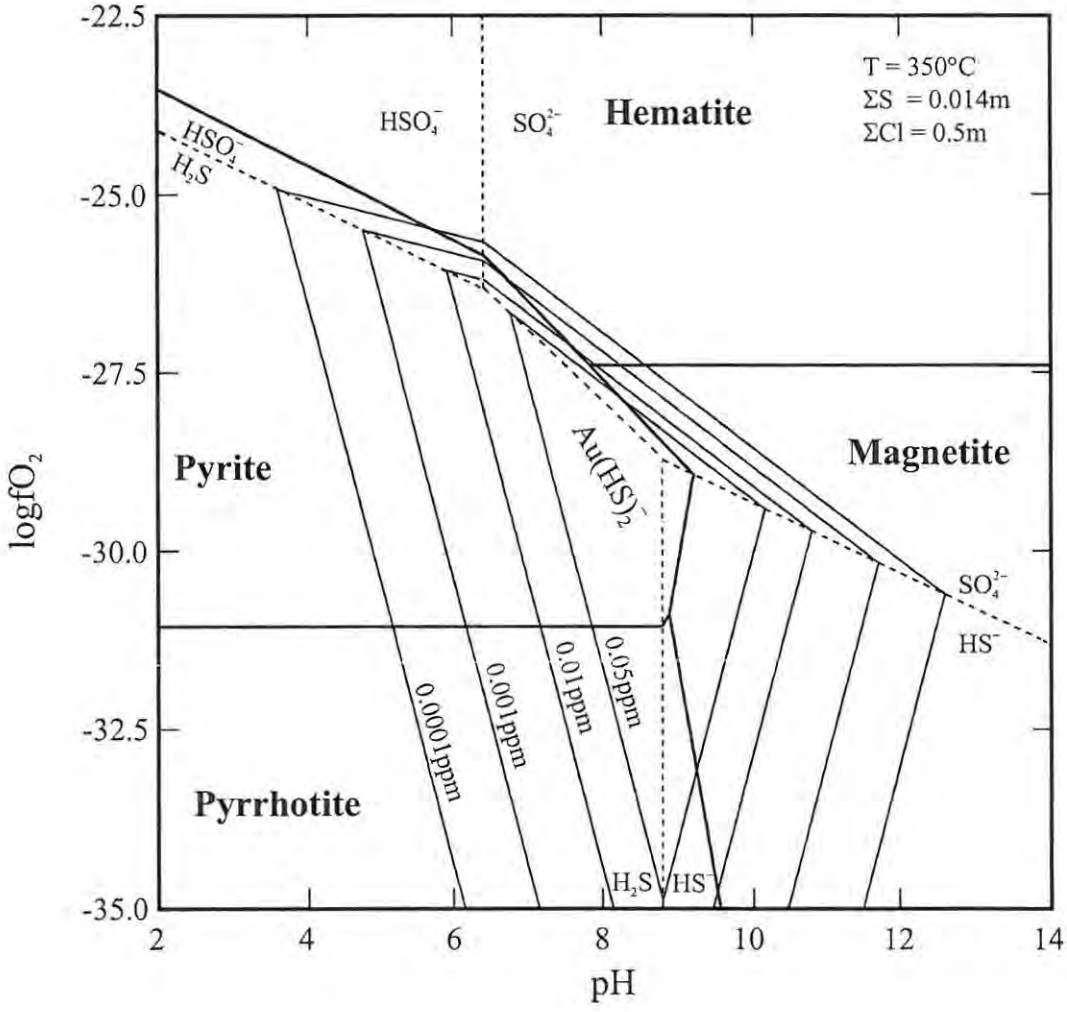

Figure 7.2. Solubility contours for gold as $Au(HS)_2^-$ at T = 350°C, ΣS = 0.014m and ΣCl= 0.5m, shown as a function of fO_2 and pH at Kalahari Goldridge deposit. Thermodynamic data for calculating gold solubility contours are from Helgeson (1969), Robie et al. (1978) and Shenberger and Barnes (1989)

7.2.2.2: Depositional models

Gold deposition is fundamentally controlled by factors which induce changes in the gold-bearing hydrothermal fluid. This invariably affects the solubility of the gold complex by destabilizing it, and efficiently removes gold from solution. Broadly, four processes have been invoked as the principal mechanisms for destabilizing the gold-complexes in hydrothermal ore solutions. These include (i) temperature decrease (ii) dilution, (iii) phase separation and (iv) fluid interaction with wall rock. One or a combination of these could trigger gold precipitation in the high-temperature ore fluids.

Temperature

The effect of temperature is shown to have little significance with regard to gold deposition in Archaean lode gold systems (e.g., Seward, 1973; Phillips and Powell, 1993; Benning and Seward, 1996). Benning and Seward (1996) showed that gold solubility decreases with decreasing temperatures, but at conditions below which mesothermal lode gold deposits can occur (<200°C). Benning and Seward (1996) also indicated that the cooling effect of gold-sulphide complex solution reduces the total sulphur content. However, at temperatures greater than 350°C, the effect is nullified by the high gold solubility at such temperatures.

Dilution

Dilution as a mechanism for gold deposition has been attributed to the mixing of two or more contrasting fluid compositions (e.g., Cox et al., 1991; Anderson et al., 1992). For example, mixing of deeply sourced fluids and surface-derived fluids, or mixing of metamorphic and deeper magmatic or mantle-derived fluids due to varied chemical conditions or temperatures. In gold deposits where fluid mixing operated in gold precipitation, the evidence of fluid mixing is monitored in fluid inclusions, where such changes are represented by the co-occurrence of two chemically and/or contrasted physically contrasting types of fluid inclusion in the same sample, resulting from successive trapping of different fluids (Pichavant et al., 1982). Stable isotopes of oxygen have a useful role in monitoring such processes. Isotopic signatures would be marked by wide variation if the mixing fluids have different isotopic compositions (McCuaig and Kerrich, 1998).

Phase separation

Phase separation results as a response to episodic pressure drops during hydraulic fracturing. Evidence for phase separation as a mechanism for gold precipitation is closely associated with primary fluid inclusions hosted in gold-bearing quartz veins, such as the coexistence of end-member aqueous and carbonic inclusions, heterogeneous trapping of CO_2-H_2O-rich fluids, and a wide range of CO_2 homogenization temperatures (e.g., Robert and Kelly, 1987; Sibson et al. 1988; Fedorowick et al., 1991; Ansdell and Kyser, 1992). During phase separation, volatiles such as CO_2, H_2S, H_2, SO_2 and CH_4, etc. are partitioned into the vapour phase. However, the reduced species, H_2S, H_2, and CH_4 are more volatile and are lost preferentially to the oxidized species CO_2, SO_2, SO_3. This acts to oxidize the residual fluid by increasing the activity of SO_4^{2-} and decreasing the reduced sulphur (H_2S) activity according to equation 7.5 (Drummond and Ohmoto, 1985; Naden and Shepherd, 1989).

$$SO_4^{2-} + 2H^+ = H_2S\uparrow + O_2 \qquad [7.5]$$

$H^+ + HCO_3^- \Leftrightarrow H_2O + CO_2\uparrow$ [7.6]

On the other hand, the loss of CO_2 and H_2S causes a rise in the pH in the residual solution (equations 7.5 and 7.6).

According to the above reactions, phase separation would generally result in pH increase, oxidation and the reduction in the total sulphur content of the ore fluid. However, Bowers (1991) showed that with gold deposition accompanying phase separation, there are competing effects in the relative magnitudes of the changes of these parameters involved in the ore fluid, where the Au is carried as a bisulphide complex according to the reaction:

$Au + 2H_2S = Au(HS)_2^- + H^+ + 1/2H_2$ [7.7].

It was shown that while H_2S loss pushes the reaction to the left, which facilitates Au precipitation, an increase in pH resulting from equations 7.5 and 7.6, and H_2 loss will drive the reaction to the right, resulting in increased Au solubility. Thus, whether or not gold precipitation will take place depends on the initial oxidation state and pH conditions of the fluid and the relative magnitude of the fO_2 and pH increases.

Fluid-rock interaction

In fluid-rock interaction, mineralization is attributed to chemical reaction between circulating hydrothermal fluid and wall rock. As hydrothermal fluid infiltrates wall rock, disequilibrium occurs between circulating fluid and surrounding wall rock, resulting in the precipitation of new mineral phases or dissolution of wall rock components as well as changes in the physico-chemical conditions (e.g., pH, fO_2, ΣS, and ΣC) of the ore fluid, to facilitate the establishment of chemical equilibrium. These processes are characteristic in the development of hydrothermal alteration in wall rocks, and have been identified as an important mechanism for producing large average-grade gold deposits (Groves and Foster, 1993).

In Fe-rich sediments such as dolerites, basalts and iron-formations, the precipitation of sulphides and carbonates in the form of pyrite, pyrrhotite, siderite and ankerite may be characteristic features. This consequently leads to a chemical modification of the fluid by lowering the ΣS and destabilizing the gold-complexes with the subsequent precipitation of gold (Phillips and Groves, 1983; Groves and Phillips, 1987).

$$Au(HS)_2^- + H^+ + FeO_{(silicates,\ oxides)} = Au + \text{sulphide } (FeS_2 \text{ and/or } FeS) + H_2O \qquad [7.8]$$

In carbonaceous sediments, fluid-wall rock interaction results in the generation of CH_4 in the fluid, which consequently decreases the redox condition of the fluid, thereby promoting gold precipitation by destabilizing the gold-complex according to equations 7.9 and 7.10 (Springer, 1985; Cox et al., 1991; Phillips et al., 1996).

$$2C + 2H_2O = CH_4 + CO_2 \qquad [7.9]$$

$$4Au(HS)_2^- + CH_4 + 4H^+ + O_2 = 4Au + CO_2 + 8H_2S \qquad [7.10]$$

Fluid-rock interaction also causes pH decrease by K- and CO_2-fixation reactions in wall rocks resulting from acid production by these reactions (e.g., Kishida and

Kerrick, 1987). Therefore, in rocks with low pH buffering capacity, gold precipitation can be facilitated.

At the Kalahari Goldridge deposit, evidence from fluid inclusions, stable isotopes and composition of certain alteration assemblages (e.g., chlorite) do not support major changes in temperature, mixing or fluid unmixing as potential parameters to have caused gold precipitation. In addition, the relatively narrow range of the isotopic compositions of carbon, sulphur and oxygen in mineral phases associated with the mineralization indicates an evolution of the ore fluid from a homogenous unique source and rules out any possibilities of mixing of variable fluid sources.

Intense brecciation, extensive wall rock alteration and close association of gold with sulphides and carbonate gangue in altered samples suggest that gold precipitation was largely due to the decrease in sulphur activity resulting in the destabilization of the gold-complex and the synchronous precipitation of gold and Fe-sulphides. Furthermore, extensive K-metasomatism and carbonation associated with wall rock alteration shown in equations 5.6 and 5.7 (Chapter 5) and which is reproduced below, also indicate that decrease in pH possibly played an important in gold deposition at Kalahari Goldridge.

$125/3SiO_2 + 35/6Chl\text{-}3 + 35/12H_2O + 12Chl\text{-}2 + 25/4K^+ = 10Stilp + 25/4H^+ + 7Chl\text{-}1$ [5.6]

$X^{2+} + CO_2 + H_2O = XCO_3 + 2H^+$ [5.7] where $X = Fe + Mg + Mn$

The high Au values in certain areas close to carbonaceous phyllites suggests that local reduction in fO_2, is also likely to have activated gold precipitation.

7.3: Genetic Implication

7.3.1: Significance of competency contrast

In spite of some irregular distribution of high gold grades at the Kalahari Goldridge deposit, the most economically viable part of the orebody appears to lie in the most competent and Fe-rich part of the stratigraphy, which consists of the BIF unit in the central portion of the orebody. This section of the orebody is characterized by brecciation and shearing. The localization of high gold grades in the BIF units and the associated fracturing and shearing, outlines the importance of host-rock competence and fluid focusing in ore deposition, where low-tensile rocks serve as important sites for fluid focusing and localization of ore deposits. This relationship has been documented by several workers (Cox et al., 1991; Ridley, 1993) and has been widely observed in Archaean gold deposits.

In particular, Foster and Gilligan (1987) documented that the geometry of lode deposits in iron-formation depends largely on the rheological behaviour, either in a brittle or ductile manner. They noted that when subjected to high fluid pressures and high strain rates, magnetite-rich iron-formations in low-grade metamorphic rocks are more prone to brittle deformation. At Kalahari Goldridge, the close association of boudins and tight isoclinal folds in the cherty BIF are characteristic of ductile deformation. However, the selective extension veins in Fe-rich layers in the BIF, indicate that brittle deformation was prominent. This suggests that mineralization at the Kalahari Goldridge deposit was accompanied by a brittle-ductile deformation.

The less permeable pelitic lithologies, which sandwich the BIF horizon may have acted as fluid barriers to upwelling hydrothermal fluids that localized the flow of fluid in the more competent BIF units, thereby facilitating hydraulic fracturing and subsequently promoting subhorizontal vein growth. It is worth noting that although the pelitic sediments interbedded with the BIF are less mineralized, foliation planes in these sediments as well as lithological discontinuities between BIF and pelitic sediments are also likely to have served as initial conduits for upward migrating ore fluids. In places, this is evidenced by the complete replacement of narrow magnetite mesobands interlayered with schist by pyrrhotite. These observations are consistent features of most mineralized greenstone sequences in which the competency contrast of the host rock plays a major role in the localization of the advecting ore fluid (e.g. Phillips and Groves, 1983; Houstoun, 1987).

7.3.2: Influence of chemical condition of host rock

Examination of assay samples at the Kalahari Goldridge deposit indicates that sulphide-rich samples in the BIF give consistently high gold grades. In contrast, samples from pelitic schist interbedded with the BIF give low gold grades. The veins associated with the mineralization rarely carry significant gold in themselves but gold is closely associated with sulphides and carbonates in the alteration assemblage. Most of the visible gold occurs as inclusions in pyrite. The gold also occurs in textural equilibrium with the sulphides and carbonate gangue and in microcrack-fillings in pyrite. The high carbonate and sulphide alteration associated with the Fe-rich BIF and the close association of gold within the alteration zone provides evidence that the chemical conditions of the host BIF (high Fe/Fe+Mg) played a critical role in controlling gold deposition (refer to Fig. 2.8). Locally, high gold values have been found in close proximity to carbonaceous phyllites at contacts between the footwall and BIF horizon. The occurrence of gold in pyrite fractures may indicate introduction of gold during a later deformational event. This may be remobilized from earlier gold associated with the alteration event or gold released from lattice sites of the early sulphides. The observations as outlined above, suggest that fluid access via hydraulic fracture played a critical role in the distribution of the alteration zone and Au distribution and that Au was added to the iron-formation from an external source.

7.3.3: Comparison with other Archaean deposits

Several features associated with the Kalahari Goldridge deposit are comparable with epigenetic gold deposits in other Archaean iron-formations described by several authors (e.g., Phillips et al. 1984; Wyman et al., 1986; Groves et al., 1987; Lhotka and Nesbitt, 1989; Vielreiher et al., 1994; Newton et al., 1997). In all these deposits, a close genetic relationship has been observed between quartz veins, sulphides and Au distribution in alteration zones. The mineralized veins served as conduits for introduction of ore solution. Fluid interaction with host rock along fluid conduits resulted in selective replacement of iron oxides and iron silicates by sulphides and carbonates, which are characteristic features. These features provide authentic evidence that Au and associated elements (e.g., As, S, Bi, Te and Ag) were derived from an external source and added to the iron formation.

The ore shoots in most Archaean lode gold deposits are documented as occurring at intersections between shear zones or major faults and other planar structures, and also exhibit plunges that are subparallel to mineral elongation lineations in the host rock, which emphasizes a structural relationship between stretching and the development of fluid-focusing conduits (Groves and Foster, 1993). In particular, the gold mineralization hosted by BIF is stratabound and exhibits strong structural control, with the ore shoots commonly associated with linear structures, fold closures resulting from structural thickening of BIF, minor fold structures, fault and shear fractures (Cox et al. 1991; Peters, 1993). Although the lengths of the orebodies are highly variable, the width is largely controlled by the thickness of the BIF with ore shoots commonly exhibiting down-dip continuity. Examples of the structural controlling features of these ore shoots, have been reported in several BIF-hosted deposits (e.g. Fumani, Pretorius et al., 1988; Mt. Morgans, Vielreicher, 1994; Santa Craze, Newton et al., 1997). At the Fumani mine in South Africa, Pretorius et al. (1988) observed Au mineralization to be concentrated parallel to mineral elongation lineation within shear zones in BIF. Similarly, at the Santa Craze BIF-hosted deposit in Western Australia, Newton et al. (1997) also determined the plunge of the shoots to correspond to the intersection between the BIF and sub-horizontal quartz-carbonate veins. Similar relationship was reported at Mt. Morgans in the Yilgarn block of Western Australia where Vielreicher (1994) noted economic gold mineralization within faulted and folded pyrite-rich zones in oxide facies BIF.

Evaluation of textural relationships, geochemical data and structural information at the Kalahari Goldridge deposit, suggests that gold mineralization postdates chemical sedimentation of the ferruginous host rock and therefore supports an epigenetic model. Furthermore, the low base metals associated with the sulphide mineralogy rules out possible submarine volcanic activity for the genesis of gold at Kalahari Goldridge.

An epigenetic model for the mineralization is supported by the following observations:

1. Close association with hydrothermal alteration and quartz-carbonate extension veins which crosscut lithological layering of host BIF.
2. Meso- and micro-scale foliation-parallel replacement of magnetite by pyrite, pyrrhotite and siderite along vein contacts with host BIF.
3. Close association of Au with sulphides in altered BIF samples and
4. Absence or minimal occurrence of sulphidization and carbonation as well as low Au tenors in less altered BIF samples.

7.4: Model for Exploration

In most gold terranes, conventional geochemical methods have commonly been used for exploring concealed deposits. In this method, coherent correlation between Au and rare elements such As, Bi, W, Te, Sb and Se has proved useful in targeting concealed deposits. At the Kalahari Goldridge deposit, the current study has revealed no coherent correlations between Au and these elements and therefore makes it difficult to use typical pathfinder elements as an exploration tool. However, despite lack of coherent correlation between Au and other gold-related rare elements, the mass action calculation shows that an increase in Au is accompanied by co-enrichment in some major (K, Mg and Na) and trace elements (As, Te, Bi and Ag, Rb, Ba, Zr and Sc). On this basis, it is suggested that all trace elements that show anomalous enrichment (As, Te, Bi, Ag, K, Rb, Ba, Zr and Sc) with Au at Kalahari Goldridge should be used as pathfinders in the BIFs, but particularly, the extremely high enrichment of Sc may serve as an important geochemical tool for exploration in ferruginous sediments in the Kraaipan region.

Empirical observations of $\delta^{13}C$ and fluid composition in mineralized quartz veins and geochemical analyses of host rocks also suggest that the zone of wall rock alteration may define potential targets for exploration in the Kalahari Goldridge area. Several lines of evidence suggest that the stable isotope data on mineral phases from alteration samples reflects the fluid/rock ratios operating during alteration. In particular, carbonate alteration by fluid interaction with wall-rocks from a discrete conduit may show a systematic decrease in carbonate content and increase in carbonate $\delta^{13}C$ with increasing distance from the conduit, due to evolution of a finite reservoir of the fluid carbon as observed in several Archaean lode Au deposits. In most cases, the stable isotope composition of carbonates in wall rock show a systematic variation with proximity to the fluid conduit that is commonly characterized by veins.

At the Kalahari Goldridge deposit, the coherent $\delta^{13}C$ values of carbonates in mineralized veins and BIF provide evidence that ore fluid equilibration with host rock took place during the mineralization episode. The absence or minimal occurrence of carbonates in the least altered BIF further suggests that carbonate precipitation was largely due to the ore fluid associated with the mineralization. In addition, the heavy $\delta^{13}C$ signatures of carbonates in the early metamorphic veins (Group I, −2.7 to −2.0 ‰) in comparison with the mineralized veins (−8.0 to −5.6 ‰) and altered BIF (−6.7 to −5.4 ‰), suggest the $\delta^{13}C$ signatures may be used to distinguish between alteration by metamorphic fluids and mineralized zones in the Kalahari Goldridge area.

7.5: Conclusions

The gold was mobilized by a deep-seated transgressing fluid and focused into structurally structural controlled sites and chemically favourable Fe-rich sediments. The characteristics of the ore fluid suggest that Au was transported as a sulphide complex, $Au(HS)_2^-$. Gold deposition was largely controlled by linear structures characterized by mineral elongation and the intersection of planes of shallow-dipping quartz-carbonate veins and host BIF. The overall competence of the BIF and the high Fe contents provided an ideal site for hydraulic fracturing and gold deposition respectively. Differences in competence between the BIF and enclosing pelitic sediments resulted in brittle-ductile deformation in the BIF and consequently creating favourable conduits for ore-fluid ingress into the host rock. The high silica content of the BIF is also likely to have enhanced ductile shearing in the BIF during deformation. Gold precipitation was facilitated by the interaction between ore fluid and the chemically Fe-rich sediments resulting in extensive carbonation, sulphidation and K-metasomatism. In particular, sulphidation reactions led to a decrease in the $m_{\Sigma S}$, while the dual effect of K-metasomatism and carbonation led to the decrease in the pH. These effects destabilized the $Au(HS)_2^-$ complex and consequently depositing gold. The gold mineralization was associated with two structural events, which were separated in time during a D_2 deformational event.

The stable isotope and fluid inclusion data do not provide an unequivocal distinction between a magmatic or metamorphic fluid source for mineralization at Kalahari Goldridge deposit. However, the relatively narrow range of the ore fluid isotopic compositions of carbon, sulphur and oxygen suggest that the fluid evolved from a homogenous unique source.

Table 7.1. Summary of physicochemical conditions associated with lode gold deposits in Archaean greenstone belts.

Parameter	Archaean	Barberton	This study (Goldridge)
T°C	200–450	290–310	340–400
P_{fluid} (Kbars)	1.0–3.0 (generally 1.0–2.0)	~0.9	0.75–2.0
XCO_2	0.03–0.25 (generally 0.10–0.15)	~0.1	0.05–0.16
Salinity (wt % NaCl equiv.)	< 6 (generally <2)	5–6	0.0 to 5.77 (mean = 3.25±0.25)
$\log fO_2$ (bars)	−33 to −29.7 (reducing)	n/a	−32.96 to −29.98 (reducing)
$m_{\Sigma S}$	10 to $10^{-3.5}$	n/a	0.011–0.018
pH	near-neutral to alkaline		
ρ_{fluid}(g/cm^3)	0.8–0.9 (generally 0.9)		0.76–0.88
$\delta^{13}C_{carbonate}$ (‰)	−10 to +2.2 (generally −8.5 to −2.5)	−4.5 to −2.5	−7.56 to −5.42
$\delta^{13}C_{fluid}$ (‰)	−7.0 to +1 (generally −4 to −2)	n/a	−7.37 to −6.0
$\delta^{18}O_{quartz}$ (‰)	+8 to +16 (generally +11 to +14)	+12 to +13	+11.96 to +14.54
$\delta^{18}O_{fluid}$ (‰)	+2.5 to +10 (generally +5 to +8)	+5.1 to 5.8	+6.65 to +10.48
$\delta^{34}S_{pyrite}$ (‰)	+0.8 to +8.1 (generally +1 to +5; Golden Mile −9.5 to −1.6)	+1.4 to +3.9	+2.69 to + 4.94
$\delta^{34}S_{pyrrhotite}$ (‰)			+1.95 to +4.05
$\delta^{34}S_{fluid}$ (‰)	+1 to +3	n/a	+1.69 to +4.0

Data for Archaean from Perring et al. (1987) except $m_{\Sigma S}$ (Mikucki, 1998). Data for Barberton from de Ronde et al. (1992). n/a = not available.

The lack of data on the Kraaipan greenstone belt with respect to history of the mineralization and fluid evolution precludes any regional comparison. Available data on the nature and composition of the ore fluid associated with several deposits in the Barberton greenstone belt (de Ronde et al., 1992) also on the Kaapvaal Craton, however, exhibit some intrinsic differences from that of Kalahari Goldridge (Table 7.1). This suggests that gold mineralization in both greenstone belts was possibly associated with discrete fluid events. A comparison of the Kalahari Goldridge data with other worldwide deposits shows that it falls within the range reported for Archaean lode deposits in other cratons. This lends credence to the fact that unique fluid history and physico-chemical conditions are associated with gold mineralization in Archaean greenstone belts.

An important distinguishing feature of the Kalahari Goldridge deposit from several studied BIF-hosted deposits is the relatively high potassic enrichment consisting typically of stilpnomelane and muscovite. In most BIF-hosted gold deposits, potassic enrichment is negligible because of the low concentration of Al_2O_3 in the BIF to stabilize K-bearing phases (Groves et al., 1985).

Anderson, M. R., Rankin, A. H., and Spiro, B., (1992) Fluid mixing in the generation of mesothermal gold mineralization in the Transvaal Sequence, Transvaal, South Africa. European Journal of Mineralogy 4: 933-948.

Anhaeusser, C. R and Walraven, F., (1999) Episodic granitoid emplacement in western Kaapvaal Craton: evidence from the Archaean Kraaipan granite-greenstone terrane, South Africa. Journal of African Earth Sciences 28: 289-309.

Anhaeusser, C. R., (1986) Archaean gold mineralisation in the Barberton Mountain land. In: Anhaeusser, C. R., and Maske, S., (eds). Mineral Deposits of Southern Africa. Geological Society of South Africa, 113-154.

Barton, M. D., Ilchik, R. P., and Marikos, M. A., (1991). Metasomatism. In: Kerrick, D. M., (ed) Contact metamorphism. Mineralogical Society of America, Reviews in Mineralogy 26: 321-350.

Becker, R. H., and Clayton, R. N., (1976) Oxygen isotope study of a precambria iron-formation. Hamersley Range. Western Australia Geochimica et Cosmochimica Acta 40: 1153-1165.

Benning, L.G., and Seward, T. M., (1996) Hydrosulphide complexing of Au (I) in hydrothermal solutions from 150-400C and 500-1500 bar. Geochimica et Cosmochimica Acta 60: 1849-1871.

Bloem, E. J. M., Dalstra, H. J., Groves, D. I., and Ridley, J. R., (1994) Metamorphic and structural setting of Archaean amphibolite-hosted gold deposits near Southern Cross, Southern Cross Province, Yilgarn Block, Western Australia. Ore Geology Reviews 9: 183-208.

Bodnar, R. J., Reynolds, T. J., and Kuehn, C. A., (1985) Fluid inclusion systematics in epithermal systems: In: Berger, B. R. and Bethke, P. M., (eds) Geology geochemistry of epithermal systems, Reviews in Economic Geology: Society of Economic Geologists 2: 73-97.

Bohlke, J. K., (1989) Comparison of metasomatic reactions between a common CO_2-rich vein fluid and diverse wall rocks: intensive variables, mass transfers, and Au mineralization at Alleghany, California. Economic Geology 84: 291-327.

Borthwick, J, and Harmon, R. S., (1982) A note regarding ClF_3 as an alternative to BrF_5 for oxygen isotope analysis. Geochimica et Cosmochimica Acta 46: 1665-1668

Bottinga, Y., (1969) Calculated fractionation factors for carbon and hydrogen isotope exchange in the system calcite-CO_2-graphite-methane-hydrigen and water vapour: Geochimica et Cosmochimica Acta 33: 49-64.

Bowers, T. S., and Helgeson, H. C., (1983) Calculation of the thermodynamic and geochemical consequences of non-ideal mixing in the system H_2O-CO_2-NaCl on phase relations in geologic systems: Equation of state for H_2O-CO_2-NaCl fluids at high pressures and temperatures. Geochimica et Cosmochimica Acta 47: 1247-1275.

Boyle, R., (1979) The geochemistry of gold and its deposits. Canada. Geological Survey Bulletin 280: 584pp

Bozzo, A. T., Chen, H. S., Kass, J. R., and Barduhn, A. J., (1975) The properties of the hydrates of chlorine and carbon dioxide. Desalination. 16: 303-320.

Brown, E. H., (1971) Phase relations of biotite and stilpnomelane in the greenschist facies. Contributions to Mineralogy and Petrology 31: 1153 -1165.

Brown, E. H., (1975) A petrogenic grid for reactions producing biotite and other Al-Fe-Mg silicates in the greenschist facies. Journal of Petrology 16: 257-271.

Brown, P. E., and Lamb, W. M., (1989) P-V-T properties of fluids in the system $H_2O \pm CO_2 \pm NaCl$: New graphical presentations and implications for fluid inclusion studies. Geochimica et Cosmochimica Acta 53: 1209 -1221.

Burger, A. J., and Walraven, F., (1979) Summary of age determinations carried out the period from April 1977 to March (1978). Annals Geological Survey South Africa 12: 209-218.

Burrows, D. R., Wood, P. C., and Spooner, E. T. C., (1986) Carbon isotope evidence for magmatic origin for Archaean gold-quartz vein ore deposits. Nature 321: 851-852.

Burrows, D. R., Spooner, E. T. C., (1987) Generation of magmatic H_2O-CO_2 fluid enriched in Mo, Au, and W within an Arcahean sodic granodiorite stock, Mink Lake, northwestern Ontario. Economic Geology 82: 1931-1957.

Burrows, D. R., Spooner, E. T. C., (1987) Relationship between Archaean gold quartz vein-shear zone mineralisation and igneous intrusion in the Val d'Or and Timmins areas, Abitibi subprovince, Canada. Economic Geology Monograph 6: 424-444.

Burruss, R. C., (1981) Analysis of fluid inclusions: Phase equilibria at constant volume. American Journal of Science 281: 1104-1126.

Burruss, R. C., (1981) Analysis of phase equilibria in C-O-H-S fluid inclusions, In: Hollister, L. S., and Crawford, M. L., (eds). Short course in fluid inclusions: Applications to petrology. Mineralogical Association of Canada. 39-74.

Caddey, S. W., Bachman, R. L., Campbell, T. J., Reid Rolland, R. R., and Roben, P. O., (1991) The Homestake gold mine, an early Proterozoic iron-formation hosted gold deposit. Lawerence County, South Dakota. U.S. Geological Survey Bullettin. 1857-J67.

Cassidy, K. F., and Bennet, J. M., (1993) Gold mineralization at the Lady Bountiful mine, Western Australia: An example of a granitoid hosted Archaean lode gold deposit Mineralium Deposita 28: 388-408.

Cameron, E. M., (1988) Archaean gold: Relation to granulite formation and redox zoning in the crust. Geology 16: 109-112.

Cameron, E. M., and Hattori, K., (1987) Archaean gold lode mineralization and oxidized hydrothermal fluids. Economic Geology 82: 1177-1191.

Cathelineau, M., (1988) Cation site occupancy in chlorites and illites as a function of temperature. Clay Minerals 23: 471-485.

Cathelineau, M., and Nieva, D., (1985) A chlorite solid solution geothermometer. The Los Azufres geothermal system (Mexico). Contributions to Mineralogy and Petrology 91: 235-244.

Clark, M. E., Carmichael, D. M., Hodgson, C. J., and Fu, M., (1989) Wall-rock alteration, Victory gold mine, Kambalda, Western Australia: processes and P-T-XCO_2 conditions of metasomatism. Economic Geology Monograph 6: 445-459.

Clayton, R. N., and Mayeda, T. K., (1963) The use of bromine pentafluoride in the extraction of oxygen from oxides and silicates for isotopic analysis. Geochimica et Cosmochimica Acta 27: 43-52.

Clayton, R. N., Muffler, L.J. P., White, D. E., (1968) Oxygen isotope study of calcite and silicates of the River Ranch No1 well, Salton sea geothermal field, Carlifonia: American Journal of Science 266: 968-979.

Collins, P.L.F, (1979) Gas hydrates in CO_2-bearing fluid inclusions and the use of freezing data for estimation of salinity. Economic Geology 74:1435-1444.

Colvine, A, C., (1989) An empirical model for the formation of Archean gold deposits: Products of final cratonization of the Superior province, Canada: Economic Geology Monograph 6: 37-53.

Colvine, A. C., Fyon, J. A., Heather, K. B., Marmont, S., Smith, P. M., and Troop, D. G., (1988) Archean lode gold deposits in Ontario Geological Survey Miscellaneous Paper. 139.136.

Cox, S. F., (1987) Antitiaxial crack-seal vein microstructures and their relationship to displacement paths. Journal of Structural Geology 9: 779-787.

Cox, S. F., and Etheridge, M. A., (1983) Crack-seal fibre growth mechanisms and their significance in the development of oriented layer silicate microstructures. Tectonophysics 92: 147-170.

Cox, S. F., Wall, V. J., and Etheridge, M. A and Potter, T. F., (1991) Deformation and metamorphic processes in the formation of mesothermal vein-hosted gold deposits- examples from the Lachlan Fold Belt in the central Victoria, Australia. Ore Geology Reviews 6: 391-423.

de Ronde, C. E. J., Spooner, E. T. C., de Wit, M. J., and Bray, C. J., (1992) Shear zone-related, Au quartz vein deposits in the Barberton greenstone belt, South Africa: Field and petrographic characteristics, fluid properties, and light stable isotope geochemistry. Economic Geology 87: 366-402.

Desborough, G. A, Heidel, R. H., Raymond, W. H., and Tripp, J., (1971) Primary distribution of silver and copper in native gold from six deposits in the western United States. Mineralium Deposita 6: 321-334

Diamond, L.W., (1992) Stability of CO_2 clathrate hydrate + CO_2 liquid + CO_2 vapour + aqueous KCl-NaCl solutions: Experimental determination and application to salinity estimates of fluid inclusions. Geochimica et Cosmochimica Acta 56: 273-280.

Du Toit, A. L., (1908) Geological Survey of portion Mafeking and Vryburg. Annual report of the Geological Commission of the Cape of Good Hope (1907): 123-157.

Duane, Z., and Moller, N., and Weare, J. H., (1992) An equation of state for the CH_4-CO_2-H_2O system: II. Mixtures from 50° to 1000°C and 0 to 1000 bar. Geochimica et Cosmochimica Acta 56: 2619-2631.

Dymek, R.F., and Klein, C., (1988) Chemistry, petrology and origin of banded iron-formation lithologies from the 3800 Ma Isua supracrustal belt, West Greenland. Precambrian Research 39: 247-302.

Eggleton, R. A., (1972) The crystal structure of stilpnomelane, Part II. The full cell. Mineralogical Magazine 38: 693-711.

Eggleton. R. A., and Chappell. B. W., (1978) The crystal structure of stilpnomelane, Part III. Chemistry and physical properties. Mineralogical Magazine 42: 361-368.

Eilu, P, Mikucki, E. J and Groves, D. I., (1997) Wallrock alteration and primary geochemical dispersion in lode-gold exploration. Society for Geology Applied to Ore deposits Short Course, Volume 1, 65p.

Eilu, P., Mikucki, E. J., and Dugdale, A.L., (2001) Alteration zoning and primary geochemical dispersion at the Bronzewing lode-gold deposit, Western Australia. Mineralium Deposita 36: 13-31.

Ely, J. F., Haynes, W. M., and Bain, B. C., (1989) Isochoric (p, V_m, T) measurement on CO_2 and on ($0.982CO_2$ + 0.018N2) from 250 to 330K at pressures to 35 MPa: Journal of Chemical Thermodynamics 21: 879-894.

Etheridge, M. A., (1983) Differential stress magnitudes during regional deformation and metamorphism: Upper bound imposed by tensile fracturing. Bureau of Mineral Resources. 11: 231-234.

Fan, H., Groves, D. I., Mikucki, E. J., McNaughton, N. J., (2000) Contrasting fluid types at the Nevoria gold deposit in the Southern Cross greenstone, Western Australia: Implication of auriferous fluids depositing ores within an Archaean banded iron-formation. Economic Geology 95: 1527-1536.

Floran, R. J., and Papike, J. J., (1975) Petrology of the low-grade rocks of the Gunflint Iron-formation, Ontario-Minnesota. Geological Society America Bulletin 86: 1169-1190.

Floran, R. J., and Papike, J. J., (1978) Mineralogy and Petrology of the Gunflint Iron Formation, Minnesota-Ontario: correlation of compositional and assemblage variations at low to moderate grade. Journal of Petrology 19: 215-288.

Foster, R. P., ed. (1984) Gold'82: The Geology, Geochemistry and Genesis of Gold Deposits. Balkema, Rotterdam. 753pp.

Foster, R. P., (1985) Major controls of Archaean gold mineralisation in Zimbabwe. Transactions of Geological Society of South Africa 88: 109-133.

Foster, R. P., (1989) Archaean gold mineralisation, Zimbabwe: Implication for metallogenesis and exploration. Economic Geology Monograph 6: 54-70.

Foster, R. P., and Gilligan, J. M., (1987) Archaean iron-formation and gold mineralization in Zimbabwe. In: Appel., and LaBerge, G. L., (eds). Precambrian iron-formations. Athens, Theophrasus publication, 635-674.

French, B. M., (1973) Mineral assemblages on diagenetic and low grade metamorphic iron-formation. Economic Geology 168: 1063-1074.

Fripp, R. E. P., (1976) Stratabound gold deposits in Archean banded Iron-formation, Rhodesia. Economic Geology 71: 58-75.

Frost, B. R., (1979) Metamorphism of Iron-Formation: Parageneses in the System Fe-Si-C-O-H. Economic Geology 74: 775-785

Gebre-Miriam, M., Groves, D. I., McNaughton, N. J., Mikucki, E. J., and Vearncombe, J. R., (1993) Archaean Au-Ag mineraligation at Race-track near Kalgoorlie, Western Australia. A high crustal-level expression of the Achaean composite lode-gold system. Mineralium Deposita 28: 375-387.

Gehrig, M., (1980) Phasengleichgewichte und PVT-Daten ternärer Mischungen aus Wasser, Kohlendioxid und Natriumchlorid bis 3kbar und 550°C. Doctoral dissertation, Freiburg, W. Germany, Hochschulverlag.

Gibert, F., Pascal, M. L., and Pichavant, M., (1998) Gold solubility and speciation in hydrothermal solutions: Experimental study of the stability of hydrosulphide complex of gold (AuHS) at 350 to 450 bars. Geochimica et Cosmochimica Acta 62: 2931-2947.

Golding, S. D., and Wilson, A, F., (1983) Geochemical and stable isotope studies of the No. 4 Lode, Kalgoorlie, Western Australia. Economic Geology 78: 438-450.

Golding, S. D., Clark, M. E., Keele, R. A., Wilson, A. F., and Keays, R. R., (1990) Geochemistry of Archaean epigenetic gold deposits in the Eastern Goldfields In: Herbet, H. K., Ho, S. E (eds) Stable isotopes and fluid processes in mineralization, Geology Department and University Extension, University of Western Australia publication number 23: 141-176.

Golding, S. D., McNaughton, N. J., Barley, M. E., Groves, D. I., Ho, S. E., Rock, N. M. S., and Turner, J. V., (1989) Archean carbon and oxygen reservoirs: Their significance for fluid sources and circulation paths for Archean mesothermal gold deposits of the Norseman-Wiluna belt, Western Australia. Economic Geology Monograph 6: 376-388.

Gole, M. J., (1980) Mineralogy and Petrology of very low-grade metamorphic Archean banded iron-formations. Weld Range, Western Australia. American Mineralogy 65: 8-25.

Gole, M. J., (1981) Archean banded iron-formations, Yilgarn Block, Western Australia. Economic Geology 76: 1954-1974.

Gole, M. J., and Klein, C., (1981a) Banded iron-formation through much of the Precambrian time. Journal of Geology 89: 169-183.

Gross, G. A., (1988) Genetic concepts for Iron-formation and associated metalliferous sediments. Economic Geology Monograph 8: 51-81.

Gross, G. A., and McLeod, C. R., (1980) A preliminary assessment of the chemical composition of iron-formations in Canada. Canadian Mineralogy 18: 223-229.

Groves, D. I and Foster, R. P., (1993) Archaean lode gold deposit. In: Foster, R. P (ed). Gold Metallogeny and Exploration. Chapman and Hall. 63-103.

Groves, D. I., Golding, S. D., Rock, N. M. S., Barley, M. E., and McNaughton, N. J., (1988) Archean carbon reservoirs and their relevance to the fluid source for gold deposits: Nature 331: 254-257.

Groves, D. I and Philips, G. N., (1987) The genesis and tectonic control on Archaean gold deposits of the Western Australian Shield- A metamorphic replacement model. Ore Geology Reviews 2: 287-322.

Groves, D. I., Phillips, G. N., Falconer, L. J., Houstoun, S. M, Ho, S. E, Browning, P., Dahl, N., McNaughton, N. J., (1987). Evidence for an epigenetic origin for BIF-hosted gold deposits in greenstone belts of the Yilgan block, Western Australia. In: Ho S. E and Groves D. I (eds). Recent Advances in Understanding Precambrian Gold Deposits. Geology Department and University Extension, The University of Western Australia, Publication number 11: 167-179.

Groves, D. I., Phillips, G. N., Ho, S. O., and Henderson, C. A., Clark, M, E.., and Woad, G. M., (1984) Control and distribution Archaean gold deposits of Western Australia. In: Foster, R. P., (ed). Gold'82: The Geology, Geochemistry and Genesis of Gold Deposits. Balkema, Rotterdam. 753pp.

Guilhaumou, N., Santos, M., Touray, J. C, Benny, C and Dardenne, M (1990) Multiphase methane-rich fluid inclusions in gold-bearing quartz as illustrated at Pontal (Goias, Brazil). Mineralogical Magazine 54: 257-266.

Hall, D. L., Sterner, S. M., and Bodnar, R. J., (1988) Freezing point depression of $NaCl-KCl-H_2O$ solutions. Economic Geology 83: 197-202.

Harris, D. C (1986) Minerals in Main Hemlo gold deposit, Ontario Geological Survey of Canada paper 86-1A: 49-54.

Hayashi, K. I., and Ohmoto, H., (1991) Solubility of gold in NaCl- and H_2S-bearing aqueous solutions at 250°-350°C. Geochimica et Cosmochimica Acta 55: 2111-2126.

Helgeson, H. C (1969) Thermodynamics of thermal system at elevated temperatures and pressures. American Journal of Science 267: 729-804.

Helgeson, H. C., Kirkman, D. H., and Flower, G. C., (1981) Theoretical predictions of the thermodynamic behavior of aqueous electrolytes at high pressures and temperatures: IV. Calculations of activity coefficients, osmotic coefficients, and apparent molal and standard and relative partial molal properties to 600C and 5Kb. American Journal of Science **281**: 1249-1516.

Henley, R. W., (1973) Solubility of gold in hydrothermal chloride solutions: Chemical Geology **11**: 73-78.

Hey, M. H., (1954) A new review of the chlorites. Mineralogical Magazine **30**: 277

Hilliard, P., (1996) Kraaipan Greenstone Belt structural study: Results of feasibility study and preliminary findings. Unpublished report. West Rand Consolidated Mines, Johannesburg. 25pp.

Ho, S. E., Groves, D. I., and Phillips, G. N., (1990) Fluid inclusions in quartz veins associated with Archaean gold mineralisation: clues to ore fluids and ore depositional conditions and significance to exploration. . In: Hubert, H. K and Ho, S. E (eds). Stable isotopes and fluid processes in mineralisation. Geology Department and University Extension, The University of Western Australia, Publication number **23**: 35-50.

Ho, S. E., and Groves, D. I., (eds), (1987) **Recent Advances in Understanding Precambrian Gold Deposits**. Geology Department and University Extension, The University of Western Australia, Publication number **23**: 368pp.

Hodgson, C. J and Hamilton, J. V (1989) Gold mineralisation in the Abitibi Greenstone Belt: End-stage result of Archaean collisional tectonics. Economic Geology Monograph **6**: 86-100.

Hollister, L. S., (1990) Enrichment of CO_2 in fluid inclusions in quartz by removal of H_2O during crystal-plastic deformation. Journal of Structural Geology **12**: 895-901.

Holloway, J. R., (1977) Fugacity and activity of molecular species in supercritical fluids. In: D. G. Fraser (ed), Thermodynamics in Geology. 161-181.

Holloway, J. R., (1981) Composition and volumes of supercritical fluids in the earth's crust. In: Hollister, L. S., Crawford, M. L (eds) Short Course in Fluid Inclusion: Application to Petrology, Mineralogical Association of Canada, 13-35.

Hynes, H., (1980) Carbonatization and mobility of Ti, Y and Zr in Ascot formation metabaslts, SE Quebec. Contributions to Mineralogy and Petrology **75**: 79-87.

James, H. L., (1954) Sedimentary facies in iron-formation. Economic Geology 68: 235-293.

Jones, I. M., and Anhaeusser, C. R., (1993) Accretionary lapilli associated with Archaean banded iron formations of the Kraaipan Group, Amalia greenstone belt. South Africa. Precambrian Research 61: 117-136.

Kerrich, R., and Watson, G. P., (1984) The Marcassa mine Archaean lode gold deposit, Kirland Lake, Ontario: Geology, patterns of alteration, and hydrothermal regimes. Economic Geology 79: 1104-1130.

Kerrich, R., (1987) The stable isotope geochemistry of Au-Ag vein deposits in metamorphic rocks: Mineralogical Association of Canada Short Course Handbook. 13: 287-336.

Kerrich, R., (1989) Geochemical evidence on the source of fluids and solutes for shear zone hosted mesothermal Au deposits. Geological Association of Canada Short Course Notes 6: 129-198

Kerrick, R, and Fryer, B. J., (1979) Archaean precious metal hydrothermal systems, Dome Mine, Abitibi greenstone belt. Canadian Journal of Earth Sciences 16: 440-458

Kerrick, R and Fyfe, W. S., (1981) The gold-carbonate association: Sources of CO_2 and CO2 fixation reactions in Archaean lode deposits: Chemical Geology 33: 265-294.

Kerswill, J. A., and Aglin, C. D., (1984) Some thoughts on gold deposits hosted by iron-formation with particular reference to the Lupin Mine, Contwoyto Lake area, NWT, and gold mineralization in the Geraldton Camp. Ontario [abstract] Geological Survey of Canada, Paper 84-8: 6

Kishida, A., and Kerrich, R., (1987) Hydrothermal alteration zoning and gold mineralization at the Kerr Addison Archean lode gold deposit, Kirkland Lake, Ontario. Economic Geology 82: 649-690.

Klein, C., (1974) Greenalite, stilpnomelane, minnesotaite, crocidolite and carbonates in a very low-grade metamorphic Precambrian iron-formation. Canadian Mineralogy 12: 475-498.

Klein, C., (1978) Regional metamorphism of the Proterozoic iron-formation, Labrador Trough, Canada. American Mineralogy **63**: 898-912.

Klein, C., (1983) Diagenesis and metamorphism of Precambrian banded iron-formation. In: Trendall A. F and Morris, R. C (eds). Iron formations: facts and problems. Elsevier, Amsterdam, 417-469.

Klein, C., and Fink, R. P., (1976) Petrology of the Sokoman Iron Formation of the Howells River area, at the western edge of the Labrador Trough. Economic Geology **71**: 453-488.

Klein, C., and Gole, M. J., (1981) Mineralogy and petrology of parts of Marra Mamba Iron Formation, Hamersley basin, Western Australia. American Mineralogy **66**: 507-525.

Kreulen, R., and Schuiling, R, D., (1982) N_2-CH_4-CO_2 fluids during formation of the Dome de I' Agout, France. Geochimica et Cosmochimica Acta **46**: 193-203.

Laberge, G. L (1973) Possible biological origin of Precambrian iron-formations. Economic Geology **68**: 1098-1109.

Ladeira, E. A., (1991) Genesis of gold in the Quadrilátero Ferrifero: A remarkable case of permanency, recycling and inheritance - A tribute to Djalma, Guimaraes, Pierre Routhier and Hans Ramsberg. In: Ladeira, E. A., (ed). Gold '91,Balkama publications, Rotterdam, 11-30.

Laird, J (1982) Amphibolite in metamorphosed basalts rock: greenschist to amphibolite facies and blueschist-greenschist-eclogite relations. In: Veblen, D. R and Ribbe, P. H (eds), Amphiboles: petrology and experimental phase relations, Reviews in Mineralogy **9B**: 113-159.

Lambert, I. B., Phillips, G. N., and Groves, D. I., (1984) Sulphur isotope compositions and genesis of Archaean gold mineralization, Australia and Zimbabwe. In: Foster, R. P (ed). Gold'82: The Geology, Geochemistry and Genesis of Gold Deposits. Balkema, Rotterdam. 753pp. 373 -387.

Langmuir, D., (1979) Techniques of estimating thermodynamic properties for aqueous complexes of geochemical interest. In: Jenne, E. A (ed), Chemical modelling - speciation, sorption, solubility and kinetics in aqueous systems. American Chem. Soc. Sym Washington DC **93**: 353-387.

Lobato, L, M., Ribeiro-Rodrigues, L. C., and Vierra, F. W. R., (2001) Brazil's premier gold province. Part II: geology and genesis of gold in the Archaean Rio das Velhas greenstone belt, Quadrilatero Ferrifero. Mineralium Deposita 36: 249-277.

Leitch, C. H. B., and Lentz, D. R., (1994) The Gresens approach to mass balance constraints of alteration. Methods, pitfalls, examples. In Alteration and alteration processes associated with ore-forming systems. In: Lentz, D. R (ed) Geological Association of Canada Short Course Notes 11: 161-192.

Lesher, C. M., (1978) Mineralogy and petrology of the Sokoman Iron-formation near Ardua Lake, Quebec. Canadian Journal of Earth Science 15: 480-500

Lesher, C. M., Phillips, G. N., Groves, D. I., and Campbell, I. H (1991) Immobility of REE and most high field-strength elements and the first transition series metals during Archaean gold-related hydrothermal alteration of metabasalts at the Hunt mine. Western Australia. In: Ladiera, E.A. (ed). Proceedings of Brazil Gold 91. Balkema. Rotterdam. 327-334

Lhotka, P. G., and Nesbitt, B.E., (1989) Geology of unmineralized and gold-bearing iron-formation, Contwoyto Lake-Point Lake region, Northwest Territories, Canada. Canadian Journal of Earth Sciences 26: 46-64.

Ludden J. N, Daigneault, R, Robert, F and Taylor, R. P., (1984) Trace element mobility in alteration zones associated with Archaean Au lode deposits. Economic Geology 79: 1131-1141.

MacLean, W. H and Kranidiotis, P., (1987) Immobile elements as monitors of mass transfer in hydrothermal alteration: Phelps Dodge massive sulphide deposit, Matagami, Quebec. Economic Geology 82: 951-962.

MacLean, W. H and Barrett, T. J., (1993) Lithogeochemical techniques using immobile elements. Journal of Geochemical Exploration 48:109-133.

Manikyamba, C., Balaram, V and Naqvi, S. M., (1993) Geochemical signatures of polygenetic origin of a banded iron-formation (BIF) of the Archaean Sandur greenstone belt (schist belt) Karnataka nucleus, India. Precambrian Research 61: 137-164.

Marchig, V., Gundlach, H., Moller, P., Schley, F., (1982) Some geochemical indicators for discrimination between hydrothermal metaliferous sediments. Marine Geology 50: 241-256.

Marsh, J. S., (1979) A manual for X-ray fluorescence determination of major and trace elements in natural silicate rock materials. Unpublished manual, Rhodes University, 41pp.

Marcoux, E., Moelo, Y and Leistel, J. M., (1996) Bismuth and cobalt minerals as indicators of stringers zones to massive sulphide deposits, Iberian Pyrite Belt. Mineralium Deposita 31: 1-26.

Mathews, A., and Katz, A. A., (1977) Oxygen isotope fractionation during dolomitization of calcium carbonate. Geochimica et Cosmochimica Acta 41: 1431-1438.

Matsuhisa, Y., Goldsmith, J., Clayton, R. N., (1979) Oxygen isotopic fractionation in the system quartz-albite-anorthite-water. Geochimica et Cosmochimica Acta 43: 1131-1140.

McCrea, J. M (1950) On the isotopic chemistry of carbonates and paleotemperature scale. Journal of Chemical Physics 18: 849-857.

McCuaig, T. C and Kerrick, R., (1998) P-T-t-deformation-fluid characteristics of lode gold deposits: Evidence from alteration systematics. Ore Geology Reviews 12: 381-453.

McNaughton, N.J., Barley, M. E., Cassidy, K. F., Golding, S. D., Groves, D. I., Ho, S. E., Hronsky, J. M. A., Sang, J. H., and Turner, J. V., (1990) Carbon isotope studies In: Ho, SE, Groves, D. I., Bennett, J. M., (eds). Gold deposits of the Archaean Yilgam Craton: nature, genesis and exploration guides. Geology Department and University Extension. University of Western Australia publication number 20: 246-251

Mikucki, E. J., (1998) Hydrothermal transport and depositional processes in Archean lode-gold systems: A review. Ore Geology Reviews 13: 307-321.

Mikucki, E. J., and Groves, D. I., (1990) Gold transport and depositional models. In: Ho, S. E., Groves, D. I and Bennet, J. M (eds). Gold deposits of Archaean Yilgarn Block, Western Australia: Nature Genesis and Exploration Guides.

Geology Department and University Extension, The University of Western Australia, Publication number 20: 278-284.

Mikucki, E. J., and Ridley, J. R., (1993) The hydrothermal fluid of Archaean lode gold deposit at different metamorphic grades: compositional constraints from ores and wall rock alteration assemblages. Mineralium Deposita, 28: 469-481.

Miyano, T., (1982) Stilpnomelane, Fe-rich mica, K-felspar and hornblende in iron-formation assemblages of the Dales Gorge Member, Hamersley Group, Western Australia. Canadian Mineralogy 20: 189-202.

Miyano, T., and Klein, C., (1989) Phase equilibria in the system K_2O-FeO-MgO-Al_2O_3-SiO_2-H_2O-CO_2 and the stability limit of stilpnomelane in metamorphosed Precambrian iron- formations. Contributions to Mineralogy and Petrology 102: 478-491.

Moritz, R. P., and Crocket, J. H., (1991) Hydrothermal wall-rock alteration of the gold-bearing quartz-fuchsite vein at the Dome mine, Timmins Area, Ontario, Canada. Economic Geology 86: 620-641.

Morrison, G. W., Jose, W. J., and Jaireth, S., (1991) Geological and geochemical controls on the silver content (fineness) of gold in gold-silver deposits. Ore Geology Reviews 6: 333-364.

Mullis, J., (1987) Fluid inclusion studies during very low-grade metamorphism. In: Frey, M (ed). Low temperature metamorphism, Glasgow, Blackie, 162-199.

Murphy, J. B., and Hynes, A. J., (1986) Contrasting secondary mobility of Ti, P, Zr, Nb and Y in two metamorphic suite in the Appalachians. Canadian Journal of Earth Sciences 23: 1138-1144.

Neall, F. B., and Phillips, G. N., (1987) Fluid-wall rock interaction in an Archean hydrothermal gold deposit: A thermodynamic model for the Hunt Mine, Kambalda. Economic Geology 82: 1679-1695.

Nesbitt, B. E., and Muehlenbachs, K., (1989) Geology, geochemistry, and genesis of mesothermal lode gold deposits of the Canadian Cordillera: Evidence for ore formation from evolved meteoric water. Economic Geology Monograph 6: 553-570.

Newton, P. G. N., Ridley, J. R., Groves, D. I., Khosrowshahi, S and Smith, B (1997) Intergration of directional variography and structural geology: an example from the Santa-Craze BIF-hosted Au deposit, near Kalgoolie, Western Australia. Chronique de la Recherche Miniere 529: 105-125.

Niu, Y., and Lesher, C. M., (1991) Hydrothermal alteration of mafic metavolcanics and genesis of Fe-Zn-Cu sulfide deposits, Stone Hill District, Alabama. Economic Geology 86: 983-1001.

Oberthur, T., and Saager, R., (1986) Silver and Mercury in gold particles from Proterozoic Witwatersrand placer deposit of South Africa-Metallogenic and geochemical implications. Economic Geology 81: 20-31.

Ohmoto, H., (1972) Systematics of sulfur and carbon isotopes in Hydrothermal Ore Deposits. Economic Geology 67: 551-579.

Ohmoto, H., (1986) Stable isotope geochemistry of ore deposits: Mineralogical Society of America, Reviews in Mineralogy 16: 491-560.

Ohmoto, H., and Kerrick, D., (1977) Devolatilization equilibria on graphitic systems. American Journal of Science 277: 1013-1011.

Ohmoto, H., and Rye, R. O., (1979) Isotopes of sulfur and carbon. In: Barnes, H. L (ed). Geochemistry of Hydrothermal Ore Deposits. John Wiley, 509-567.

Oliver, N. H. S., Hoering, T. C, Johnson, J. W, Rumble III, D and Shanks III, W. C., (1992) Sulphur isotopic disequilibrium and fluid-rock interaction during metamorphism of sulphidic black shales from the Waterville Augusta area, Maine, USA. Geochimica et Cosmochimica Acta 56: 4257-4265.

Perring, C. S., Groves, D. I., and Ho, S. E., (1987) Constraints on the source of auriferous fluids for Archaean gold deposits. In: Ho, S. E., and Groves, D. I (eds) Recent Advances in Understanding Precambrian Gold Deposits. Geology Department and University Extension, University of Western Australia, Publication number 11, 287-306.

Peters, S. G., (1993) Nomenclature, concepts, and classification of oreshoots in vein deposits. Ore Geology Review 8: 3-22.

Phillips, G. N., (1986) Geology and alteration in the Golden Mile, Kalgoolie. Economic Geology 81: 779-808.

Phillips, G. N., and Groves, D. I., (1983) The nature of Archaean gold bearing fluids as deduced from gold deposits of western Australia: Geological Society Australia Journal 30: 25-40.

Phillips, G. N., and Groves, D. I., (1984) Fluid access and fluid wallrock interaction in the genesis of the Archean gold-quartz vein deposit at Hunt mine, Kambalda, Western Australia. In: Foster, R.P (ed). Gold '82: The Geology, Geochemistry and Genesis of Gold deposits, Rotterdam, A.A. Balkama Publication. 689-712.

Phillips, G. N., Groves, D. I., Martyn, J. E., (1984) An epigenetic origin for Archean banded iron-formation-hosted gold deposits. Economic Geology 79: 162-171.

Phillips, G.N., Groves, D.I., and Kerrich, R., (1996) Factors in the formation of the giant Kalgoorlie gold deposit. Ore Geology Reviews 10: 295-317.

Pichavant, M., Ramboz, C., and Weisbrod, A., (1982) Fluid immiscibility in natural processes: Use and misuse of fluid inclusion data. Chemical Geology 37: 1-27.

Potter, R. W., and Brown, D. L., (1977) The volumetric properties of aqueous sodium chloride solutions from 0 to 500C at pressures up to 2000 bars based on a regression of available data in the literature. U.S. Geological Survey Bulletin. 1421-C36.

Poujol, M., Anhaeusser, C. R., and Armstrong, R. A (2000) Episodic Archaean granitoid emplacement in the Amalia-Kraaipan terrane, South Africa: New evidence from single zircon U-Pb geochronology with implications for the age of the western Kaapvaal Craton. Information Circular, Economic Geology Research Institute, University of Witwatersrand 346: 1-21.

Pretorius, A. I., van Reenen, D. D and Barton Jr, J. M (1988) BIF-hosted gold mineralisation at the Fumani Mine, Sutherland greenstone belt, South Africa. South African Journal of Geology 91: 429-438.

Ramboz, C., Pichavant, M., and Weisbrod, A., (1982) Fluid immiscibility in natural processes: Use and misuse of fluid inclusion data. Chemical Geology 37: 29-48.

Ramsay, J. G., (1980) The crack-seal mechanism of rock deformation. Nature 284: 135-139.

Ramsay, J. G., and Huber, M. I,, (1983) The techniques of modern structural analysis. Volume 1: Strain Analysis, London, Academic Press, 307p.

Renders, P. J and Seward, T. M (1989) The stability of hydrosulphido- and sulphido-complexes of Au (I) and Ag (I) at 25°C. Geochimica et Cosmochimica Acta 35: 245-253.

Ridley, J., (1993) The relations between mean rock stress and fluid flow in the crust: With reference to vein- and lode-style gold deposits. Ore Geology Reviews 8: 23-37.

Ridley, J., Mikucki, E. J., and Groves, D. I., (1996) Archean lode-gold deposits: fluid flow and chemical evolution in vertically extensive hydrothermal systems. Ore Geology Reviews 10: 279-293.

Robie, R. A., Hemingway, B. S., and Fisher, J. R., (1978) Thermodynamic properties of minerals and related substances at 298.15K and 1 bar (105 Pascals) pressure and at higher temperatures. US Geological Survey Bulletin 1452.

Roedder, E., (1984) Fluid inclusions; Mineralogical Society of America, Reviews in Mineralogy 12: 646pp.

Rye, R. O., and Ohmoto, H., (1974) Sulphur and carbon isotopes and ore genesis: A review. Economic Geology 69: 826-642.

Ryzhenko, B. N., (1971) Fugacity coefficients of some gases in a broad range of temperatures and pressures. Geochemical International 8: 468-481.

Ryznar, G, Campbell, F. A., and Krouse, H. R., (1967) Sulphur isotopes and the origin of the Quemont orebody. Economic Geology 62: 664-678

Saager, R., Oberthür, T., and Tomschi, H., (1987) Geochemistry and mineralogy of banded iron-formation-hosted gold mineralization in the Gwanda Greenstone Belt, Zimbabwe. Economic Geology 82: 2017-2032.

SACS (South African Committee for Stratigraphy) (1980) Stratigraphy of South Africa. Part I. (Compiler, L. E Kent) Lithostratigraphy of the Republic of South Africa, South West Africa/Namibia, and the Republics of Bophuthatswana, Transkei and Venda. Handbook, Geological Survey of South Africa 8, 690p.

Schwartz, M. O., (1989) Determining phase volumes of mixed CO_2-H_2O inclusions using microthermometric measurements. Mineralium Deposita 24: 43-47.

Seguin, M. K., (1971) Phase relations in the Fe-C-O-S-H_2O system and its geological application. Chemical Geology 7: 5-18.

Seifried, W. E., and Janecky, D. R., (1985) Heavy metal and sulphur transport during subcritical and supercritical hydrothermal alteration of basalt: Influence of fluid pressure and basalt composition and crystallinity. Geochimica et Cosmochimica Acta 49: 2545-2560.

Seward, T. M., (1973) Thio complexes of gold in hydrothermal ore solutions: Geochimica et Cosmochimica Acta 37: 379-399.

Seward, T. M., (1984) The transport and deposition of gold in hydrothermal systems. In: Foster, R. P (ed). Gold' 82, The Geology, Geochemistry and Genesis of Gold Deposits. Balkama, Rotterdam, 165-181.

Seward, T. M., (1993) The hydrothermal geochemistry of gold. In: Foster, R. P (ed). Gold Metallogeny and Exploration. Chapman and Hall. 37-62.

Shenberger, D. M., and Barnes, H. L., (1989) Solubility of gold in aqueous sulfide solutions from 150° to 350°C. Geochimica et Cosmochimica Acta 53. 269-278.

Sheppard, S. M. F., and Schwarcz, H.P., (1970) Fractionation of carbon and oxygen isotopes and magnesium between coexisting metamorphic calcite and dolomite. Contributions to Mineralogy and Petrology 26: 161-198.

Sibson, R. H., (1987) Earthquake rupturing as a hydrothermal mineralising agent in hydrothermal systems. Geology 15: 701-704.

Sibson, R. H, Robert, F, Pouslen K. H., (1988) High-angle reverse faults, fluid pressure cycling, and mesothermal gold-quartz deposits. Geology 16: 551-555.

Sibson, R.H. and Scott, J. (1998) Stress/fault controls on the containment and release of overpressured fluids: examples from gold-quartz vein systems in Juneau, Alaska, Victoria, Australia, and Otago, New Zealand. Ore Geology Reviews 13: 293-306

Springer, J. S (1985) Carbon in Archaean rocks of the Abitibi belt (Ontario-Quebec) and its relationship to gold distribution. Canadian Journal of Science 22:1945-1951.

Taylor, H. P., Jr (1974) The application of oxygen and hydrogen isotope studies to problems of hydrothermal alteration and ore deposition. Economic Geology 69: 843-883.

Taylor, H. P., (1997) Oxygen and hydrogen isotope relationship in hydrothermal mineral deposits. In Barnes, H. L (ed) Geochemistry of hydrothermal ore deposits 3rd edition, Wiley, New York, 259-303.

Touret, J., (1977) The significance of fluid inclusions in metamorphic rock. In Fraser, D. G (ed), Thermodynamics in Geology. 203-227.

Trendal, A. F., (1973) Precambrian iron formations of Australia. Economic Geology 68: 1023-1023.

Truesdell, A. H., (1984) Introduction to chemical calculations. In: Henley, R. W., Truesdell, A. H and Barton, P. B (eds). Fluid-mineral equilibria in hydrothermal systems. Reviews in Economic Geology 1: 1-8.

Van Eden, O, R., de Wet, N. P., Strauss, C. A., (1963) The geology of the area around Schweizer-Reneke. Explanation Sheets 2724B (Pudimoe) and 2725A (Schweizer-Reneke). Geological Survey of South Africa, 76p.

Vielreicher, R. M., Groves, D. I., Ridley, N. J., and McNaughton, N. J., (1994) A replacement origin for the BIF-hosted gold deposit at Mt. Morgans, Yilgarn Block, W.A. Ore Geology Reviews 9: 325-347.

Walshe, J. L (1986) A six-component chlorite solid solution model and the conditions of chlorite formation in hydrothermal and geothermal systems: Economic Geology 81: 681-703.

Watson, E. B., and Brenan, J. M., (1987) Fluid in the lithosphere, 1. Experimentally-determined wetting characteristics of CO_2-H_2O fluids and their implications of fluid transport, host rock physical properties and fluid inclusion formation. Earth and Planat.ary Science Letters 85: 496-515.

Windley, B. F., (1986) The Evolving Continents- 2nd ed. Wiley, Chichester, 399pp.

Yanagisawa, F., and Sakai, H., (1983) Thermal decomposition of bariumsulfate-vanadium pentaoxide-silica glass mixtures for preparation of sulfur dioxide in sulfur isotope ratio measurements. Analytical Chemistry 55: 985-987.

Zang, Y-G., and Frantz, J., D., (1987) Determination of homogenisation temperatures and densities of supercritical fluids in the system NaCl-KCl-$CaCl_2$-H_2O using synthetic fluid inclusions. Chemical Geology 89: 1469-1491.

Zhou, T., Dobos, S. K., and Dong, G., (1994) Origin and fluid geochemistry of unconformity-related gold at the Black Ridge gold deposit, Clermont, Queensland. Economic Geology 89: 1469-1491.

Zimmermann, O. T., and Anhaeusser, C. R., (1991) The northern Kraaipan granite-greenstone terrane. In: Anhaeusser, C. R (ed). The Archaean Kraaipan Group volcano-sedimentary rocks and associated granites and gneisses of the southwestern Transvaal, northern Cape Province and Bophuthatswana. Information Circular, Economic Geology Research Unit, University of Witwatersrand 244: 26-28.

Zotov, A. V., Baranova, N, N., Daryina, T, G., and Bannykt, L. M (1981) Gold (I) complexing in the KCl-HCl-H_2O system at 450°C and 500 atm. Geochemistry International 26: 66-75.

Appendix I

Logged boreholes at the Kalahari Goldridge mine.

Thickness/m	Description
GDP 529 Cross-section 13250	
0-52	Chlorite schist with quartz-carbonate veins with disseminated to euhedral pyrite crystals. Conglomeric pebbles in places.
52-75	Graywacke
75-96	Undifferentiated chloritic/meta-pelitic sequence with pyrite mineralization in meta-pelite.
96-106	Interbedded chlorite schist/chert BIF. Euhedral pyrite in magnetite-rich bands of BIF and thin continous of pyrite in schist units. Quartz-carbonate veins (96-97; 97.11-97.41 inclined at 50°).
106-124	Brecciated massive cherty BIFwith intense veining and pyrite/pyrrhotite replacement. Very high gold grades
124-154.1	Interbedded chlorite schist/cherty BIF with folding in places. Unit cut by dolerite dyke (140-143m).
154-175.6	Banded chert. Less sulphide replacement. Intersection by dolerite dyke (162-164.2m).
175.6 to end of hole	Footwall mafic schist.
GDP 531 Cross-section 13350	
0-90	Graywacke
90-104	Undifferentiated sequence of meta-pelite and schist. Quartz and pyrite stringers in places. Mafic dyke from 101 - 102m
104-147.25	Interbedded chlorite schist/cherty BIF. Quartz-carbonate and pyrite veins at low angle. Intense pyrite/pyrrhotite replacement. Quartz-carbonate vein (147-147.25m).
147.25-168.9	Interbedded chlorite schist/chert BIF. Highly folded (163.7-164.7m).
170-178.3	Footwall mafic schist (highly bleached).
GDP 588 Cross-section 13350	
0-231	Graywacke. Conglomeritic from 143 to 145m.
231-267	Undifferentiated schist/meta-pelite sequence.
267-307	Interbedded chlorite schist/chert BIF. Quartz-carbonate veining in places (291-292m; 293-394m). Carbonaceous meta-pelite sequence from 305-307m.
307-332	Intensely brecciated cherty BIF. Pyrrhotite replacement in entire section. Significant microfolds in places
332-387	Interbedded chlorite/chert BIF with minor folding in places. Quartz-carbonate vein from 383-386m.
387-388	Footwall mafic schist.
GDP 524 Cross-section 13350	
0-23.5	Undifferntiated schist/meta-pelitic sequence with disseminated pyrite in meta-pelites.
23.5-43.6	Interbedded chlorite schist/chert BIF. Mafic dyke from 36.31 to 41m.
43.6-117	Cherty BIF with intense pyrrhotite and pyrite replacement.
117-133.4	Interbedded chlorite schist/chert BIF with microfolding at 125.4 to 125.7m. High pyrite concentration in fractures. quartz-carbonate vein in places.
133.4-end of hole	Footwall mafic schist.
GDP 532 Cross-section 13650	
0-49	Graywacke unit. Conglomeritic from 4 to 16m and 25 to 37m. Mafic dyke intersection, 4.5 to 6m.
49-74	Undifferentiated schist/meta-pelitic unit. Chloritic from 49.4 to 56.3m.
74-121	Interbedded chlorite/chert BIF. High grade in more brecciated and folded areas (75-108m). carbonaceous meta-pelites (114.4-115.8m) and (119.6-121). Multiple quartz-carbonate veining.
121-132	Massive cherty BIF with intense replacement of magnetite by pyrite/pyrrhotite.
132 to end of hole	Footwall mafic schist.
GDP 587 Cross-section 13650	
0-172	Undifferentiated schist/meta-pelitic squence. Disseminated pyrites in meta-pelites.
172-199	Interbedded chlorite/chert BIF.Pyrite/quartz veining. Dolerite dyke intersection (180-187.0m).
199-215	Massive chert BIF. Intense fracturing and high gold grades. Minor foldings in places.
215-253	Interbedded chlorite/chert BIF.Pyrite/quartz veining. Quartz veining (233.8-234.8m).
253 to end of hole	Footwall mafic schist.
GDP 525 Cross-section 13650	
0-19.2	Graywacke. Very conglomeritic from 0.0 to 10.2m.
19.2-47.7	Undifferentiated schist/meta-pelitic sequence. Abundant quartz-carbonate stringers in unit.
47.7-55.0	Interbedded chlorite schist/chert BIF.
55-73	Brecciated cherty BIF. Intensse pyrite/pyrrhotite mineralization and high gold grades.
73-104.3	Fine interlayering of chert/chlorite BIF. Carbonaceous meta-pelites from 84-86m and 99 to 100.5m. Fine lamination of pyrite along foliation plane of meta-pelite.
104.3 to end of hole	Footwall mafic schist.
GDP 527 Cross-section 13950	
0-35	Undifferentiated schist/meta-pelitic sequence. Meta-pelites from 30 to 35m
35-43	Interbedded chlorite schist/cherty BIF. Carbonaceous meta-pelites unit from 38.7 to 41.23m
43-61	Highly brecciated Cherty-BIF with intense pyrite/pyrrhotite replacement. High grade ore.
61-78	Interbedded chlorite schist/chert BIF. Minor folding and kinks. Fine pyrite lamination in schist unit.
78 to end of hole	Footwall mafic schist.
GDP 452 Cross-section 13950	
0-30m	Graywacke
30-35	Undifferentiated chlorite schist/ carbonaceous meta-pelites.
35-41	Interbedded chlorite schist/cherty BIF.
41-60.26	Massive cherty BIF and intensively brecciated.Cut by several quartz-carbonate veins and pyrite/pyrrhotite replacement. Thin layer of carbonaceous meta-pelite (50.7-51.85m). Banded chert from 51.85-60.26m
60.26-80.66	Interbedded chlorite schist/cherty BIF.
80.66-87.36	Thin layer of carbonaceous meta-pelites. Pyrite laminations in foliation plane. Also pyrite veins cutting at high angles to core.
87.36-89.66	Banded chert interlayered with thin beds of carbonaceous meta-pelites. quartz stringers abundant throughout. Commonly replacement of magnetite by pyrite-pyrrhotite-carbonate.
93.9 to end of hole	Footwall mafic schist.

APPENDIX II

Appendix IIA: X-RAY Flourescence (XRF)

Major elements and volatiles as loss on ignition (LOI) were determined for all lithologies while trace elements were determined for selected samples using the XRF technique of Norrish and Hutton (1969). All analyses were performed at the Department of Geology, Rhodes University using a Phillips PW 1410 XRF spectrometer operated at 55kV and 40mA using $K\alpha$-emission lines for all major and trace elements except Ba where an L spectral line was used. All counting on spectral line peaks for trace elements was fixed at 200 seconds and 100 seconds for backgrounds.

Selected homogenous samples from drill cores were washed and air-dried. Portions of these samples were jaw-crushed into smaller fragments. These were then crushed in swing mill into fine powder.

Combined volatiles (H_2O+, CO_2 and S) were determined by loss on ignition (LOI). About 2 gm of sample was weighed into platinum crucibles. This was placed in an oven maintained at 100°C overnight. The weight loss is calculated as loss on ignition of H_2O-. The crucibles with the samples were again ignited at 1000°C for about 6hrs. Further weight loss corresponds to other volatiles including CO_2, SO_2, SO_3 and H_2O+.

Major oxides except Na were analysed in duplicates on glass disks prepared from the fusion of ashed powder samples, lithium tetraborate, lithium carbonate and lanthanum oxide flux. Trace elements consisting of V, Sc, Ba, Nb, Y, Zr, Rb, Zn, Cu, Ni, Co, Cr and the major oxide Na were analysed on 5g pressed powder pellets using boric acid as backing agent. Corrections were made for spectral and tube-peak interferences, instrumentation drift, background intensities and matrix effects. A number of international locally prepared standards were used for calibration for analysed elements. These include NIM-N, BCR, GSP, AVG, G-2, DTS, PCC, NIM-G, BHVO, SCO, SDC, S-15 and S-12. The lower limits of detection (lld) for the trace elements were determined from the computer program of Marsh (1979) and presented below.

Element	lld/ppm	Element	lld/ppm
Zr	1.73	Ni	2.85
Y	1.77	Co	2.77
Sr	1.75	Cr	1.77
Rb	1.82	V	2.59
Ba	1.7	Nb	1.88
Zn	2.58	Ce	5.57
Cu	2.92	Nd	2.97
		La	2.59

Appendix IIB: ICP-MS Analysis

50 mg of sample powder are digested in closed teflon beakers using ultra-clean HF and HNO3. The digested samples are re-dissolved in 5% HNO3 for analysis. Calibration is by external standardisation using a range of standards made from commercial multi-element solutions. All analyses are done on a Perkin Elmer/ Sciex Elan 6000 ICP-MS at the University of Cape Town using a standard cross-flow nebuliser and a Scott-type spray-chamber. Typical instrument operating conditions are as follows: nebuliser gas flow: ~0.8 L/min, main gas flow: ~ 15 L/min, auxillary gas flow: ~0.75 L/min, ICP RF power: 1100 W. Typical instrument sensitivity (for Rh103): ~20 000 cps/ppb. Internal standards used: Rh103, In115, Re187, Bi209. The lower limits of detection (lld) for the trace elements are given in the table below.

Element	lld/ppm	Element	lld/ppm
Zn	0.0511	La	0.0033
Cu	0.0313	Nb	0.0086
Ni	0.0435	Zr	0.0512
Co	0.0143	Y	0.0056
Cr	0.3267	Ag	0.0008
V	0.0657	Sb	0.0094
Sc	0.1551	As	0.0037
Ba	0.028	W	0.0998
Sr	0.0863	Bi	0.0015
Rb	0.0017	Te	0.0037
Ce	0.0074	Au	0.0014
Nd	0.0058		

Appendix IIC: Microprobe Analysis

All analytical data of mineral compositions were acquired by wavelength dispersive (WDS) and energy dispersive (EDS) spectrometers using a Jeol CXA-733 Superprobe at the Department of Geology, Rhodes University. Analyses were performed on carbon-coated polished thin sections and briquettes. The carbonate analysis was performed using EDS at 15kV operating voltage and 20nA beam current at 100secs counting time. The silicates, electrum and ore minerals were obtained by WDS at 15kV operating voltage and 20nA beam current for silicates, and 20kV and 30nA for electrum and ore minerals. Counting time was maintained at 20 seconds for all elements. Calibrations were done using international standards and data corrected using ZAF corrections. Data reduction was done using the software package Probe for Windows.

Appendix IID: X-ray diffraction (XRD)

XRD data were obtained from bulk-rock powder samples using a Phillips PW1390 automated diffractometer with graphite monochromator and CuKα-radiation to define principal minerals. Operating conditions were maintained at 40kV operating voltage and 30nA current. Scan range were set from 0 to 60° (2θ) at a speed of 15sec/degree at intervals of 0.05°. The phase identification was done semi-automatically using Phillips X-Pert analytical package.

Appendix III

(i) Debye-Hückle equation (Helgeson et al., 1981)

$$\mathrm{Log}\ \gamma_i\,(T,\bar{I}) = \frac{-A_{(T)}\cdot Z_i^2\cdot\sqrt{\bar{I}}}{1 + \mathring{a}_{i(T)}\cdot B_{(T)}\cdot\sqrt{\bar{I}}} + B'_{(T)}\cdot\bar{I}$$

where,

γ_i = the activity coefficient of the ith ion present in small concentrations in the solution.

A, B and $\bar{I}$ are molal Debye-Hückle parameters defined at a particular temperature.

$\bar{I}$ = true ionic strength of the solution.

$\mathring{a}_i$ = coefficient representing the distance of closest ions in the electrolyte solution is taken from Truesdell (1984)

Z_i = charge on the ith species.

B′ = deviation function from the mean activity coefficient at 25°C.

The mean activity coefficient $\gamma_\pm = [(\gamma_+)^{v+}\cdot(\gamma_-)^{v-}]^{1/v}$

where

v_+ = number of moles of cations in 1 mole of a given salt,

v_- = number of moles of anions in one mole of a given salt and v = number of moles of ions in one mole of a given salt.

(ii). CO_2 density calculation (Ely et al., 1989)

The saturated liquid density ρ_{CO2} (g/cm^3) along the liquid-vapour curve between -56° and +31°C is given by:

$\rho_{CO2}(\mathrm{liq}) = \{(b_1\tau^{0.35} + b_2\tau^2 + b_3\tau^3)/(1 + b_4\tau^{0.65}) + 1.0\}\cdot\rho_C$

$\rho_{CO2}(\mathrm{vap}) = MW_{CO2}\cdot P_{CO2}/RTZ$

$P_{CO2} = \exp(a_1\tau^{1.9} + a_2 + a_3/T_R + a_4T_R + a_5T^2_R + a_6T^3_R)$

$Z = 1.0 + P_R/T_R(Z_C - 1.0) \times \{1.0 + \tau^{0.35}(c_1 + T_R(c_2 + T_R(c_3 + c_4T_R)))\}$

Where,

ρ_{CO_2} = density of CO_2 in g/cm^3 of liquid or vapour CO_2

T_C = CO_2 critical temperature (304.127°K); P_C = CO_2 critical pressure (73.7479bars);

ρ_C = 0.466504 g/cm^3; R = 83.145cm3kJ/moleK; $Z_C = P_C MWCO_2/(R\rho_C T_C)$;

$P_R = P/P_C$; P_{CO2} = vapour pressure along the liquid-vapour curve in bars; $T_R = T/T_C$, T in Kelvin; and $\tau = 1.0-T_R$. The coefficients a_i, b_i and c_i are given in the table below.

I	equation 1 ai	equation 2 bi	equation 3 ci
1	22.1121612	2.0012154	20.73159133
2	20.7511138	-1.648614	-68.35708515
3	-13.591939	2.2667362	76.95423388
4	-13.164693	-0.46534	-30.13409019
5	24.3661239		
6	-14.059953		

(iii). Density calculation of aqueous chloride solution

The density of aqueous chloride solution (ρ_{aq}) is calculated by the regression equation of Potter and Brown (1977):

$\rho_{aq} = (1000\rho_o + M_{NaCl} m\rho_o)/(1000 + A_o m\rho_o + B_o m^{3/2}\rho_o + C_o m^2\rho_o)$

where ρ_o = the density of water at 40°C in g/cm^3 = 0.99164,

M_{NaCl} = molecular weight of NaCl = 58.5,

m = the molal concentration of NaCl in solution

A_o = 17.45, B_o = 1.71 and C_o = 0.040.

(iv). Salinity [(Bozzo et al. (1975); Hall et al. (1988)]

(i) Estimate from clathrate melting temperatures:

Salinity from clathrate melting temperatures is estimated based on the data of Bozzo et al. (1975):

Salinity (wt % NaCl) = $15.52022 - 1.02342t - 0.05286t^2$

Where t = clathrate melting temperature in °C.

(ii) Estimate from ice melting temperatures:

Salinity estimate from the ice melting in H_2O–NaCl inclusions is based on the data of Hall et al. (1988):

Salinity (wt % NaCl) = $0.00 + 1.78\,\theta - 0.0442\,\theta^2 + 0.000557\,\theta^3$

Where θ = depression of freezing point in degree Celsius.

(v). <u>Equation of state of Zhang and Frantz (1987)</u>

$P = A_1 + A_2 T$

with

$A_1 = 6.100\text{x}10^{-3} + (2.385\text{x}10^{-1} - a_1)Th - (2.855\text{x}10^{-3} + a_2)Th^2 - (a_3 Th + a_4 Th^2)m$

$A_2 = a_1 + a_2 Th + 9.88\text{x}10^{-6} Th^2 + (a_3 + a_4 Th)m$

Where m = molality; Th = homogenization temperature; a_1, a_2, a_3 and a_4 are constant fit to the data set provided in the table below for NaCl–H_2O system

	a_1	a_2	a_3	a_4
NaCl–H_2O	28.7300	−0.06477	−0.2009	0.00319

(vi). <u>Activity Models [Miyano and Klein (1989); Walshe, (1986)]</u>

Stilpnomelane: = $23.1(X_{Fe}.\text{oct})^6(X_{Al}.\text{tet})(X\text{si}.\text{tet})^8$; Miyano and Klein (1989)

Minnesotaite: = $(X_{Fe}.\text{oct})^3(X_{Si}.\text{tet})^4$; Miyano and Klein (1989)

Chlorite (Clinochlore, daphnite, and Al-free chlorite; Walshe, 1986)

Clinochlore (chl-1) = $59.72(X_{Mg}.oct)^5(X_{Al}.oct)^6)(X_{Si}.tet)(X_{Al}.tet)$

Daphnite (chl-2) = $59.72(X_{Fe}.oct)^5(X_{Al}.oct)^6)(X_{Si}.tet)(X_{Al}.tet)$

Al-free chlorite (chl-3) = $(X_{Mg}.oct)^6(X_{Si}.tet)^2$

(vii). Equilibrium Isotopic Fractionation Equations

Quartz (Qtz)-Water (H_2O): $1000\ln\alpha_{Qtz-H2O} = 3.34[10^6/T^2 - 3.31]$ (t = 250-500°C) Matsuhisa et al (1979).

Siderite (Sid)-Water (H_2O): $1000\ln\alpha_{Sid-H_2O} = [2.89(10^6/T^2) - 2.81]$ Becker and Clayton (1976),

Dolomite (dol) = Ankerite(ank) - CO_2:
$1000\ln\alpha_{dol-CO2} = [-8.914/T^3*10^8 + 8.737/T^2*10^6 - 18.11/T*10^3 + 8.44]$ (Ohmoto and Rye, (1979), $t \leq 600°C$).

Pyrite (py)-H_2S: $1000\ln\alpha_{py-H_2S} = [0.40/T^2*10^6]$ (Ohmoto and Rye, (1979), t = 200°-700°C)

Pyrrhotite (po)-H_2S: $1000\ln\alpha_{po-H2S} = [0.10/T^2*10^6]$ Ohmoto and Rye, (1979), t = 200° -600°C

CO_2-CH_4: $1000\ln\alpha_{CO_2-CH4} = [22166/T - 13.86]$ Bottinga, (1969), t = 200° -800°C.

Appendix IV: Structural data on Kalahari Goldridge deposit.

Foliation (S1)	
Strike	Dip
358	72
337	62
336	71
349	70
346	67
359	65
349	70
349	76
341	80
331	65
331	85
335	65
360	75
356	75
008	70
356	71
341	81
358	69
354	72
339	75
14	80
339	75
315	70
346	69
353	70
322	76
321	62
330	66
296	82
336	54
4	71
316	59
352	61
316	56
341	60
345	64
330	68
345	74
344	62
346	67
340	69
327	66
319	67
342	70
329	71
350	63
329	61
339	56
349	54
011	60
001	62
25	62
340	68
360	64
334	64
341	70
332	64
356	66
356	66
324	74
334	67
009	66
357	53
020	65
010	68
015	65
010	68
005	60
010	68
339	65
006	62
000	68
342	64
334	77
348	22
340	76
337	67
330	66
335	67
335	73
324	72
328	65
335	65
337	60
334	66
343	62
346	62
346	65
009	63

Bedding plane (So)	
Strike	Dip
336	74
344	75
342	66
356	67
330	69
371	60
335	63
338	68
342	60
331	61
329	78
325	66
340	70
329	78
325	66
340	70
339	59
341	59
349	61
344	64
348	58
347	67
320	72
350	60
005	61
348	65
305	65
335	80
352	65
014	66
344	64

Axial plane (isoclinal fold)	
Strike	Dip
335	55
345	54
340	47
319	57
314	58
344	78
340	76

Shear plane	
Strike	Dip
345	68
333	64
334	72
335	79
350	80
337	79
342	69
333	75

Joints	
Strike	Dip
032	25
081	88
171	10
106	20
156	10
150	19
191	35
236	11
236	20
102	18
165	8
155	30
125	21
142	20
139	19
033	23
276	66
165	15
275	8
205	35
207	59
186	45
065	87

Mineral elongation lineation	
Trend	Plunge
080	62
085	60
050	69
078	73
087	64
067	79
069	82
078	75
108	61
075	67
079	66
082	68
079	65
049	65
068	65
043	70
082	70
070	68
080	45
073	65
049	50
092	70
098	71
043	75
057	70
081	70
065	75
017	70
051	75
063	45
048	65
065	72
072	72
069	59
070	79
067	76
015	72
045	60
050	61
045	64
090	59
090	62
100	68
115	58
011	50
065	75

Steep veins (Group I)	
Strike	Dip
088	75
020	71
086	80
099	86
098	83
101	56
066	68
092	67
030	53
036	78
065	55
084	70
060	72
069	88
069	85
113	85
035	65

Steep veins (Group III)	
Strike	Dip
280	82
275	72
292	68
275	74
292	68
275	74
310	88
269	52
255	76
295	72
254	85
261	82
253	60
252	82
250	73
265	76
260	65
275	75
238	86
248	85

Shallow veins (Group II)	
Strike	Dip
178	52
144	12
201	45
177	44
246	20
190	18
125	14
165	22
220	23
235	14
200	27
238	21
180	26
155	17
210	8
180	16
220	19
200	25
190	20
165	15
195	23
165	35
207	37
151	25
211	33
240	36
150	20
149	19
123	31
109	16
191	10
184	10
126	15
244	31
169	10
155	21
144	40
171	28
180	10
161	8
154	30
168	22
155	16
162	14
161	21
121	10

Appendix V: X-ray data of Fe-silicates at the Kalahari Goldridge Mine

Chlorite

Sample No.	Lithology					
588/5	Interbedded schist	d-spacing	14.04	7.00	4.70	3.53
		Intensity (I/Io)	14	100	16.85	56.17
588/20A	Interbedded schist	d-spacing	14.10	7.05	4.70	3.52
		Intensity (I/Io)	10	100	17.1	94.9
527/9B	altered BIF	d-spacing	14.08	7.09	4.71	3.53
		Intensity (I/Io)	13.33	100	20	56.66
527/11	Interbedded schist	d-spacing	14.09	7.05	4.68	3.52
		Intensity (I/Io)	14.04	100	17.13	91.19
452/10A	altered BIF	d-spacing	14.24	7.07	4.72	3.53
		Intensity (I/Io)	15	100	32	60
452/20D	Interbedded schist	d-spacing	14.29	7.20	4.72	3.54
		Intensity (I/Io)	13.33	100	13.35	50

Minnesotaite

Sample No	Host lithology		
527/3A	less altered BIF	d-spacing	9.17
		Intensity (I/Io)	100
527/3B	less altered BIF	d-spacing	9.55
		Intensity (I/Io)	100
527/4	less altered BIF	d-spacing	9.45
		Intensity (I/Io)	100

Stilpnomelane

Sample No	Host lithology		
527/3B	less alteredBIF	d-spacing	12.18
		Intensity (I/Io)	100
527/6D	altered BIF	d-spacing	12.00
		Intensity (I/Io)	100
527/8A	altered BIF	d-spacing	12.12
		Intensity (I/Io)	100
527/9B	Interbedded schist	d-spacing	12.14
		Intensity (I/Io)	100
452/10A	altered BIF	d-spacing	12.18
		Intensity (I/Io)	100
452/20D	Interbedded schist	d-spacing	12.18
		Intensity (I/Io)	100
588/6	Interbedded schist	d-spacing	12.12
		Intensity (I/Io)	100
588/9A	altered BIF	d-spacing	12.10
		Intensity (I/Io)	100
588/20A	Interbedded schist	d-spacing	12.11
		Intensity (I/Io)	100
13175/2B	altered BIF	d-spacing	12.10
		Intensity (I/Io)	100

Appendix VI: Microthermometric data of individual inclusions in Group 1 quartz veins at the Kalahari goldridge deposit.

Sample no.	Type of inclusion	No. of phases Room temp (21–22°C)	Tm_{CO2} °C	Tm_{ice} °C	$Th_{clathrate}$ °C	Th_{CO2} °C	Th_{total} °C	ρ_{CO2} g/cm^3	$\rho_{aqueous}$ g/cm^3	Salinity (wt% NaCl)	Salinity (molal)	X_{CO2}	X_{CO2}	X_{H2O}	X_{NaCl}
NQH-013	Type I	1	nd			9.7L		0.819							
NQH-013	"	1	nd			11.5L		0.809							
NQH-013	"	1	nd			13.5L		0.796							
NQH-013	"	1	nd			13.5L		0.796							
NQH-013	"	1	nd			14.5L		0.789							
NQH-013	"	1	-60.3			12.9L		0.8							
NQH-013	Type II	2	-60.0		9.0	12.2L	263D	0.804	1.005	2.03	0.35				
NQH-013	"	2	-59.5		9.0	12.9L	249D	0.8	1.005	2.03	0.35				
NQH-013	"	2	-61.1		13.5	9.4L	247D	0.821							
NQH-013	"	2	-61.9		15.0	13.5L	280V	0.796							
NQH-013	"	2	-61.0		15.5	14.0L	290V	0.793							
NQH-013	"	2	-62.0		16.0	14.2L	290V	0.791							

V = Homogenization to the vapour phase; L = Homogenization to the liquid phase; D = Decrepitation

Appendix VIII: Microthermometric results of individual inclusions in Group IIB quartz veins at the Kalahari Goldridge deposit.

Sample number	Inclusion type	No. of phases Room temp (21-22°C)	Tm_{CO2} °C	Tm_{ice} °C	$Th_{clathrate}$ °C	Th_{CO2} °C	Th_{CH4} °C	Th_{total} °C	ρ_{CO2} g/cm^3	$\rho_{aqueous}$ g/cm^3	Salinity (wt% NaCl)	Salinity (molal)	V_{CO2}(40°C)	X_{CO2} graphic estimate	X_{CO2} calculated	X_{H2O}	X_{NaCl}	ρ_{bulk} g/cm^3
525/21	Type II	2	-57.6		8.5	20.4L		266D	0.74	1.012	3.00	0.53						
525/21	"	2	-57.1		8.5	20.8L		285V	0.74	1.012	3.00	0.53	0.75	0.51	0.48	0.52	0.005	0.81
525/21	"	2	-57.6		8.1	20.9L		263D	0.74	1.018	3.76	0.67						
525/21	"	2	-57.5		8.0	17.8L		303V	0.77	1.019	3.95	0.70	0.78	0.56	0.53	0.47	0.006	0.82
525/21	"	2	-57.6		8.8	19.1L		236D	0.75	1.008	2.42	0.42						
525/21	"	2	-60.5		8.0	13.7L		285V	0.79	1.019	3.95	0.70	0.8	0.59	0.57	0.43	0.005	0.84
525/21	"	2	-61.0		11.2	16.5L		308V	0.78									
525/21	"	2	-58.5		9.0	21.3L		248D	0.73	1.006	2.03	0.35						
525/21	Type I	1					-96.5											
525/21	"	1					-96.4											
525/21	"	1					-96.0											
525/21	"	1	-64.3			8.4L			0.83									
589/3	Type II	2	-57.6		8.1	16.1L		282V	0.78	1.018	3.76	0.67	0.8	0.59	0.56	0.43	0.005	0.83
589/3	"	2	-60.0		8.0	10.3L		284V	0.82	1.019	3.95	0.70	0.8	0.6	0.57	0.42	0.005	0.86
589/3	"	2			9.0	20.6L		250D	0.74	1.006	2.03	0.35						
589/3	"	2			8.3	20.8L		248V	0.74	1.015	3.38	0.60						
589/3	"	2			7.5	18.9L		195D	0.76	1.025	4.87	0.88						
589/3	"	3			9.0	24.2L		233D	0.70	1.006	2.03	0.35						
589/3	"	2	-57.2		7.0	16.8L		310V	0.77	1.032	5.77	1.05	0.93	0.8	0.81	0.19	0.004	0.79
589/3	"	2			8.0	22.3L		264V	0.72	1.019	3.95	0.70	0.9	0.77	0.73	0.27	0.003	0.75
589/3	"	3			7.6	19.2L		244D	0.75	1.024	4.69	0.84						
589/3	"	3			9.2	19.5L		208D	0.75	1.003	1.63	0.28						
589/3	"	2			9.4	10.9L		230D	0.81	1.000	1.23	0.21						
589/3	"	2			7.8	9.3L		250D	0.82	1.022	4.32	0.77						
589/3	"	2			9.6	10.0L		274V	0.82	0.997	0.82	0.14	0.74	0.52	0.49	0.51	0.001	0.86
589/3	"	2			9.0	12.1L		282V	0.80	1.006	2.03	0.35	0.7	0.44	0.44	0.56	0.004	0.87
589/3	"	2			9.0	9.3L		287V	0.82	1.006	2.03	0.35	0.69	0.42	0.43	0.57	0.004	0.88
589/3	Type III	2		-1.9				255D		1.014	3.23	0.57						
532/11A	Type II	2	-57.9		9.5	20.1L		270V	0.75	0.999	1.03	0.18	0.8	0.56	0.55	0.45	0.001	0.80
532/11A	"	3	-57.1		9.2	21.9L		290V	0.73	1.003	1.63	0.28	0.67	0.37	0.38	0.62	0.003	0.82
532/11A	"	2	-57.9		9.5	13.7L		255V	0.79	0.999	1.03	0.18	0.88	0.67	0.71	0.29	0.001	
532/11A	"	2	-57.4		8.2	20.3L		300V	0.74	1.016	3.57	0.63	0.78	0.53	0.52	0.47	0.005	0.80
532/11A	"	2	-59.6		8.4	13.9L		251D	0.79	1.014	3.19	0.56						
532/11A	"	2	-58.4		8.5	16.1L		248D	0.78	1.012	3.00	0.53						
532/11A	"	3			9.2	23.8L		305V	0.71	1.003	1.63	0.28	0.68	0.38	0.38	0.61	0.003	0.80
532/11A	Type III	3		-2.4				306V		1.020	4.03	0.72						
532/11A	"	2		-2.7				290L		1.023	4.49	0.80						
532/11A	"	2		-2.8				295L		1.024	4.65	0.83						
532/11A	"	2		-3				305L		1.026	4.96	0.89						
525/16B	Type II	3	-56.8		8.7	23.4L		277V	0.71	1.010	2.62	0.46	0.76	0.49	0.48	0.51	0.004	0.78
525/16B	"	2	-59.1		8.0	9.1L		280V	0.82	1.019	3.95	0.70	0.8	0.6	0.58	0.42	0.005	0.86
525/16B	"	2	-59.0		7.9	14.7L		300V	0.79	1.020	4.14	0.74	0.79	0.57	0.55	0.44	0.006	0.84
525/16B	"	2			8.5	20.5L		214D	0.74	1.012	3.00	0.53						
525/16B	"	3			8.1	21.4L		268D	0.73	1.018	3.76	0.67						
525/16B	"	2	-57.8		8.5	16.0L		250D	0.78	1.012	3.00	0.53						
525/16B	"	3	-57.0		8.9	21.3L		248D	0.73	1.007	2.22	0.39						
525/16B	"	2	-57.2		9.0	18.8L		256D	0.76	1.006	2.03	0.35						
525/16B	"	2	-58.0		9.8	10.5L		295V	0.81	0.995	0.41	0.07	0.62	0.28	0.35	0.65	0.001	0.88
117/02/3	Type II	2	-58.5		9.0	13.2L		231D	0.80	1.006	2.03	0.35						1.01
117/02/3	"	2	-57.0		8.9	11.1L		290V	0.81	1.007	2.22	0.39	0.6	0.33	0.33	0.66	0.005	0.89
117/02/3	"	2	-57.9		10.0	15.3L		303V	0.78	0.992	0.00	0.00	0.5	0.25	0.24	0.76	0.000	0.89
117/02/3	"	2	-58.1		9.0	11.9L		242D	0.81	1.006	2.03	0.35						
117/02/3	Type III	2		-3.1				271L		1.027	5.11	0.92						

V = Homogenization to the vapour phase; L = Homogenization to the liquid phase; D = Decrepitation; nd = not determined

Appendix VIII continued.

Sample number	Inclusion type	No. of phases Room temp (21-22°C)	Tm_{CO2} °C	Tm_{ice} °C	$Th_{clathrate}$ °C	Th_{CO2} °C	Th_{CH4} °C	Th_{total} °C	ρ_{CO2} g/cm^3	$\rho_{aqueous}$ g/cm^3	Salinity (wt% NaCl)	Salinity (molal)	V_{CO2}(40°C)	X_{CO2} graphic estimate	X_{CO2} calculated	X_{H2O}	X_{NaCl}	ρ_{bulk} g/cm
MSH/W-1	Type II	2	-57.6		9.5	16.1L		260D	0.78	0.999	1.03	0.18						
MSH/W-1	"	2	-58.5		9.4	15.8L		256D	0.78	1.000	1.23	0.21						
MSH/W-1	"	2	-60.5		8.9	13.0L		256D	0.80	1.007	2.22	0.39						
MSH/W-1	"	2	-58.9		9.0	11.2L		305V	0.81	1.006	2.03	0.35	0.69	0.41	0.43	0.57	0.004	0.87
525/16B	Type II	2	-60.0		9.9	10.8L		239D	0.81	0.993	0.21	0.04						
525/16B	Type III	2		-2.1				250D		1.016	3.55	0.63						
525/16B	"	2		-2.7				235D		1.023	4.49	0.80						
525-16B	"	2		-2.4				280L		1.020	4.03	0.72						
587/8D	Type II	2	-57.1		9.6	20.1L		290V	0.75	0.997	0.82	0.14	0.6	0.32	0.32	0.68	0.002	0.85
587/8D	"	2			10.0	19.6L		301V	0.75	0.992	0.00	0.00	0.6	0.25	0.32	0.68	0.000	0.85
588/18C	Type II	2	-57.3		7.8	21.5L		295V	0.73	1.022	4.32	0.77	0.8	0.6	0.55	0.45	0.006	0.79
588/18C	"	2			7.7	19.3L		288V	0.75	1.023	4.51	0.81	0.82	0.62	0.59	0.41	0.006	0.80
588/18C	"	2	-57.3		8.0	16.8L		245D	0.77	1.019	3.95	0.70						
588/18C	"	2	-57.1		7.9	15.2L		308V	0.78	1.020	4.14	0.74	0.78	0.56	0.53	0.46	0.006	0.84
588/18C	"	2	-58.4		8.0	13.7L		291V	0.79	1.019	3.95	0.70	0.79	0.58	0.55	0.44	0.006	0.84
588/18C	"	2	-58.3		8.3	16.1L		221D	0.78	1.015	3.38	0.60						
588/18C	"	3			7.6	23.8L		305V	0.71	1.024	4.69	0.84	0.81	0.6	0.55	0.44	0.007	0.77
588/18C	"	2	-57.2		7.5	16.6L		290V	0.77	1.025	4.87	0.88	0.84	0.64	0.63	0.37	0.006	0.81
588/18C	"	2			7.6	15.0L		230D	0.79	1.024	4.69	0.84						
588/18C	"	2			8.0	17.5L		291V	0.77	1.019	3.95	0.70	0.8	0.58	0.56	0.44	0.006	0.82
588/18C	"	2			8.3	20.5L		278V	0.74	1.015	3.38	0.60	0.77	0.55	0.51	0.49	0.005	0.81
117/02/6	Type II	2	-60.1		13.3	9.9L		293V	0.82									
117/02/6	"	2	-59.0		13.0	10.6L		288V	0.81									
117/02/6	"	2	-56.9		9.5	14.4L		303V	0.79	0.999	1.03	0.18	0.6	0.33	0.33	0.67	0.002	0.87
117/02/6	"	2	-57.3		9.5	11.5L		299V	0.81	0.999	1.03	0.18	0.6	0.33	0.33	0.66	0.002	0.88
117/02/6	"	2	-57.6		9.5	16.8L		268D	0.77	0.999	1.03	0.18						
117/02/6	"	2	-58.3		8.1	14.5L		295V	0.79	1.018	3.76	0.67	0.77	0.55	0.52	0.47	0.006	0.84
531/16B	Type II	1	-61.5			14.8L			0.79									
531/16B	"	1	-59.5			13.3L			0.80									
531/16B	"	1	-59.7			11.0L			0.81									
531/16B	"	1	-59.5			10.9L			0.81									
531/16B	"	1	-59.9		7.9	17.1L		240D	0.77	1.020	4.14	0.74						
531/9B	"	2			8.6	17.0L		273V	0.77	1.011	2.81	0.49	0.87	0.63	0.68	0.32	0.003	
531/9B	"	2	-57.3		8.5	18.2L		226D	0.76	1.012	3.00	0.53						
531/9B	"	2			8.4	17.0L		246D	0.77	1.014	3.19	0.56						
531/9B	"	2			9.0	19.6L		225D	0.75	1.006	2.03	0.35						
531/9B	"	3	-57.2		9.2	21.5L		254V	0.73	1.003	1.63	0.28	0.89	0.7	0.71	0.29	0.001	0.76
531/9B	"	3	-57.1		8.9	22.6L		221D	0.72	1.007	2.22	0.39						
531/9B	"	2	-59.9		7.5	11.4L		252D	0.81	1.025	4.87	0.88						
531/9B	"	2	-60.0		7.9	11.9L		200D	0.81	1.020	4.14	0.74						
531/9B	"	2	-60.2		7.8	13.8L		238D	0.79	1.022	4.32	0.77						
531/9B	"	2	-58.0		9.4	18.3L		275V	0.76	1.000	1.23	0.21						
531/9B	"	2	-58.8		9.2	14.5L		263D	0.79	1.003	1.63	0.28						
531/9B	"	1	-58.5			12.5L			0.80									

V = Homogenization to the vapour phase; L = Homogenization to the liquid phase; D = Decrepitation; nd = not determined

Appendix IX: Microthermometric data of individual inclusions in Group III quartz veins at the Kalahari Goldridge deposit.

Sample no.	Type of inclusion	No. of phases Room temp (21-22°C)	Tm_{CO_2} °C	Tm_{ice} °C	$Th_{clathrate}$ °C	Th_{CO2} °C	Th_{total} °C	ρ_{CO2} g/cm^3	$\rho_{aqueous}$ g/cm^3	Salinity (wt% NaCl)	Salinity (molal)
NQH-005	Type I	1	-70			0.7		0.88			
NQH-005	Type II	2	-60.1		11.5	9.9L	249D	0.83			
NQH-005	"	2	-65		13	1.6V	220V				
NQH-005	Type III	2		-2.6			283L		1.022	4.34	0.78
NQH-005	"	2		-0.6			249L		0.999	1.05	0.18
NQH-005	"	2		0.5			355L		0.998	0.88	0.15
NQH-005	"	2		-3.5			362L		1.031	5.71	1.04
NQH-005	"	2		-3.4			300L		1.030	5.56	1.01
NQH-005	"	2		-1.8			260V		1.013	3.06	0.54
NQH-005	"	2		-0.8			300V		1.001	1.4	0.24
NQH-005	"	2		-1			350L		1.004	1.74	0.30
NQH-005	"	2		-2.4			217V		1.020	4.03	0.72

V = Homogenization to the vapour phase; L = Homogenization to the liquid phase; D = Decrepitation

Appendix XA: Microprobe analyses of individual chlorite grains in interbedded interbedded schist at the Kalahari Goldridge deposit.

	Interbedded schist						
Sample	452-25B	452-25B	DD17-3B	DD17-3B	DD17-3B	DD17-3B	525-20
No. of analyses	2	2	1	2	2	3	1
SiO_2	25.92	25.65	22.97	23.73	23.41	23.73	23.36
TiO_2	0.07	0.06	0.07	0.09	0.06	0.08	0.06
Al_2O_3	21.15	21.24	20.72	20.59	21.25	21.13	21.15
FeO	33.33	32.73	32.28	33.16	32.68	33.62	34.64
MnO	0.27	0.28	0.12	0.11	0.10	0.14	0.13
MgO	10.05	9.96	7.81	8.51	7.99	8.39	8.69
CaO	0.12	0.05	0.08	0.04	0.11	0.09	0.03
Na_2O	0.15	0.13	0.06	0.02	0.06	0.01	0.00
K_2O	0.10	0.03	0.02	0.02	0.04	0.02	0.03
Total	91.17	90.12	84.12	86.26	85.68	87.20	88.08
Si	2.73	2.73	2.65	2.67	2.64	2.64	2.59
Al (iv)	1.27	1.27	1.35	1.33	1.36	1.36	1.41
Tetrahedral total	4.00	4.00	4.00	4.00	4.00	4.00	4.00
Al (vi)	1.36	1.39	1.46	1.39	1.47	1.41	1.35
Ti	0.01	0.00	0.01	0.01	0.00	0.01	0.00
Fe^{2+}	2.94	2.91	3.11	3.12	3.09	3.13	3.21
Mn	0.02	0.03	0.01	0.01	0.01	0.01	0.01
Mg	1.58	1.58	1.34	1.42	1.34	1.39	1.43
Octahedral total	5.91	5.91	5.92	5.95	5.92	5.95	6.02
Ca	0.01	0.01	0.01	0.00	0.01	0.01	0.00
Na	0.03	0.03	0.01	0.00	0.01	0.00	0.00
K	0.01	0.00	0.00	0.00	0.01	0.00	0.00
Totals	0.06	0.04	0.03	0.01	0.03	0.01	0.01
Temperature (°C)	345.88	347.30	374.11	367.34	374.77	375.55	392.02
Fe/(Fe+Mg)	0.65	0.65	0.70	0.69	0.70	0.69	0.69
$X_{Al.Tet}$	0.32	0.32	0.34	0.33	0.34	0.34	0.35
$X_{Si.Tet}$	0.68	0.68	0.66	0.67	0.66	0.66	0.65
$X_{Al.Oct}$	0.23	0.24	0.25	0.23	0.25	0.24	0.23
$X_{Fe.Oct}$	0.50	0.49	0.52	0.52	0.52	0.53	0.53
$X_{Mg.Oct}$	0.27	0.27	0.23	0.24	0.23	0.23	0.24
Act. of Daphnite	9.05E-02	8.84E-02	1.31E-01	1.22E-01	1.29E-01	1.27E-01	1.33E-01
Act. of Clinochlore	4.06E-03	4.14E-03	1.95E-03	2.44E-03	2.01E-03	2.22E-03	2.37E-03
Act. Al-free Chlorite	1.70E-04	1.69E-04	5.87E-05	8.35E-05	6.00E-05	7.12E-05	7.71E-05

Appendix XA continued.

	Interbedded schist						
Sample	525-20	525-20	525-20	NQH/19B-1	NQH/19B-2	589/19G-1	589/19G-2
No. of analyses	3	1	2	2	2	2	2
SiO_2	23.67	24.20	23.11	23.66	24.13	23.32	23.38
TiO_2	0.06	0.08	0.07	0.08	0.09	0.07	0.05
Al_2O_3	22.02	21.88	19.95	20.00	20.92	21.00	21.48
FeO	36.09	37.13	36.30	35.35	37.24	37.15	36.55
MnO	0.10	0.17	0.06	0.19	0.19	0.12	0.11
MgO	8.37	8.82	8.01	7.47	7.47	6.68	6.49
CaO	0.01	0.02	0.04	0.08	0.03	0.01	0.03
Na_2O	0.03	0.00	0.03	0.07	0.00	0.00	0.10
K_2O	0.01	0.00	0.02	0.02	0.01	0.01	0.08
Total	90.36	92.30	87.60	86.92	90.08	88.35	88.26
Si	2.57	2.58	2.61	2.67	2.64	2.61	2.61
Al (iv)	1.43	1.42	1.39	1.33	1.36	1.39	1.39
Tetrahedral total	4.00	4.00	4.00	4.00	4.00	4.00	4.00
Al (vi)	1.38	1.32	1.26	1.34	1.34	1.38	1.44
Ti	0.01	0.01	0.01	0.01	0.01	0.01	0.00
Fe^{2+}	3.27	3.30	3.43	3.34	3.41	3.48	3.41
Mn	0.01	0.02	0.01	0.02	0.02	0.01	0.01
Mg	1.35	1.40	1.35	1.26	1.22	1.11	1.08
Octahedral total	6.02	6.04	6.05	5.97	6.00	5.99	5.95
Ca	0.00	0.00	0.01	0.01	0.00	0.00	0.00
Na	0.01	0.00	0.01	0.01	0.00	0.00	0.02
K	0.00	0.00	0.00	0.00	0.00	0.00	0.01
Totals	0.01	0.00	0.01	0.03	0.00	0.00	0.04
Temperature (°C)	399.84	396.70	385.97	364.67	375.12	385.11	385.12
Fe/(Fe+Mg)	0.71	0.70	0.72	0.73	0.74	0.76	0.76
$X_{Al.Tet}$	0.36	0.36	0.35	0.33	0.34	0.35	0.35
$X_{Si.Tet}$	0.64	0.64	0.65	0.67	0.66	0.65	0.65
$X_{Al.Oct}$	0.23	0.22	0.21	0.22	0.22	0.23	0.24
$X_{Fe.Oct}$	0.54	0.55	0.57	0.56	0.57	0.58	0.57
$X_{Mg.Oct}$	0.22	0.23	0.22	0.21	0.20	0.19	0.18
Act. of Daphnite	1.50E-01	1.46E-01	1.65E-01	1.63E-01	1.78E-01	2.06E-01	2.04E-01
Act. of Clinochlore	1.81E-03	1.98E-03	1.55E-03	1.24E-03	1.04E-03	6.93E-04	6.46E-04
Act. Al-free Chlorite	5.31E-05	6.36E-05	5.21E-05	3.93E-05	3.08E-05	1.76E-05	1.52E-05

Appendix XB: Microprobe analyses of individual chlorite grains in mineralized BIF at the Kalahari goldridge deposit.

	Mineralized BIF												
Sample	NQH/10A	525/12A-1	525/12A-2	525/12A-3	589/4-1	589/4-2	524/8-1	524/8-2	524/8-3	524/8-4	13175 /2C	532/9-1	532/9-2
No. of analyses	7	2	3	3	1	1	2	3	1	2	1	2	2
SiO_2	23.48	22.71	23.33	22.55	23.60	22.38	23.08	22.25	22.80	23.36	22.13	22.45	21.76
TiO_2	0.05	0.07	0.06	0.05	0.05	0.03	0.05	0.06	0.04	0.04	0.05	0.09	0.08
Al_2O_3	19.23	20.66	20.87	19.79	19.67	19.60	19.52	20.32	19.74	20.67	19.61	20.54	20.00
FeO	39.74	39.17	38.28	37.46	35.32	40.56	41.76	41.84	41.17	42.05	36.62	40.11	40.76
MnO	0.07	0.06	0.09	0.04	0.11	0.11	0.08	0.09	0.10	0.07	0.16	0.08	0.07
MgO	4.84	4.81	6.34	6.24	8.49	4.75	4.42	3.67	4.54	4.35	5.37	4.69	3.62
CaO	0.03	0.07	0.04	0.11	0.08	0.02	0.04	0.07	0.03	0.01	0.10	0.04	0.13
Na_2O	0.05	0.14	0.01	0.02	0.04	0.02	0.03	0.07	0.04	0.01	0.24	0.12	0.01
K_2O	0.03	0.09	0.00	0.03	0.08	0.00	0.01	0.01	0.00	0.00	0.09	0.09	0.00
Total	87.52	87.79	89.01	86.30	87.45	87.47	88.98	88.39	88.45	90.56	84.37	88.20	86.43
Si	2.70	2.60	2.61	2.61	2.65	2.60	2.64	2.57	2.62	2.62	2.62	2.57	2.57
Al (iv)	1.30	1.40	1.39	1.39	1.35	1.40	1.36	1.43	1.38	1.38	1.38	1.43	1.43
Tetrahedral total	4.00	4.00	4.00	4.00	4.00	4.00	4.00	4.00	4.00	4.00	4.00	4.00	4.00
Al (vi)	1.31	1.39	1.36	1.31	1.26	1.28	1.27	1.34	1.29	1.34	1.36	1.35	1.35
Ti	0.00	0.01	0.01	0.00	0.00	0.00	0.00	0.00	0.00	0.00	0.00	0.01	0.01
Fe^{2+}	3.82	3.75	3.58	3.62	3.32	3.94	3.99	4.04	3.95	3.94	3.63	3.85	4.02
Mn	0.01	0.01	0.01	0.00	0.01	0.01	0.01	0.01	0.01	0.01	0.02	0.01	0.01
Mg	0.83	0.82	1.06	1.08	1.42	0.82	0.75	0.63	0.78	0.73	0.95	0.80	0.64
Octahedral total	5.97	5.98	6.01	6.02	6.02	6.05	6.03	6.02	6.03	6.02	5.96	6.01	6.02
Ca	0.00	0.01	0.00	0.01	0.01	0.00	0.00	0.01	0.00	0.00	0.01	0.00	0.02
Na	0.01	0.03	0.00	0.01	0.01	0.00	0.01	0.02	0.01	0.00	0.06	0.03	0.00
K	0.00	0.01	0.00	0.00	0.01	0.00	0.00	0.00	0.00	0.00	0.01	0.01	0.00
Totals	0.02	0.05	0.01	0.02	0.03	0.01	0.01	0.03	0.01	0.00	0.08	0.04	0.02
Temperature (°C)	355.87	388.77	386.21	386.16	371.68	389.43	375.85	398.37	382.93	383.93	381.88	397.43	399.39
Fe/(Fe+Mg)	0.82	0.82	0.77	0.77	0.70	0.83	0.84	0.86	0.84	0.84	0.79	0.83	0.86
$X_{Al,Tet}$	0.32	0.35	0.35	0.35	0.34	0.35	0.34	0.36	0.35	0.35	0.34	0.36	0.36
$X_{Si,Tet}$	0.68	0.65	0.65	0.65	0.66	0.65	0.66	0.64	0.65	0.65	0.66	0.64	0.64
$X_{Al,Oct}$	0.22	0.23	0.23	0.22	0.21	0.21	0.21	0.22	0.21	0.22	0.23	0.22	0.22
$X_{Fe,Oct}$	0.64	0.63	0.60	0.60	0.55	0.65	0.66	0.67	0.66	0.65	0.61	0.64	0.67
$X_{Mg,Oct}$	0.14	0.14	0.18	0.18	0.24	0.14	0.12	0.10	0.13	0.12	0.16	0.13	0.11
Act. of Daphnite	0.31	0.31	0.23	0.23	0.14	0.34	0.36	0.41	0.35	0.36	0.26	0.33	0.41
Act. of Clinochlore	1.49E-04	1.53E-04	5.14E-04	5.42E-04	2.05E-03	1.32E-04	8.60E-05	3.87E-05	1.02E-04	7.70E-05	3.14E-04	1.30E-04	4.05E-05
Act. Al-free Chlorite	3.29E-06	2.81E-06	1.25E-05	1.40E-05	7.64E-05	2.63E-06	1.66E-06	5.51E-07	1.95E-06	1.31E-06	6.97E-06	2.33E-06	5.73E-07

Appendix XC: Microprobe analyses of individual chlorite grains in mineralized veins at the Kalahari Goldridge deposit.

	Group IIA veins									
Sample	525/12A-1	525/12A-2	525/12A-3	13175 /2C	531/184-1	531/184-2	531/184-3	534/184m	PH/6-1	PH/6-2
No. of analyses	2	2	2	2	4	1	3	4	3	3
SiO_2	23.93	24.74	25.40	23.41	23.58	22.63	24.36	24.72	23.28	24.13
TiO_2	0.04	0.04	0.05	0.05	0.01	0.05	0.03	0.05	0.03	0.06
Al_2O_3	19.35	21.07	20.92	20.28	19.33	19.20	19.74	22.54	19.90	19.27
FeO	34.68	33.07	34.19	34.82	35.95	35.45	36.82	36.08	37.01	35.76
MnO	0.10	0.07	0.07	0.11	0.02	0.03	0.06	0.05	0.17	0.12
MgO	7.90	9.31	8.86	5.72	6.79	6.70	7.76	7.31	6.56	6.76
CaO	0.08	0.02	0.04	0.09	0.00	0.00	0.01	0.03	0.10	0.09
Na_2O	0.03	0.07	0.04	0.43	0.01	0.03	0.01	0.02	0.01	0.01
K_2O	0.15	0.03	0.03	0.15	0.00	0.00	0.00	0.00	0.00	0.00
Total	86.26	88.41	89.58	85.06	85.69	84.08	88.78	90.79	87.06	86.21
Si	2.72	2.70	2.68	2.71	2.72	2.66	2.70	2.65	2.65	2.76
Al (iv)	1.28	1.30	1.32	1.29	1.28	1.34	1.30	1.35	1.35	1.24
Tetrahedral total	4.00	4.00	4.00	4.00	4.00	4.00	4.00	4.00	4.00	4.00
Al (vi)	1.31	1.40	1.43	1.47	1.34	1.33	1.29	1.50	1.33	1.35
Ti	0.00	0.00	0.00	0.00	0.00	0.00	0.00	0.00	0.00	0.01
Fe^{2+}	3.34	3.05	3.12	3.37	3.46	3.49	3.42	3.24	3.53	3.41
Mn	0.01	0.01	0.01	0.01	0.00	0.00	0.01	0.00	0.02	0.01
Mg	1.34	1.51	1.42	0.99	1.17	1.18	1.28	1.17	1.11	1.15
Octahedral total	6.00	5.97	5.99	5.84	5.97	6.00	6.00	5.91	5.99	5.93
Ca	0.01	0.00	0.00	0.00	0.00	0.00	0.00	0.00	0.01	0.01
Na	0.01	0.02	0.01	0.01	0.00	0.01	0.00	0.00	0.00	0.00
K	0.02	0.00	0.00	0.00	0.00	0.00	0.00	0.00	0.00	0.00
Totals	0.04	0.02	0.02	0.01	0.00	0.01	0.00	0.01	0.02	0.01
Temperature (°C)	350.36	358.12	362.35	354.62	351.59	368.58	355.09	372.39	371.19	337.26
Fe/(Fe+Mg)	0.71	0.67	0.69	0.77	0.75	0.75	0.73	0.73	0.76	0.75
$X_{Al.Tet}$	0.32	0.33	0.33	0.32	0.32	0.33	0.32	0.34	0.34	0.31
$X_{Si.Tet}$	0.68	0.67	0.67	0.68	0.68	0.67	0.68	0.66	0.66	0.69
$X_{Al.Oct}$	0.22	0.23	0.24	0.25	0.22	0.22	0.21	0.25	0.22	0.23
$X_{Fe.Oct}$	0.56	0.51	0.52	0.58	0.58	0.58	0.57	0.55	0.59	0.58
$X_{Mg.Oct}$	0.22	0.25	0.24	0.17	0.20	0.20	0.21	0.20	0.19	0.19
Act. of Daphnite	1.51E-01	1.07E-01	1.21E-01	2.10E-01	1.92E-01	1.96E-01	1.69E-01	1.66E-01	2.10E-01	1.83E-01
Act. of Clinochlore	1.57E-03	3.19E-03	2.39E-03	4.51E-04	8.29E-04	8.49E-04	1.26E-03	1.02E-03	6.58E-04	7.98E-04
Act. Al-free Chlorite	5.68E-05	1.19E-04	8.06E-05	1.06E-05	2.55E-05	2.51E-05	4.39E-05	2.62E-05	1.82E-05	2.53E-05

Appendix XC continued.

	Group IIB veins								
Sample	532/11A	532/11A	585/20	585/20	587/2C-1	587/2C-2	587/2C-3	587/2C-4	DD17/183
No. of analyses	3	2	2	2	4	3	3	3	2
SiO_2	23.88	24.86	25.64	24.95	25.58	25.26	23.31	23.52	22.95
TiO_2	0.08	0.05	0.06	0.04	0.06	0.07	0.05	0.05	0.07
Al_2O_3	19.40	19.83	21.05	21.72	17.93	18.40	20.25	20.55	20.17
FeO	34.72	32.37	28.73	29.20	33.97	32.08	31.67	31.76	36.11
MnO	0.12	0.12	0.08	0.09	0.15	0.21	0.18	0.16	0.11
MgO	8.78	10.38	12.73	11.62	9.44	10.13	9.23	9.42	6.27
CaO	0.02	0.05	0.07	0.02	0.04	0.02	0.05	0.00	0.00
Na_2O	0.01	0.02	0.04	0.02	0.02	0.03	0.01	0.02	0.00
K_2O	0.01	0.01	0.01	0.01	0.00	0.00	0.00	0.00	0.00
Total	87.04	87.69	88.40	87.66	87.18	86.19	84.74	85.48	85.69
					2.36	2.42	2.72	2.73	2.74
Si	2.69	2.73	2.73	2.69	2.85	2.82	2.65	2.65	2.65
Al (iv)	1.31	1.27	1.27	1.31	1.15	1.18	1.35	1.35	1.35
Tetrahedral total	4.00	4.00	4.00	4.00	4.00	4.00	4.00	4.00	4.00
Al (vi)	1.28	1.29	1.37	1.44	1.21	1.25	1.37	1.38	1.39
Ti	0.01	0.00	0.01	0.01					
Fe^{2+}	3.27	2.97	2.56	2.63	3.17	3.00	3.02	2.99	3.48
Mn	0.01	0.01	0.00	0.00	0.01	0.02	0.02	0.02	0.01
Mg	1.47	1.70	2.02	1.86	1.57	1.69	1.57	1.58	1.08
Octahedral total	6.03	5.97	5.96	5.94	5.96	5.95	5.97	5.97	5.97
Ca	0.00	0.01	0.00	0.00	0.00	0.00	0.01	0.00	0.00
Na	0.01	0.01	0.02	0.00	0.00	0.01	0.00	0.00	0.00
K	0.00	0.00	0.00	0.00	0.00	0.00	0.00	0.00	0.00
Totals	0.01	0.02	0.02	0.01	0.01	0.01	0.01	0.00	0.00
Temperature (°C)	361.02	346.92	347.08	361.15	308.10	317.07	371.37	372.42	373.09
Fe/(Fe+Mg)	0.69	0.64	0.56	0.59	0.67	0.64	0.66	0.65	0.76
$X_{Al.Tet}$	0.33	0.32	0.32	0.33	0.00	0.00	0.00	0.00	0.00
$X_{Si.Tet}$	0.67	0.68	0.68	0.67	1.00	1.00	1.00	1.00	1.00
$X_{Al.Oct}$	0.21	0.22	0.23	0.24	1.00	1.00	1.00	1.00	1.00
$X_{Fe.Oct}$	0.54	0.50	0.43	0.44	0.00	0.00	0.00	0.00	0.00
$X_{Mg.Oct}$	0.24	0.28	0.34	0.31	1.00	1.00	1.00	1.00	1.00
Act. of Daphnite	1.30E-01	8.52E-02	4.35E-02	5.42E-02	3.01E-01	4.21E-01	2.37E-01	4.71E-01	3.80E-01
Act. of Clinochlore	2.41E-03	5.24E-03	1.34E-02	9.72E-03	1.46E-01	1.98E-01	1.68E-01	1.53E-01	1.07E-01
Act. Al-free Chlorite	9.52E-05	2.48E-04	7.08E-04	4.30E-04	1.24E-02	1.29E-02	1.28E-02	6.60E-03	1.67E-03

Appendix XIA: Microprobe analyses of individual siderite grains in BIF at the Kalahari Goldridge deposit

	Less-Altered BIF							Altered BIF					
Sample number	527/3A-1	527/3A-2	527/3A-3	527/3A-4	13175/2A	13175/2A	13175/2A	13175/2C-3	13175/2C-4	588/10C-2	588/10C-3	532/9-10	532/9-11
Number of analyses	2	2	1	1	1	1	1	3	2	3	1	3	2
FeO	37.09	36.80	36.80	34.20	37.03	39.90	38.53	45.54	50.34	50.70	49.08	45.95	42.95
MnO	5.18	5.18	4.74	11.55	4.32	1.26	0.75	3.37	2.95	1.23	0.88	4.95	1.29
MgO	15.39	14.82	15.30	11.72	10.45	13.46	13.98	7.64	4.65	3.73	4.98	7.35	12.08
CaO	0.66	0.77	0.57	1.04	1.03	0.36	0.45	0.52	0.59	0.28	0.43	0.32	0.78
Total	58.32	57.58	57.41	58.52	52.83	54.98	53.71	57.07	58.51	55.94	55.37	58.56	57.09
Cations on the basis of 2 (Fe+Mg+Mn+Ca)													
Fe	1.05	1.06	1.06	1.00	1.21	1.22	1.19	1.44	1.61	1.72	1.65	1.43	1.29
Mn	0.15	0.15	0.14	0.34	0.14	0.04	0.02	0.11	0.10	0.04	0.03	0.16	0.04
Mg	0.78	0.76	0.78	0.61	0.61	0.73	0.77	0.43	0.27	0.23	0.30	0.41	0.64
Ca	0.02	0.03	0.02	0.04	0.04	0.01	0.02	0.02	0.02	0.01	0.02	0.01	0.03
Fe/(Fe+Mg)	0.58	0.58	0.57	0.62	0.67	0.62	0.61	0.77	0.86	0.88	0.85	0.78	0.67
Molecular proportion of carbonates													
$FeCO_3$	52.54	52.99	52.88	50.20	60.36	60.80	59.48	72.01	80.74	85.99	82.63	71.29	64.32
$MnCO_3$	7.45	7.55	6.90	17.18	7.13	1.94	1.17	5.40	4.78	2.11	1.50	7.78	1.96
$MgCO_3$	38.83	38.04	39.17	30.66	30.35	36.55	38.46	21.54	13.28	11.28	14.94	20.31	32.23
$CaCO_3$	1.18	1.42	1.05	1.96	2.15	0.70	0.89	1.05	1.20	0.62	0.93	0.63	1.50
Activity of $FeCO_3$	0.53	0.53	0.53	0.50	0.60	0.61	0.59	0.72	0.81	0.86	0.83	0.71	0.64

Appendix XIA continued.

	Altered BIF													
Sample number	532/9-12	532/9-13	532/9-14	525/12A-9	524/8-1	524/8-2	524/8-3	532/11A-	532/11A-2	NQH/10A	531/184-1	587/2C-2	587/2C-3	588/10C-1
Number of analysis	1	3	2	1	3	5	2	1	4	7	2	4	3	4
FeO	48.69	43.91	48.68	45.97	47.29	45.10	50.58	47.04	44.13	49.83	43.14	48.22	46.73	48.62
MnO	1.07	1.69	0.30	0.83	0.60	1.51	0.65	1.14	4.52	1.25	0.60	2.37	2.70	1.16
MgO	6.67	11.89	4.79	8.68	6.61	9.68	5.54	9.47	8.46	5.56	11.68	1.91	2.42	8.26
CaO	0.56	0.93	1.16	0.73	0.47	0.81	1.15	0.89	0.19	0.67	0.64	2.09	3.16	0.84
Total	56.99	58.41	54.93	56.21	54.98	57.09	57.91	58.54	57.29	57.31	56.06	54.59	55.01	58.88
Cations on the basis of 2 (Fe+Mg+Mn+Ca)														
Fe	1.56	1.29	1.65	1.45	1.57	1.39	1.62	1.42	1.38	1.61	1.32	1.70	1.62	1.48
Mn	0.03	0.05	0.01	0.03	0.02	0.05	0.02	0.03	0.14	0.04	0.02	0.08	0.09	0.04
Mg	0.38	0.62	0.29	0.49	0.39	0.53	0.32	0.51	0.47	0.32	0.64	0.12	0.15	0.45
Ca	0.02	0.03	0.05	0.03	0.02	0.03	0.05	0.03	0.01	0.03	0.03	0.09	0.14	0.03
Fe/(Fe+Mg)	0.80	0.67	0.85	0.75	0.80	0.72	0.84	0.74	0.75	0.83	0.67	0.93	0.92	0.77
Molecular proportion of carbonates														
$FeCO_3$	78.06	64.57	82.51	72.72	78.45	69.47	80.82	71.04	68.94	80.50	65.98	85.03	80.82	74.12
$MnCO_3$	1.74	2.51	0.51	1.33	1.01	2.35	1.04	1.75	7.14	2.05	0.93	4.23	4.73	1.78
$MgCO_3$	19.05	31.18	14.47	24.47	19.55	26.59	15.78	25.49	23.54	16.00	31.84	6.01	7.45	22.45
$CaCO_3$	1.14	1.74	2.52	1.48	1.00	1.60	2.35	1.72	0.38	1.40	1.25	4.73	7.00	1.65
Activity of $FeCO_3$	0.78	0.65	0.83	0.73	0.78	0.69	0.81	0.71	0.69	0.81	0.66	0.85	0.81	0.74

Appendix XIB: Microprobe analyses of individual ankerite grains in interbedded schist at the Kalahari Goldridge deposit

	Schist					
Sample number	452/25B-1	452/25B-2	525/20	DD17/3B-1	DD17/3B-2	DD17/3B-3
Number of analyses	2	2	1	1	2	2
FeO	19.82	16.50	19.59	10.77	7.70	13.65
MnO	3.07	3.17	2.12	0.67	0.76	0.82
MgO	6.31	9.01	7.37	14.35	16.86	11.71
CaO	28.41	28.38	28.37	32.87	33.86	29.71
Total	57.60	57.05	57.46	58.66	59.18	55.89
Cations on the basis of 2 (Fe+ Mg+ Mn+ Ca)						
Fe	0.56	0.46	0.55	0.27	0.19	0.37
Mn	0.09	0.09	0.06	0.02	0.02	0.02
Mg	0.32	0.45	0.37	0.65	0.73	0.57
Ca	1.03	1.01	1.02	1.06	1.06	1.04
Fe/(Fe+ Mg)	0.64	0.51	0.60	0.30	0.20	0.40
Molecular proportion of carbonates						
$FeCO_3$	28.11	22.88	27.50	13.61	9.40	18.61
$MnCO_3$	4.41	4.45	3.02	0.85	0.94	1.13
$MgCO_3$	15.90	22.26	18.45	32.31	36.69	28.43
$CaCO_3$	51.58	50.40	51.03	53.22	52.97	51.84
Activity of $FeCO_3$	0.28	0.23	0.28	0.14	0.09	0.19

Appendix XIC: Microprobe analyses of individual carbonate grains in Group IIA (ladder) veins at the Kalahari Goldridge deposit

	Ankerite								**Siderite**						
Sample number	525/12A-1	525/12A-2	531/184-2	531/184-3	PH/6	PH/6	PH/6-1	13175/2C-1	525/12A-3	525/12A-4	525/12A-5	525/12A-6	525/12A-8	13175/2C-5	88/10C-1
Number of analyses	2	1	3	3	3	3	3	2	3	3	1	3	1	3	4
FeO	15.42	13.74	13.34	18.19	15.64	16.06	16.63	15.87	37.89	39.91	39.40	38.32	40.89	39.94	48.62
MnO	1.69	1.88	1.29	0.91	3.45	2.39	2.25	3.21	2.06	0.91	0.41	0.96	0.70	4.11	1.16
MgO	10.40	10.63	11.34	8.14	8.68	8.71	8.51	9.99	14.78	14.59	14.27	14.48	10.90	12.85	8.26
CaO	26.81	27.39	26.97	25.84	27.30	25.51	26.22	26.02	1.70	0.80	0.36	0.28	0.68	1.19	0.84
Total	54.32	53.64	52.94	53.08	55.07	52.66	53.60	55.08	56.43	56.22	54.44	54.03	53.17	58.08	58.88
Cations on the basis of 2 (Fe+ Mg+ Mn+ Ca)															
Fe	0.44	0.39	0.38	0.55	0.45	0.48	0.47	0.45	1.11	1.18	1.20	1.17	1.32	1.17	1.48
Mn	0.05	0.05	0.04	0.03	0.10	0.07	0.05	0.09	0.06	0.03	0.01	0.03	0.02	0.12	0.04
Mg	0.53	0.54	0.58	0.43	0.44	0.47	0.49	0.51	0.77	0.77	0.77	0.79	0.63	0.67	0.45
Ca	0.98	1.01	1.00	0.99	1.01	0.98	0.99	0.95	0.06	0.03	0.01	0.01	0.03	0.04	0.03
Fe/(Fe+ Mg)	0.45	0.42	0.40	0.56	0.50	0.51	0.49	0.47	0.59	0.61	0.61	0.60	0.68	0.64	0.77
Molecular proportion of carbonates															
$FeCO_3$	22.03	19.72	19.22	27.26	22.48	24.08	23.47	22.58	55.31	58.80	59.96	58.56	66.06	58.30	74.12
$MnCO_3$	2.44	2.73	1.88	1.38	5.02	3.62	2.43	4.63	3.04	1.36	0.63	1.48	1.15	6.07	1.78
$MgCO_3$	26.47	27.19	29.12	21.74	22.23	23.28	24.73	25.33	38.46	38.32	38.70	39.42	31.38	33.41	22.45
$CaCO_3$	49.06	50.36	49.79	49.62	50.28	49.02	49.38	47.46	3.19	1.52	0.70	0.54	1.41	2.23	1.65
Activity of $FeCO_3$	0.22	0.20	0.19	0.27	0.22	0.24	0.23	0.23	0.55	0.59	0.60	0.59	0.66	0.58	0.74

Appendix XID: Microprobe analyses of individual carbonate grains in Group IIB (large) veins at the Kalahari Goldridge deposit

	Ankerite										Siderite		
Sample number	532/9-1	532/9-2	532/9-4	585/20A-1	585/20A-2	585/20A-3	585/20A-4	585/20A-5	587/2C-1	DD17/183	532/11A-3	532/11A-4	532/9-9
Number of analyses	2	2	3	3	3	3	3	3	4	3	5	1	3
FeO	13.11	14.35	13.27	10.59	12.34	9.62	11.25	11.84	14.73	15.89	39.01	38.41	37.51
MnO	3.98	3.65	3.70	1.89	1.50	0.77	1.63	1.59	2.11	0.97	5.82	4.55	6.36
MgO	10.25	9.47	10.69	13.77	12.41	15.70	12.50	12.64	10.16	9.78	12.52	12.61	12.99
CaO	29.11	29.51	28.00	29.54	29.11	29.10	30.17	28.44	25.44	25.96	0.69	0.35	1.68
Total	56.45	56.99	55.66	55.80	55.35	55.19	55.56	54.51	52.44	52.60	58.04	55.92	58.54
Cations on the basis of 2 (Fe+Mg+Mn+Ca)													
Fe	0.36	0.39	0.37	0.28	0.34	0.25	0.30	0.33	0.44	0.47	1.146	1.17	1.08
Mn	0.11	0.10	0.10	0.05	0.04	0.02	0.04	0.04	0.06	0.03	0.173	0.14	0.19
Mg	0.50	0.46	0.53	0.66	0.60	0.74	0.60	0.62	0.54	0.52	0.655	0.68	0.67
Ca	1.03	1.04	1.00	1.01	1.02	0.99	1.05	1.01	0.96	0.98	0.026	0.01	0.06
Fe/(Fe+Mg)	0.42	0.46	0.41	0.30	0.36	0.26	0.34	0.34	0.45	0.48	0.64	0.63	0.62
Molecular proportion of carbonates													
$FeCO_3$	18.04	19.73	18.45	14.14	16.84	12.72	15.24	16.35	21.80	23.52	57.28	58.25	54.16
$MnCO_3$	5.54	5.08	5.21	2.56	2.07	1.03	2.24	2.22	3.16	1.46	8.65	6.99	9.30
$MgCO_3$	25.12	23.21	26.48	32.76	30.18	36.98	30.17	31.11	26.80	25.79	32.76	34.08	33.43
$CaCO_3$	51.31	51.98	49.86	50.53	50.91	49.27	52.36	50.33	48.24	49.23	1.31	0.68	3.11
Activity of $FeCO_3$	0.18	0.20	0.18	0.14	0.17	0.13	0.15	0.16	0.22	0.24	0.57	0.58	0.54

Appendix XII: List of samples from the Kalahari Goldridge Mine

Drill hole: DD 17: Section: 12950			Drill hole: GDP 529 Section: 13250			Drill hole: GDP 589: Section: 13250		
Sample no.	Depth/m	Location in deposit	Sample no.	Depth/m	Location in deposit	Sample no.	Depth/m	Location in deposit
X-1	115.21	Hanging wall	1	256.65	Hanging wall	1A	434.03	Hanging wall
X-2	139	Hanging wall	2	265.65	Hanging wall	1B	434.11	Hanging wall
X-3	145	Hanging wall	3	274.91	Hanging wall	2	435.35	Orebody
X-4	149.1	Hanging wall	4A	279.90	Hanging wall	3	440.84	Orebody
1A	151.27	Orebody	4B	280.00	Hanging wall	4	442.52	Orebody
1B	151.37	Orebody	5	282.58	Hanging wall	5	445.76	Orebody
1C	151.51	Orebody	6A	283.95	Orebody	6A	454.10	Orebody
2	154.5	Orebody	6B	284.11	Orebody	6B	454.21	Orebody
3A	156.1	Orebody	6C	284.17	Orebody	6C	454.32	Orebody
3B	156.34	Orebody	6D	284.28	Orebody	6D	454.43	Orebody
4A	158.02	Orebody	6E	284.49	Orebody	7A	455.99	Orebody
4B	158.12	Orebody	7A	292.79	Orebody	7B	456.13	Orebody
4C	158.22	Orebody	7B	292.95	Orebody	8A	460.11	Orebody
5	158.54	Orebody	7C	293.16	Orebody	8B	460.20	Orebody
6	163.01	Orebody	7D	293.33	Orebody	8C	460.35	Orebody
7	166.02	Orebody	8	293.64	Orebody	8D	460.45	Orebody
X-5	178	Orebody	9A	296.50	Orebody	8E	460.56	Orebody
X-6	180.92	Orebody	9B	296.70	Orebody	9A	462.00	Orebody
X-7	182.5	Orebody	9C	296.80	Orebody	9B	462.08	Orebody
X-8	183	Orebody	X-1	298.65	Orebody	9C	462.13	Orebody
8	189.84	Footwall	X-2	299.77	Orebody	10	462.42	Orebody
9	190.1	Footwall	10A	301.12	Orebody	11	473.17	Orebody
10	193.48	Footwall	10B	301.20	Orebody	12A	474.41	Orebody
11	195.06	Footwall	10C	301.34	Orebody	12B	474.59	Orebody
12	199.94	Footwall	11A	302.24	Orebody	12C	474.69	Orebody
13	203.14	Footwall	11B	302.40	Orebody	13A	475.86	Orebody
14	204.05	Footwall	11C	302.60	Orebody	13B	475.98	Orebody
15	215.94	Footwall	12A	305.19	Orebody	13C	476.06	Orebody
16	216.93	Footwall	12B	305.39	Orebody	13D	476.18	Orebody
17A	225	Footwall	12C	305.50	Orebody	13E	476.19	Orebody
17B	225.12	Footwall	12D	305.60	Orebody	13F	476.25	Orebody
17C	225.18	Footwall	12E	305.85	Orebody	14A	477.58	Orebody
			13	309.92	Orebody	14B	477.64	Orebody
			14A	320.27	Orebody	15A	477.71	Orebody
			14B	320.43	Orebody	15B	485.61	Orebody
			14C	320.46	Orebody	15C	485.79	Orebody
			15	323.53	Orebody	15D	485.91	Orebody
			16A	336.48	Orebody	16A	486.03	Orebody
			16B	336.84	Orebody	16B	494.34	Orebody
			17	341.18	Orebody	16C	494.58	Orebody
			18	342.48	Orebody	17A	495.55	Orebody
			19	351.10	Orebody	17B	495.70	Orebody
			20	359.27	Orebody	17C	495.84	Orebody
			21	362.92	Footwall	17D	495.94	Orebody
						17E	496.01	Orebody
						18	499.22	Orebody
						19A	504.17	Orebody
						19B	504.23	Orebody
						19C	504.32	Orebody
						19D	504.36	Orebody
						19E	504.48	Orebody
						19F	504.57	Orebody
						19G	504.73	Orebody
						19H	504.80	Orebody
						20A	510.30	Orebody
						20B	510.40	Orebody
						20C	510.49	Orebody
						20D	510.59	Orebody
						21	516.64	Footwall
						22	517.64	Footwall
						23	526.80	Footwall
						24	527.20	Footwall

Appendix XII continued.

Drill hole: GDP 588; Section: 13350		
Sample no.	Depth/m	Location in deposit
Q-1	374.86	Hanging wall
Q-2	391.44	Hanging wall
1A	401.72	Hanging wall
1B	401.81	Hanging wall
1C	401.85	Hanging wall
1D	401.89	Hanging wall
1E	401.92	Hanging wall
1F	401.94	Hanging wall
2A	403.19	Hanging wall
2B	403.31	Hanging wall
3	424.94	Orebody
4A	430.5	Orebody
4B	430.58	Orebody
4C	430.71	Orebody
5	431.33	Orebody
X-1A	432.1	Orebody
X-1B	432.36	Orebody
6	437.01	Orebody
7	444.24	Orebody
8	445.5	Orebody
X-2A	447.4	Orebody
X-2B	447.54	Orebody
9A	452.11	Orebody
9B	452.26	Orebody
10A	458.69	Orebody
10B	458.83	Orebody
10C	458.99	Orebody
10D	459.11	Orebody
11A	461.82	Orebody
11B	461.94	Orebody
11C	462.08	Orebody
X-3	463.29	Orebody
X-4	463.77	Orebody
11D	463.9	Orebody
12	463.97	Orebody
13A	465.48	Orebody
13B	465.58	Orebody
X-5	467.39	Orebody
14A	468.31	Orebody
14B	469.52	Orebody
15	469.52	Orebody
16	474.45	Orebody
17	480.27	Orebody
18A	487.93	Orebody
18B	488.01	Orebody
18C	488.05	Orebody
19A	496.11	Orebody
19B	496.18	Orebody
19C	496.26	Orebody
19D	496.32	Orebody
20A	505.69	Orebody
20B	505.82	Orebody
21B	506.96	Orebody
22A	512.63	Orebody
22B	512.74	Orebody
22C	512.85	Orebody
23	514.71	Orebody
24A	521.32	Orebody
24B	521.42	Orebody
24C	521.46	Orebody
25A	523.64	Footwall
25B	523.85	Footwall
26	526.82	Footwall

Drill hole: GDP 524; Section: 13350		
Sample no.	Depth/m	Location in deposit
1A	210.49	Orebody
1B	210.53	Orebody
1C	210.55	Orebody
1D	210.67	Orebody
1E	210.96	Orebody
1F	211.03	Orebody
2A	216.71	Orebody
2B	216.87	Orebody
3A	217.38	Orebody
3B	217.57	Orebody
4A	220.93	Orebody
4B	221.02	Orebody
5	222.65	Orebody
6A	223.99	Orebody
6B	224.26	Orebody
7	228.36	Orebody
8	236.2	Orebody
9A	236.62	Orebody
9B	250.29	Orebody
10A	250.5	Orebody
10B	253.67	Orebody
10C	253.81	Orebody
11A	259.73	Orebody
11B	259.8	Orebody
12A	259.91	Orebody
12B	260.07	Orebody
12C	259.91	Orebody
12D	260.07	Orebody
13	266.46	Orebody
14	273.27	Footwall

Drill hole: GDP 524; Section: 13650		
Sample no.	Depth/m	Location in deposit
1	162.27	Hanging wall
2A	169.45	Orebody
2B	169.55	Orebody
3A	170.35	Orebody
3B	170.5	Orebody
3C	170.65	Orebody
4	172.78	Orebody
5	172.84	Orebody
6	174.6	Orebody
7A	176.55	Orebody
7B	176.65	Orebody
7C	176.7	Orebody
8A	189.47	Orebody
8B	189.52	Orebody
8C	189.58	Orebody
9A	191.34	Orebody
10A	192.26	Orebody
10B	196.76	Orebody
10C	196.84	Orebody
10D	196.86	Orebody
11A	196.91	Orebody
11B	204.41	Orebody
12A	204.6	Orebody
12B	205.06	Orebody
13	205.19	Orebody
14	205.7	Orebody
15A	205.9	Orebody
15B	205.98	Orebody
15C	216.06	Orebody
15D	216.15	Orebody
15E	216.22	Orebody
16A	218.02	Orebody
16B	218.08	Orebody
17A	220.05	Orebody
17B	220.17	Orebody
17C	220.21	Orebody
17D	220.24	Orebody
18A	222.59	Orebody
18B	222.72	Orebody
18C	222.82	Orebody
19A	225.7	Orebody
19B	225.87	Orebody
19C	225.93	Orebody
20A	232.42	Orebody
20B	232.56	Orebody
20C	232.7	Orebody
21	239.01	Orebody
22	244.3	Orebody
23A	246.86	Orebody
23B	247.02	Orebody
24	255.08	Footwall
25A	259.26	Footwall
25B	259.38	Footwall
25C	259.45	Footwall

Appendix XII continued.

Drill hole: GDP 587; Section: 13650

Sample no.	Depth/m	Location in deposit
1A	373.77	Hanging wall
1B	373.98	Orebody
2A	376.03	Orebody
2B	376.17	Orebody
2C	376.38	Orebody
2D	376.55	Orebody
3A	379.97	Orebody
3B	380.14	Orebody
4A	390.84	Orebody
4B	390.99	Orebody
5	392.04	Orebody
6	394.23	Orebody
7	396.02	Orebody
8A	402.37	Orebody
8B	402.42	Orebody
8C	402.66	Orebody
8D	402.83	Orebody
8E	402.91	Orebody
8F	403	Orebody
9	405.77	Orebody
10A	409.15	Orebody
10B	409.38	Orebody
11A	411.87	Orebody
11B	412.15	Orebody
11C	412.82	Orebody
12	412.85	Orebody
13A	415.02	Orebody
13B	415.13	Orebody
13C	415.26	Orebody
13D	415.39	Orebody
13E	415.5	Orebody
13F	415.6	Orebody
13G	415.66	Orebody
13H	415.76	Orebody
14A	420.13	Orebody
14B	420.39	Orebody
15	429.2	Orebody
16A	429.44	Orebody
16B	429.51	Orebody
16C	434.24	Orebody
17A	434.39	Orebody
17B	436.88	Orebody
18A	437.15	Orebody
18B	443.97	Orebody
X-1	447.4	Orebody
X-2	447.54	Orebody
19	448.2	Orebody
20	452.71	Orebody
21	453.71	Orebody
22A	453.77	Orebody
22B	453.98	Orebody
22C	454.2	Orebody
23A	455.13	Footwall
23B	455.28	Footwall
24C	455.6	Footwall
X-3	463.77	Footwall

Drill hole: GDP 527; Section: 13950

Sample no.	Depth/m	Location in deposit
X-1	182.9	Hanging wall
1A	189.2	Hanging wall
1B	189.31	Hanging wall
2A	196.92	Orebody
2B	197.08	Orebody
3	200.21	Orebody
4A	201	Orebody
4B	201.08	Orebody
4C	201.15	Orebody
4D	201.27	Orebody
5A	206.12	Orebody
5B	212.21	Orebody
6A	212.89	Orebody
6B	213.1	Orebody
6C	213.14	Orebody
6D	213.2	Orebody
7	217.48	Orebody
8A	222.71	Orebody
8B	222.83	Orebody
8C	222.86	Orebody
8D	222.97	Orebody
9A	225.66	Orebody
9B	225.7	Orebody
9C	225.81	Orebody
10A	227.03	Orebody
10B	227.09	Orebody
10C	227.27	Orebody
11A	231	Orebody
11B	231.06	Orebody
11C	231.19	Orebody
12A	237.35	Footwall
12B	237.61	Footwall
12C	237.96	Footwall

Drill hole: GDP 452; Section: 13950

Sample no.	Depth/m	Location in deposit
1A	236.67	Hanging wall
1B	236.86	Hanging wall
2A	243.55	Hanging wall
2B	244.77	Hanging wall
3A	247.9	Hanging wall
3B	248.2	Hanging wall
4A	252.7	Hanging wall
4B	252.85	Hanging wall
5A	273.98	Orebody
5B	274.07	Orebody
5C	274.11	Orebody
5D	274.14	Orebody
6	281.02	Orebody
7	281.5	Orebody
8	282.2	Orebody
9A	285.09	Orebody
9B	285.21	Orebody
9C	285.3	Orebody
9D	285.46	Orebody
10A	292.29	Orebody
10B	292.39	Orebody
11A	294	Orebody
11B	296.07	Orebody
12	296.1	Orebody
13	297.37	Orebody
14	302.07	Orebody
15	302.33	Orebody
16A	302.63	Orebody
16B	302.8	Orebody
17A	305.19	Orebody
17B	305.26	Orebody
17C	305.37	Orebody
17D	305.45	Orebody
18A	306.61	Orebody
18B	306.72	Orebody
18C	309.38	Orebody
19A	308.48	Orebody
20A	310.22	Orebody
20B	310.33	Orebody
20C	310.42	Orebody
20D	310.5	Orebody
20E	310.65	Orebody
21	316.08	Orebody
22A	316.92	Orebody
22B	316.98	Orebody
22C	317.05	Orebody
23A	319.03	Orebody
23B	319.06	Orebody
23C	324.84	Orebody
24A	324.77	Orebody
24B	324.84	Orebody
25A	328.33	Orebody
25B	328.49	Orebody
26A	329.6	Orebody
26B	329.78	Orebody
27	332.28	Footwall
28A	340.24	Footwall
28B	340.48	Footwall

Appendix XII continued.

Samples from orebody in open pit			Floating samples from pit	
Sample no.	Position in pit	Description	Sample no.	Description
114/02/1	(13180-13230N) south pit	Quartz-calcite vein	EH-001	BIF
114/02/2	(13180-13230N) south pit	BIF	EH-002	BIF
114/02/3	(13180-13230N) south pit	Quartz-calcite vein	EH-003	BIF
114/02/4	(13180-13230N) south pit	BIF	EH-004	BIF
116/005/1	(13340-13380N) central pit	BIF	EH-005	BIF
117/17/1	(13730-13780N) north pit	BIF	EH-006	BIF
117/17/2	(13730-13780N) north pit	Quartz-calcite vein	EH-007	BIF
117/17/3	(13730-13780N) north pit	BIF	EH-008	BIF
117/17/4	(13730-13780N) north pit	BIF	EH-009	BIF
117/18/1	(13780-13830N) north pit	BIF	EH-010	Schist in hanging wall
117/02/3	(13480-13540N) central pit	BIF	EH-011	BIF
117/02/4	(13480-13540N) central pit	BIF	EH-012	BIF
114/02/6	(13480-13540N) central pit	BIF	PH-001	BIF
114/02/8	(13480-13540N) central pit	BIF	PH-002	BIF
114/02/9	(13480-13540N) central pit	BIF	PH-003	BIF
118/21/1	(13930-13980N) north pit	BIF	PH-004	BIF
118/21/2	(13930-13980N) north pit	BIF	PH-005	BIF
118/21/3	(13930-13980N) north pit	BIF	PH-006	BIF
118/21/4	(13930-13980N) north pit	BIF	PH-007	Volcanic clast in hanging wall
118/21/5	(13930-13980N) north pit	BIF	PH-008	BIF
118/21/6	(13930-13980N) north pit	BIF	PH-009	Tuff in hanging wall
118/21/7	(13930-13980N) north pit	BIF	NQH-001	Quartz-carbonate vein
118/21/8	(13930-13980N) north pit	BIF	NQH-002	BIF
118/21/9	(13930-13980N) north pit	BIF	NQH-003	BIF
118/21/10	(13930-13980N) north pit	BIF	NQH-004	BIF
118/21/11	(13930-13980N) north pit	BIF	NQH-005	BIF
118/21/12	(13930-13980N) north pit	BIF	NQH-006	BIF
118/21/13	(13930-13980N) north pit	BIF	NQH-007	Quartz-carbonate vein
118/21/14	(13930-13980N) north pit	BIF	NQH-008	BIF
118/21/15	(13930-13980N) north pit	BIF	NQH-009	BIF
118/21/16	(13930-13980N) north pit	BIF	NQH-010	BIF
			NQH-011	BIF
			NQH-012	BIF
			NQH-013	Schist
			NQH-014	BIF
			NQH-015	BIF
			NQH-016	BIF
			NQH-017	BIF
			NQH-018	BIF
			NQH-019	Schist
			MSH/W-1	BIF
			MSH/W-2	BIF
			13175/2A	BIF
			13175/2B	BIF
			13175/2C	BIF
			131775/2D	BIF